

TIMESCALES AND CONDITIONS FOR THE AQUEOUS ALTERATION  
OF CHONDRITES

A DISSERTATION SUBMITTED TO THE GRADUATE DIVISION OF THE  
UNIVERSITY OF HAWAI'I AT MĀNOA IN PARTIAL FULFILLMENT OF THE  
REQUIREMENTS FOR THE DEGREE OF

DOCTOR OF PHILOSOPHY

IN

GEOLOGY & GEOPHYSICS

AUGUST 2015

By

Christine E. Jilly

Dissertation Committee:

Gary R. Huss, Chairperson

Julia E. Hammer

Alexander N. Krot

Michael J. Mottl

G. Jeffrey Taylor

Keywords: Meteorites; Carbonaceous Chondrites; Astrobiology; Solar System Formation;  
Secondary Ion Mass Spectrometry

## ACKNOWLEDGEMENTS

I thank my great research advisor Gary Huss for helping me on this journey to a Ph.D. I came into the Geology and Geophysics department after receiving my undergraduate degree in Astronomy. Despite the large learning curve involved with changing disciplines, Gary was willing to take me on as a graduate student and showed nothing but patience over the years. I couldn't have completed this degree without his wisdom and insight. I thank Ed Scott for opening my eyes to the world of planetary geology. Sasha Krot was instrumental throughout the entire course of my study, for both his vast knowledge of chondritic processes, and for his deadpan humor. I would like to thank Jeff Gillis-Davis for hiring me as a research assistant studying the lunar surface, which was fascinating, and opened the door to many other research opportunities. I thank Jeff Taylor for keeping me entertained with his endless wit and knowledge about all things planetary. Thank you to Julia Hammer for helping me understand petrology and mineralogy, and to Eric Hellebrand for teaching me the ways of the electron microprobe. The HIGP cosmochemistry group (past and present) was a great research family, and I benefitted greatly from conversations and discussions with the following researchers and collaborators: Trish Doyle, Manavi Jadhav, Klaus Keil, Kazu Nagashima, Ryan Ogliore, Devin Schrader, Myriam Telus, and Aurelien Thomen. Similarly, countless colleagues within the UH NASA Astrobiology Institute have helped me along the way, including Stephen Freeland, Lydia Hallis, Karen Meech, and Mike Mottl. My graduate studies were greatly enhanced by internships and field programs with David Kring, Ian Hutcheon, and Ben Jacobsen.

This research would not have been possible without the various funding sources from NASA. This work was supported by NASA Headquarters under the NASA Earth and Space Science Fellowship Program - Grant NNX14AO29H, as well as NASA cosmochemistry grants NNX11AG78G and NNX14AI19G (G. R. Huss, PI), and NAI cooperative agreement NNA04CC08A (K. Meech, PI). I thank the Johnson Space Center's Meteorite Working Group, the Museum of Natural History Vienna, and the Smithsonian Institution for providing the meteorite samples and for the special thin section preparations.

On a more personal note, I thank my wonderful G&G friends for their moral support. I especially thank my amazing parents for convincing me to leave my job at the toy company and move to a tiny island, and for supporting me in every way possible. I thank the rest of my family – Nicole, Mike, Catalina, and the Rehaks – for their love and encouragement. Last (but not least), I thank my incredible husband Josh for always loving me and holding my hand through the ups and downs of grad school.

## ABSTRACT

It has become well-recognized that water played a critical role in the early geological evolution of materials through observation of hydrated phases in chondritic meteorites. However, details about the mechanism, timing, and conditions of aqueous alteration are poorly constrained. This dissertation investigates water-driven processes in Renazzo-like (CR) carbonaceous chondrites, with some comparison to the heavily altered and Mighei-like (CM) chondrites. CR chondrites were chosen as the focus of this study, as they are the only chondrite group to range from practically anhydrous to completely hydrated, providing petrographic context for the aqueous alteration process.

The central goal of the thesis is to elucidate the complete mechanism of aqueous alteration, from primary anhydrous components to secondary minerals. This research uses a variety of micro-analytical techniques to address three main objectives: 1) to detail the petrographic context, 2) to quantify the onset and duration of alteration using radiometric dating, and 3) to constrain the fluid chemistry and conditions for aqueous alteration. On a microscopic scale, fine-grained matrices and glassy mesostases were the first phases to become altered, allowing for elemental transport over short distances ( $< 100$  microns). As alteration progressed, the iron-metal was oxidized, and silicate phenocrysts were pseudomorphically replaced.  $^{53}\text{Mn}$ - $^{53}\text{Cr}$  radiometric dating of secondary carbonates in CR chondrites show that aqueous alteration began quickly after accretion of the parent body,  $\sim 4$  Myr after the beginning of the Solar System. This is contemporaneous with dolomite formation in the CM chondrite Sutter's Mill and with carbonate formation in other CM chondrites. However, the calcite age from a heavily hydrated CR lithology indicates that late-stage alteration occurred  $\sim 12$  Myr after the beginning of the Solar System. The oxygen isotopic compositions of magnetite and carbonate minerals reveal that altering fluid evolved toward lighter oxygen composition as alteration progressed on the CR parent body. Oxygen isotope geothermometry indicates low precipitation temperatures (near  $\sim 40^\circ\text{C}$ ) for CR alteration assemblages. Simple geochemical models of secondary assemblages reveal that alteration occurred under neutral to alkaline pH ( $>7$ ), and under high  $\text{H}_2\text{S}$  fugacity relative to  $\text{O}_2$ . This research shows that the aqueous alteration process was spatially variable on the CR parent body, and that the localized environmental conditions contributed to unique alteration assemblages.

## TABLE OF CONTENTS

ACKNOWLEDGEMENTS .....	ii
ABSTRACT.....	iii
TABLE OF CONTENTS.....	iv
LIST OF TABLES .....	viii
LIST OF FIGURES .....	ix
LIST OF ABBREVIATIONS, MINERALS, AND VARIABLES .....	xiv
CHAPTER 1:	
INTRODUCTION .....	1
1.1 Chondrites: Time capsules for the earliest Solar System processes .....	1
1.2 The timescales for alteration.....	2
1.3 The origin of water in the Solar System .....	4
CHAPTER 2:	
ALTERATION ASSEMBLAGES IN CR CHONDRITES AND THE MINERALOGICAL CONSTRAINTS ON FLUID CHEMISTRY .....	6
2.1 INTRODUCTION.....	7
2.2 APPROACH .....	9
2.2.1 Thin Section Petrography .....	9
2.2.2 Geochemical Modeling.....	11
2.3 RESULTS.....	12
2.3.1 Descriptions of CR chondrites.....	12
2.3.2 Geochemical modeling of CR alteration lithologies .....	36
2.4. DISCUSSION .....	40
2.4.1 Carbonate-magnetite-sulfide lithologies.....	40
2.4.2 The origin of phosphates .....	42
2.4.3 Formation of calcium-iron silicates in MIL 090292,12 .....	43
2.4.4 Is MIL 090292 a CR chondrite? .....	44
2.5 CONCLUSIONS.....	45
CHAPTER 3:	

<sup>53</sup> MN- <sup>53</sup> CR RADIOMETRIC DATING OF SECONDARY CARBONATES IN CR CHONDRITES: TIMESCALES FOR PARENT BODY AQUEOUS ALTERATION .....	47
3.1 INTRODUCTION.....	48
3.2 ANALYTICAL METHODS.....	50
3.2.1 Thin section mineralogy and petrography .....	50
3.2.2 Secondary Ion Mass Spectrometry (SIMS).....	51
3.2.3 <sup>55</sup> Mn/ <sup>53</sup> Cr relative sensitivity factors.....	53
3.3 RESULTS.....	55
3.3.1 Sample petrography.....	55
3.3.2 Manganese-chromium isotopes in matrix calcite .....	57
3.3.3 Manganese-chromium isotopes in dolomite from a dark inclusion .....	60
3.4 DISCUSSION .....	62
3.4.1 Validity of isochron diagrams .....	62
3.4.2 Absolute ages and anchoring to D’Orbigny .....	64
3.4.3 Aqueous alteration in the CR parent body.....	68
3.5 CONCLUSIONS.....	75
CHAPTER 4:	
<sup>53</sup> MN- <sup>53</sup> CR DATING OF AQUEOUSLY FORMED CARBONATES IN THE CM2 LITHOLOGY OF THE SUTTER’S MILL CARBONACEOUS CHONDRITE .....	76
4.1 INTRODUCTION.....	77
4.2 SAMPLES AND ANALYTICAL METHODS.....	78
4.2.1 Sutter’s Mill SM51-1.....	78
4.2.2 Secondary Ion Mass Spectrometry (SIMS).....	80
4.2.3 Relative Sensitivity Factors (RSF) .....	81
4.3 RESULTS.....	83
4.4 DISCUSSION .....	89
4.4.1 Aqueous alteration in the CM parent body.....	89
4.4.2 Relative ages of dolomite and calcite .....	94
4.4.3 Relevance to other measured isotopic systems in Sutter’s Mill .....	95
4.5 CONCLUSIONS.....	97
CHAPTER 5:	

LOW TEMPERATURE AQUEOUS ALTERATION ON THE CR CHONDRITE PARENT BODY: IMPLICATIONS FROM <i>IN SITU</i> OXYGEN ISOTOPES.....	98
5.1 INTRODUCTION.....	99
5.2 EXPERIMENTAL TECHNIQUES .....	101
5.2.1 CR chondrite samples and petrography.....	101
5.2.2 Secondary Ion Mass Spectrometry (SIMS).....	102
5.3 RESULTS.....	104
5.3.1 Thin section mineralogy and petrography .....	104
5.3.2 Oxygen isotopes in calcite.....	108
5.3.3 Oxygen isotopes in dolomite .....	112
5.3.4 Oxygen isotopes in magnetite.....	113
5.4 DISCUSSION .....	116
5.4.1 Influence of terrestrial weathering.....	117
5.4.2 Distinct properties of MIL 090292.....	119
5.4.3 Carbonate oxygen isotopes: A proxy for fluid evolution on the CR parent body .....	120
5.4.4 Magnetite oxygen isotopes: Orientation effects in SIMS or fluid evolution?.....	122
5.4.5 Models of asteroidal fluid evolution.....	125
5.4.6 Lithologies and mineral contributions to the CR whole-rock mixing line.....	128
5.4.7 Oxygen isotope geothermometry.....	135
5.4.8 The evolving oxygen composition of fluid on the CR parent body .....	138
5.5 CONCLUSIONS.....	140
CHAPTER 6:	
CONCLUDING REMARKS AND FUTURE STEPS .....	142
6.1 Classification of MIL 090292.....	143
6.2 Methods for more precise and accurate $^{53}\text{Mn}$ - $^{53}\text{Cr}$ dating.....	143
6.3 $^{26}\text{Al}$ - $^{26}\text{Mg}$ chondrule-forming ages in CR chondrites.....	144
6.4 SIMS crystal orientation effects in magnetite .....	144
6.5 Investigations into oxygen isotope trends for CR lithologies.....	145
APPENDIX A:	
METHODS FOR DETERMINING THE CARBONATE MINERAL RELATIVE SENSITIVITY FACTORS .....	146

A.1 Experiments on the synthesis of manganese and chromium bearing calcite .....	146
Saturation.....	148
A.2 Manganese and chromium ion implantation studies .....	150
APPENDIX B:	
PETROGRAPHY AND CLASSIFICATION OF NWA 7402: A NEW SULFIDE-RICH UNEQUILIBRATED ORDINARY CHONDRITE .....	154
B.1 INTRODUCTION.....	155
B.2 PETROGRAPHY .....	155
B.3 TECHNIQUES AND SAMPLE CLASSIFICATION .....	157
B.3.1 Compositional classification.....	157
B.3.2 Petrologic type. ....	160
B.3.3 Weathering grade. ....	164
B.3.4 Shock classification. ....	165
B.4 DISCUSSION.....	165
B.4.1 Sulfide abundances in Ordinary Chondrites. ....	166
B.4.2 Anomalous chromium composition of iron-bearing olivines. ....	166
B.5 CONCLUSION .....	167
APPENDIX C:	
THIN SECTION IMAGES.....	168
REFERENCES .....	192

## LIST OF TABLES

<b>Table 2.1</b>	List of CR chondrites in petrography study.....	10
<b>Table 2.2</b>	EPMA analyses for CR3 matrices.....	23
<b>Table 2.3</b>	EPMA analyses of andradite in MIL 090292 .....	26
<b>Table 3.1</b>	List of CR chondrites in manganese-chromium study.....	51
<b>Table 3.2</b>	Manganese-chromium isotopes in CR calcite.....	59
<b>Table 3.3</b>	Manganese-chromium isotopes in CR dolomite.....	60
<b>Table 4.1</b>	Manganese-chromium isotopes in the CM chondrite Sutter's Mill.....	87
<b>Table 5.1</b>	List of CR chondrites in oxygen-isotope study.....	102
<b>Table 5.2</b>	Oxygen isotopic compositions of calcite in CR chondrites .....	109
<b>Table 5.3</b>	Oxygen isotopic compositions of dolomite in CR chondrites .....	112
<b>Table 5.4</b>	Oxygen isotopic compositions of magnetite in CR chondrites.....	114
<b>Table A1</b>	List of reagents in calcite precipitation experiment #1 .....	148
<b>Table A2</b>	List of reagents in calcite precipitation experiment #2 .....	148
<b>Table B1</b>	EPMA analyses of olivine grains in NWA 7402 .....	159
<b>Table B2</b>	Modal abundance of opaques in NWA 7402 .....	159

## LIST OF FIGURES

<b>Figure 2.1</b>	BSE images of fine-grained lithologies in Al Rais, USNM 6997 .....	13
<b>Figure 2.2</b>	BSE image of a dark inclusion from EET 87770,30 .....	15
<b>Figure 2.3</b>	BSE images of dolomite and a type II chondrule in EET 92159,20 .....	17
<b>Figure 2.4</b>	BSE image of secondary phases in the matrix of GRO 95577,69.....	18
<b>Figure 2.5</b>	Optical photomicrograph and BSE image of a chondrule pseudomorph in GRO 95577,69.....	20
<b>Figure 2.6</b>	BSE images of terrestrial weathering and a dark inclusion in MET 00426,60 .....	21
<b>Figure 2.7</b>	Fe-Si-Mg ternary diagram for matrix compositions of MET 00426,60 and QUE 99177,69 compared with other CR chondrites .....	24
<b>Figure 2.8</b>	BSE image of a magnetite nodule in MIL 090292,12.....	26
<b>Figure 2.9</b>	BSE images of a dark inclusion in QUE 99177,06 and a metamorphosed clast in QUE 99177,69 .....	29
<b>Figure 2.10</b>	BSE image and false-color x-ray maps of a partially altered chondrule in Renazzo, N1127.....	32
<b>Figure 2.11</b>	S-Fe-Ni ternary diagram for sulfide compositions in Renazzo N1127 .....	33
<b>Figure 2.12</b>	BSE image and false-color x-ray map of a calcite-sulfide-magnetite lithology in Renazzo, N1127.....	34
<b>Figure 2.13</b>	BSE images of dark inclusion morphologies in Renazzo, N1127.....	35
<b>Figure 2.14</b>	Bivariate activity plots of H <sub>2</sub> S/O <sub>2</sub> versus pH for varying temperatures.....	37
<b>Figure 2.15</b>	BSE image and EDX line-scan of a phosphate-magnetite assemblage in Renazzo, N1127.....	38
<b>Figure 2.16</b>	Bivariate activity plots of O <sub>2</sub> versus pH for varying SiO <sub>2</sub> activities.....	39
<b>Figure 2.17</b>	BSE images of calcium-iron-silicates in MIL 090292,12 .....	43
<b>Figure 3.1</b>	BSE image of fine-grained calcite in the matrix of Renazzo, N1126 .....	50
<b>Figure 3.2</b>	BSE images of calcite morphologies in the Renazzo, N1127 matrix.....	56
<b>Figure 3.3</b>	BSE image of a dark inclusion in Renazzo, N1126 .....	56
<b>Figure 3.4</b>	BSE image of matrix phases in GRO 95577,69 .....	57
<b>Figure 3.5</b>	BSE images of manganese-chromium SIMS pits for calcite and dolomite measured in CR chondrites.....	58

<b>Figure 3.6</b> Manganese-chromium isochron diagrams for calcite in Renazzo, N1127 and GRO 95577,69.....	60
<b>Figure 3.7</b> Manganese-chromium isochron diagrams for dolomite in Renazzo, N1126, for two values of RSF.....	61
<b>Figure 3.8</b> Manganese-chromium isotope diagram depicting the effect of RSF on the slope of the isochron.....	62
<b>Figure 3.9</b> Graphs of $\delta^{53}\text{Cr}^*$ versus $1/^{52}\text{Cr}^+$ for calcite and dolomite in CR chondrites.....	63
<b>Figure 3.10</b> Plot depicting the absolute ages of carbonates in CR chondrites measured by manganese-chromium compared with literature data.....	66
<b>Figure 4.1</b> BSE images of intergrown calcite and dolomite grains in SM 51-1 .....	78
<b>Figure 4.2</b> BSE image of a chondrule pseudomorph in SM 51-1 .....	79
<b>Figure 4.3</b> BSE image of synthetic manganese and chromium bearing calcite used for standardization .....	82
<b>Figure 4.4</b> Graph depicting the heterogeneity of manganese and chromium composition in the synthetic calcite standards.....	84
<b>Figure 4.5</b> The RSF of standard measurements for San Carlos olivine and a synthetic manganese and chromium-bearing calcite.....	85
<b>Figure 4.6</b> BSE images of SIMS pits in SM 51-1 dolomite grains measured for manganese-chromium .....	86
<b>Figure 4.7</b> Manganese-chromium isochron diagram for dolomite in Sutter's Mill 51-1.....	87
<b>Figure 4.8</b> Manganese-chromium isotope diagram depicting the effect of RSF on the slope of the dolomite isochron.....	88
<b>Figure 4.9</b> Graphs of $\delta^{53}\text{Cr}$ vs. $1/^{52}\text{Cr}^+$ and $^{55}\text{Mn}$ vs. $1/^{52}\text{Cr}^+$ for dolomite in Sutter's Mill. 90	
<b>Figure 4.10</b> Plot depicting the absolute ages of carbonates in CR chondrites measured by manganese-chromium compared with literature data.....	92
<b>Figure 5.1</b> BSE images of calcite in the GRO 95577,69 matrix.....	105
<b>Figure 5.2</b> BSE images of magnetite morphologies in GRO 95577,69 .....	106
<b>Figure 5.3</b> BSE images of calcite and magnetite in Renazzo, N1127 and QUE 99177,06 .....	107
<b>Figure 5.4</b> BSE images of characteristic SIMS pits in CR chondrite carbonate grains measured for oxygen isotopes .....	110
<b>Figure 5.5</b> Three oxygen-isotope diagram for secondary calcites in CR chondrites .....	111

<b>Figure 5.6</b>	Three oxygen-isotope diagram for secondary dolomites in CR chondrites .....	113
<b>Figure 5.7</b>	BSE images of characteristic SIMS pits in CR chondrite magnetite grains measured for oxygen isotopes .....	115
<b>Figure 5.8</b>	Three oxygen-isotope diagram for secondary magnetites in CR chondrites .....	116
<b>Figure 5.9</b>	Three oxygen-isotope diagram comparing the magnetite and carbonate trends for CR chondrites .....	128
<b>Figure 5.10</b>	Three oxygen-isotope diagrams for secondary minerals in CR chondrites, in terms of petrologic type, and distinct lithologies.....	130
<b>Figure 5.11</b>	Graph depicting the variation of oxygen isotopes for matrix calcite versus the petrologic type for four CR chondrites .....	133
<b>Figure 5.12</b>	BSE image and false-color x-ray maps of a unique dark inclusion found in Renazzo N1126.....	134
<b>Figure 5.13</b>	Diagram of fractionation curves for precipitation of magnetite and calcite from an aqueous solution at varying temperature .....	136
<b>Figure 5.14</b>	BSE image of a calcite and magnetite assemblage in Al Rais, USNM 6997 .....	137
<b>Figure 5.15</b>	Three oxygen-isotope diagram depicting the mass-dependent fractionation trends between calcite and magnetite in Al Rais, USNM 6997 and GRO 95577,69 .....	138
<b>Figure 5.16</b>	Model for the evolution of CR water during progressive alteration.....	139
<b>Figure A1</b>	Photographs of precipitation experiment apparatus and solutions .....	150
<b>Figure A2</b>	Photomicrograph of chromium-implanted carbonate samples .....	151
<b>Figure A3</b>	Characteristic implant profiles of chromium isotopes measured with SIMS .....	152
<b>Figure B1</b>	Photograph of the NWA 7402 whole rock .....	155
<b>Figure B2</b>	BSE image of NWA 7402 thin section showing variation in chondrule size and fragmented matrix .....	156
<b>Figure B3</b>	BSE image of an aluminous chondrule in NWA 7402 .....	157
<b>Figure B4</b>	Histograms of fayalite content in chondrule olivines from NWA 7402 .....	161
<b>Figure B5</b>	Histograms for the chromium content in chondrule olivine grains with FeO > 2 wt% from NWA 7402 .....	162
<b>Figure B6</b>	A plot of the standard deviation versus the mean of the Cr <sub>2</sub> O <sub>3</sub> content of ferroan olivine (FeO > 2 wt%) for NWA 7402 olivines .....	162

<b>Figure B7</b> A plot of Raman spectral parameters for NWA 7402 compared with classified chondrites .....	164
<b>Figure C1</b> Al Rais USNM 6997 Optical microscope (transmitted light) mosaic .....	168
<b>Figure C2</b> Al Rais USNM 6997 Backscattered electron map .....	168
<b>Figure C3</b> Al Rais USNM 6997 false-colored x-ray map (RGB = FeCaS).....	169
<b>Figure C4</b> Al Rais USNM 6997 false-colored x-ray map (RGB = MgCaAl) .....	169
<b>Figure C5</b> EET 87770,30 Backscattered electron map.....	170
<b>Figure C6</b> EET 87770,30 false-colored x-ray map (RGB = FeCaS) .....	170
<b>Figure C7</b> EET 87770,30 false-colored x-ray map (RGB = MgCaAl).....	171
<b>Figure C8</b> EET 92159,20 Backscattered electron map.....	171
<b>Figure C9</b> EET 92159,20 false-colored x ray map (RGB = FeCaS) .....	172
<b>Figure C10</b> EET 92159,20 false-colored x-ray map (RGB = MgCaAl).....	172
<b>Figure C11</b> GRA 95229,18 Optical microscope (cross-polarized light) mosaic .....	173
<b>Figure C12</b> GRA 95229,18 Optical microscope (reflected light) mosaic .....	173
<b>Figure C13</b> GRO 95577,69 Optical microscope (reflected light) mosaic .....	174
<b>Figure C14</b> GRO 95577,69 Optical microscope (stereo microscope) mosaic.....	174
<b>Figure C15</b> GRO 95577,69 Backscattered electron map.....	175
<b>Figure C16</b> GRO 95577,69 false-colored x-ray map (RGB = FeCaS).....	175
<b>Figure C17</b> GRO 95577,69 false-colored x-ray map (RGB = MgCaAl) .....	176
<b>Figure C18</b> MAC 87320,9 Backscattered electron map .....	177
<b>Figure C19</b> MAC 87320,9 false-colored x-ray map (RGB = FeCaS) .....	178
<b>Figure C20</b> MAC 87320,9 false-colored x-ray map (RGB = FeCaS) .....	179
<b>Figure C21</b> MET 00426,60 Optical microscope (transmitted light) mosaic .....	180
<b>Figure C22</b> MET 00426,60 Optical microscope (reflected light) mosaic .....	180
<b>Figure C23</b> MET 00426,60 Backscattered electron map.....	181
<b>Figure C24</b> MET 00426,60 false-colored x-ray map (RGB = FeCaS).....	181
<b>Figure C25</b> MET 00426,60 false-colored x-ray map (RGB = MgCaAl) .....	182
<b>Figure C26</b> MIL 090292,12 Optical microscope (stereo microscope) mosaic.....	183
<b>Figure C27</b> MIL 090292,12 Backscattered electron map.....	183
<b>Figure C28</b> MIL 090292,12 false-colored x-ray map (RGB = FeCaS).....	184
<b>Figure C29</b> MIL 090292,12 false-colored x-ray map (RGB = MgCaAl).....	184

<b>Figure C30</b>	QUE 99177,06 Backscattered electron map.....	185
<b>Figure C31</b>	QUE 99177,69 Optical microscope (reflected light) mosaic.....	185
<b>Figure C32</b>	QUE 99177,69 Backscattered electron map.....	186
<b>Figure C33</b>	QUE 99177,69 false-colored x-ray map (RGB = FeCaS).....	186
<b>Figure C34</b>	QUE 99177,69 false-colored x-ray map (RGB = MgCaAl).....	187
<b>Figure C35</b>	Renazzo N1126 Backscattered electron map .....	187
<b>Figure C36</b>	Renazzo N1126 false-colored x-ray map (RGB = FeCaS).....	188
<b>Figure C37</b>	Renazzo N1126 false-colored x-ray map (RGB = MgCaAl) .....	188
<b>Figure C38</b>	Renazzo N1127 Backscattered electron map .....	189
<b>Figure C39</b>	Renazzo N1127 false-colored x-ray map (RGB = FeCaS).....	190
<b>Figure C40</b>	Renazzo N1127 false-colored x-ray map (RGB = MgCaAl) .....	190
<b>Figure C41</b>	Renazzo UH 1 false-colored x-ray map (RGB = MgCaS) .....	191
<b>Figure C42</b>	Renazzo UH 1 false-colored x-ray map (RGB = FeNiS) .....	191

## LIST OF ABBREVIATIONS, MINERALS, AND VARIABLES

$\alpha$	oxygen isotope fractionation factor
Albite	$\text{NaAlSi}_3\text{O}_8$
Andradite	$\text{Ca}_3\text{Fe}_2\text{Si}_3\text{O}_{12}$
Anorthite	$\text{CaAl}_2\text{Si}_2\text{O}_8$
at. %	atomic percent
BSE	Back-Scattered Electron
Calcite	$\text{CaCO}_3$
CCAM	Carbonaceous Chondrite Anhydrous Mineral line
Chlorapatite	$\text{Ca}_{10}(\text{PO}_4)_6(\text{Cl})_2$
Chlorite	$(\text{Mg,Fe})_5\text{Al}(\text{Si}_3\text{Al})\text{O}_{10}(\text{OH})_8$
Chrysotile	$\text{Mg}_3\text{Si}_2\text{O}_5(\text{OH})_4$
CI	Ivuna-like Carbonaceous chondrite
CK	Karoonda-like Carbonaceous chondrite
CM	Mighei-like Carbonaceous chondrite
CO	Ormans-like Carbonaceous chondrite
CR	Renazzo-like Carbonaceous chondrite
CV	Vigarano-like Carbonaceous chondrite
DI	Dark Inclusion
Dolomite	$\text{CaMg}(\text{CO}_3)_2$
EDX	Energy-Dispersive X-ray spectroscopy
EET	Elephant Moraine
EPMA	Electron Probe Micro-Analysis
Epsomite	$\text{MgSO}_4 \cdot 7\text{H}_2\text{O}$
Ferrihydrite	$5\text{Fe}_2\text{O}_3 \cdot 9\text{H}_2\text{O}$
$f_{\text{O}_2}$	Oxygen fugacity
Goethite	$\text{FeO}(\text{OH})$
GRA	Graves Nunataks
GRO	Grosvenor Mountains
Gypsum	$\text{CaSO}_4 \cdot 2\text{H}_2\text{O}$

Hematite	$\text{Fe}_2\text{O}_3$
Hydroxyapatite	$\text{Ca}_{10}(\text{PO}_4)_6(\text{OH})_2$
Kirschsteinite	$\text{CaFe}(\text{SiO}_4)$
MAC	MacAlpine Hills
Magnetite	$\text{Fe}_3\text{O}_4$
Merrillite	$\text{Ca}_9\text{NaMg}(\text{PO}_4)_7$
MET	Meteorite Hills
MIL	Miller Range
OC	Ordinary Chondrite
Pentlandite	$(\text{Fe},\text{Ni})_9\text{S}_8$
pH	the negative log of the $\text{H}^+$ activity in solution
Plagioclase	solid solution between $\text{NaAlSi}_3\text{O}_8$ and $\text{CaAl}_2\text{Si}_2\text{O}_8$
Pyrrhotite	$\text{Fe}_{(1-x)}\text{S}$ ; where $x = 0$ to $0.2$
QUE	Queen Alexandra Range
RSF	Relative Sensitivity Factor
Saponite	$\text{Ca}_{0.25}(\text{Mg},\text{Fe})_3((\text{Si},\text{Al})_4\text{O}_{10})(\text{OH})_2 \cdot n\text{H}_2\text{O}$
SEM	Scanning Electron Microscope
Serpentine	$(\text{Mg},\text{Fe})_3\text{Si}_2\text{O}_5(\text{OH})_4$
Siderite	$\text{FeCO}_3$
SIMS	Secondary Ion Mass Spectrometry
Spinel	$\text{MgAl}_2\text{O}_4$
Taenite	$\gamma\text{-(Ni,Fe)}$
TFL	Terrestrial Fractionation Line
Troilite	$\text{FeS}$
UOC	Unequilibrated Ordinary Chondrite
vol.%	volume percent
Whitlockite	$\text{Ca}_9(\text{MgFe})(\text{PO}_4)_6\text{PO}_3\text{OH}$
W/R	water to rock ratio
wt.%	weight percent
Wüstite	$\text{FeO}$
$\chi_{\text{red}}^2$	reduced chi-squared

# CHAPTER 1

## INTRODUCTION

### 1.1 Chondrites: Time capsules for the earliest Solar System processes

Meteorites have been recognized as important investigative tools in the field of cosmochemistry for over 200 years. Once meteorites were accepted in the scientific community as extraterrestrial material, it became clear that they held invaluable information about Solar System processes. Approximately 86% of all meteorites are chondrites, which are primitive rocks composed of undifferentiated material assembled within a few million years after the birth of the sun. Chondrites are mixtures of components that were present or formed in the solar disk, including chondrules, refractory inclusions, fine-grained silicate dust, and metals and sulfides (McSween and Huss, 2010). In addition, petrologic studies have shown that many chondrites contain hydrated minerals formed via aqueous alteration of these primitive components (e.g., Brearley, 2006). These observations reveal that water played an important role in the geologic evolution of the Solar System.

This dissertation investigates water-driven processes in chondrites to understand the action and origin of water in the early Solar System. Among the various chondrite groups, the Ivuna-like (CI) and the Mighei-like (CM) chondrites dominate aqueous alteration literature, as they are the most extensively hydrated. The relative amount of secondary processing, including both aqueous alteration and thermal metamorphism, is classified in terms of the “petrologic type”. Meteoritic petrologic types range from 1 to 6, reflecting different degrees of parent body processing. Type 3 is considered to be the least altered, while values greater than 3 represent increasing degrees of thermal metamorphism, and values less than 3 indicate increasing aqueous alteration (e.g., Weisberg et al., 2006). The type 3 chondrites can be subdivided from 3.0 to 3.9 to describe the degree of iron equilibration due to minor thermal processing. All CI chondrites are designated as petrologic type 1, meaning that they are heavily aqueously altered, while CM chondrites range from type 1 to type 2. No primitive type 3 CM chondrites have been documented. The heavily altered nature of the CI and CM groups allows for in-depth study of the hydrated mineralogy (Brearley, 2006). However, primary phases are rare in CM and CI chondrites, and therefore the mineralogy of the precursor material is based upon many

assumptions. Conversely, the Renazzo-like (CR) chondrites range from practically anhydrous type 3, to completely hydrated type 1 (Weisberg et al., 1993; Weisberg and Huber, 2007; Abreau and Brearley, 2010). Most CR chondrites are classified as type 2 where some, but not all, of the primary phases have been altered; such partial replacement provides petrographic context for the aqueous alteration mechanism. A second alteration scheme has been proposed for chondrites, which reserves a type 1 classification for chondrites without chondrules; therefore, only CI chondrites are classified as type 1 (Rubin et al., 2007; Harju et al., 2014). In this scheme, the CM and CR chondrites are placed on an alteration scale ranging from type 2.0 (completely hydrated) to 3.0 (primitive anhydrous), where CM chondrites range from type 2.0 to 2.6, and CR chondrites range from type 2.0 to 2.8. In addition, most CR meteorites have escaped thermal metamorphism that can obscure aqueous alteration signatures, as has occurred in Vigarano-like (CV) chondrites (Krot et al., 1998). For these reasons, CR chondrites provide a unique view into the action of water.

Chapter two investigates the interactions between water and primitive rock in a detailed petrographic study of CR chondrites. As stated above, CR chondrites retain both primary and secondary minerals, essentially providing a snapshot of the progression of alteration. The least-altered CR specimens serve as a proxy for the early stages of water-rock interaction, and can be compared with the most heavily hydrated samples. Balanced chemical reactions are determined from the changes in mineralogy to describe the physical alteration process. Simple geochemical modeling is explored in Chapter two to constrain the pH, fluid chemistry, and oxygen fugacity conditions required to form the observed secondary mineral assemblages.

## **1.2 The timescales for alteration**

Radiometric dating of secondary minerals in chondrites has suggested that water altered the primitive material within the first few million years after the formation of calcium-aluminum-rich inclusions (CAIs), thought to be the earliest objects to form in the solar system (Krot et al., 2006; Connelly et al., 2012). It is generally agreed that most aqueous alteration processes occurred on the asteroidal parent body after accretion; however, it has also been argued that some alteration features observed in chondrites must have been formed before the final assembly of the meteorite parent bodies (e.g., Weisberg and Prinz, 1998). Radiometric

dating, combined with mineralogical and isotopic studies, can be used to constrain the location of alteration of chondritic material. The solar disk is thought to have dissipated within ~5 Myr after CAI formation (Cyr et al., 1998; Brearley et al., 2006), due to the accretion of dust and gas by the sun and planets and dispersal by strong solar winds. Observations of young stellar objects in clusters in our galaxy indicate that nearly half have lost their accretion disks by ~3 Myr, and nearly all have lost the disks by 6 Myr (Haisch et al., 2001). This hypothesis is corroborated by the lack of fine-grained matrix in the late-formed CH and CB chondrites (e.g., Weisberg et al., 2006). Chondritic parent bodies are thought to have accreted perhaps as early as about 2 Myr (Krot et al., 2006) and no later than 3-4 Myr after CAI formation (Cohen and Coker, 2000). Bodies formed before ~1.5 Myr after CAI formation would have had high enough abundances of heat-producing  $^{26}\text{Al}$  to melt the planetary body. Aqueous alteration occurring > 4-5 Myr after CAI formation would therefore favor an asteroidal setting for alteration.

Recent developments in techniques for measuring the  $^{53}\text{Mn}$ - $^{53}\text{Cr}$  radiometric system have allowed for more accurate and consistent ages for secondary minerals in chondrites. Aqueously formed minerals (dolomite, calcite, fayalite) in CI, CM, CV, Ornans-like (CO), and unequilibrated ordinary chondrites (UOCs) have been more precisely measured using matrix-matched standards. The current state of research suggests that alteration began quickly after the accretion of the chondritic parent bodies, driven by internal heating from the decay of  $^{26}\text{Al}$  (e.g., Krot et al., 2006; Fujiya et al., 2012; 2013; Doyle et al., 2015). Chapters three and four investigate the timing of aqueous alteration by measuring the manganese-chromium systematics in CR and CM chondrites. The CR chondrites were of particular interest for this study, as no resolved ages of secondary alteration had ever been reported. Chapter three details the first resolved ages of carbonate formation in two CR chondrites of different petrologic type, providing important constraints on the duration of alteration on the CR parent body. Implications for the heating mechanisms and size of the parent body are discussed.

Chapter four is a radiometric dating case study of a new CM meteorite, Sutter's Mill, which fell in California in 2012. Falls are of particular interest to the meteorite community, because if they are collected quickly they largely escape terrestrial weathering and provide an excellent account of primitive processes. The manganese-chromium system was measured in dolomite from the heavily altered Sutter's Mill chondrite. These measurements are particularly important to this dissertation, as the results are in excellent agreement with recent CM carbonate

ages from the literature. The results from this study therefore validate the methods used in chapters three and four, and provide exciting results on a sought-out sample.

### **1.3 The origin of water in the inner Solar System**

One motivation for this dissertation is the big-picture problem of the origin of water in the inner Solar System, less than about 5 AU from the Sun. Over the past century, we have made vast contributions to understanding the formation of the Solar System through the study of meteorites and development of spacecraft that explore and orbit planets and small bodies (including asteroids and comets). However, an important fundamental question remains unanswered: what is the origin of water on Earth and the terrestrial planets?

With about 70% of its surface area covered by oceans, the Earth stands out as a distinctive planet in the Solar System, being the only terrestrial planet to house liquid water at its surface. We take this for granted; without water, the unique geologic processes that we observe on Earth, such as plate tectonics, could not occur. In addition, water is the foundation of biology and life on Earth, which has not (yet) been found to exist elsewhere. Two main fields of thought currently exist. First, water could have been delivered to the inner planets after accretion from an exogeneous source, such as hydrated asteroids or comets (e.g., Drake and Righter, 2002). The second hypothesis is that the terrestrial planets accreted wet, such that both anhydrous and hydrous minerals were accreted in high enough abundances that the water was not lost during subsequent heating (Drake, 2005). Extensive geological processing on Earth over the past 4.5 billion years overprints the primitive record of planetary formation, obscuring our understanding of our most valuable resource. However, chondrites offer a unique glimpse into the action of water in the early Solar System.

The oxygen isotopic abundances in altered and unaltered minerals can help to constrain the role of volatiles in the early Solar System. The oxygen isotopic composition in a sample reflects processes that occurred both in the nebular environment, and on the asteroidal parent body (e.g. Clayton and Mayeda, 1984; 1999), acting as a tracer for oxygen reservoirs. Chapter five is a systematic study of the oxygen isotopes of secondary minerals in CR chondrites. In this chapter, the compositions of secondary minerals are investigated to understand the fluid evolution on the CR parent body. These analyses have broader implications regarding

temperatures of alteration, and the oxygen composition of the accreted ice. Such analyses allow us to piece together the origin and composition of the water reservoir in early chondritic material. Oxygen isotopic studies of chondrites alone will not likely solve the big picture problem of the origin of Earth's water. However, they will provide important constraints onto the compositions of water and ice in the asteroid belt that may have been transported to the inner planets, providing essential pieces to the larger puzzle.

## CHAPTER 2

### ALTERATION ASSEMBLAGES IN CR CHONDRITES AND THE MINERALOGICAL CONSTRAINTS ON FLUID CHEMISTRY

In preparation for publication as Jilly-Rehak C. E. and Huss G. R. *Alteration assemblages in CR chondrites and the mineralogical constraints on fluid chemistry.*

*Abstract-* Meteorite specimens in the CR chondrite class have experienced varying degrees of aqueous alteration, ranging from fully altered to nearly anhydrous. While much is known about the general mineralogy and petrography of CR chondrites, the alteration process and fluid conditions are poorly constrained. The main purpose of this paper is to provide detailed petrographic information about CR chondrite specimens from all stages of aqueous alteration, to document the alteration mechanism. We describe alteration assemblages in 13 CR chondrite thin sections, ranging from the most heavily altered specimen GRO 95577 (CR1 or 2.0), to the least altered QUE 99177 (CR3 or 2.8). Balanced replacement reactions can be determined from the observed primary and secondary phases in an alteration lithology. We apply simple geochemical models based upon the minimization of Gibb's energy to constrain important alteration conditions, including pH, oxygen fugacity, and fluid chemistry. The alteration assemblages observed in the CR chondrites generally require neutral to alkaline pH conditions. High abundances of sulfides in heavily altered regions (such as matrices and dark inclusions) indicate that the alteration occurred under low oxygen fugacity and high hydrogen-sulfide fugacity. Our study shows that the secondary assemblages observed here were highly dependent on the fluid micro-environments during alteration. As alteration progressed, the small fluctuations in fluid chemistry could have changed the mineral phase stability, accounting for the abundance differences in minerals across distinct CR clasts.

## 2.1 INTRODUCTION

The Renazzo-like (CR) chondrites are a class of carbonaceous chondrites that have undergone varying degrees of aqueous alteration. Unlike the Ivuna-like (CI) and Mighei-like (CM) chondrites — heavily altered chondrites that have undergone extensive aqueous alteration to the point that most primary minerals have been replaced — many CR chondrites have experienced incomplete alteration and retain a record of both the primary minerals and their secondary replacement products. For this reason, the CR chondrite group provides a unique view into the action of water in the early Solar System.

Most CR chondrites are breccias (Brearley, 2006), consisting of the CR host lithologies mixed with clasts of fine-grained dark inclusions. Comprehensive studies of have detailed the mineralogy, bulk chemistry, and isotopic compositions for whole-rock CR chondrites, as well as for chondrite components (Weisberg et al., 1993; Kallemeyn et al., 1994; Clayton and Mayeda, 1999; Krot et al., 2002; Schrader et al., 2011; 2013; 2014; Alexander et al., 2013; Bonal et al., 2013; Harju et al., 2014; Abreu, 2015; Jilly-Rehak et al., 2015). In general, the bulk elemental compositions of CR chondrites are depleted in elements more volatile than chromium relative to CI chondrites, but do not exhibit metal-silicate fractionation (Kallemeyn et al., 1994; Huss, 2004). Bulk oxygen isotopic compositions of CR chondrites form a unique mixing line of slope  $\sim 0.7$  on an oxygen three-isotope plot, between the terrestrial fractionation line and the carbonaceous chondrite anhydrous mineral line (e.g., Clayton and Mayeda, 1999; Schrader et al., 2011). This mixing line generally reflects the progressive alteration of a  $^{16}\text{O}$ -enriched anhydrous reservoir by a more  $^{17,18}\text{O}$ -rich  $\text{H}_2\text{O}$  reservoir (Clayton and Mayeda, 1999; Choi et al., 2009; Schrader et al., 2011).

The progressive oxygen-isotope trend has been used, along with petrographic observations, in an attempt to quantify the degree of alteration for each CR meteorite (Harju et al., 2014). In this alteration scheme, the CR chondrites are scaled from type 2.0 (fully altered, corresponding to type 1 in the Meteoritical Bulletin) to 2.8 (nearly anhydrous, sometimes referred to as type 3 in literature). Alternative methods for classifying the CR petrologic types have also been proposed (Alexander et al., 2013; Schrader et al., 2014; Abreu, 2015; Howard et al., 2015), but no scheme can fully account for the complex variations in clast, component, and dark-inclusion abundances across the CR spectrum. For the purpose of this paper, we will refer

to the official petrologic types assigned in the Meteoritical Bulletin Database, as well as the new petrologic types of Harju et al. (2014).

CR chondrites are highly unequilibrated, and most samples have escaped thermal metamorphism (Brearley et al., 2006). Most CR chondrites exhibit incomplete aqueous alteration where some, but not all, of the primary anhydrous phases have been altered into secondary minerals. CR chondrites are primarily characterized by large ~0.7 mm type I chondrules that are reduced and FeO-poor; many are Fe<sup>0</sup> metal-rich (Brearley and Jones, 1998). The type I chondrules are often concentrically layered, consisting of an olivine- and pyroxene-rich core, followed by iron-nickel metal nodules, then finer-grained olivine and pyroxene, and another layer of metal, with a rim of fine-grained phyllosilicates or carbonates. The silicate phenocrysts are embedded within calcium- and aluminum-rich chondrule mesostases, which can be either glassy or contain crystals of plagioclase and/or calcium-rich pyroxene. In more aqueously altered samples, the metal has been replaced by iron-bearing phases, mostly as magnetite and sulfides, and chondrule silicates and mesostases are replaced by phyllosilicates, usually serpentine and chlorite, respectively (Weisberg et al., 1993; Kallemeyn et al., 1994). Some chondrules also exhibit a fine-grained rim of phyllosilicates that may contain intergrown calcium-carbonate, magnetite, or sulfides.

CR chondrites are comprised of ~30-50 vol.% matrix material, along with fine-grained dark inclusions that exist as lithic clasts (Weisberg et al., 1993; Kallemeyn et al., 1994). The fine-grained matrix is generally composed of both hydrated and anhydrous silicates, although the degree of hydration varies among meteorites. Amorphous silicates have also been reported (Abreu and Brearley, 2010). Electron microprobe analyses of matrix material have shown that the fine-grained material is depleted in calcium, likely due to the formation of coarser-grained calcium-rich phases such as calcite, but is otherwise relatively unfractionated compared with CI chondrites (Zolensky et al., 1993; Brearley, 2006). The dark inclusions are compositionally similar to the interchondrule matrix material, with slight enrichments of sodium and potassium compared with bulk matrix chemical composition (Weisberg et al., 1993). The dark inclusions are more hydrated than the interchondrule matrix, but clast boundaries generally remain sharp, taken as an indicator that the clasts were altered before final lithification of the breccia. Refractory inclusions are rare in CR chondrites, with specimens containing <1 vol.% calcium-aluminum-rich inclusions (CAIs).

While much is known about the general mineralogy and petrography of CR chondrites, the alteration process and fluid conditions are poorly constrained. The primary goal of this research is to document the complete mechanism of aqueous alteration, from primary anhydrous components to hydrated secondary minerals. Using a variety of micro-analytical techniques, we detail the petrographic context of alteration, and document secondary alteration assemblages common to CR chondrites. The petrographic observations are used to identify key water-rock reactions that occurred during aqueous alteration. The reactions are used as inputs for simple geochemical models to constrain the fluid conditions on the CR parent body. We investigate how fluctuations in temperature, pressure, pH, oxygen fugacity, and fluid chemistry can influence the secondary mineralogy in CR chondrites.

## **2.2 APPROACH**

### **2.2.1 Thin Section Petrography**

A detailed petrographic survey was conducted for CR chondrites of all petrologic type. We studied 13 thin sections (Table 2.1) spanning the full alteration spectrum from petrologic type 2.0 (completely altered) to type 2.8 (nearly anhydrous). Primary characterization of thin sections was conducted with optical microscopy. High-resolution optical maps were compiled using an automated mapping system (Ogliore and Jilly, 2013). The system employs focus stacking and high-dynamic-range imaging to create gigapixel images that can be viewed and magnified using a web-browser as a “virtual microscope”. After optical microscopy, thin sections were given a ~20 nm carbon coating for electron microprobe analysis (EPMA) and for use in the scanning electron microscope (SEM). A polished brass surface was used to monitor the coating thickness.

Multi-element X-ray maps were taken using the JEOL Hyperprobe JXA-8500F Electron Microprobe at the University of Hawaii. X-ray maps were taken at slightly different conditions depending on the composition of the thin section, ranging from 15 – 20 keV accelerating voltage, 40 – 50 nA beam current, 3 – 5  $\mu\text{m}$  beam diameter, and 25 msec dwell time. Back-scattered electron (BSE) maps were taken for some thin sections using the JEOL JSM 5900LV SEM set to 15 keV accelerating voltage. After mapping, all thin sections were studied using the SEM

coupled with energy-dispersive x-ray spectroscopy (EDX) for qualitative mineral phase identification. Phyllosilicate minerals were identified by EDX analyses, observations of textures and morphology, and optical properties under transmitted light microscopy.

**Table 2.1.** List of CR chondrite thin sections in this study.

Meteorite	Petrologic Type <sup>a</sup>	Find/Fall	Weathering Grade <sup>b</sup>	Special Prep
Al Rais 6997	CR 2.3	Fall	N/A	made w/o water
EET 87770,30	CR 2.8	Find	B	
EET 92159,20	CR 2.8	Find	B/C	made w/o water
GRA 95229,18	CR 2.7	Find	A	
GRO 95577,69	CR 2.0	Find	B	made w/o water
MAC 87320,9	CR 2	Find	Be	
MET 00426,60	CR 2.8	Find	B	made w/o water
MIL 090292,12	(CR 2.0)*	Find	B	made w/o water
QUE 99177,06	CR 2.8	Find	Be	
QUE 99177,69	CR 2.8	Find	Be	made w/o water
Renazzo N1126	CR 2.4	Fall	N/A	made w/o water
Renazzo N1127	CR 2.4	Fall	N/A	made w/o water
Renazzo UH 1	CR 2.4	Fall	N/A	

<sup>a</sup> Petrologic types from Harju et al. (2014) and the Meteoritical Bulletin.

<sup>b</sup> Weathering grades for Antarctic meteorites from JSC. A = minor rustiness, B = moderate rustiness; C = severe rustiness; e = evaporite minerals visible to the naked eye.

\* Oxygen isotopes and petrography suggest that this sample may not be a CR chondrite; see text.

Quantitative elemental analyses were conducted using EPMA. Parts of the matrix were analyzed in MET 00426,60 and QUE 99177,69 with a 5- $\mu$ m broad beam at 20 nA. These two specimens are considered to be minimally aqueously altered, so the matrices were analyzed for comparison to more altered CR matrices measured by Zolensky et al. (1993). Sulfides in Renazzo,N1127 and silicates in MIL 090292,12 were measured at 20nA with a focused beam. The sulfide analyses were taken for comparing primary versus secondary sulfide compositions. Some calcium- and iron- bearing silicates that are unique to MIL 090292,12 were measured to determine the mineral phase. For all analyses, magnesium, aluminum, silicon, phosphorous, sulfur, calcium, chromium, manganese, iron, and nickel were measured at an accelerating voltage of 15 keV for 30 seconds each. The matrix and silicate elemental analyses are reported as weight percent (wt.%) oxide. Sulfur in the matrix analyses are calculated in wt.%, while the

individual sulfide-grain analyses are reported in atomic percent (at.%) to ease the identification of non-stoichiometric sulfide phases.

### 2.2.2 Geochemical Modeling

The petrographic context of primary and secondary mineral phases is essential to the development of geochemical models for the aqueous alteration process. Balanced replacement reactions can be determined from the observed primary and secondary phases in an alteration lithology. Partially altered CR chondrites are particularly useful for defining the alteration reactions, as they retain primary phases while exposing the secondary phases that have formed from aqueous interaction. Thermodynamics dictates the relative stability of mineral phases, and can be used to constrain conditions during aqueous alteration on the asteroidal parent body.

We utilize modeling software Geochemist's Workbench 9.0 to determine the theoretical mineral stability fields under varying pH and oxygen fugacity ( $f_{O_2}$ ). The simple geochemical models presented here are based upon the minimization of Gibb's free energy for defined alteration reactions. The Gibb's free energy of a reaction ( $\Delta G_{rxn}$ ) is defined in Eqn. 1, where R is the gas constant ( $J\ mol^{-1}\ K^{-1}$ ), T is the temperature (K), and K is the equilibrium constant/solubility product.

$$\Delta G_{rxn} = -RT \ln K \quad (1)$$

Bivariate activity plots were created for O-H-C-S-Mg-Fe-Ca-Si-P water-rock-gas systems reflecting alteration lithologies observed in the CR chondrites. We assume local thermodynamic equilibrium in a closed system for the small-scale (<1 mm) alteration lithologies modeled here, due to the apparent low rate of fluid flow and low permeability of the chondritic material (Bland et al., 2009). Alteration in CR chondrites has been shown to be essentially isochemical (e.g., Kallemeyn et al., 2014; Bland et al., 2009), supporting these assumptions. For simplicity, we do not consider brines or saline solutions. This modeling employs the "thermo.dat" dataset developed at the Lawrence Livermore National Laboratory, where activity coefficients are calculated from an extended form of the Debye-Hückel equation. The database includes all primary and secondary minerals documented in this study for CR chondrites, with the exception

of pentlandite, which lacks reliable thermodynamic data. Therefore, all secondary sulfides are taken to be pyrrhotite for the purpose of modeling. Activities for ions from precipitated minerals are assumed to be at saturation, and are determined by the temperature-dependent solubility product. The activities for non-saturated ionic species are estimated from chemical equilibrium models for CR chondrites (Zolotov et al., 2015). The models output bivariate activity plots, and can be set for a range of temperatures and pressures. Calculations were performed for  $T = 0\text{--}150$  °C, and for  $P = 0.1\text{--}100$  bar, within the range of temperatures and pressures considered reasonable for the CR parent body during aqueous alteration (Zolensky et al., 1993; Brearley, 2006). We will present representative diagrams for temperatures 25 °C and 60 °C, end-member alteration temperatures for CR chondrites determined from calcite-magnetite oxygen isotopic fractionation (Jilly-Rehak et al., 2015).

## 2.3 RESULTS

We present petrographic descriptions of the CR-chondrite thin sections studied here. The following descriptions include both new observations and literature data to provide context for understanding the alteration process for CR chondrites. For each sample, we describe the common primary and alteration assemblages and lithologies observed, which serve as the basis for the geochemical modeling. Not all thin sections will be described in the same amount of detail, as many of the characteristics of partially altered or paired meteorites are essentially the same. Additional details on specific CR specimens can be found in the literature (e.g., Weisberg et al. 1993; Kallemeyn et al. 1994; Krot et al., 2002; Weisberg and Huber, 2007; Abreu and Brearley, 2010; Schrader et al, 2013; Harju et al., 2014). All optical and X-ray maps of the thin sections can be found in Appendix C.

### 2.3.1 Descriptions of CR chondrites

*Al Rais 6997*: Al Rais is officially classified as a type 2 anomalous CR chondrite, or a type 2.3 according to the petrologic type scheme of Harju et al. (2014). The anomalous nature of Al Rais is due to the high abundance of fine-grained material and dark inclusions, up to 70–90% in some samples (Weisberg et al., 1993). Al Rais is a fall, and has experienced only minor

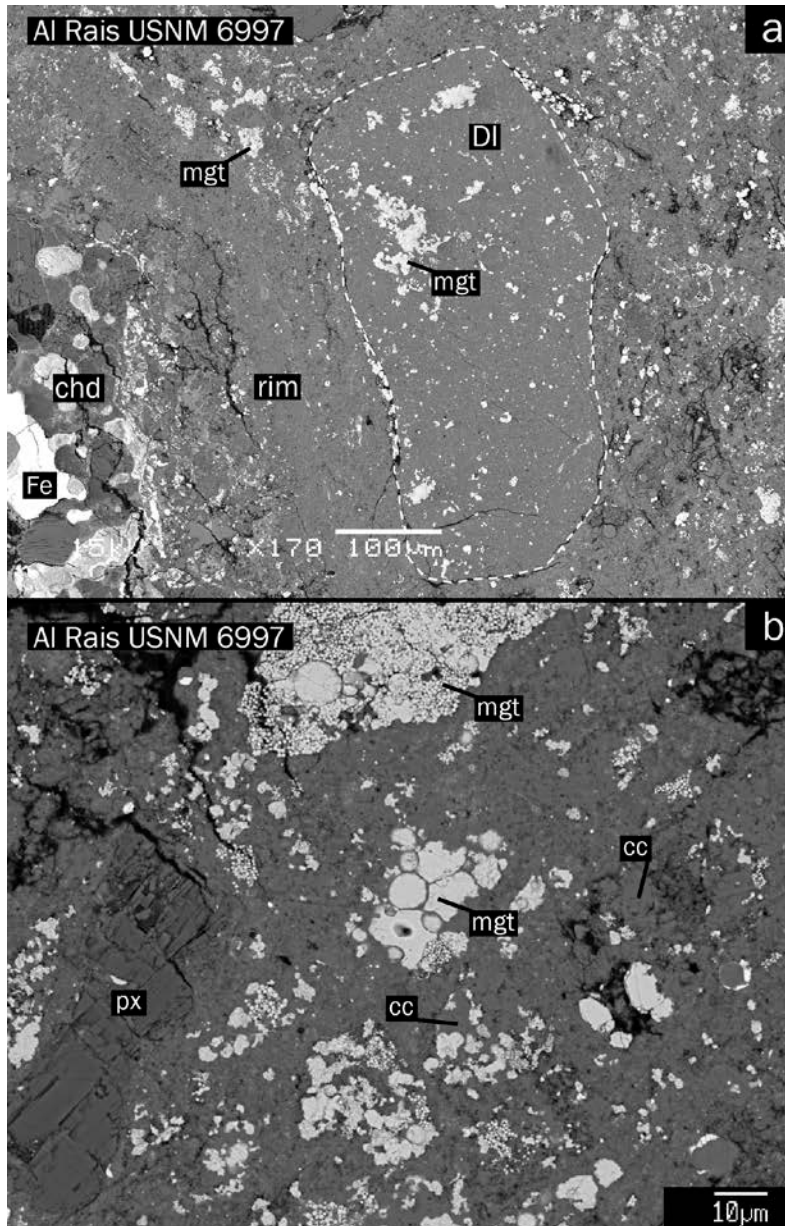


**Figure 2.1.** Backscattered electron (BSE) images of fine-grained lithologies in Al Rais, USNM 6997. (a) The dashed white line depicts the outline of a dark inclusion containing framboidal magnetite. The inclusion is embedded in the matrix next to a chondrule rim. (b) Image of the fine-grained inter-chondrule matrix in Al Rais, USNM 6997, containing abundant framboidal magnetite and magnetite spherules. The magnetite is associated with fine-grained calcite. cc = calcite, chd = chondrule, DI = dark inclusion, Fe = iron-nickel metal, mgt = magnetite, px = pyroxene, rim = chondrule rim.

terrestrial weathering. In the section studied here, the majority of fine-grained material resides in the inter-chondrule matrix. The matrix is composed primarily of fine-grained phyllosilicates,

containing a variety of accessory minerals scattered throughout. Calcium carbonate commonly occurs as mottled fine-grained aggregates in within the matrix, often intergrown with the phyllosilicate material. Magnetite is extremely common in Al Rais, usually occurring as frambooids or as large spherules (Fig. 2.1). Calcium carbonate usually surrounds the frambooids, forming calcite-magnetite assemblages that are abundant in the sample. Sulfides occur in the matrix as sub-micron grains embedded within the fine-grained phyllosilicate or mottled carbonate material, though larger ~5 to 10  $\mu\text{m}$  rounded grains also exist to a lesser extent. Forsteritic olivine grains are present in the matrix, likely originating from fragmented chondrules.

Two dark inclusions are observed in thin section 6997. One is a ~ 200  $\times$  400  $\mu\text{m}$  clast (Fig. 2.1), with a composition essentially identical to that of the matrix, but with less fine-grained carbonate material and less pore space. The clast contains abundant frambooidal magnetite set within a phyllosilicate groundmass, along with sulfide laths of ~10  $\mu\text{m}$  in length. The second dark inclusion resides near the edge of the thin section where it has been polished too thinly for detailed analysis.

Though the Al Rais section is heavily altered, many primary chondrule silicates remain. Olivine and pyroxene phenocrysts within the large (roughly 500-1000  $\mu\text{m}$  in diameter) chondrules remain largely unaltered, though the chondrule mesostases have been completely replaced by aluminum-rich phyllosilicates. Large iron-nickel metal nodules on the interiors of chondrules remain partly unoxidized. EDX spectra show that native phosphorous resides in the metal phase of Al Rais chondrules, similar to reports in other CR chondrites (Zanda et al., 1994). Most iron-nickel metal grains in chondrules have been partially altered to iron oxides and iron-nickel sulfides; these metal-sulfide-magnetite assemblages typically appear as layered structures, sometimes showing signs of further replacement to phyllosilicate material. Coarse-grained sulfides are most common in chondrule interiors and rims, existing as both pentlandite and pyrrhotite.

*EET 87770,30*: This meteorite is classified as a CR2 in the Meteoritical Bulletin Database, and as a weakly altered CR2.8 according to Harju et al. (2014). It is one of many CR2 chondrites that are part of the Antarctic EET 87711 pairing group. Chondrules in the thin section studied here have retained much of their glassy mesostasis, in agreement with the classification

as minimally altered. A study of the macromolecular structure of organic material suggests that EET 87770 may have experienced mild thermal metamorphism (Pearson et al., 2006).

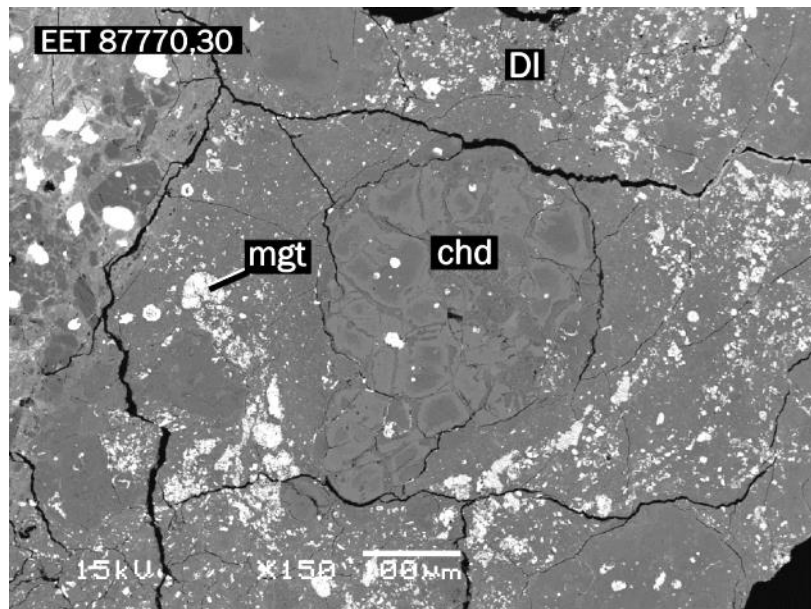


**Figure 2.2.** BSE image of a dark inclusion from EET 87770,30. The inclusion contains a high abundance of framboidal magnetite and numerous altered chondrules. DI = dark inclusion, chd = chondrule, mgt = magnetite.

EET 87770,30 retains most of its primary phases within chondrules. Nearly all chondrule silicates are unaltered, and mesostasis is glassy, or contains small quenched plagioclase or calcium-rich pyroxene crystallites. The majority of chondrule metal remains unoxidized, though some metal nodules display iron-oxide rims, and some nodules have experienced even further alteration into phyllosilicate material. The thin section studied here has undergone substantial terrestrial weathering, apparent under the optical microscope as rust-colored staining and iron-rich veins that cross cut the fusion crust. EDX analysis shows that the terrestrial weathering veins contain substantial amounts of sulfur, in addition to the oxidized iron. Under the SEM, the degree of parent-body alteration appears to be minimal, but is largely obscured by the extensive terrestrial weathering. Some chondrules exhibit compacted rims where iron has diffused outward from metal and silicate grains, possibly indicating some degree of thermal alteration. The matrix of EET 87770,30 is composed of fine-grained silicates, though the extent of alteration to phyllosilicates has not been quantified. Primary silicate fragments, each about 10-40  $\mu\text{m}$  in width, are embedded throughout. Nickel-bearing iron sulfides and magnetite spherules are

commonly embedded within the fine-grained phyllosilicate groundmass, though carbonates are less frequent in the EET 87770 matrix than they are in more altered CR specimens.

There are four dark inclusions in this section, each about 1 mm wide. All four dark inclusions are comprised of the same minerals, though the abundances are clearly variable. The dark inclusions consist of a magnesium- and iron-bearing phyllosilicate groundmass, containing 5-10  $\mu\text{m}$  sized sulfides and framboidal magnetite. In all dark inclusions, some forsterite and calcium-pyroxene grains exist unaltered within the hydrated groundmass. One dark inclusion (Fig. 2.2) contains a much higher abundance of magnetite than the other dark inclusions, along with many lath-shaped iron-nickel-sulfides and numerous heavily altered chondrule pseudomorphs. The replaced phenocrysts are composed of phyllosilicates of varying iron-composition, giving them a leached appearance (Fig. 2.2).

*EET 92159,20*: This sample is classified as a CR2 (Meteoritical Bulletin) or CR2.8 (Harju et al., 2014), and is a part of the EET 92011 pairing group. The EET 92011 pairing group is also considered to be part of the EET 87711 pairing group discussed above, as the specimens are very similar. Under optical microscopes, the sample shows limonitic staining and some rust-colored terrestrial weathering products. The terrestrial weathering is heterogeneous, and some chondrules appear to have largely escaped weathering, while others appear extensively weathered. A thin fusion crust remains intact along the edges of the thin section. Similar to EET 87770,30, most chondrules appear relatively unaltered, and contain mesostasis with small calcium-pyroxene and plagioclase crystallites; two chondrules contain glassy transparent mesostasis. Significant terrestrial weathering veining can be seen cross cutting the fusion crust, and creating rust halos around metal nodules in chondrules. These terrestrial weathering veins are sulfur-rich, similar to those in EET 87770.

The EET 92159,20 thin section is composed of the main CR host lithology, with one large  $\sim 2$  mm dark inclusion. The matrix in the host lithology contains abundant sulfide grains, with only a few isolated magnetite grains. Some regions of mottled calcite occur in the matrix, but no coarse-grained calcites were identified. However, one large dolomite aggregate is found in the dark inclusion. This dolomite encompasses three forsteritic olivine grains and is intergrown with iron-sulfide crystals, but otherwise appears to be out of equilibrium with the surrounding phyllosilicate groundmass. The edge of the dolomite-sulfide aggregate displays a reaction rim, where it has been altered to phyllosilicates (Fig. 2.3a). The dark inclusion contains

iron-sulfide and magnetite spherules (~ 5  $\mu\text{m}$ ) embedded in a dense fine-grained phyllosilicate groundmass. Both magnetite and sulfide spherules are often surrounded by fine-grained calcium-carbonate material that contains minor amounts of magnesium and silicon, likely due to intergrown phyllosilicates. In the dark inclusion, some sulfides are intergrown with calcium phosphate (likely hydroxyapatite). Phosphates occur in a number of CR specimens, although they are not as common as calcium carbonates (e.g., Jilly and Huss, 2012). The dark inclusion contains some remnant olivine grains that remain unaltered. Inside of the dark inclusion there is a type II chondrule that contains abundant fractal, euhedral, iron-rich olivine phenocrysts (Fig. 2.3b). The chondrule contains large iron-sulfides (likely pyrrhotite), surrounded by nickel-rich pyrrhotite or pentlandite grains. The sulfide blebs contain small amounts of unoxidized iron-nickel metal with a high concentration of nickel (~42 wt.%), possibly in the taenite phase. The mesostasis contains unaltered pyroxene crystallites, even though the surrounding material is heavily altered.

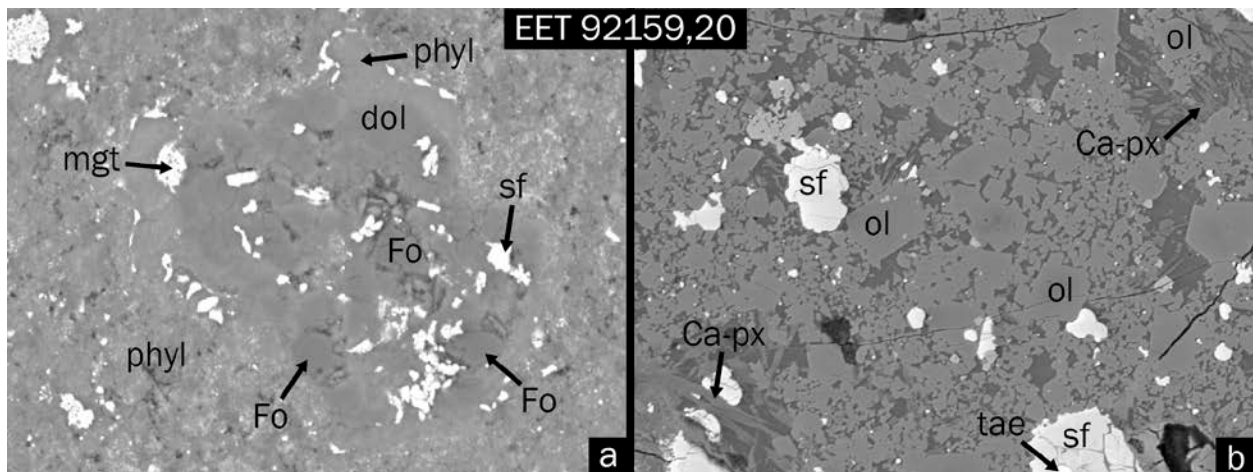


**Figure 2.3.** BSE images of phases in EET 92159,20. (a) Dolomite grains within a dark inclusion have been partially altered to phyllosilicates. (b) Image of an unaltered type II chondrule inside of the same dark inclusion, containing nickel-rich metal and sulfides, and euhedral iron-rich olivine phenocrysts. Ca px = Calcium-pyroxene, dol = dolomite, FO = forsterite; mgt = magnetite, ol = iron-rich olivine, phyl = phyllosilicate, sf = iron-sulfide, tae = taenite.

*GRA 95229,18:* This meteorite is categorized as a C2 in the Meteoritical Bulletin, or as petrologic type 2.7 according to Harju et al. (2014). GRA 95229 appears less terrestrially weathered than many other Antarctic CR specimens, though some iron-oxide veining does occur near metal-rich regions. The sample is densely packed with chondrules, containing many chondrule fragments embedded within the interchondrule matrix. The chondrules are almost

exclusively metal-rich type-I chondrules typical of CR chondrites. The chondrule mesostases are largely composed of small grains of plagioclase and calcium-rich pyroxene. Clear glassy mesostases are less common. Iron-nickel metal remains mostly intact, with some minor alteration to magnetite. The matrix of GRA 95229,18 contains many unaltered silicate grains within a phyllosilicate groundmass. Carbonates are less abundant in the matrix compared with more altered CRs such as Renazzo and Al Rais, but fine-grained calcite does occur in two dark inclusions.

*GRO 95577,69*: GRO 95577 is classified as a CR1 in the Meteoritical bulletin, meaning that it has undergone extensive aqueous alteration. In the petrologic scheme developed by Harju et al. (2014), this sample is a type 2.0, as they retain the type 1 designation for chondrites that contain no chondrules (such as CI chondrites). The fusion crust remains intact on the top and bottom edges of the thin section, and optical images show clear signs of heating within ~ 1 mm of the fusion crust (See optical map in Appendix C). In addition, terrestrial weathering has caused limonitic staining and some oxidation of remnant chondrule metal. Small sulfate veins (likely gypsum) are observed near large cracks and near the fusion crust, characteristic of evaporites formed during Antarctic weathering. The center of the thin section appears relatively unaffected by the weathering or entry heating.

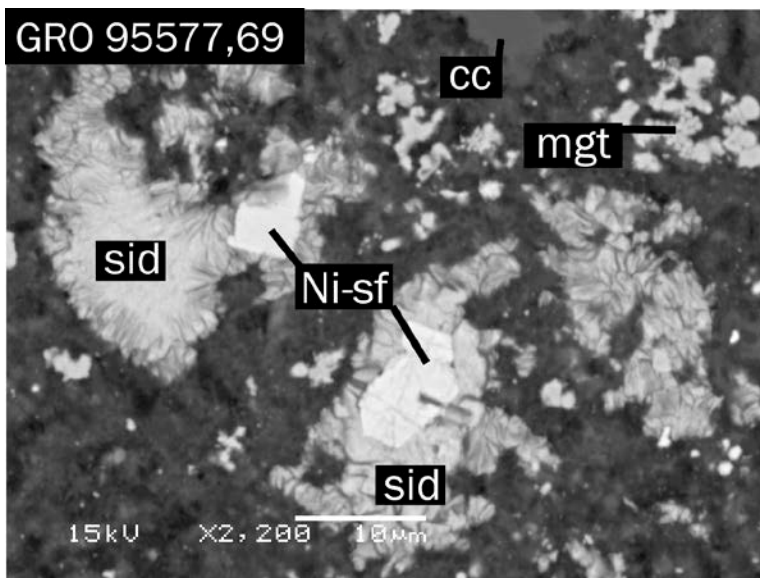


**Figure 2.4.** BSE image of secondary phases embedded in the phyllosilicate matrix of GRO 95577,69. cc = calcite, mgt = magnetite, Ni-sf = iron-nickel sulfide, sid = siderite.

The thin section of GRO 95577 studied here is composed entirely of phyllosilicates and other secondary minerals that have pseudomorphed the primary rock. There is a high abundance of matrix that contains small (~200  $\mu\text{m}$ ) heavily altered chondrules, while a few large (~700  $\mu\text{m}$ ), metal-rich chondrules characteristic of CR chondrites appear to reside in a distinct smaller clast. The main matrix-rich lithology is similar to the dark lithology reported by Weisberg and Huber (2007) and Tyra et al. (2010), containing abundant calcite set within a magnesium-rich phyllosilicate or clay matrix. The calcite occurs as anhedral ~10-50  $\mu\text{m}$  grains, often intergrown with euhedral sulfide plaquettes or framboidal magnetite. The study of Tyra et al. (2010) found abundant manganese- and magnesium-bearing “siderite” within the GRO 95577 matrix. This same phase is observed in GRO 95577,69, containing roughly 9 wt.% manganese and 9 wt.% magnesium. However, the phase here also contains a significant proportion of silicon (~10 wt.%), and displays a heterogeneous marbled texture (Fig. 2.4). The “siderite” grains typically surround nickel-rich sulfide grains. Magnetite occurs primarily as framboids, and is less common in GRO 95577 than in the dark inclusions of other CR chondrites, such as Al Rais and Renazzo.

The matrix and fine-grained rims around the large chondrules in the small CR-like clast contain very little calcite in comparison to the dark lithology. The fine grained chondrule rims are composed of magnesium-rich phyllosilicates or clays, and are littered with small < 2  $\mu\text{m}$  sulfides. The sulfides have variable nickel contents, suggesting that the phase is pyrrhotite.

Chondrule phenocrysts have been replaced by optically green serpentine (Fig. 2.5a). The serpentine pseudomorphs of the chondrule phenocrysts exhibit abundant pore space, which is sometimes filled with iron oxides. The chondrule mesostases have been altered to calcite and chlorite (Fig. 2.5b). Most metal nodules have been altered, primarily to magnetite, although some nodules contain layered deposits of iron oxides and iron sulfides. In one chondrule, some nodules near the chondrule boundary have been partially replaced with magnesium-rich phyllosilicates. Some of the calcite and magnetite grains in the chondrule interiors are embayed and have reaction rims, indicating that they were out of equilibrium with the serpentine that pseudomorphs the chondrule silicates. The petrographic context suggests that the mesostases and metal grains were altered first, followed by the alteration of the silicate phenocrysts. Iron-sulfide grains (~20  $\mu\text{m}$ ) occur on the boundary of one chondrule, while another is rimmed by magnetite.

*MAC 87320,9*: This sample is classified as CR2 in the Meteoritical Bulletin, and was not studied by Harju et al (2014). However, whole-rock oxygen-isotope analyses (Weisberg et al.,

1993; Clayton and Mayeda 1999) indicate that the sample lies in the middle of the progressive alteration trend. The thin section studied here is small, and contains typical features for a CR chondrite. It consists primarily of type I chondrules, though there are two type II chondrules, one of them similar in morphology and mineralogy to the one observed in EET 92159 (Fig 2.3). The metal grains are partially altered, exhibiting iron-oxide halos. The fine-grained matrices contain magnetite, sulfides, and carbonates embedded within a typical phyllosilicate groundmass. One dark inclusion ~1 mm wide occurs in the thin section, and it contains a higher abundance of calcite and sulfides than the inter-chondrule matrix.

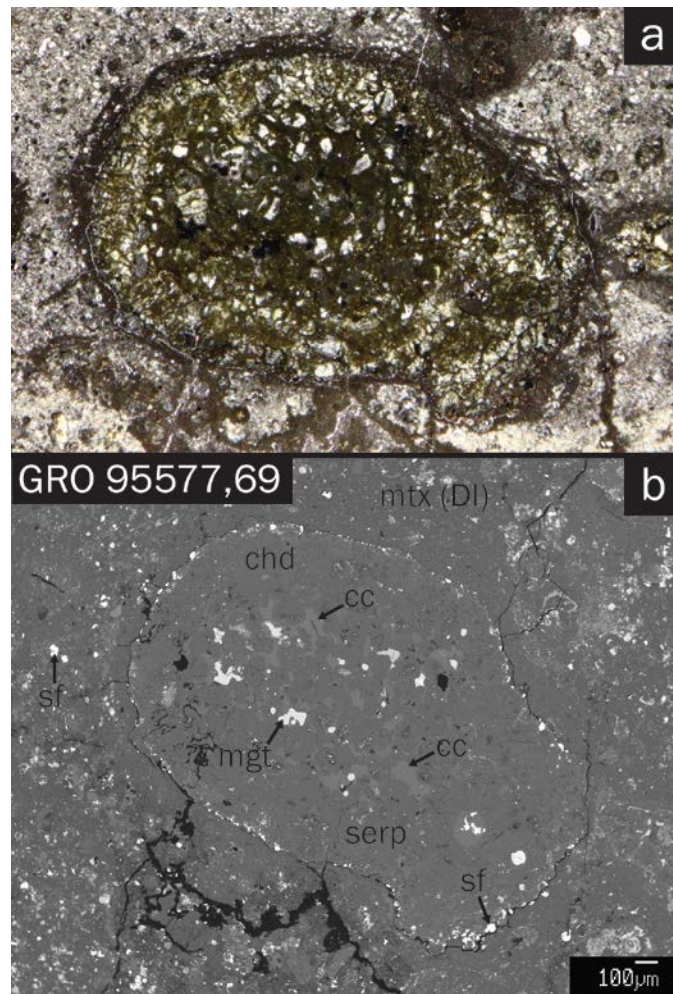


**Figure 2.5.** (a) Stereo optical micrograph of a serpentinized chondrule in GRO 95577. The green color comes from the replacement of chondrule phenocrysts by serpentine, and parts of the mesostasis by chlorite. (b) BSE image of the same chondrule. cc = calcite, chd = chondrule, DI = dark inclusion, mgt = magnetite, mtx = matrix, serp = serpentine, sf = iron-sulfide.

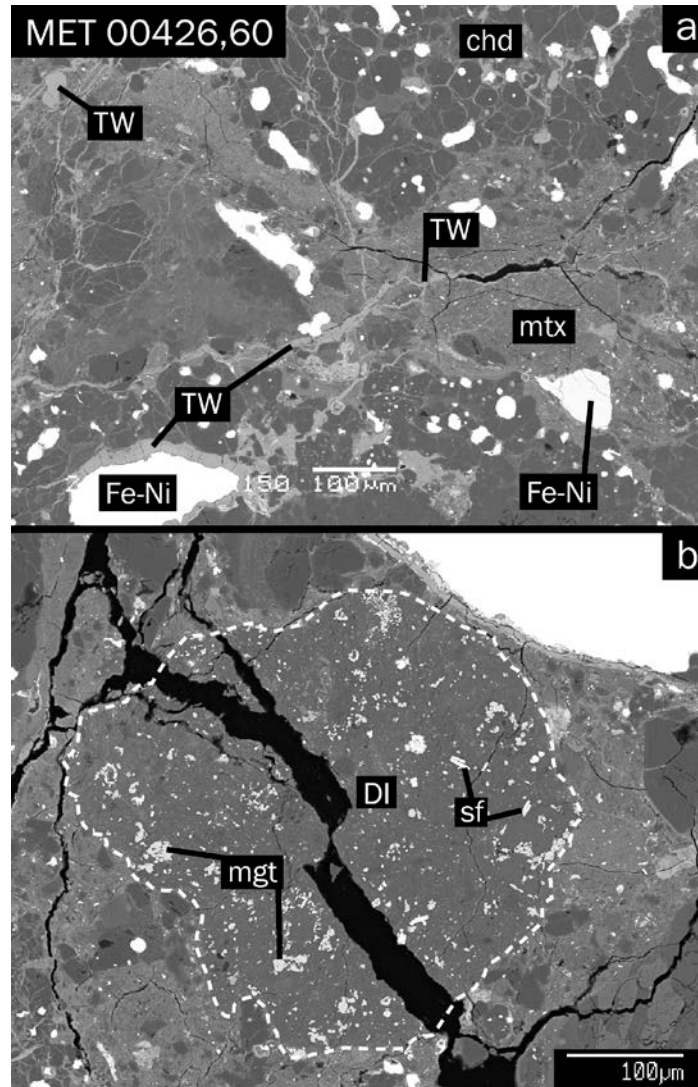


**Figure 2.6.** BSE images of MET 00426,60. (a) Images of a heavily weathered region, where a network of iron-oxide veins are cross-cut chondrules and matrix. (b) A dark inclusion in MET 00426,60 that contains lath-shaped iron-sulfides, and abundant framboidal magnetite within a phyllosilicate groundmass. Chd = chondrule, DI = dark inclusion, Fe-Ni = iron-nickel metal, mgt = magnetite, mtx = matrix, sf = iron-sulfide, TW = terrestrial weathering.

*MET 00426,60*: The CR chondrite MET 00426 is considered to be one of the least aqueously altered CR samples, other than QUE 99177 (Abreu and Brearley, 2010). In the Meteoritical Bulletin, MET 00426 is classified as a CR2, but it is commonly referred to as a CR3, reflecting a low degree of aqueous alteration. Harju et al. (2014) have classified the specimen as a CR2.8, as there are some secondary minerals that indicate that the sample did not

avoid alteration all together. The chondrule metal shows extensive weathering close to the edges of the sample. Some metal nodules have been replaced completely by iron-oxides, while others remain nearly entirely unaltered. A large network of iron-oxide terrestrial weathering veins, each ~1–30  $\mu\text{m}$  in width, crosscut chondrule mesostases, silicate phenocrysts, and matrix. The oxide (likely goethite, hematite, or ferrihydrite) fills in cracks and along grain boundaries (Fig. 2.6a).

The thin section studied here is comprised predominantly of type I chondrules. All of the type I chondrules contain unaltered mesostasis, some glassy and some containing plagioclase and calcium-pyroxene crystallites. Half of a large type II chondrule is present, containing euhedral olivine phenocrysts that are normally zoned with magnesium-rich cores and iron-rich rims. Some planar parallel fracture features are apparent in olivine under the optical microscope, indicating that the chondrule or chondrite has experienced minor shock. The chondrule mesostasis is glassy and optically clear, with a few calcium-pyroxene crystallites. The chondrule is metal-poor, but contains a large sulfide grain containing exsolved pyrrhotite and pentlandite. Two large (~600  $\mu\text{m}$  in diameter) “metal chondrules” occur in MET 00426,60. Inside are small round inclusions that contain multiple silicate phases including pyroxene and glass.

Fine-grained material is not as abundant in MET 00426,60 as in more heavily altered CR specimens. Most of the fine-grained material resides in the matrix, with only a few chondrules exhibiting fine-grained rims. One dark inclusion of ~300  $\mu\text{m}$  in diameter is observed in this thin section (Fig. 2.6b). The dark inclusion is mineralogically similar to other CR dark inclusions. It is primarily composed of magnesium-rich phyllosilicates, and contains abundant framboidal magnetite and lath-shaped sulfides. The matrix contains fine-grained silicate material, including phyllosilicates and amorphous silicates (Abreu and Brearley, 2010), and numerous fragmented chondrules. Isolated sulfide grains are common within the matrix, but magnetite is rare. There are some free-standing iron-nickel blebs that remain un-weathered in the matrix, supporting the hypothesis of Abreu and Brearley (2010) that terrestrial weathering is restricted to fluid transport along veins, without much diffusion into the sample. However, sulfur-rich alteration fronts occur in some heavily weathered regions of the matrix, and it is unclear whether such features were formed by asteroidal alteration or by terrestrial weathering.

Electron microprobe analyses of fine-grained matrices in MET 00426 are presented in Table 2.2. The data are presented in weight percent oxide (except S, which is calculated in elemental wt. %). The analysis totals are low, due to a number of reasons: First, the high porosity

**Table 2.2.** Electron microprobe matrix analyses for minimally altered MET 00426,60 and QUE 99177,69 (in wt.%)

Meteorite	Analyses	SiO <sub>2</sub>	Na <sub>2</sub> O	MgO	CaO	MnO	Al <sub>2</sub> O <sub>3</sub>	FeO	NiO	Cr <sub>2</sub> O <sub>3</sub>	S	TOTAL
MET 00426,60	Mtx #1	29.4	0.32	17.3	0.69	0.26	1.59	29.3	1.61	0.42	2.46	83.3
	Mtx #2	31.0	0.15	15.8	0.39	0.19	1.82	30.7	1.76	0.42	2.64	84.8
	Mtx #3	29.5	0.18	16.1	0.21	0.16	1.54	30.5	1.67	0.33	2.49	82.6
	Mtx #4	31.5	0.29	15.2	0.50	0.17	1.55	31.9	1.73	0.35	2.57	85.8
	Mtx #5	26.8	0.48	13.0	0.61	0.24	1.76	37.8	2.19	0.40	3.81	87.0
	Mtx #6	23.3	0.29	9.8	0.60	0.12	2.24	39.2	2.68	0.27	2.68	81.1
	Mtx #7	28.6	0.29	19.0	1.58	0.40	1.74	30.8	2.46	0.59	3.25	88.7
	Mtx #8	19.0	0.39	16.0	1.56	0.66	1.28	29.0	1.74	0.19	1.39	71.1
	Mtx #9	28.0	0.29	13.5	0.75	0.87	1.58	35.8	2.55	0.49	3.33	87.1
	Mtx #10	25.5	0.49	13.5	0.72	0.25	1.49	30.6	1.95	0.30	2.33	77.1
	Mtx #11	27.9	0.25	15.7	0.58	0.18	1.76	32.6	1.56	0.33	1.32	82.2
	Mtx #12	27.9	0.26	14.2	0.57	0.19	1.85	33.9	2.28	0.38	2.70	84.2
	Mtx #13	28.4	0.32	15.5	0.87	0.27	1.62	33.5	2.59	0.39	3.53	87.0
	Mtx #14	29.1	0.30	13.7	0.71	0.55	1.60	33.9	2.46	0.38	2.73	85.3
	Mtx #15	38.3	0.61	4.9	0.28	0.25	3.65	32.6	0.05	0.06	0.36	80.9
	Mtx #16	42.0	0.23	13.7	1.75	1.48	2.44	23.4	0.12	0.70	0.06	85.9
	Mtx #17	31.2	0.12	15.9	0.23	0.08	2.30	27.0	1.68	0.42	1.95	80.8
	Mtx #18	28.3	0.09	14.7	1.30	0.14	2.14	30.1	1.66	0.35	2.40	81.1
	Mtx #19	28.3	0.19	14.9	0.35	0.07	2.24	28.5	1.73	0.38	2.86	79.6
	Mtx #20	32.0	0.18	18.1	0.54	0.12	2.55	25.5	1.93	0.45	2.01	83.4
	Mtx #21	28.8	0.28	18.9	0.26	0.18	1.68	25.7	1.54	0.28	3.34	81.0
	Mtx #22	37.4	0.40	21.4	2.70	0.66	2.43	21.9	1.58	0.52	2.05	91.1
	Mtx #23	29.6	0.27	14.5	0.27	0.13	2.20	27.3	1.80	0.39	2.23	78.7
	Mtx #24	26.8	0.27	14.4	3.43	0.36	1.67	29.7	2.25	0.39	2.64	81.8
	Mtx #25	28.2	0.29	15.1	0.76	0.27	1.80	32.5	1.65	0.40	2.63	83.7
	Mtx #26	29.0	0.23	14.9	0.52	0.28	1.92	30.7	2.64	0.40	2.49	83.0
	Mtx #27	28.6	0.08	22.1	0.22	0.46	2.14	21.5	1.15	0.37	0.58	77.3
	Mtx #28	31.5	0.08	21.0	0.24	0.23	2.33	20.8	1.42	0.44	0.64	78.7

	Mtx #29	29.5	0.11	22.1	0.19	0.44	2.18	21.9	1.50	0.40	0.73	79.0
	Mtx #30	33.3	0.09	22.1	0.19	0.19	2.12	21.4	1.19	0.47	0.60	81.6
QUE 99177,69	Mtx#1	25.7	0.46	13.2	3.79	0.22	1.71	30.2	1.56	0.29	3.39	80.6
	Mtx#2	28.3	0.53	17.6	0.75	0.22	1.75	27.2	1.90	0.39	3.69	82.4
	Mtx#3	27.5	0.41	13.9	0.62	0.19	1.88	30.4	1.54	0.32	3.71	80.5
	Mtx#4	28.7	0.32	17.3	0.24	0.24	1.84	26.9	1.70	0.31	3.23	80.8
	Mtx#5	30.5	0.38	16.8	2.09	0.24	3.59	28.4	1.61	0.46	2.58	86.5
	Mtx#6	27.0	0.30	19.7	0.49	0.25	1.36	29.8	2.37	0.41	5.66	87.3

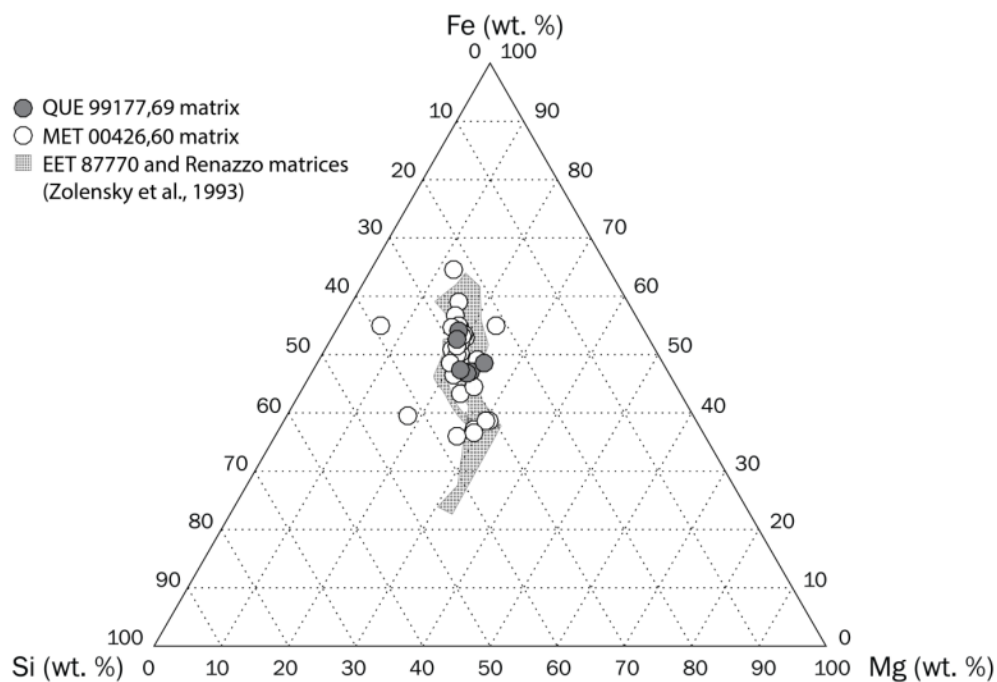


**Figure 2.7.** Ternary diagram depicting EPMA analyses for MET 00426,60 (white) and QUE 99177,69 (grey) matrices. Measurements were taken using a 5  $\mu$ m beam, and are presented in elemental weight percent.

and presence of H<sub>2</sub>O, which is not directly measured, can contribute to low analysis totals. In addition, both iron and nickel are calculated as oxides even though they likely exist in multiple valence states in metal, sulfides, oxides, and silicates. Lastly, a number of elements were not measured and are likely present, including carbon, phosphorous, and potassium. The variable microprobe totals may reflect differences in the water content of the matrix, as well as chemical variations on a point-by-point basis. The abundances of iron, silicon, and magnesium are plotted in a ternary diagram in elemental weight percent (Fig. 2.7) for comparison to similar measurements of matrices in the hydrated CR chondrites Renazzo and EET 87770 (Zolensky et al., 1993). The results are in good agreement.

*MIL 090292,12*: This thin section is one of two specimens classified as a CR1 in the Meteoritical Bulletin. According to the classification scheme of Harju et al. (2014), the specimen is a CR2.0, the same petrologic type as GRO 95577. However, oxygen isotopic studies of magnetite have suggested that the sample is anomalous, and possibly not related to the CR group (Jilly-Rehak et al., 2015). *MIL 090292,12* is brecciated, composed of clasts of similar lithologies ranging in size from ~1–5 mm. Under transmitted light microscopy, the *MIL 090292,12* thin section shows limonitic staining from Antarctic weathering that is particularly evident around the edges of the thin section near the fusion crust. Under the SEM, sulfate weathering veins are clearly visible. Small gypsum veins permeate the entire thin section, and epsomite occurs within nearly all of the large cracks in the sample.

The majority of the chondrules in *MIL 090292,12* are pseudomorphs of type I chondrules typical of CR chondrites. However, the chondrules do not display the same layered textures or fine-grained rims as many CR chondrules do. Only a few unaltered silicate grains were found in the section, existing in two chondrules that had not been completely replaced by secondary products. All other chondrule silicates have been replaced by magnesium-rich phyllosilicates. Some of these altered phenocrysts show light green-yellow pleochroism upon rotation of the stage. The altered chondrule mesostases are usually composed of magnesium and aluminum-rich phyllosilicates, possibly chlorite.

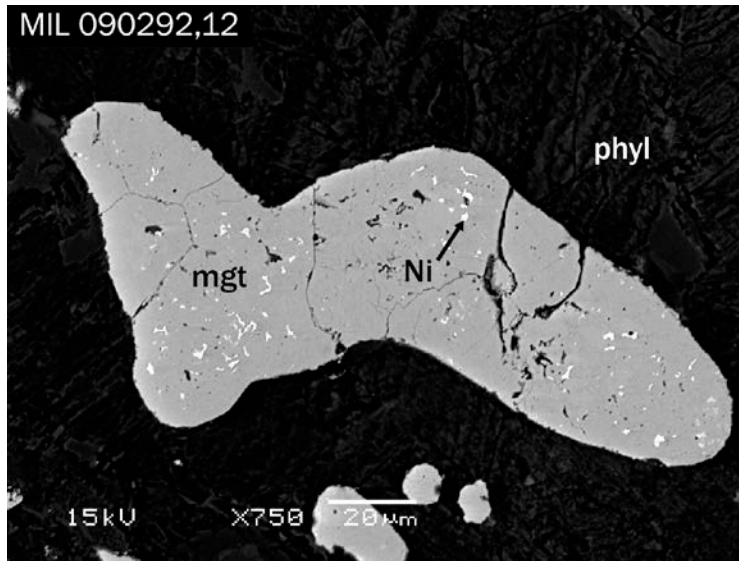


**Figure 2.8.** BSE image of a magnetite nodule from MIL 090292,12 showing remnant bits of nickel-rich (~88 wt.% nickel) metal. mgt = magnetite, Ni = nickel-rich metal, phyl = phyllosilicate.

There are some stark mineralogical and petrographical differences between this sample and the other CR2.0, GRO 95577. MIL 090292 contains an extraordinary amount of magnetite, both within chondrules and within the matrix. The magnetite grains that replace metal nodules in chondrules all contain small ~1-3  $\mu\text{m}$  nickel-metal grains (~88 wt% nickel), apparently as remnant products from the primary chondrule metal (Fig. 2.8). The chondrule magnetite contains trace amounts of phosphorous, evident in the EDX spectra. It is unclear what valence state the phosphorous is in, whether it has been oxidized or remains in the native state, as it exists in magnetite rather than metal (Zanda et al., 1994). This may suggest the formation of a P-bearing magnetite before separation into phosphates (such as seen in Renazzo, c.f. Fig. 2.15), or it may reflect fine-scale intergrowths of phosphates with magnetite on a scale that can't be resolved with EDX. Magnetite within the matrix exists as rounded spherules, euhedral platelets, and as felted aggregates of small crystals that aren't quite framboidal in morphology. Sulfides, both pentlandite and pyrrhotite, are common as anhedral grains and aggregates in the matrix. Unlike all other CR chondrites, no carbonates were found in MIL 090292,12. Instead, calcium resides in two distinct calcium and iron rich silicate phases, and minor calcium phosphate. Calcium- and iron-rich pyroxenes are common replacement products found inside of chondrules and along chondrule-rim boundaries. The secondary pyroxenes occur to a lesser extent in the matrix, as

small anhedral masses. A second, less common calcium and iron-rich silicate was found in the matrix, and as a replacement product inside of a CAI. Electron microprobe analyses confirm that this second phase is andradite (Table 2.3). All iron is assumed to exist in the Fe<sub>2</sub>O<sub>3</sub> oxidation state; the high electron microprobe totals may indicate that not all iron exists in the octahedral site as Fe<sup>3+</sup>, and that a small portion may occupy the cubic cation site as Fe<sup>2+</sup>. While calcium and iron-bearing silicates are not documented in other CR chondrites, they are common secondary products in CV chondrites (Krot et al., 1998).

**Table 2.3.** Electron microprobe analyses of the andradite grains in MIL 090292,12 (in wt.%).

Oxide	And #1	And #2	And #3	And #4	And #5	And #6
SiO <sub>2</sub>	35.9	35.6	35.6	34.9	35.4	35.6
TiO <sub>2</sub>	bdl	bdl	bdl	0.28	0.01	0.02
Al <sub>2</sub> O <sub>3</sub>	0.47	0.45	0.48	0.71	0.68	0.76
Cr <sub>2</sub> O <sub>3</sub>	bdl	bdl	bdl	bdl	bdl	bdl
Fe <sub>2</sub> O <sub>3</sub> *	31.5	32.3	32.3	32.5	31.9	31.9
MnO	0.04	0.05	0.05	0.02	0.03	0.02
MgO	0.28	0.24	0.30	0.30	0.23	0.16
CaO	34.1	34.3	34.1	34.5	34.1	34.2
Na <sub>2</sub> O <sub>3</sub>	bdl	bdl	bdl	bdl	bdl	bdl
Total	102.2	102.9	102.8	103.0	102.3	102.6

\* Re-calculated as Fe<sub>2</sub>O<sub>3</sub> from FeO oxide weight percent. bdl = below detection limits

*QUE 99177,06 and QUE 99177,69:* This meteorite is classified as a CR2 on the Meteoritical Bulletin, or as a type 2.8 according to Harju et al. (2014). QUE 99177 has commonly been referred to as a CR 3, and the least altered of the CR specimens. Many of the chondrules show signs of terrestrial weathering, and parts of the thin section are rust-colored due to the oxidation of native iron-nickel metal. The weathering veins are thought to be iron oxyhydroxides (Abreu and Brearley, 2010), contributing to a deep red color in parts of the thin section. The fusion crust remains intact along one edge of QUE 99177,06, and two edges of QUE 99177,69.

Thin section QUE 99177,06 is composed mainly of metal-rich type I porphyritic olivine and pyroxene chondrules. There are two barred olivine chondrules, one cryptocrystalline chondrule, and one type II chondrule (iron-oxide rich, metal poor). Chondrule silicates show few signs of alteration. Most of the chondrules contain mesostasis that is finely crystalline, while two

chondrules have clear, unaltered glassy mesostases. The distribution of fine-grained matrix is heterogeneous and occurs in clumps. The matrix is composed of silicates, occurring as phyllosilicates and amorphous silicates (Abreu and Brearley, 2010). Embedded within the silicate groundmass are 5–10  $\mu\text{m}$  magnetite spherules, along with occasional magnetite framboids. Carbonates occur in both matrix and dark inclusions, but are more common in the dark inclusions. Small  $\sim 5$   $\mu\text{m}$  sulfides are embedded within the silicate groundmass, with occasional mottled carbonate material. In some cases, the matrix is difficult to distinguish from dark inclusions, as the clast boundaries are not always obvious. At least three distinct dark inclusions occur in QUE 99177,06, with the largest being  $\sim 2$  mm in width. Carbonates and magnetite are more common in the dark inclusions, where the magnetite exists as 5–10  $\mu\text{m}$  spherules and framboids (Fig. 2.9a). The carbonates in the dark inclusions range in size from  $\sim 5$   $\mu\text{m}$  anhedral grains to large carbonate aggregates extending over  $\sim 50$   $\mu\text{m}$ . Carbonates in the dark inclusions are often associated with both magnetite and sulfide minerals.

The general description of thin section QUE 99177,69 is the same as QUE 99177,06 above. However, there are a few distinct features worth mentioning. This section is substantially less terrestrially weathered, though many metal grains still show some oxide formation. The majority of the fine-grained material occurs as inter-chondrule matrix, and two dark inclusions with similar compositions to those in QUE 99177,06 are present. Six broad-beam matrix measurements were taken in the interchondrule matrix and in a dark inclusion (Table 2). The results are reported in weight percent oxide. The iron abundance is reported as FeO for comparison to measurements of CR matrices in Zolensky et al. (1993), even though iron likely exists as a mixture of metal,  $\text{Fe}^{2+}$ , sulfides, and  $\text{Fe}^{3+}$ . Iron, magnesium, and silicon are plotted on a ternary diagram (Fig. 7), along with the data from MET 00426. The compositions of the matrices overlap, and are in good agreement with the measurements from Renazzo and EET 87770 from Zolensky et al. (1993).

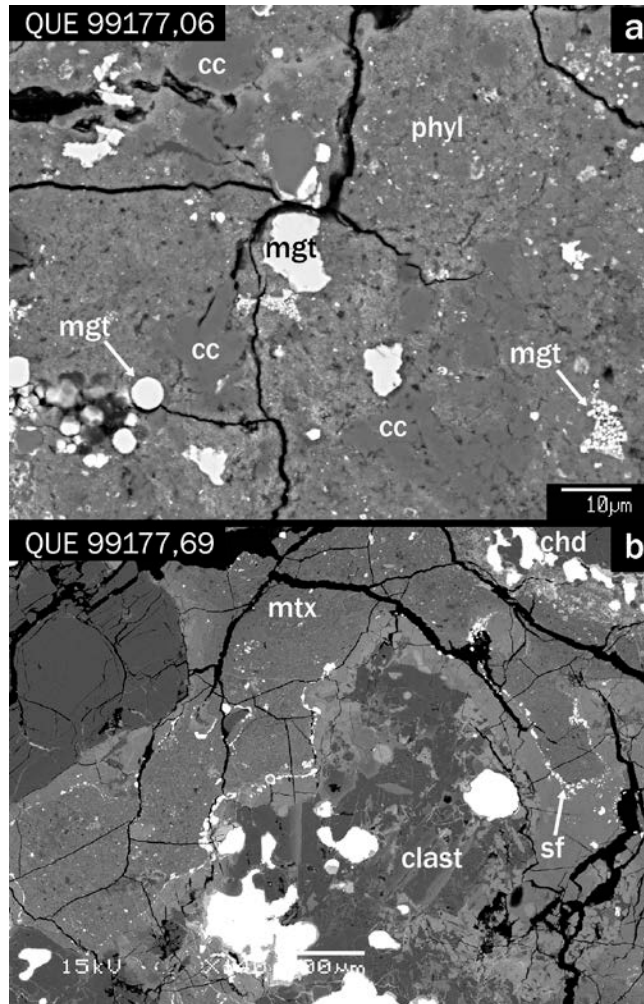


**Figure 2.9.** BSE images of QUE 99177. (a) Image of a dark inclusion in QUE 99177,06, showing crystal morphologies of magnetite and calcite, set within a phyllosilicate groundmass. (b) Image of a thermally-metamorphosed clast in QUE 99177-69, consisting of multiple chondrules that have undergone iron-diffusion, annealed matrix, and a rim of iron-nickel sulfides. The clast resides next to matrix material in the CR host lithology. cc = calcite, chd = chondrule, clast = altered clast, mgt = magnetite, mtx = matrix, phyl = phyllosilicate, sf = iron and nickel sulfide.

There is a distinct ~2-mm-long clast near the center of the thin section that appears to be thermally metamorphosed (Fig. 2.9b), based on the following observations. The entire clast contains four chondrules that appear to have been metal-rich, type I chondrules, along with some fine-grained silicates. The fine-grained material has annealed, and there are no longer distinct chondrule-matrix boundaries. Iron from the chondrule silicates shows evidence for diffusion or mobilization into the surrounding groundmass. The chondrules are comprised of both

magnesium-rich and iron-rich olivine, along with abundant enstatite. Some of the chondrules retain glassy mesostasis that contains minor amounts of aluminum and calcium, as well as calcium-rich pyroxene crystallites. There is also a region of a chondrule that contains pure SiO<sub>2</sub>, with no trace elements that are usual in chondrule mesostases. This phase could either be glass or a high-pressure crystalline form of SiO<sub>2</sub>, such as cristobalite, if the clast was formed by shock. The olivine grains in the clast show some evidence for undulatory extinction and mosaicism, indicators of shock, though it is not extreme. Some small round metal beads occur within the chondrule mesostases and in some silicate grains, indicative of iron reduction processes (e.g., Jones and Grossman, 2005).

*Renazzo N1126, N1127, and UH 1:* In the Meteoritical Bulletin, Renazzo is classified as a CR2, or a type 2.4 according to the classification scheme of Harju et al. (2014). Renazzo is one of two CR witnessed falls, along with Al Rais, and has experienced only minor rusting of metal grains. This study focuses on thin sections N1126 and N1127, as they were specifically made without water for the purpose of this study. The UH 1 thin section is in poor condition, and the thin sectioning process used water, which can compromise the study of aqueously altered materials. Renazzo is a breccia, and contains multiple clasts of similar CR lithologies, along with numerous dark inclusions. The dark inclusions have easily identifiable boundaries under optical microscope and in the SEM. The majority of chondrules are type I porphyritic olivine and pyroxene chondrules, though some barred olivine, radiating pyroxene, and type II chondrules occur. A total of three CAIs occur in the three thin sections. The CAIs contain either gehlenite or anorthite, and a rim of a chlorine-bearing alteration phase (possibly sodalite). Small perovskite and spinel grains are present.

Most chondrules in Renazzo are partially altered. In the chondrules, silicate phenocrysts remain as olivine and pyroxene, but the mesostases have undergone various stages of alteration, where the majority has been replaced by aluminum-bearing phyllosilicates. Some calcium-pyroxene crystallites remain in the centers of large chondrules. Metal nodules have been partially replaced by magnetite, which forms rings around the metal nodules. In one chondrule from Renazzo N1127, the metal nodules have been replaced by magnetite-phosphate assemblages. The phosphates are calcium-rich, and are likely hydroxyapatite. Elemental maps of heavily altered chondrules show that mobile elements were transported during the alteration process. Most often, calcium was leached from the calcium-rich mesostasis phases, and re-precipitated as

carbonates in the nearby matrix (Fig. 2.10). Iron was oxidized during alteration, being replaced in nodules and also transported into the matrix or chondrule rims where it precipitated as magnetite. Primary troilite from matrix grains or from chondrule rims is altered into pyrrhotite or magnetite. Some chondrules exteriors exhibit large ~50–100  $\mu\text{m}$  secondary sulfide blebs formed by the sulfidization of iron-nickel metal. In some cases, the metal nodules are not completely altered and contain iron metal in the center of the grain.

We measured 33 sulfide grains in Renazzo N1127 and UH 1 to determine the range in iron and nickel compositions for primary and secondary sulfides (Fig. 2.11). Measurements were taken from sulfides of varying textures from seven different type I chondrules, one type II chondrule, and one large metal-sulfide aggregate. Nickel content in the sulfides varied from 0–21 at.% (up to about 27 wt.%). Sulfides with primary textures occurring in Type I chondrule nodules or within metal-sulfide opaque assemblages contained <0.2 at.% nickel. The sulfides in the type II chondrule varied from 0.3–2.6 at.% nickel, and are likely also primary features formed at high temperatures during chondrule cooling (Schrader et al., 2015). Sulfides with secondary textures, located on the edges of type I chondrules or within the fine grained rims varied in nickel content from 0.3–21.4 at.%. These results are consistent with previous observations that nickel-rich sulfides form as the product of aqueous alteration (Brearley, 2006). We did not document any high-nickel primary sulfides, though a high-temperature mechanism for formation of pyrrhotite and pentlandite phases has been hypothesized for some CR chondrules (Schrader et al., 2015).

Most chondrules in Renazzo do not contain fine-grained rims, though there are some instances of complex rims for a few chondrules. Figure 2.12 is an example of a layered chondrule rim from Renazzo N1127. The chondrule is partially altered and is rimmed with a layer of sulfides, magnetite framboids with mottled calcite, a layer of phyllosilicates altered chondrule, and then more magnetite and calcite.

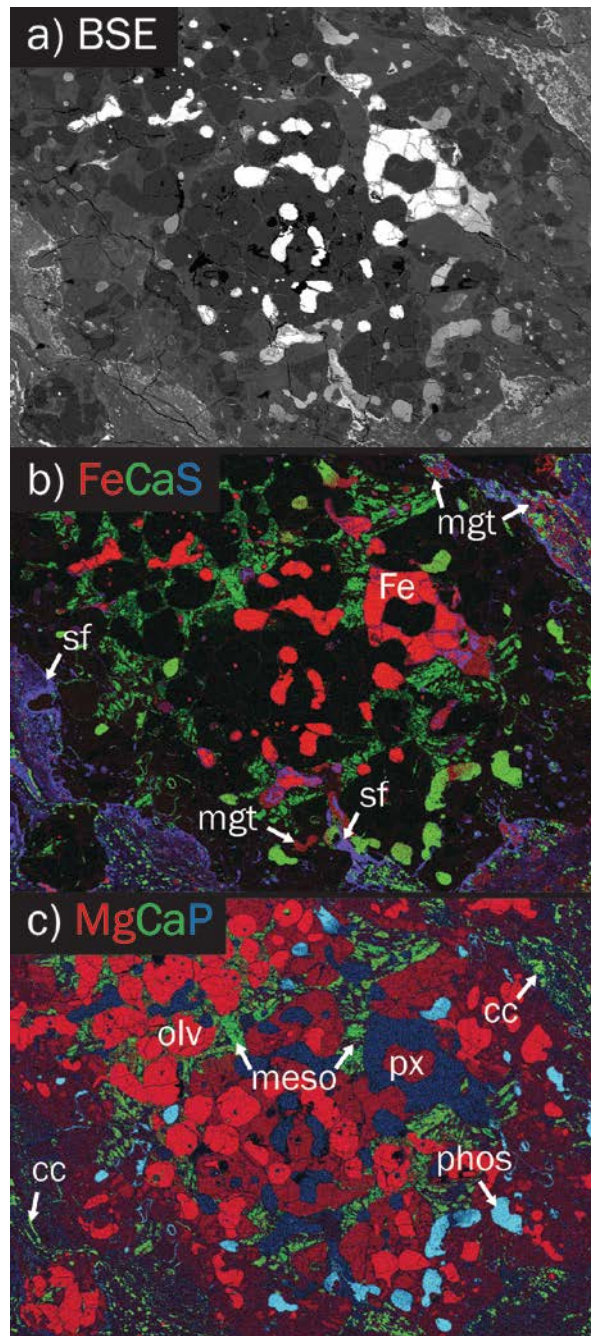


**Figure 2.10.** Images of a partially altered chondrule in Renazzo N1127. The first X-ray map depicts iron, calcium, and sulfur in red, blue, and green false color. The second map depicts silicon, calcium, and phosphorous. These false-colored maps show that the exterior of the chondrule has been partially altered, where calcium, aluminum, iron, and silicon have all been mobilized. Calcium has precipitated in the matrix as calcite, and within chondrule nodules as hydroxyapatite. Iron has been mobilized from the metal nodules into the matrix as magnetite. Sulfur is mobilized from the matrix into the chondrule, replacing iron-metal with iron-sulfides. cc = calcite, Fe = iron-metal, meso = calcium-bearing mesostasis, mgt = magnetite, olv = primary olivine, phos = phosphate (likely hydroxyapatite), px = primary pyroxene, sf = sulfide.

The fine-grained matrices of Renazzo are composed primarily of phyllosilicates and clays. Carbonates are ubiquitous in the Renazzo matrix, and exhibit three morphologies (Jilly-Rehak et al., 2015). The most common is as mottled fine-grained aggregates that are intergrown with the phyllosilicate ground mass. Such masses are usually found in chondrule rims and in the matrices surrounding heavily altered chondrules, where the mesostasis has been replaced. Carbonates also occur as coarse-grained veins, extending up to ~100  $\mu\text{m}$  in the matrix, and ~10  $\mu\text{m}$  in thickness. The third morphology is as coarse stand-alone grains, either in the matrix or in dark inclusions. All three carbonate morphologies are associated with small Ni-bearing sulfides. Sulfides are common in the fine-grained matrix as ~5  $\mu\text{m}$  spherules, ranging in composition from pyrrhotite to pentlandite. Magnetite spherules also occur in the matrix, but to a lesser extent. Magnetite is instead much more prevalent in dark inclusions.

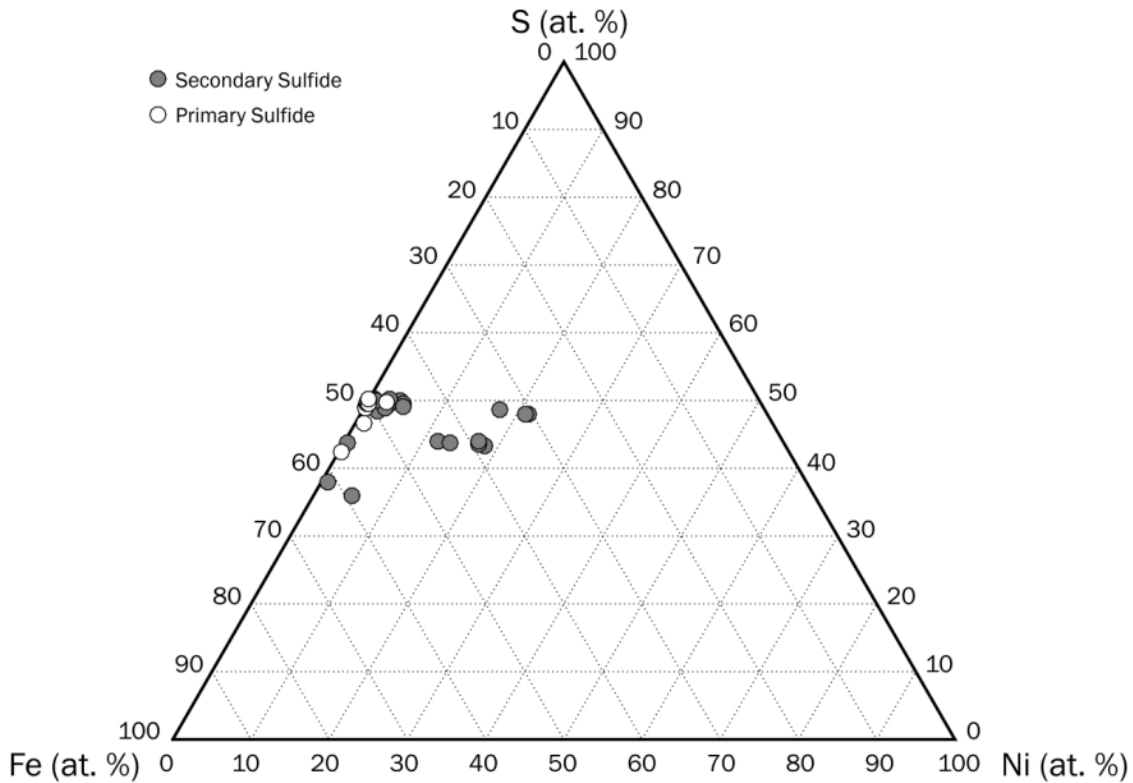


**Figure 2.11.** Ternary diagram depicting the sulfur, iron, and nickel contents of 33 sulfide grains from Renazzo N1127 and UH 1. Abundances are given in atomic percent. Stoichiometric troilite ( $\text{FeS}$ ) is only formed as a primary mineral, containing 50% iron and sulfur with no nickel. The white points represent primary sulfides from type I chondrules, type II chondrules, and opaque assemblages. The grey points represent secondary sulfides, which have higher concentrations of nickel.

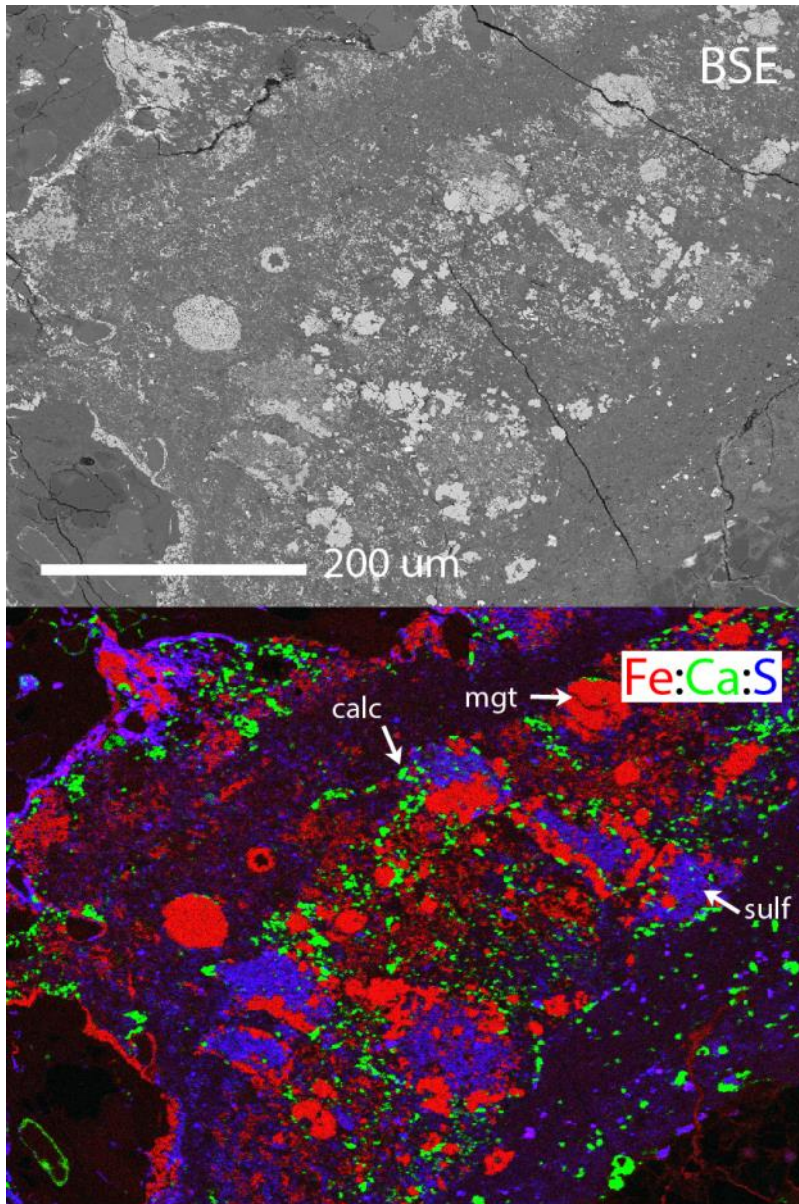


**Figure 2.12.** A complex alteration assemblage in a fine-grained rim from Renazzo N1127. The top image is a BSE image, and the bottom is a false-colored map. The red minerals are framboidal magnetite, the purple are iron-nickel-rich sulfides, and the green phases are calcite. All three minerals have grain sizes ranging from  $< 1 \mu\text{m}$  to  $\sim 5 \mu\text{m}$ . The minerals are all embedded within a phyllosilicate groundmass. Calc = calcite, mgt = magnetite, sulf = sulfide.

The dark inclusions in the Renazzo thin sections are similar to those in other CR chondrites, but show variability in mineral morphologies. Most dark inclusions contain a phyllosilicate groundmass with abundant magnetite and sulfide grains. Renazzo N1126 contains

three distinct dark inclusions (Fig. 2.13). The first contains spheroidal and framboidal magnetite, sulfide grains (about 5  $\mu\text{m}$  in diameter), and calcite that varies from mottled to coarse-grained

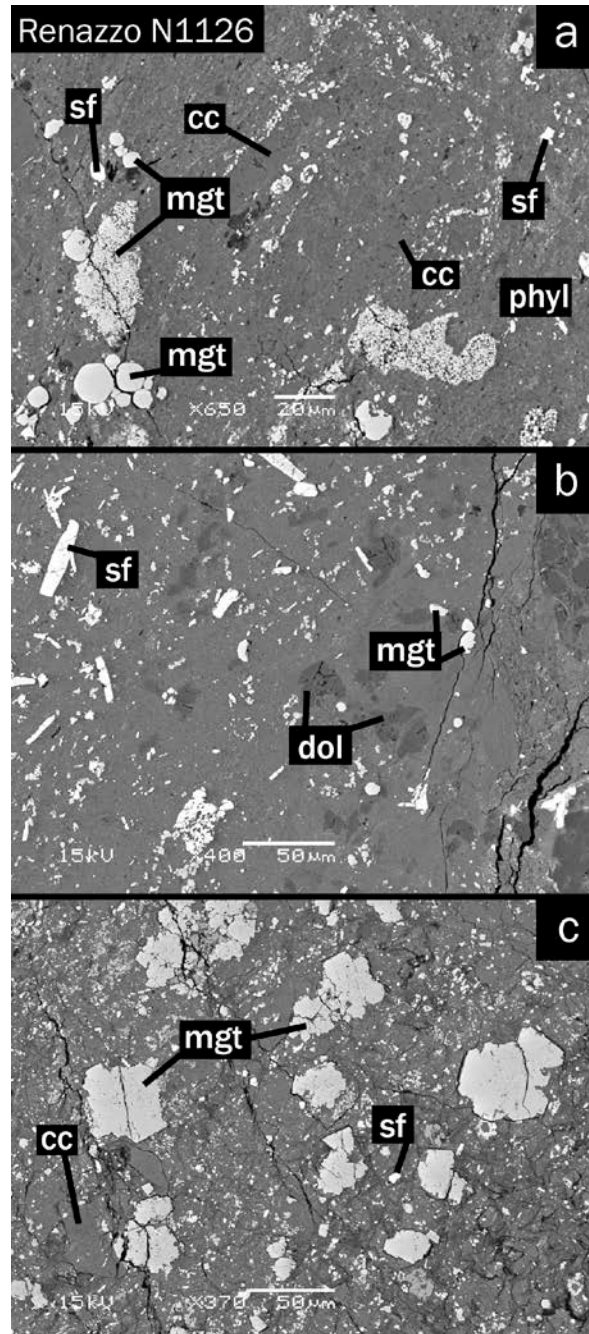
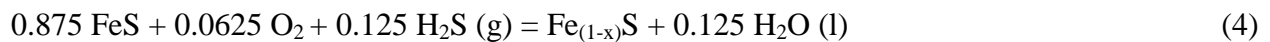
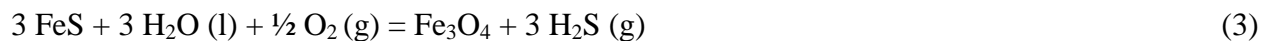


**Figure 2.13.** BSE images of three distinct dark inclusions in Renazzo N1126. All three lithologies contain sulfide, magnetite, and carbonate within a phyllosilicate matrix, but the crystal morphologies and the carbonate phases vary (see text). cc = calcite, dol = dolomite, mgt = magnetite, phyl = phyllosilicate, sf = sulfide.

texture. The dark inclusion has a phyllosilicate groundmass, and is very similar to the dark inclusions observed in QUE 99177. The second dark inclusion in Renazzo N1126 contains abundant magnetite framboids and spherules, and elongated lath-shaped sulfide crystals. Instead of calcite, the dark inclusion contains dolomite, a rare phase in CR chondrites. This dark inclusion is most similar to the inclusion from EET 92159,20 (Fig. 2.3) that also contains dolomite, though the lath-shaped sulfides are reminiscent of the dark inclusion from MET 00426,60 (Fig. 2.6). The third dark inclusion has crystal morphologies unlike any other dark inclusions in this study. The magnetite morphology is blotchy and subhedral. The dark inclusion contains one large calcite grain (~50  $\mu\text{m}$ ) that is very pure in composition and surrounded by both magnetite and sulfide grains. Some smaller mottled calcites are imbedded within the magnetite-rich matrix. The dark inclusion is extremely heterogeneous in the calcite distribution. Nearly all of the mottled calcites are confined to a rounded region within the dark inclusion. Furthermore, on one edge of the dark inclusion where there is no calcium carbonate, there are abundant calcium-iron silicates with compositions similar to kirschsteinite, as analyzed by EDX.

### 2.3.2 Geochemical modeling of CR alteration lithologies

As described above, calcite, sulfide, and magnetite assemblages are common in CR chondrites, most often occurring in dark inclusions and chondrule rims, and occasionally in heavily altered matrices. Figure 2.12 shows an example of such an assemblage in a chondrule rim from Renazzo N1127. The alteration reactions supported by these observations include the following:



We modeled this assemblage in an O-H-C-S-Mg-Fe-Ca-Si closed system, in the presence of calcite and serpentine (modeled as chrysotile) to determine the pH and fugacity conditions for formation. Fig. 2.14 illustrates the iron-bearing phases formed from a fluid, in the context of pH

versus the oxygen/hydrogen-sulfide ratios. The temperatures and pressures in Fig. 2.14 are 1 bar at 25 °C, and 10 bars at 60 °C. These temperatures were determined from oxygen isotopic fractionation between secondary magnetite and calcite in CR assemblages (Jilly-Rehak et al., 2015), and are used here as representative alteration temperatures. Changes in pressure have a minimal effect on the phase diagrams; the variations are dominated by changes of temperature.

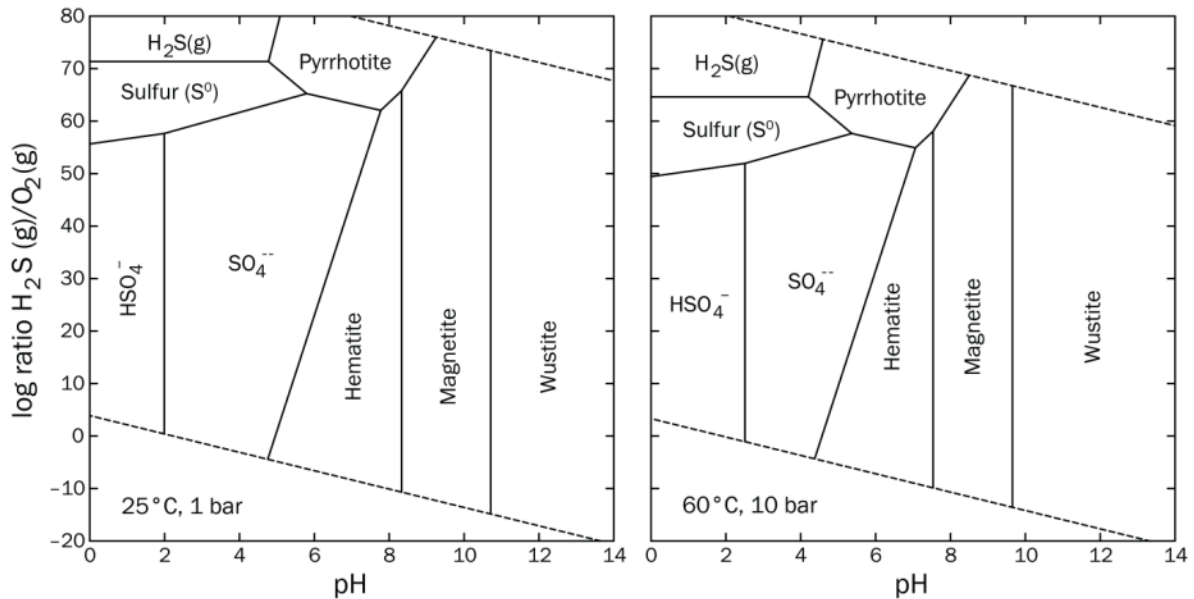


**Figure 2.14.** Bivariate activity plots from geochemical modeling, depicting the effect of pH on the stability of iron- and sulfide-bearing minerals, as a function of the H<sub>2</sub>S and O<sub>2</sub> fugacities. The dashed lines depict the stability field of liquid water, while solid lines separate the stability fields for minerals or species. The diagrams are model outputs at 25 °C at 1 bar (left) and 60 °C at 10 bar, both calculated for the same O-H-C-S-Mg-Fe-Ca-Si system. Calcite and chrysotile are included in the model basis as being saturated (i.e., precipitated) in solution. The magnetite-pyrrhotite-calcite assemblages in CR chondrites would require low partial pressure of O<sub>2</sub> and/or high partial pressure of H<sub>2</sub>S to form sulfides, while magnetite requires an alkaline environment. For both to form in equilibrium would require strict pH and fugacity environments along the mineral tie line.

We used an Fe<sup>2+</sup> activity of  $5.6 \times 10^{-7}$ , determined by converting an Fe<sup>2+</sup> molality of  $1 \times 10^{-5}$  estimated from geochemical models of CR chondrite alteration (Zolotov et al., 2015) into mass fraction, and assuming a dilute solution. This value is conservative estimate for iron activity in a silicate-rich fine-grained rim, where the iron-nickel metal mass fraction is taken to be < 0.7. Lower activities of Fe<sup>2+</sup> would shift the diagram towards more alkaline fluid pH, and higher activities would shift the diagram towards lower pH. However, under acidic conditions, iron and

sulfate ions remain dissolved in solution, rather than precipitating as a mineral. The results show that secondary pyrrhotite formation requires elevated  $H_2S/O_2$  concentration. An abundance of  $H_2S$  can be supplied during the oxidation of primary sulfide into magnetite (Eqn. 3). If the magnetite and pyrrhotite were formed in equilibrium, they would require neutral to basic fluid conditions (pH ~7-9).

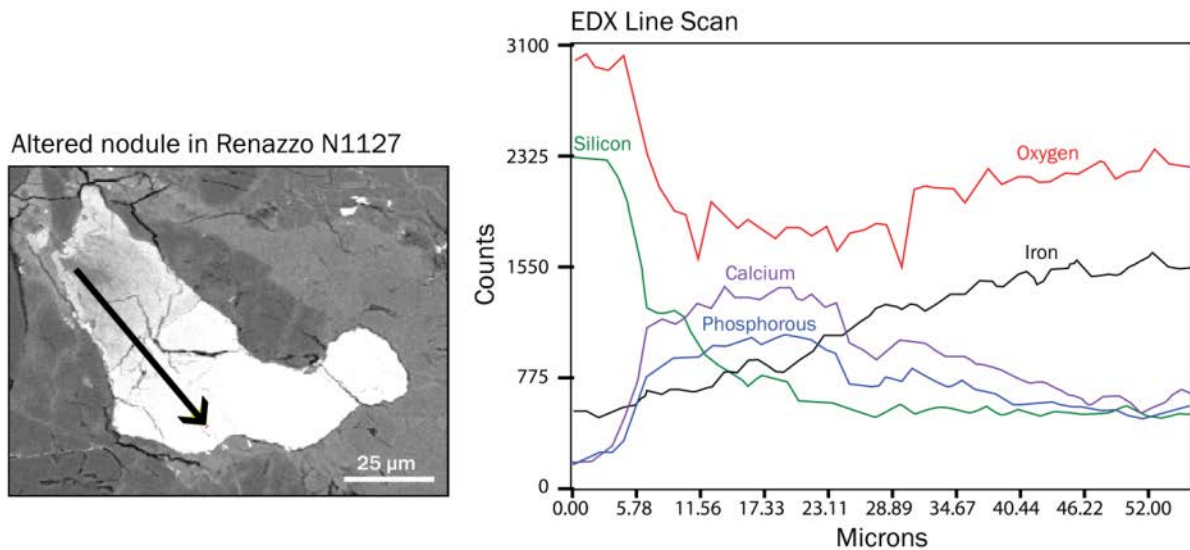


**Figure 2.15.** Image of a chondrule nodule in Renazzo N1127 that has been replaced by fine-grained silicates, phosphates, and magnetite. The minerals are zoned and intergrown in sub-micron crystals. The black arrow depicts the track of the X-ray line scan, shown on the right. The most altered region at the beginning of the transit is a silicon-iron-rich phyllosilicate, that rapidly decreases in concentration. Calcium-rich phosphate (hydroxyapatite) is then crystallized, indicated by the rapid increase of calcium and phosphorous, which show similar spectra. Magnetite becomes increasingly abundant along the transit, coupled with a gradual decrease in the apatite abundance.

The second assemblage modeled is a fine-grained phosphate and magnetite assemblage. Phosphates are observed as a minor accessory phase in CR chondrites, and can occur intergrown with magnetite as a replacement product for metal nodules in chondrules (Figs. 2.10, 2.15). In this example, a chondrule nodule has been replaced by a zoned fine-grained assemblage. At the very center is a silicate-rich alteration product, which is then intergrown with the phosphate, along with an increasing abundance of magnetite toward the edge of the grain. The phosphate mineral occurs as hydroxyapatite, which is evident in EDX spectra and in an x-ray line scan of the fine-grained assemblage (Fig. 2.15). The iron and magnesium abundances in the assemblage do not correlate with the phosphorous signal as they would for whitlockite, which is an iron- and

magnesium-bearing calcium phosphate with different molar proportions than the apatite minerals. The assemblages are zoned from an iron-bearing silicate phase, through hydroxyapatite, and into magnetite.

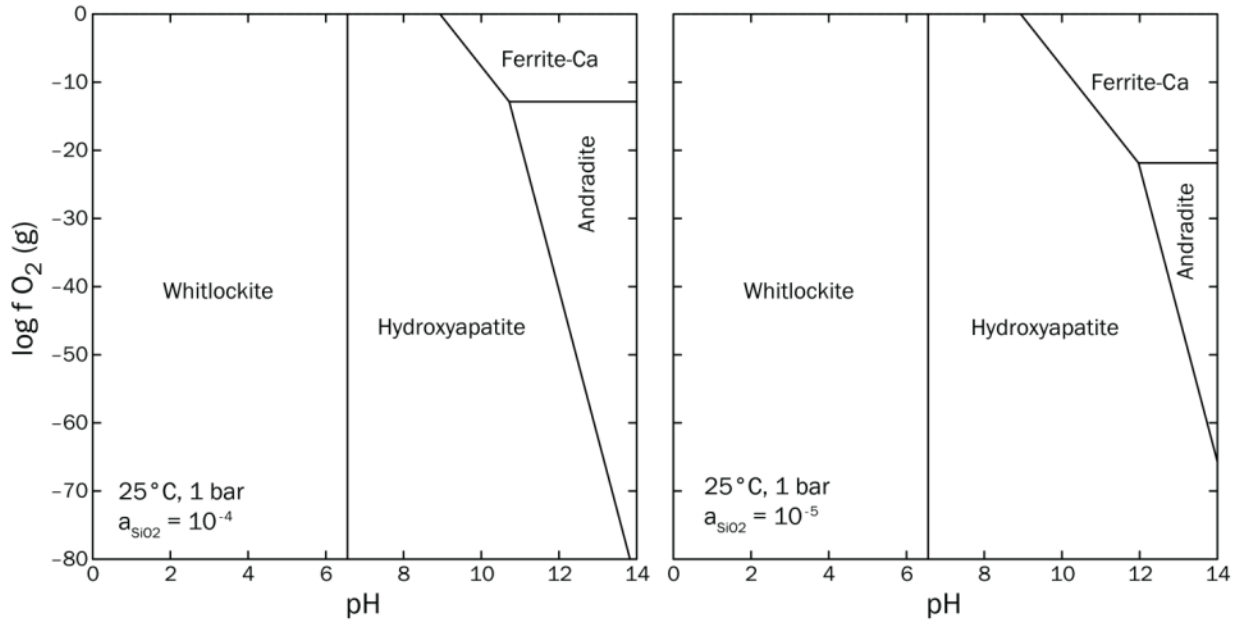


**Figure 2.16.** Bivariate activity plots from geochemical modeling, depicting the effect of pH on the stability of calcium-bearing minerals, as a function of  $O_2$  fugacity. The solid lines separate the stability fields for minerals formed from water-rock reactions. Both diagrams depict model outputs at 25 °C at 1 bar, since temperature and pressure had negligible effect on the stability fields. The two diagrams depict the effect of varying  $SiO_2$  activity, with  $a = 10^{-4}$  (left) and  $a = 10^{-5}$  (right). The hydroxyapatite observed in the Renazzo nodules is formed at alkaline pH.

In addition to Eqns. 2 and 3, the formation of magnetite-phosphate assemblages is driven by the hydroxyapatite reaction:



We modeled this phosphate-magnetite assemblage in an O-H-Mg-Fe-Ca-Si-P closed system, in the presence of aqueous  $SiO_2$  (Fig. 2.16). The activity of the phosphate ion ( $\text{HPO}_4^{2-}$ ) is taken as 0.015 in solution, determined by converting a  $\text{P}^{5+}$  molality of 0.5 into mass fraction of ( $\text{HPO}_4^{2-}$ ), assuming that the metal nodule replacement occurred under a high iron-nickel metal mass fraction of  $\sim 0.8$  (Zolotov et al., 2015). Changes in temperature from 25 to 100 °C and changes in

pressure from 1 to 100 bar had negligible effects on the phosphate stability fields; they only change the stability range of fluid water. However, the activity of SiO<sub>2</sub> in solution has a large effect on the stability of calcium-bearing silicates, such as andradite. Fig. 2.16 presents the modeled phase diagrams at a temperature of 25 °C and pressure of 1 bar, and for SiO<sub>2</sub> activities of 10<sup>-4</sup> and 10<sup>-5</sup>. Hydroxyapatite is favored at neutral to alkaline conditions, while whitlockite is stable under acidic conditions. Sulfur was not included in the models as it was not found to co-exist in the magnetite and phosphate assemblage. The inclusion of sulfur yields similar results, but requires low oxygen fugacities of log (f<sub>O<sub>2</sub></sub>) < -50 for phosphates to become stable over calcium-sulfates such as gypsum or anhydrite, which are not observed as pre-terrestrial products in CR chondrites.

## 2.4. DISCUSSION

The CR chondrites have undergone various degrees of alteration. In this section, we outline new observations and unusual or rare features from some of the CR specimens, such as the presence of dolomite in dark inclusions or the existence of calcium-iron-pyroxenes in MIL 090292, and examine possible formation mechanisms. Comprehensive discussions of the typical CR chondrite alteration processes can be found in the literature (e.g., Weisberg et al., 1993; Kallemeyn et al., 1994; Clayton and Mayeda, 1999; Krot et al., 2002; Schrader et al., 2011; 2013; 2014; Alexander et al., 2013; Bonal et al., 2013; Harju et al., 2014; Abreu, 2015; Jilly-Rehak et al., 2015). We will discuss specific minerals and alteration assemblages, and provide important constraints on the fluid chemistry and localized conditions during the progressive alteration of CR chondrites.

### 2.4.1 Carbonate-magnetite-sulfide lithologies

In nearly every CR specimen in this study, carbonates occur within dark inclusions and to some extent in the fine-grained matrices, along with magnetite and sulfide grains. Although the relative abundance, size, and shape of the minerals differ on a clast-by-clast basis, the mineralogy is essentially the same. The calcite grains are usually associated with an iron-bearing phase, either magnetite or pyrrhotite, and likely formed in neutral to alkaline fluid conditions (pH

> 7; Fig. 2.14). Such assemblages could only be compatible with acidic conditions ( $\text{pH} < 6$ ) if the iron activity (or effective concentration) was higher than  $\sim 0.006$ , which is unreasonable in the context of these CR assemblages. This observation is in general agreement with chemical modeling of CR chondrite fluids (Zolotov et al., 2015), where they find that the pH of solution is alkaline when calcite, pyrrhotite and magnetite co-exist.

The formation of dolomite over calcite in some CR chondrites is enigmatic. There is a general lack of understanding of how low-temperature dolomites form, despite being an extremely common mineral in the chondritic meteorite – and terrestrial sedimentary – record (e.g., Rodriguez-Blanco et al., 2015). Many natural dolomites are explained by the dolomitization of calcium-carbonate precursor minerals, rather than having been precipitated as dolomite from solution. The dolomite grains observed in CR chondrites all appear to be pseudomorphs of what were previously forsteritic olivine grains (Figs. 2.3, 2.13); many texturally similar forsterite grains occur in dark inclusions that have not been altered into a secondary phase. Such dolomite grains do not appear to have been dolomitized from pre-existing calcium-carbonates, but rather were formed by the replacement of magnesium-rich silicates.

In laboratory solution crystallization experiments, the presence of the  $\text{Mg}^{2+}$  ion actually inhibits the formation of dolomite, instead favoring the formation of other carbonates such as aragonite or magnesite (e.g., Medlin, 1959; Zhang et al., 2012; Ichimura and Sugiura, 2015; Rodriguez-Blanco et al., 2015). However, more recent experiments have shown that dolomite can form directly from solution via Ostwald-ripening, where nano-crystalline carbonate aggregates slowly accumulate and transform into stoichiometric dolomite (Rodriguez-Blanco et al., 2015). The conditions necessary to form small amounts of dolomite in the laboratory are strict; the experiments described in literature required specific temperatures (ranging from 100 to 250 °C), pH (6.5 to 9.4), and Ca/Mg ratios ( $\sim 0.2$  to 1.4) that were varied depending on the analytical procedures involved (Medlin, 1959; Zhang et al., 2012; Ichimura and Sugiura, 2015; Rodriguez-Blanco et al., 2015). Such stringent conditions may account for the rarity of dolomite in CR chondrites. A recent study by Zhang et al. (2012) suggests that the presence of dissolved sulfide in pore waters may act as a catalyst for the precipitation of disordered dolomite, a precursor to stoichiometric dolomite. In this hypothesis, the dissolved sulfide lowers the energy barrier for the dehydration of  $\text{Mg}^{2+}$  water complexes in solution, allowing the magnesium ion to more readily incorporate onto growing carbonate surfaces. Small changes in dark-inclusion

microenvironments, such as the dissolution of sulfides, may have been enough to favor the local formation of dolomite over other carbonate minerals.

#### **2.4.2 The origin of phosphates**

Phosphates are common minor minerals in chondrites, formed by both low-temperature aqueous processes and high-temperature thermal processes. As secondary thermal alteration products, chlorapatite, whitlockite, and merrillite can be formed by high-temperature (>725 °C) reactions at metal-silicate interfaces (Ruzicka et al., 2005). Phosphates also occur as minor primary high-temperature phases in opaque assemblages in OC (ordinary chondrites), CO, CV, K (Kakangari-like), and R (Rutimuri-like) chondrites (Rubin, 1997; Brearley and Jones, 1998).

As secondary aqueously-formed products, phosphates are generally found as smaller grains in calcium-rich phases. For example, fluid activity in OC and CO chondrites can alter the above primary phosphates into more calcium-rich phases, such as hydroxyapatite (Lauretta et al., 2001). Aqueously formed phosphates have been reported in the matrices surrounding type II chondrules in CM and CR chondrites. Phosphorous is sequestered as  $P_2O_5$  in the mesostasis of type II chondrules in chondrites; upon interaction with fluids, the phosphorous is leached into the matrix and precipitated as apatite or whitlockite (Brearley and Chizmadia, 2005).

For the predominant type I chondrules in CR chondrites, phosphorous resides in iron-nickel metal as native  $P^0$ . Unaltered metal in CR chondrites contains variable phosphorous abundances, ranging from 0.13 – 0.43 wt% in Renazzo (Zanda et al., 1994). Calcium is mobilized during the alteration of glassy chondrule mesostasis. The replacement products for chondrule mesostases are aluminum-rich phyllosilicates, while the calcium is generally transported into the matrix. Calcium phosphates can form when this calcium-rich fluid interacts with the phosphorous-bearing precursor metal, also oxidizing the iron into magnetite as seen in Fig. 15. Geochemical models of the alteration of metal in CR chondrites have suggested that the fluid pH is ~7 when the environment is metal-rich, and that the altering solution becomes more alkaline under metal-poor alteration circumstances (Zolotov et al., 2015). These observations are consistent with the phosphate-stability models reported here, showing that the alkaline pH conditions of metal alteration may have promoted hydroxyapatite growth over whitlockite, which is more stable under acidic conditions (Fig. 2.16).

### 2.4.3 Formation of calcium-iron silicates in MIL 090292,12

The MIL 090292,12 thin section does not contain calcium carbonates, a common phase in all other CR chondrite specimens. Rather, calcium primarily resides in secondary calcium-rich silicates. The calcium- and iron-rich silicates in MIL 090202 are clearly secondary in origin; they occur as replacement products in the interior of altered CAIs and chondrules, as rims around olivine pseudomorphs, and as isolated grains in the matrix (Fig. 2.17). Some of these morphologies are similar to the calcium-iron pyroxenes observed in CV chondrites (Krot et al., 1998), which replace fayalitic olivine rims around forsteritic olivine grains. However, in MIL 090292 the silicates occur in lithologies with abundant magnetite rather than fayalite, the more common phase in CV chondrites.

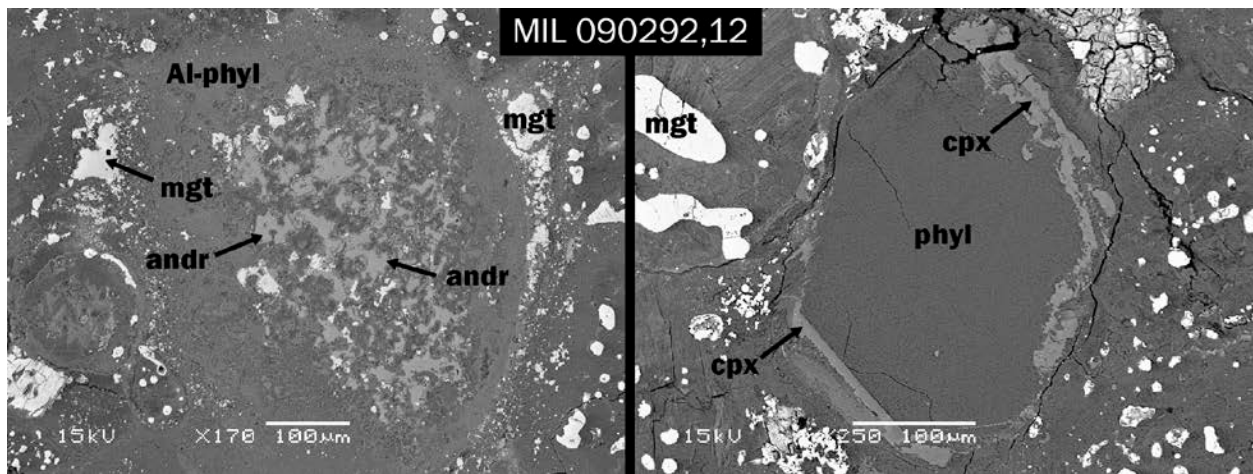


**Figure 2.17.** BSE images of calcium-iron-rich silicates in MIL 090292,12. (a) Image showing andradite replacing the interior of a CAI. The exterior portion has been completely altered into aluminum-rich phyllosilicates. (b) Image of a pseudomorphed olivine crystal, showing a distinct rim made of iron-calcium-rich pyroxene. Al-phyl = aluminum phyllosilicate, andr = andradite, cpx = calcium-iron-pyroxene, mgt = magnetite, phyl = phyllosilicate.

The lack of carbonate phases and abundance of calcium-silicates may be indicative of different alteration conditions such as higher silicon activity (Fig. 16), or higher temperatures (e.g., Krot et al., 1998; 2000). Models of secondary phases in an Fe-Si-Ca-O-H system for CV chondrites have shown that magnetite is stable compared with fayalite at higher temperatures in systems with low partial pressures of  $H_2O/H_2$ . Magnetite becomes the preferred phase at low

temperatures under H<sub>2</sub>O-dominated systems. Andradite stability increases with higher silicate activity in solution, as well as a low ratio of iron/calcium activity (Krot et al., 1998). These observations imply that the method of alteration of MIL 090292 was different than for other CR chondrites, and likely occurred at higher temperatures and different fluid chemistry.

#### **2.4.4 Is MIL 090292 a CR chondrite?**

If MIL 090292 is indeed a CR chondrite, this sample provides evidence that local alteration environments were extremely variable on the CR parent body. But despite the abundance of metal-rich chondrules, there are multiple lines of evidence to suggest that MIL 090292 is not a CR chondrite. Above, we show how the presence of secondary calcium-iron-silicates indicates that alteration conditions for MIL 090292 must have been very different than in other CR chondrites. Similarly, the MIL 090292,12 section does not contain calcite, a very common phase in all other CR-chondrite sections that we studied. Further petrographic evidence lies in the unique morphologies of magnetite observed in MIL 090292. Framboidal magnetite is rare, but small plaquettes are prolific throughout the entire matrix, even among the various clasts within the section. Iron-nickel metal nodules in chondrules have been nearly completely replaced by magnetite, with the exception of small extremely nickel-rich (88 wt.%) metal blebs. Such Ni-rich metal bits are not observed in other heavily-altered CR chondrules, even in GRO 95577, the other CR 2.0. This feature is unique to MIL 090292, and may suggest that MIL 090292 was altered under  $f_{O_2}$  conditions lower than the Ni-NiO buffer.

Perhaps the most convincing evidence lies in the oxygen isotopic compositions of magnetite in MIL 090292,12. The oxygen isotopes for magnetite in MIL 090292 diverge from a progressive alteration trend defined by magnetite from other CR specimens (Jilly-Rehak et al., 2015). Instead, the oxygen isotopic composition of MIL 090292 magnetite is similar to magnetite in some CV and CK chondrites (Choi et al., 1997; Choi and Wasson, 2003; Hsu et al., 2006; Davidson et al., 2014). The magnetite oxygen isotopic compositions have  $\Delta^{17}O$  values of approximately -3.5 ‰, which is substantially lower than the other CR values near 0 ‰. Such a deviation cannot be explained by terrestrial weathering, which would pull the oxygen isotopic compositions towards the terrestrial fractionation line. Similar oxygen isotopic discrepancies are observed in whole-rock and matrix analyses (Harju et al., 2014; Schrader et al., 2014), where

MIL 090292 defies the trends set by all other CR chondrites. In light of this evidence, we propose that MIL 090292 is misclassified as a CR chondrite, and should be considered an ungrouped C2 until studied further.

## 2.5 CONCLUSIONS

The CR chondrite group is characterized by large metal-rich chondrules set within a fine grained matrix, where primary constituents have been altered into secondary minerals to various extents. The fine-grained matrices are composed of varying amounts of phyllosilicates, anhydrous silicates, and amorphous silicates, depending on the alteration state of the sample. Bulk elemental compositions were measured for the matrices of the two least-altered CR chondrites, QUE 99177 and MET 00426, using EPMA. The bulk compositions are essentially the same as the matrices measured previously in the more aqueously altered chondrites Renazzo and EET 87770, indicating that alteration was isochemical.

Most CR chondrites contain dark inclusions that are similar in mineralogy and bulk composition to the matrices. The quantity, size, and distribution of dark inclusions vary between samples. While most dark inclusions contain the same minerals, the abundances of the minerals can differ greatly from clast to clast. The most common secondary minerals in the fine-grained matrices and dark inclusions are magnetite, iron-nickel sulfides, and calcite. Modeling of this assemblage at temperatures of 25 °C and 60 °C indicates that alteration must have occurred in an environment enriched in H<sub>2</sub>S relative to O<sub>2</sub> in order to form the observed iron-sulfides. The assemblages also require pH conditions from ~7 to 9, depending on temperature and the activity of iron in the solution. At low iron activities, the formation of such phases requires even more alkaline conditions. In two dark inclusions, dolomite grains were found as replacement products for forsterite crystals, occurring in assemblages with numerous iron-sulfide grains. Although the mechanism of dolomite formation poorly understood, it has been hypothesized that direct precipitation from a magnesium- and calcium-rich solution may have been catalyzed by the presence of dissolved sulfides.

The primary chondrule silicates from CR chondrites are hydrated into phyllosilicates during alteration. Chondrule mesostases are altered to aluminum-rich phyllosilicates and/or calcite. Metal nodules are replaced by magnetite, though layering with sulfide and silicate rich

material has been observed. In some instances, metal nodules have been replaced by phosphate-magnetite assemblages. Geochemical modeling of these phases has shown that they form at pH >7. Other calcium-bearing phases, such as andradite, may become stable under high SiO<sub>2</sub> activities or under acidic conditions. The observation of andradite and calcium-iron-pyroxene in MIL 090292 suggest that it was altered under conditions not typical for CR chondrites, and is likely not related to the CR class. Our study shows that the aqueous alteration assemblages formed in CR chondrites were highly dependent on the fluid micro-environments during alteration. Progressive alteration may have caused fluctuations in pH or oxygen fugacity, which in turn could change the mineral stability, accounting for the abundance differences in minerals across distinct CR clasts.

## CHAPTER 3

### **<sup>53</sup>MN-<sup>53</sup>CR RADIOMETRIC DATING OF SECONDARY CARBONATES IN CR CHONDRITES: TIMESCALES FOR PARENT BODY AQUEOUS ALTERATION**

In preparation for submission to *Geochimica et Cosmochimica Acta*, as Jilly-Rehak C. E., Huss G. R., and Nagashima K. <sup>53</sup>Mn-<sup>53</sup>Cr radiometric dating of secondary carbonates in CR chondrites: timescales for parent body aqueous alteration.

*Abstract*– We present the first resolved <sup>53</sup>Mn-<sup>53</sup>Cr ages of secondary carbonates from Renazzo-like (CR) chondrites. Though the process of aqueous alteration in CR chondrites is well-documented, many questions remain regarding the alteration timescales. CR chondrites range from completely altered to nearly anhydrous, and are characterized by large metal-rich chondrules, phyllosilicate-bearing fine grained matrices, and clasts of heavily hydrated material referred to as dark inclusions. <sup>53</sup>Mn-<sup>53</sup>Cr isotope systematics were measured in secondary carbonates from three different CR-chondrite lithologies. Calcite in the interchondrule matrix of Renazzo, calcite in the matrix of GRO 95577, and dolomite in a dark inclusion of Renazzo all show excess in <sup>53</sup>Cr, interpreted as the daughter product from the decay of <sup>53</sup>Mn. The Renazzo calcite yields an initial ratio of  $(^{53}\text{Mn}/^{55}\text{Mn})_0 = (3.6 \pm 2.0) \times 10^{-6}$ , and the Renazzo dark inclusion dolomite ranges from  $(^{53}\text{Mn}/^{55}\text{Mn})_0 = (3.1 \pm 1.5) \times 10^{-6}$  (corrected to the RSF of a calcite standard) to  $(3.8 \pm 1.8) \times 10^{-6}$  (corrected to a hypothesized dolomite RSF). When anchored to the D’Orbigny angrite, the Renazzo carbonates yield ages between 4562.7 to 4563.7 Ma, or ~ 3.6 to 4.6 Myr after the formation of CV CAIs. Calcite measured in the heavily altered specimen GRO 95577 yields a shallower slope of  $(^{53}\text{Mn}/^{55}\text{Mn})_0 = (7.7 \pm 2.5) \times 10^{-7}$ , corresponding to a much younger age of 4555.2 Ma, or ~ 12.1 Myr after CAI formation. The two Renazzo ages are contemporaneous with manganese-chromium ages of carbonates in Tagish Lake, CI, and CM chondrites, but the GRO 95577 age is uniquely young. These findings suggest that early aqueous alteration processes on chondritic parent bodies were a common occurrence, likely driven by internal heating from <sup>26</sup>Al decay after accretion. The young carbonate ages of GRO 95577 suggest that either the CR parent body was sufficiently large to sustain heating from <sup>26</sup>Al for ~ 8 Myr, or that late-stage impact events supplied heat to the region where GRO 95577 originated.

### 3.1 INTRODUCTION

The Renazzo-like (CR) carbonaceous chondrites are particularly useful for the study of aqueous alteration. CR chondrite lithologies range from nearly anhydrous to completely hydrated, with most samples being partially altered (Weisberg et al., 1993; Kallemeyn et al., 1994; Weisberg and Huber 2007; Abreu and Brearley 2010; Schrader et al., 2011; Harju et al., 2014). These various stages of hydration essentially document the process of alteration, revealing how elements were transported in the fluid (e.g., Burger and Brearley, 2004), and exposing the water-rock reactions that formed the secondary minerals (e.g., Weisberg et al., 1993; Clayton and Mayeda, 1999).

Though the petrographic context of CR aqueous alteration is well documented, many questions remain regarding the timescales of alteration. Alteration ages are imperative if we are to understand the location of alteration, and the heat source for melting of water ice. According to asteroidal models of alteration, secondary minerals were formed on the parent body due to the interaction between primitive chondritic rock and liquid water (McSween, 1979; Weisberg et al., 1993; Browning et al., 1996; Clayton and Mayeda, 1999; Jogo et al., 2009). These models require a source of heat to melt the accreted ice on the asteroidal parent body, usually invoking  $^{26}\text{Al}$ -decay or impact heating (e.g., Abreu and Bullock, 2013). Models of pre-accretionary aqueous alteration assert that hydrous minerals may have formed through the reaction of anhydrous nebular phases and water vapor as the solar nebula cooled (Cyr et al., 1998). An alternative pre-accretionary model suggests that hydration of silicate dust may have occurred during the passage of shock waves in an ice-enriched region of the solar nebula (Ciesla et al., 2003). Most petrographic and isotopic observations in CR chondrites support the asteroidal setting for alteration (Weisberg et al., 1993; Burger and Brearley, 2004; Brearley, 2006; Weisberg and Huber, 2007; Schrader et al., 2011; 2014; Abreu and Bullock, 2013), though observations of unaltered glass in contact with hydrated matrices have been used to invoke a pre-accretionary setting in some CR chondrites (Ichikawa and Ikeda, 1995). Brecciation after alteration on the final parent body may explain such occurrences. Radiometric dating of secondary minerals can be used to further constrain the model of alteration for CR chondrites, and to distinguish the heat source involved.

The  $^{53}\text{Mn}$ - $^{53}\text{Cr}$  system is a robust radiochronometer for dating the formation of early solar system materials. The system yields dates consistent with Pb-Pb ages for a variety of materials (Amelin et al., 2010; Bouvier and Wadhwa, 2010; Brennecka and Wadhwa, 2012), lending credence to its accuracy. Radioactive  $^{53}\text{Mn}$  decays into stable  $^{53}\text{Cr}$  via electron capture. This process has a half-life of 3.7 Myr, long enough to date minerals that were formed during the first ~20 Myr of Solar System formation (e.g., Lugmair and Shukolyukov, 1998; Shukolyukov and Lugmair, 2006). The duration of aqueous alteration of chondritic materials has previously been estimated to range from 1-15 Myr after the formation of calcium-aluminum-rich inclusions (CAIs), the first Solar System solids (Krot et al., 2006). These ages were based on manganese-chromium measurements of carbonates, as well as iodine-xenon measurements of magnetite and phyllosilicates in chondrites. However, these reported ages were based upon incorrect assumptions about mineral relative sensitivity factors, inadequate time anchors, and poorly defined initial  $^{53}\text{Mn}/^{55}\text{Mn}$  ratios (see discussion below), stressing the need for more accurate and consistent analyses.

In the literature, radiometric  $^{53}\text{Mn}$ - $^{53}\text{Cr}$  dating of secondary minerals has been dominated by studies of the Ivuna-like (CI) and Mighei-like (CM) chondrites, where carbonate minerals are generally much more abundant and coarse-grained (e.g., Endreß et al., 1996; Hoppe et al., 2007; De Leuw et al., 2009; Petit et al., 2009; 2011; Blinova et al., 2012; Lee et al., 2012). The Vigarano-like (CV) chondrites have also been studied using  $^{53}\text{Mn}$ - $^{53}\text{Cr}$  dating, but in secondary fayalite grains (e.g., Hutcheon et al., 1998; Hua et al., 2005; Jogo et al., 2009; Doyle et al., 2015). Only one study has attempted to measure CR chondrite alteration ages by looking at  $^{53}\text{Mn}$ - $^{53}\text{Cr}$  in siderite (Tyra et al., 2010). They found no resolvable age, possibly suggesting that the aqueous alteration process had lasted until the majority of  $^{53}\text{Mn}$  had decayed, later than ~20 Myr after CAI formation.

In this study, we present the first resolved  $^{53}\text{Mn}$ - $^{53}\text{Cr}$  ages of carbonates in CR chondrites. Carbonate minerals are good targets for  $^{53}\text{Mn}$ - $^{53}\text{Cr}$  dating, as they fractionate manganese and chromium during formation from aqueous fluids. We describe the mineralogy and petrology of secondary carbonates in CR chondrites, and determine the ages of calcite and dolomite in the CR chondrites Renazzo and Grosvenor Mountains (GRO) 95577. This study places important constraints on the timing and nature of the aqueous alteration process for CR chondrites, and has broader implications regarding the heat sources required for alteration to occur.

## 3.2 ANALYTICAL METHODS

### 3.2.1 Thin section mineralogy and petrography

CR chondrites are rich in carbonate material, making them potential targets for the study of manganese-chromium radiometric dating. While carbonates are prevalent, most of the material exists as fine-grained masses intergrown with matrix phyllosilicates, unsuitable for *in situ* measurement (Fig. 3.1). However, two CR specimens, Renazzo and GRO 95577, have coarse-grained carbonates large enough (greater than  $\sim 10\ \mu\text{m}$ ) for manganese-chromium dating.

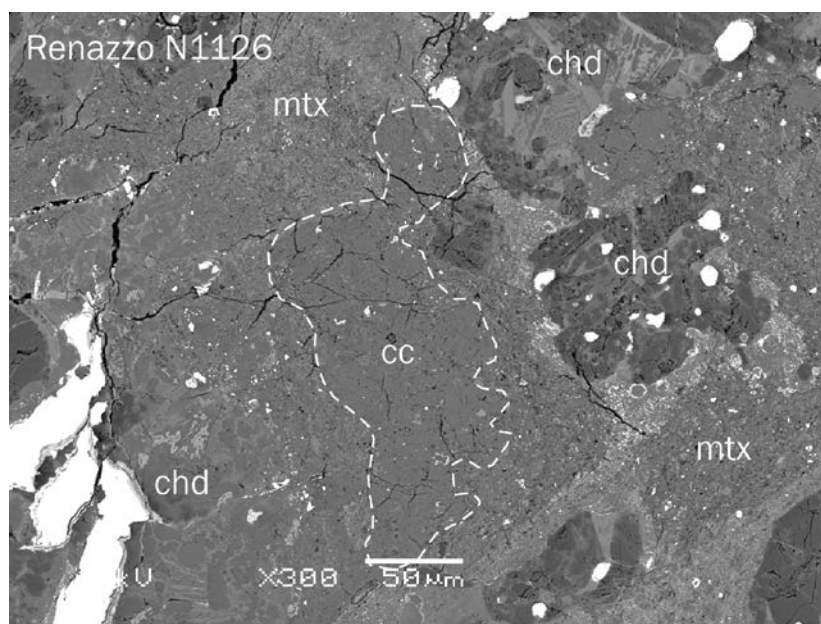


**Figure 3.1.** Backscattered electron (BSE) image of fine-grained calcium-carbonate material in the fine-grained matrix of Renazzo N1126 (outlined by the dashed line). The carbonate is intergrown with phyllosilicates and sulfides, making it unsuitable for  $^{53}\text{Mn}$ - $^{53}\text{Cr}$  measurements. chd = chondrule, cc = calcite, mtx = matrix.

A total of three sections from the two meteorites were used in this work (Table 3.1). All thin sections were initially observed and characterized using optical microscopy. After carbon-coating, element X-ray maps of each thin section were obtained using the JEOL JXA-8500F electron microprobe at the University of Hawai'i. Calcium, iron, magnesium, aluminum, and sulfur were measured using a 50 nA beam at 15.0 kV. Individual elemental maps were combined

into multi-element pseudo-mineral maps used to identify potential carbonate-rich regions for ion microprobe measurements. Sections were also analyzed by EPMA and imaged using backscattered-electron (BSE) imaging on a JEOL JSM 5900LV scanning electron microscope (SEM) set to an accelerating voltage of 15 kV. Carbonate grains for manganese-chromium isotope analysis were identified using energy dispersive x-ray spectroscopy (EDX).

**Table 3.1.** CR chondrites used in this study.

Meteorite	Petrologic Type	Fall/Find	Weathering Grade	Special Prep
GRO 95577,69	CR 2.0	Find	B	Made w/o water
Renazzo N1126	CR 2.4	Fall	N/A	Made w/o water
Renazzo N1127	CR 2.4	Fall	N/A	Made w/o water

### 3.2.2 Secondary Ion Mass Spectrometry (SIMS)

Carbonates in the three CR chondrite thin sections were measured for manganese-chromium isotopes using the University of Hawai'i Cameca IMS 1280 ion microprobe. Two calcite grains were measured in the Renazzo N1127 matrix, five calcite grains were measured in the GRO 95577,69 matrix, and seven dolomite grains were measured in a dark inclusion from Renazzo N1126. All calcite measurements were taken during a single session, and the dolomite analyses were taken during a second session under the same analytical conditions, using procedures similar to those described by Jilly et al. (2014). Measurements used the duoplasmatron  $^{16}\text{O}^-$  source set to a current of  $\sim 100$  pA and a primary beam focused to  $\sim 5$   $\mu\text{m}$  in diameter (no raster). Isotopes  $^{52}\text{Cr}^+$  and  $^{53}\text{Cr}^+$  were measured in multicollection mode (45 seconds) followed by a peak jump to  $^{55}\text{Mn}^+$  (2 seconds). All isotopes were measured by electron multipliers, and a typical measurement consisted of  $\sim 100$  cycles. For the calcite analyses,  $^{50}\text{Cr}^+$  (plus unresolved contributions from isobars  $^{50}\text{V}^+$  and  $^{50}\text{Ti}^+$ ) was also measured in multicollection mode to potentially be used for an internal mass-fractionation correction. The mass-resolving power was  $\sim 4800$  for  $^{50}\text{Cr}^+$  and  $^{52}\text{Cr}^+$ , and was  $\sim 6500$  for  $^{53}\text{Cr}^+$  and  $^{55}\text{Mn}^+$  to resolve the interference from  $^{52}\text{CrH}^+$  on  $^{53}\text{Cr}^+$ . Calcite grains were pre-sputtered for 600 s using a  $\sim 300$  pA beam and 5  $\mu\text{m}$  raster, and dolomite grains were pre-sputtered for 360 s at  $\sim 100$  pA with no raster, to remove carbon coating and surface contamination. Synthetic manganese- and

chromium-bearing calcites provided by N. Sugiura from the University of Tokyo (Sugiura et al., 2010) and San Carlos olivine were used as standards.

After measurement, the data were reduced using an in-house data reduction package. The isotope ratios were calculated using the sum of the total counts, rather than the mean of the ratios. The mean of the ratios method of averaging data has been shown to introduce statistical bias for measurements with low count rates (Ogliore et al., 2011). Uncertainties on  $^{55}\text{Mn}/^{52}\text{Cr}$  represent the combined error of the statistical uncertainty with a 10% systematic uncertainty to account for non-statistical variation in the  $^{55}\text{Mn}/^{52}\text{Cr}$  ratio ( $2\sigma$ ). In carbonates, the  $^{55}\text{Mn}/^{52}\text{Cr}$  ratios can vary within a single grain due to trace element zoning or individual crystal growths incorporating different amounts of manganese and chromium. In the case that a single measurement analyzed regions of distinct  $^{55}\text{Mn}/^{52}\text{Cr}$  ratios, the analyses were split into multiple data points, with each point representing the average  $^{55}\text{Mn}/^{52}\text{Cr}$  of that region. This method was used to avoid averaging over a very wide  $^{55}\text{Mn}/^{52}\text{Cr}$  distribution, which would introduce correlated error in the measurement. The splitting of data can re-introduce ratio bias if the total counts are sufficiently low. For our worst-case scenario, the total counts in the ratio denominator was 800, which corresponds to a maximum possible bias of  $\sim 10^{-3}$  if using the mean of the ratios method for calculating ratios, but a bias of  $\sim 10^{-4}$  with the total counts method used in this study (Ogliore et al., 2011).

The sample data were corrected for instrumental mass fractionation externally using the mean  $^{53}\text{Cr}^+ / ^{52}\text{Cr}^+$  ratios measured in the standards compared to the reference ratio of  $^{53}\text{Cr} / ^{52}\text{Cr} = 0.113459 \pm 0.000005$  (Papanastassiou, 1986). The  $^{53}\text{Cr}^+ / ^{52}\text{Cr}^+$  ratios for San Carlos olivine were consistent throughout the measurement, with a  $2\sigma$  standard error of 1.2 ‰. The  $2\sigma$  standard error for the synthetic calcite analyses was 0.83 ‰. These uncertainties were propagated into the total uncertainty for the sample  $^{53}\text{Cr} / ^{52}\text{Cr}$  analyses. An internal instrumental-mass-fractionation correction was not used, as the interferences of  $^{50}\text{V}^+$  and  $^{50}\text{Ti}^+$  on  $^{50}\text{Cr}^+$  were too large. For this reason,  $^{50}\text{Cr}^+$  was not measured during the dolomite session. The  $^{53}\text{Cr}$  excesses in the unknowns are reported as  $\delta^{53}\text{Cr}^*$ , representing the deviation of the mass-fractionation-corrected  $^{53}\text{Cr}^+ / ^{52}\text{Cr}^+$  ratio from the reference ratio in units of per mil (Eqn. 1).

$$\delta^{53}\text{Cr}^* = [({}^{53}\text{Cr}^+ / {}^{52}\text{Cr}^+)_{\text{IMF-corrected}} / 0.113459 - 1] * 1000 \quad (1)$$

### 3.2.3 $^{55}\text{Mn}/^{52}\text{Cr}$ relative sensitivity factors

The relative sensitivity factor (RSF) for manganese-chromium measurements describes the relative efficiency with which atoms sputtered from the sample are transferred to the ion detectors. The RSF is dependent on the mineral composition, the instrumental tuning, and the duration of measurement (Sugiura et al., 2010; McKibbin et al., 2013). We define the RSF as the  $^{55}\text{Mn}^+ / ^{52}\text{Cr}^+$  ratio measured by SIMS divided by the true ratio of  $^{55}\text{Mn}/^{52}\text{Cr}$  in the sample: Essentially, the RSF is a measure of the ion microprobe's relative efficiency for measuring manganese and chromium in a particular mineral.

$$\text{RSF} = [ (^{55}\text{Mn}^+ / ^{52}\text{Cr}^+)_{\text{SIMS}} / (^{55}\text{Mn} / ^{52}\text{Cr})_{\text{TRUE}} ] \quad (2)$$

The measured ratio for the sample is then divided by the RSF to give the true value of the sample. It should be noted that in some studies, the RSF value has also been described as the inverse (e.g., McKibbin et al., 2013; 2015).

Carbonates that contain measurable amounts of both chromium and manganese are extremely rare on Earth and are difficult to synthesize, as the carbonate structure does not accommodate the  $\text{Cr}^{2+}$  ion. For this reason, the  $^{55}\text{Mn}$ - $^{53}\text{Cr}$  dating of carbonates has historically been standardized to silicates, under the assumptions that the ionization potentials and matrix effects for silicates and carbonates were indistinguishable (e.g., Hoppe et al., 2007; De Leuw et al., 2009; Petit et al., 2011; Lee et al., 2012). Manganese and chromium bearing carbonates have recently been synthesized (Sugiura et al., 2010; Ichimura and Sugiura, 2015), allowing this assumption to be tested (see Appendix A for a detailed discussion about manganese- and chromium-bearing calcite standards). There is solid evidence that the  $^{55}\text{Mn}/^{52}\text{Cr}$  RSF for carbonates differs significantly from that for olivine, calling into question the accuracy of previously reported manganese-chromium ages (Sugiura et al., 2010; Fujiya et al., 2012; 2013; McKibbin et al., 2013; Ichimura and Sugiura, 2015). Numerous grains of the synthetic manganese and chromium calcite prepared by N. Sugiura and W. Fujiya were provided to the University of Hawai'i as standards for manganese-chromium dating.

The synthetic calcites are radially zoned in both manganese and chromium content, and therefore the  $^{55}\text{Mn}/^{52}\text{Cr}$  composition cannot be defined as a single value. We determined the

$(^{55}\text{Mn}/^{52}\text{Cr})_{\text{TRUE}}$  values for the synthetic calcite standards using electron microprobe analysis (EPMA) on the JEOL JXA-8500F at the University of Hawai'i. After SIMS analysis, multiple points surrounding each SIMS pit were measured. The EPMA measurements (typically four per SIMS pit) were averaged to obtain a manganese/chromium abundance ratio for each SIMS standard analysis. Manganese, chromium, iron, calcium, magnesium, and silicon were measured at an accelerating voltage of 15 keV for 30 seconds each. Since carbonates are particularly susceptible to electron beam damage and outgassing during analysis, measurements were taken at 10 nA with an 8- $\mu\text{m}$ -diameter beam. EPMA standards included terrestrial garnet, chromite, San Carlos olivine, calcite, and dolomite. The carbon content was calculated stoichiometrically relative to cations by assuming that there are 0.333 atoms of carbon per atom of oxygen. The isotopic  $^{52}\text{Cr}$  abundance of 0.83785 (Papanastassiou, 1986) was multiplied by the atomic abundance of chromium determined by EPMA. No isotopic correction factor is needed for  $^{55}\text{Mn}$ , as it is the only stable isotope of manganese.

The synthetic calcite standards had not yet been obtained during the calcite SIMS analyses for Renazzo N1127 and GRO 95577,69; we standardized to San Carlos olivine as a temporary measure. Both San Carlos olivine and the synthetic calcites were measured as standards during the dolomite SIMS analyses. The calcite measurements were later corrected for RSF using a bootstrap method once the synthetic carbonates were characterized. For this reason, the RSF was determined by taking the weighted average of measurements from this study and from those of Jilly et al. (2014), where the RSF was measured independently under the same analytical conditions. Since the instrument, conditions, and analytical setup are the same as reported here, we assume that the RSF does not vary significantly between these two studies. The  $^{55}\text{Mn}/^{52}\text{Cr}$  RSF for calcite is taken to be  $0.65 \pm 0.04$ .

The RSF for dolomite is poorly constrained. Previous studies of manganese-chromium dating have used the calcite RSF as a proxy for dolomite (e.g., Fujiya et al., 2012; 2013; Jilly et al., 2014). However, this is an active field of study where new estimates for the dolomite RSF are emerging. It has recently been suggested that the dolomite RSF may be ~20 % greater than that of calcite (Steele et al., 2014; Ichimura and Sugiura, 2015). As we do not have a dolomite standard, we will present the dolomite data for two RSF values: the calcite RSF of  $0.65 \pm 0.04$ , and a 20 % higher RSF of  $0.78 \pm 0.05$  to represent the hypothetical dolomite RSF with a similar 6% uncertainty. For RSF values  $\leq 1$ , the applied RSF increases the  $^{55}\text{Mn}/^{52}\text{Cr}$  values ratios, and

therefore decreases the slope of trends on the final  $^{53}\text{Cr}/^{52}\text{Cr}$  versus  $^{55}\text{Mn}/^{52}\text{Cr}$  diagram. The uncertainty for the calcite RSF is propagated into the  $^{55}\text{Mn}/^{52}\text{Cr}$  ratios. For the estimated dolomite 0.78 RSF, a systematic 15 % uncertainty ( $2\sigma$ ) has been incorporated into the  $^{55}\text{Mn}/^{52}\text{Cr}$  ratios since the hypothesized values are poorly constrained.

### 3.3 RESULTS

#### 3.3.1 Sample petrography

Renazzo is classified as a moderately altered CR 2.4 chondrite (Harju et al., 2014). Two thin sections of Renazzo (N1126 and N1127) were made without water for the purpose of this study at the Museum of Natural History Vienna. The host lithology is chondrule-rich, containing numerous metal-rich porphyritic chondrules within a fine-grained matrix. Both matrix and chondrules show evidence of aqueous alteration in the form of secondary minerals. The majority of chondrule mesostases are altered to phyllosilicates, while many chondrule silicates (olivine and pyroxene) remain unaltered. Much of the fine-grained matrix has been hydrated to sub-micron phyllosilicates and clays, embedded with 3–10  $\mu\text{m}$  iron-nickel sulfides and magnetite. Calcite occurs in matrix in three morphologies: as large, mottled, fine-grained masses that are intergrown with silicates (Fig. 3.1), as coarse-grained veins that extend up to a few 100  $\mu\text{m}$  in the matrix, and as individual coarse grains that occur in the matrix, often near altered chondrules (Fig. 3.2). There is abundant evidence to support that the carbonates measured here are pre-terrestrial in origin, including non-terrestrial oxygen isotopic compositions and petrographic textures inconsistent with weathering (c.f., Chapters 2 and 5). Two coarse-grained calcites from the inter-chondrule matrix were measured here for manganese-chromium.

Renazzo is a breccia, and contains numerous dark inclusions. The dark inclusions are chemically and mineralogically very similar to the CR matrix, yet tend to be more hydrated with higher abundances of phyllosilicates, carbonates, and magnetite (e.g., Weisberg et al., 1993; Kallemejn et al., 1994). These clasts do not appear to have been altered *in situ* in the Renazzo breccia, but instead were likely delivered as pre-altered clasts from a warmer, wetter region on the CR parent body (e.g., Jilly-Rehak et al., 2015). Dolomite is rare in CR chondrites, but numerous grains were found in a dark inclusion from thin section Renazzo N1126 (Fig. 3.3), and

were measured here for manganese-chromium isotope systematics. The crystals are anhedral 5-20  $\mu\text{m}$ -sized grains, existing as replacement products for calcium-rich phases within extensively altered chondrules. Other phases common to the CR matrices also occur throughout the dark inclusion, such as framboidal magnetite and iron-sulfide laths.

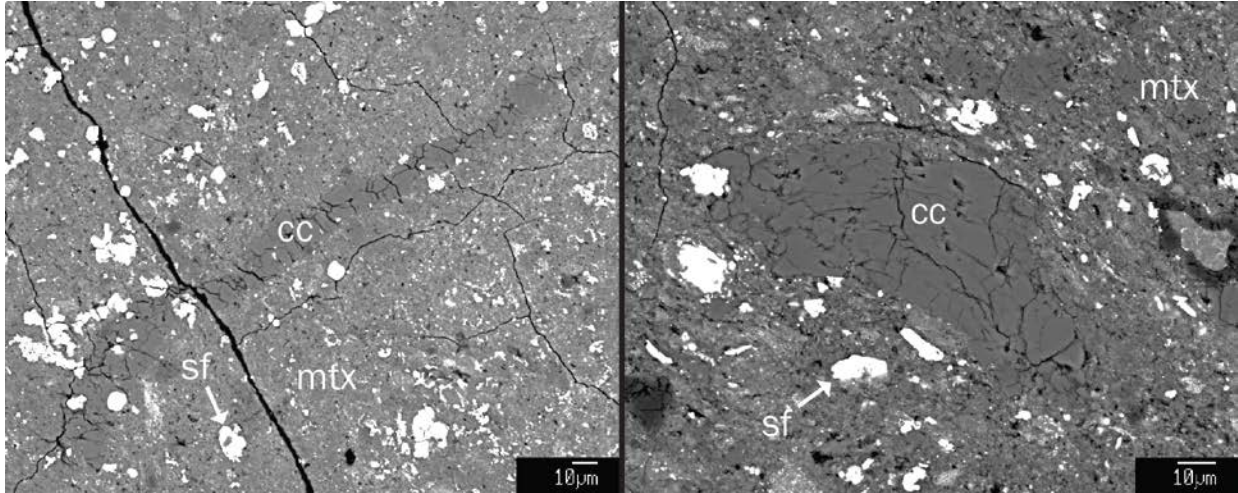


**Figure 3.2.** BSE images of calcite in the Renazzo N1127 matrix. The image on the left shows a calcite vein extending  $> 100 \mu\text{m}$  across the matrix. On the right is a coarse-grained calcite from the interchondrule matrix. The bright phases in both images are iron-sulfides. cc = calcite, mtx = matrix, sf = sulfide.

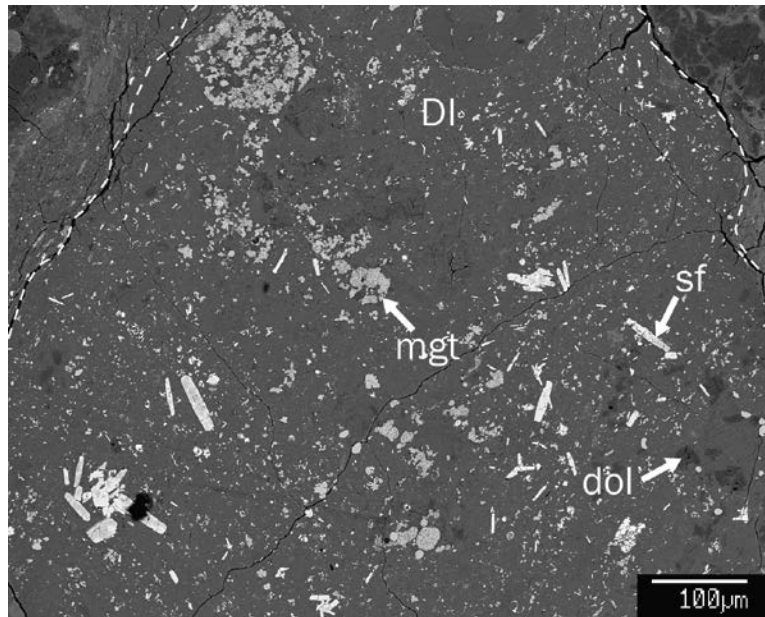


**Figure 3.3.** BSE image of a dark inclusion in Renazzo N1126. The dashed lines represent the borders of the dark inclusion clast. This lithology consists of phyllosilicate groundmass, and contains abundant magnetite framboids, sulfide laths, and dolomite crystals. dol = dolomite, mgt = magnetite, sf = sulfide.

GRO 95577 is an Antarctic meteorite of petrologic type CR 2.0 (Harju et al., 2014). Thin section GRO 95577,69 was made without water at the Johnson Space Center, and provided to us for this study. This sample is the most heavily altered CR chondrite yet documented (e.g., Weisberg and Huber et al., 2007; Schrader et al., 2011; 2014; Harju et al., 2014) and is composed almost entirely of secondary minerals. All chondrule phenocrysts occur as phyllosilicate pseudomorphs, with chlorite and/or calcite replacing chondrule mesostasis, and magnetite replacing the metal nodules (Weisberg and Huber, 2007). The matrix is composed of fine-grained clays and phyllosilicates, with abundant coarse-grained anhedral calcite (~ 5 – 50  $\mu\text{m}$  in diameter) embedded throughout. Framboidal magnetite and euhedral to subhedral sulfide platelets co-exist with the calcite in the matrix, and are often intergrown (Fig. 3.4). All calcite grains measured here come from the matrix lithology.

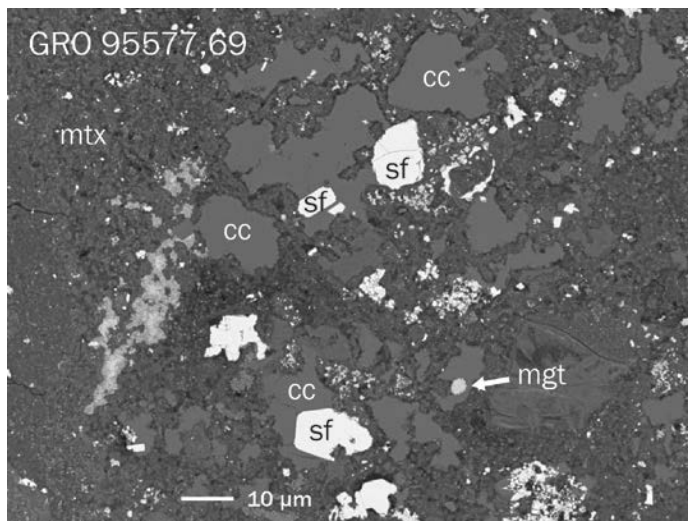


**Figure 3.4.** BSE image of matrix phases in GRO 95577,69. The matrix consists of a fine-grained phyllosilicate groundmass embedded with secondary calcite, sulfide, and magnetite grains. cc = calcite, mgt = magnetite, mtx = matrix, sf = sulfide.

### 3.3.2 Manganese-chromium isotopes in matrix calcite

Two calcite grains were measured for manganese-chromium isotope systematics in Renazzo N1127. Both grains are in the CR 2.4 host lithology. The calcite grains range from ~20  $\mu\text{m}$  in the shortest dimension, to ~100  $\mu\text{m}$  at the longest (Fig. 3.5a,b). The first grain is in the matrix adjacent to a chondrule, and the second occurs as an isolated matrix grain. Additional calcite grains were targeted, but the  $^{55}\text{Mn}^+$  and  $^{52}\text{Cr}^+$  count rates were far too low to be measured

due to high purity of the mineral. The fractionation and RSF-corrected manganese and chromium data are presented in Table 2. The  $\delta^{53}\text{Cr}^*$  values range up to  $226 \pm 144$  ‰, and the  $^{55}\text{Mn}/^{52}\text{Cr}$  ranges up to  $7548 \pm 913$ . The reported uncertainties represent combined  $2\sigma$  internal error on the measurements and the  $2\sigma$  uncertainty in the calcite RSF.

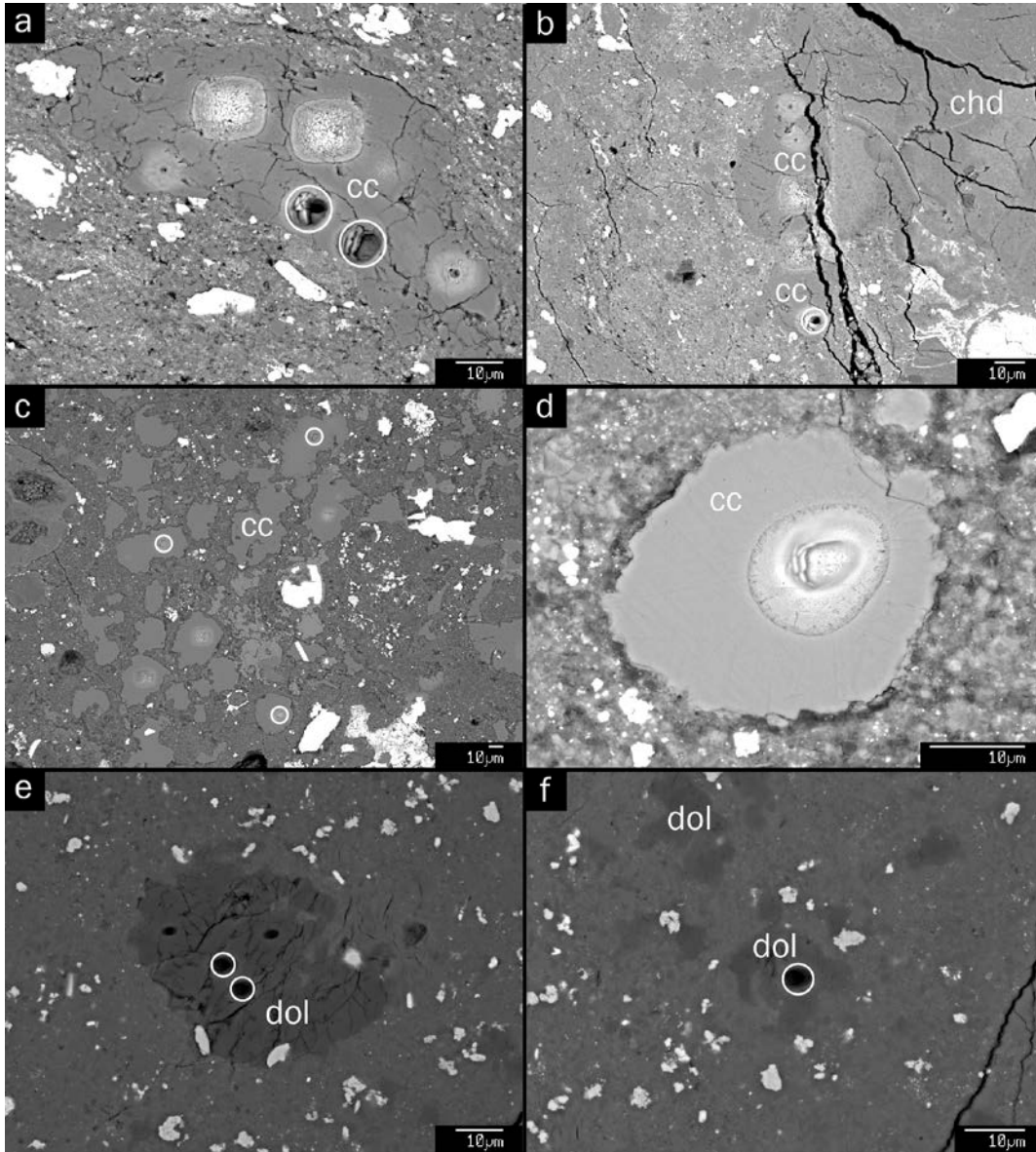


**Figure 3.5.** BSE image of typical carbonates measured for  $^{53}\text{Mn}$ - $^{53}\text{Cr}$  in this study.  $^{53}\text{Mn}$ - $^{53}\text{Cr}$  pits are circled in white. (a-b) Calcite grains in Renazzo N1127. Oxygen isotope pits and electron beam damage are also visible on both grains. (b) Calcite grains in the matrix of GRO 95577,69. Some oxygen isotope pits are visible on other grains. (d) Enlarged image of a calcite grain in GRO 95577,69 measured for  $^{53}\text{Mn}$ - $^{53}\text{Cr}$ . (e-f) Dolomite grains from a dark inclusion in Renazzo N1126. Two oxygen isotope analyses are visible in (e). chd = chondrule, cc = calcite, dol = dolomite.

Four calcite grains in GRO 95577,69 were found with high enough count rates to be measured for manganese and chromium. The measured calcite grains in GRO 95577,69 were each about 20  $\mu\text{m}$  in diameter, all existing within the altered type 2.0 matrix (Fig. 3.5c,d). The  $\delta^{53}\text{Cr}^*$  values range up to  $1045 \pm 321$  ‰ and the RSF-corrected  $^{55}\text{Mn}/^{52}\text{Cr}$  values range up to  $127,485 \pm 12,294$  (Table 3.2). The  $^{55}\text{Mn}/^{52}\text{Cr}$  uncertainties represent combined  $2\sigma$  internal error on the measurements and the  $2\sigma$  uncertainty in the calcite RSF.

**Table 3.2.** Manganese-chromium isotopes in calcite. All errors are  $2\sigma$ , including uncertainty in the RSF, and 10% systematic uncertainty to the  $^{55}\text{Mn}/^{52}\text{Cr}$  ratios.

Sample	Grain	$^{53}\text{Cr}/^{52}\text{Cr}$	$\delta^{53}\text{Cr}^*$	$^{55}\text{Mn}/^{52}\text{Cr}$	$^{55}\text{Mn}_{\text{tot}}^{\text{a}}$
Renazzo N1127	cc #2	$0.1123 \pm 0.0033$	$-10 \pm 29$	$38 \pm 5$	554
	cc #4a	$0.1199 \pm 0.0069$	$56 \pm 61$	$671 \pm 81$	1934
	cc #4b	$0.1123 \pm 0.0101$	$-10 \pm 89$	$466 \pm 56$	1918
	cc #4c	$0.1190 \pm 0.0085$	$49 \pm 75$	$2044 \pm 247$	4708
	cc #4d	$0.1391 \pm 0.0163$	$226 \pm 144$	$7548 \pm 913$	5021
GRO 95577,69	cc #1a	$0.1288 \pm 0.0212$	$135 \pm 187$	$5022 \pm 607$	2335
	cc #1b	$0.1356 \pm 0.0256$	$195 \pm 226$	$10187 \pm 1232$	3067
	cc #3a	$0.1507 \pm 0.0173$	$328 \pm 153$	$53755 \pm 6502$	65854
	cc #3b	$0.2321 \pm 0.0364$	$1045 \pm 321$	$127485 \pm 15419$	70068
	cc #4	$0.1174 \pm 0.0120$	$35 \pm 106$	$2404 \pm 291$	2786
	cc #12	$0.1240 \pm 0.0162$	$93 \pm 143$	$2307 \pm 279$	1564

<sup>a</sup>Sum of all counts per run, normalized by number of cycles per run.

The  $\delta^{53}\text{Cr}^*$  values from calcite grains in Renazzo N1127 and GRO 95577,69 are correlated with the  $^{55}\text{Mn}/^{52}\text{Cr}$  ratios. On a plot of  $^{53}\text{Cr}/^{52}\text{Cr}$  versus  $^{55}\text{Mn}/^{52}\text{Cr}$  (Fig. 3.6), the correlation trend for Renazzo calcites has a slope of  $(3.6 \pm 2.0) \times 10^{-6}$ , with  $\chi_{\text{red}}^2 = 0.73$ . The correlation trend for the GRO 95577,69 calcites has a slope of  $(7.7 \pm 2.5) \times 10^{-7}$ , with  $\chi_{\text{red}}^2 = 0.76$ . The slopes of both trends are resolved from zero, and the  $\chi_{\text{red}}^2$  values suggest that the scatter in the data can be explained by stochastic statistical fluctuation. These slopes were determined using the RSF value of  $0.65 \pm 0.04$ . The large uncertainty in the slope is dominated by the uncertainty in  $\delta^{53}\text{Cr}^*$  due to low count rates.

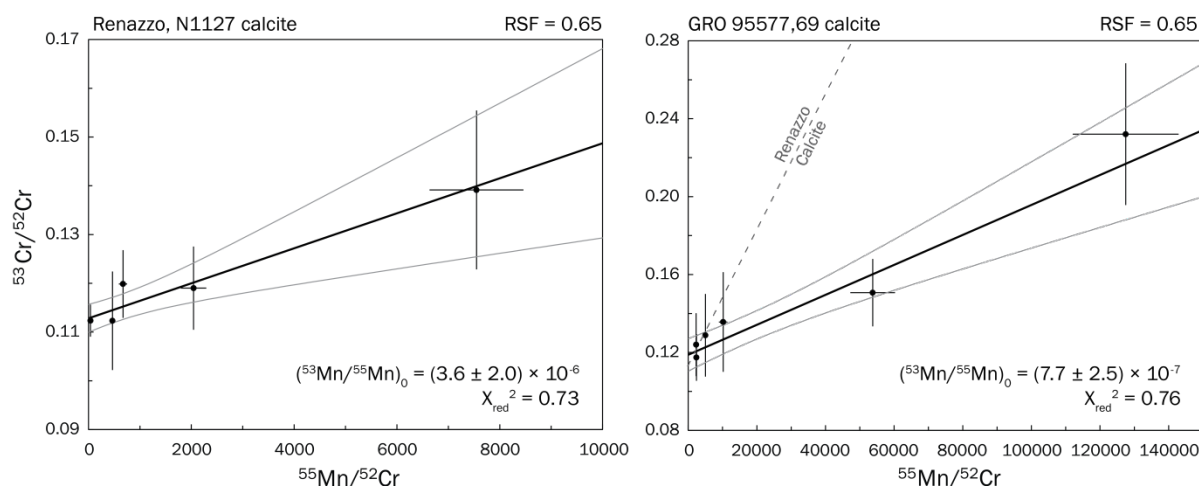


**Figure 3.6.** Diagrams depicting  $^{53}\text{Cr}/^{52}\text{Cr}$  versus  $^{55}\text{Mn}/^{52}\text{Cr}$  measured in calcites from Renazzo N1127 and GRO 95577,69. Data are fitted with an error-weighted least-squares regression, shown as a solid black line. The slope of the regression is expressed as the initial  $(^{53}\text{Mn}/^{55}\text{Mn})_0$  ratio. Error crosses represent  $2\sigma$  uncertainty, with error envelope shown in grey.

**Table 3.3.** Manganese-chromium isotopes in dolomite from Renazzo N1126. All errors are  $2\sigma$ , including uncertainty in the RSF. Data for RSF values of 0.65 and 0.78 are given.

Grain	$^{53}\text{Cr}/^{52}\text{Cr}$	$\delta^{53}\text{Cr}$	$^{55}\text{Mn}/^{52}\text{Cr}$ (RSF=0.65)	$^{55}\text{Mn}/^{52}\text{Cr}$ (RSF=0.78)	$^{55}\text{Mn}_{\text{tot}}$ <sup>a</sup>
dol #1a	$0.1177 \pm 0.0050$	$37 \pm 44$	$925 \pm 112$	$768 \pm 116$	5188
dol #1b	$0.1243 \pm 0.0112$	$95 \pm 99$	$3150 \pm 381$	$2615 \pm 400$	4019
dol #2	$0.1321 \pm 0.0132$	$164 \pm 117$	$6598 \pm 798$	$5478 \pm 842$	5686
dol #4a	$0.1232 \pm 0.0117$	$86 \pm 103$	$2281 \pm 276$	$1894 \pm 290$	4444
dol #4b	$0.1206 \pm 0.0094$	$63 \pm 83$	$1445 \pm 175$	$1199 \pm 182$	4126
dol #5	$0.1214 \pm 0.0122$	$70 \pm 107$	$5542 \pm 670$	$4600 \pm 706$	7699
dol #8	$0.1345 \pm 0.0279$	$186 \pm 246$	$5791 \pm 700$	$4807 \pm 797$	8928
dol #11a	$0.1406 \pm 0.0227$	$239 \pm 200$	$7099 \pm 859$	$5893 \pm 944$	5651
dol #11b	$0.1460 \pm 0.0285$	$286 \pm 251$	$9402 \pm 1137$	$7805 \pm 1289$	5168
dol #12	$0.1453 \pm 0.0130$	$281 \pm 115$	$5905 \pm 714$	$4902 \pm 751$	10085

<sup>a</sup> Sum of all counts per run, normalized by number of cycles per run.

### 3.3.3 Manganese-chromium isotopes in dolomite from a dark inclusion

Manganese-chromium analyses were taken from seven dolomite grains in a Renazzo N1126 dark inclusion (Fig. 3.5e,f). Similar to the calcite analyses, additional dolomite grains were targeted for measurement, but were too pure to yield adequate count rates for manganese and chromium isotopes. The dolomite  $\delta^{53}\text{Cr}^*$  values range up to  $286 \pm 251$  ‰, and  $^{55}\text{Mn}/^{52}\text{Cr}$

values range up to  $9402 \pm 1137$  for  $\text{RSF}=0.65$ , or  $7805 \pm 1289$  for  $\text{RSF}=0.78$  (Table 3.3). The calcite RSF uncertainty ( $\pm 0.04$ ) was propagated into the  $2\sigma$  internal error and 10% systematic uncertainty on  $^{55}\text{Mn}/^{52}\text{Cr}$  for the  $\text{RSF}=0.65$  data. For the dolomite data corrected to the RSF of 0.78, a 15 % systematic RSF uncertainty was combined with the  $2\sigma$   $^{55}\text{Mn}/^{52}\text{Cr}$  error.

The  $\delta^{53}\text{Cr}^*$  values correlate with the  $^{55}\text{Mn}/^{52}\text{Cr}$  ratio on a plot of  $^{53}\text{Cr}/^{52}\text{Cr}$  versus  $^{55}\text{Mn}/^{52}\text{Cr}$  (Fig. 3.7). The slope of the correlation trend depends on the RSF value used (Figure 3.8). For the RSF of 0.65, the dolomite correlation slope is  $(3.1 \pm 1.5) \times 10^{-6}$ , with  $\chi_{\text{red}}^2 = 0.85$ . Applying the hypothesized dolomite RSF of 0.78, the slope increases to  $(3.8 \pm 1.8) \times 10^{-6}$ , with  $\chi_{\text{red}}^2 = 0.84$ . The  $\chi_{\text{red}}^2$  values indicate that the fluctuations in the data are dominated by statistical variation. As the RSF decreases, the slope of the array on the manganese-chromium diagram also decreases. The calcite RSF may range from 0.61 to 0.69 (within uncertainty limits), and although the dolomite RSF has been estimated to be  $\sim 20\%$  higher, this value is very imprecise. Until a concrete dolomite RSF has been determined, all data manganese-chromium data must be interpreted cautiously with this issue in mind.

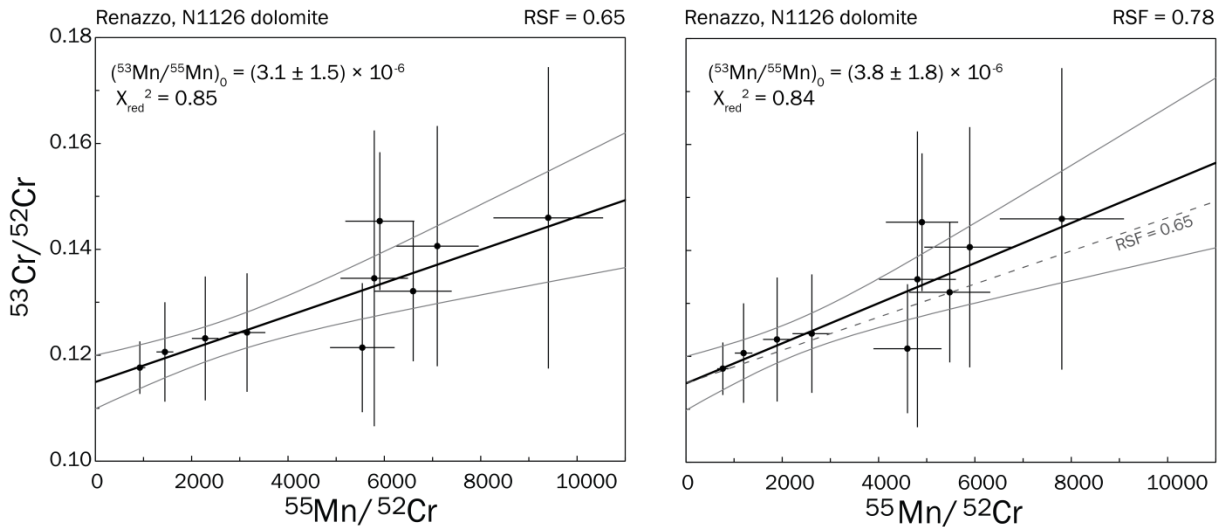


**Figure 3.7.** Diagrams depicting  $^{53}\text{Cr}/^{52}\text{Cr}$  versus  $^{55}\text{Mn}/^{52}\text{Cr}$  measured in dolomite from a Renazzo N1126 dark inclusion. The diagrams represent the same measurements corrected to different RSF values: the calcite RSF of 0.65 of the left, and a hypothesized dolomite RSF of 0.78 on the right. Data are fitted with a weighted least-squares regression, shown as a solid black line. The dashed line is a projection of the  $\text{RSF}=0.65$  slope for comparison. The regression slopes are expressed as the initial  $(^{53}\text{Mn}/^{55}\text{Mn})_0$  ratio. Error crosses represent  $2\sigma$  uncertainty.

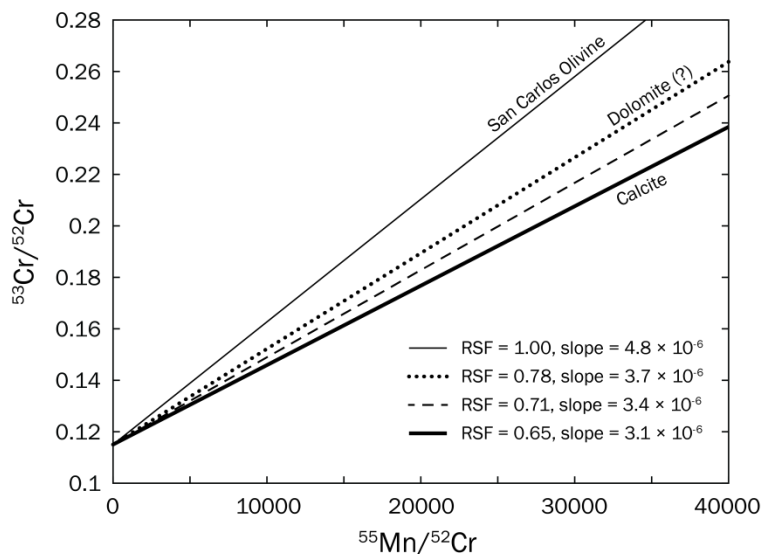


**Figure 3.8.** The effect of RSF on  $^{53}\text{Cr}/^{52}\text{Cr}$  versus  $^{55}\text{Mn}/^{52}\text{Cr}$  correlations. The trend depicted here is from the dolomite measured in Renazzo N1126. The various lines show what the inferred slope value would be for different RSF values used here and in literature.

### 3.4 DISCUSSION

#### 3.4.1 Validity of isochron diagrams

In principle, the correlation between  $\delta^{53}\text{Cr}^*$  and the  $^{55}\text{Mn}/^{52}\text{Cr}$  ratio can either reflect the radioactive decay of  $^{53}\text{Mn}$  after mineral formation, or it can represent mixing of the carbonate mineral with a chromium-rich contaminant. A mixing line without time significance would result in a better correlation on a plot of  $\delta^{53}\text{Cr}^*$  versus  $1/^{52}\text{Cr}^+$ , particularly for samples with uniform  $^{55}\text{Mn}$  abundances (Hoppe et al., 2007; Fujiya et al., 2013). This is not the case for our measurements. The correlations between  $\delta^{53}\text{Cr}^*$  and  $1/^{52}\text{Cr}^+$  are weaker than the correlations between  $\delta^{53}\text{Cr}^*$  and  $^{55}\text{Mn}/^{52}\text{Cr}$  (cf. Figs. 3.6, 3.7, 3.9). Furthermore, the  $^{55}\text{Mn}$  abundances are variable by a factor of at least two (Tables 3.2-3.3), supporting our interpretation of the  $\delta^{53}\text{Cr}^*$  and  $^{55}\text{Mn}/^{52}\text{Cr}$  correlations as isochrons. Variable manganese composition likely represents zoning or varied manganese and chromium incorporation during carbonate precipitation, rather than contamination from a chromium-bearing phase. We therefore interpret the excess of  $^{53}\text{Cr}$  in the carbonates as being the decay product of live  $^{53}\text{Mn}$  in the crystal. The slope of the correlation on the  $\delta^{53}\text{Cr}^*$  versus  $^{55}\text{Mn}/^{52}\text{Cr}$  diagram therefore represents the initial ratio of  $(^{53}\text{Mn}/^{55}\text{Mn})_0$  incorporated into the carbonate grains during the carbonate-forming aqueous-alteration events.

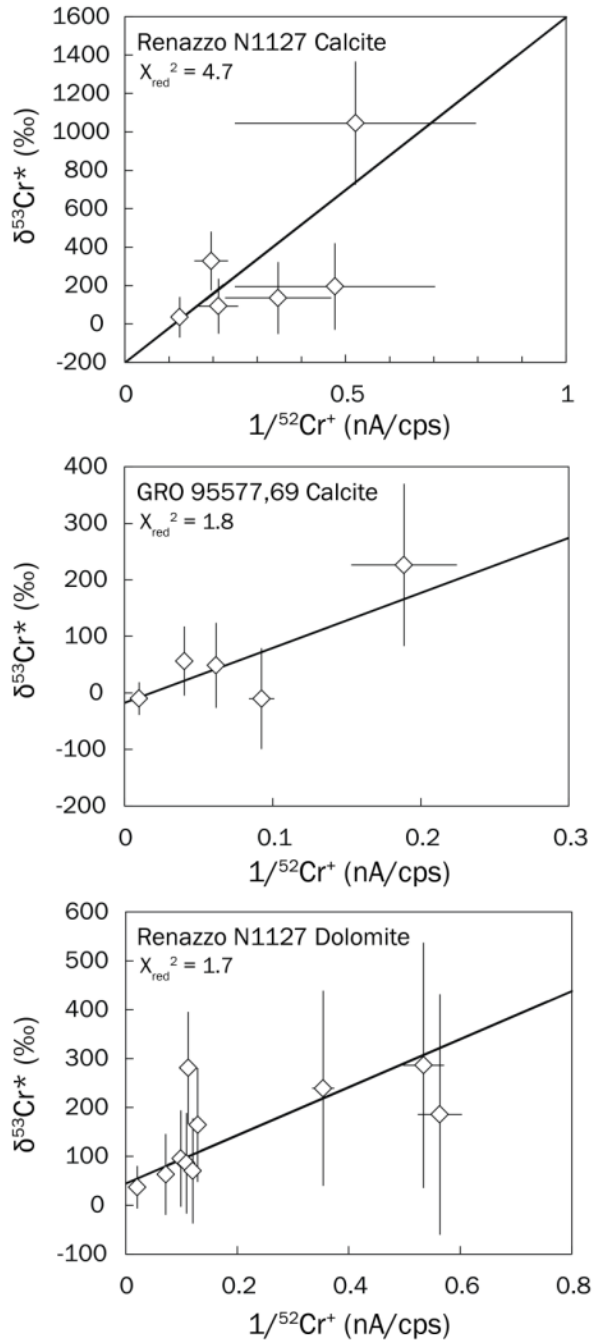


**Figure 3.9.** Graphs of  $\delta^{53}\text{Cr}^*$  versus  $1/^{52}\text{Cr}^+$ . The  $1/^{52}\text{Cr}^+$  values are given in counts per second, normalized to beam current. The variability in  $1/^{52}\text{Cr}^+$  and higher values of  $\chi_{\text{red}}^2$  support the interpretation of our data as an isochron.

The isochron validity depends on the assumption that all grains were formed during a single alteration event. This assumption is reasonable for our measurements, as the grains considered for each isochron exist in the same lithology. We only measured coarse-grained

calcites in the inter-chondrule matrix in Renazzo and GRO 95577, and the Renazzo dolomites were only measured in a single dark inclusion. By constructing isochrons only from grains in a single lithology, the problem of measuring different alteration events from multiple regions on the parent body is avoided. The oxygen isotopic compositions of the carbonates also support formation during a single event. Oxygen isotopic compositions from the two Renazzo calcite grains form a single slope-0.52 array on an oxygen three-isotope diagram, in close proximity to one another (within  $\delta^{18}\text{O} \sim 5 \text{‰}$ ; Jilly-Rehak et al., 2015). This suggests that the fluid did not evolve significantly during the formation of the carbonates, and that they were likely formed during the same event. The calcite grains from GRO 95577,69 all have the same oxygen isotopic composition, indicating that they were formed from a single uniform fluid. Similarly, three dolomite grains from the Renazzo dark inclusion have identical oxygen isotopic compositions (Jilly-Rehak et al., 2015). These petrographic and isotopic observations indicate that the carbonates in each lithology were formed contemporaneously, within the temporal resolution and uncertainty of the manganese-chromium chronometer.

### 3.4.2 Absolute ages and anchoring to D’Orbigny

The  $^{53}\text{Mn}$ - $^{53}\text{Cr}$  short-lived radionuclide system provides high-resolution relative ages for minerals that were formed within the first  $\sim 20$  Myr of Solar System’s history (e.g., Krot et al., 2006). The initial  $(^{53}\text{Mn}/^{55}\text{Mn})_{\text{SS}}$  of the Solar System is poorly constrained, with estimates ranging from  $(6.3 \pm 0.7) \times 10^{-6}$  to  $(9.1 \pm 1.7) \times 10^{-6}$  (Trinquier et al., 2008; Nyquist et al., 2009). Therefore, to obtain accurate absolute ages the measured  $(^{53}\text{Mn}/^{55}\text{Mn})_0$  must be anchored to another meteorite that has been dated using multiple short-lived and long-lived radiometric systems. Angrites – a class of igneous, achondritic meteorites – are commonly used for anchoring of manganese-chromium analyses, but there are disagreements within the scientific community regarding which angrite sample is the best time-anchor.

We anchored our measurements to the uranium-isotope-corrected lead-lead (Pb-Pb) age of the D’Orbigny angrite. D’Orbigny is a volcanic “quenched” angrite, and has been thoroughly studied with a variety of radiometric systems (e.g., Mittlefehldt et al., 2002; Glavin et al., 2004; Keil, 2012; Kleine et al., 2012; McKibbin et al., 2015). This sample makes a suitable time-anchor, as the Pb-Pb,  $^{182}\text{Hf}$ - $^{182}\text{W}$ , and  $^{53}\text{Mn}$ - $^{53}\text{Cr}$  ages are concordant. D’Orbigny is one of the

oldest angrites, and is one of only two angrites (the other is Sahara 99555) that was crystallized while  $^{26}\text{Al}$  was still alive, also providing ages for silicates using the  $^{26}\text{Al}$ - $^{26}\text{Mg}$  system (Spivak-Birndorf et al., 2009; Kleine et al., 2012). The  $^{26}\text{Al}$ - $^{26}\text{Mg}$  ages determined from plagioclase mineral separates and whole rock samples are not concordant with the Pb-Pb and  $^{182}\text{Hf}$ - $^{182}\text{W}$  ages, but differ by  $\sim 1$  Myr (Spivak-Birndorf et al., 2009; Kleine et al., 2012). There is some evidence that the  $^{147}\text{Sm}$ - $^{143}\text{Nd}$  system in a plagioclase separate from D'Orbigny had been disturbed (Tonui et al., 2003), leaving the question open as to whether  $^{26}\text{Al}$ - $^{26}\text{Mg}$  ages from D'Orbigny feldspar were also disturbed (e.g., Kleine et al., 2012). If the  $^{26}\text{Al}$ - $^{26}\text{Mg}$  systematics in plagioclase were disturbed, it could account for the non-concordant values. However, the  $^{26}\text{Al}$ - $^{26}\text{Mg}$  and  $^{147}\text{Sm}$ - $^{143}\text{Nd}$  systematics in mafic minerals from D'Orbigny and CAIs are in good agreement with the Pb-Pb and  $^{182}\text{Hf}$ - $^{182}\text{W}$  ages, suggesting that the mafic minerals were not disturbed (Tonui et al., 2003; Bouvier and Wadhwa, 2010; Brennecka and Wadhwa, 2012; Kleine et al., 2012).

D'Orbigny displays a more consistent set of ages than do the other angrites, particularly in regards to the  $^{53}\text{Mn}$ - $^{53}\text{Cr}$  systematics (e.g., Kleine et al., 2012; Brennecka and Wadhwa, 2012; McKibbin et al., 2015). Other angrites have been considered as time anchors, but are not as well-studied as D'Orbigny. Sahara 99555, the other quenched angrite, also has concordant Pb-Pb,  $^{182}\text{Hf}$ - $^{182}\text{W}$ ,  $^{53}\text{Mn}$ - $^{53}\text{Cr}$  ages that are similar to D'Orbigny, but less precise (Keil, 2012; Kleine et al., 2012; McKibbin et al., 2015). The  $^{26}\text{Al}$ - $^{26}\text{Mg}$  systematics in Sahara 99555 are also disturbed. The plutonic angrites (such as LEW 86010, NWA 4801, and Angra dos Reis) can potentially be used as time anchors. However, all plutonic angrites have much less precise  $^{53}\text{Mn}$ - $^{53}\text{Cr}$  ages than the quenched angrites (McKibbin et al., 2015). The plutonic angrites crystallized later than the quenched angrites, with no evidence for live  $^{26}\text{Al}$ . These samples were slowly cooled over millions of years, and therefore are not likely to exhibit a single closure time for all radiometric systems. LEW 86010 is likely the only quenched angrite to have  $^{53}\text{Mn}$ - $^{53}\text{Cr}$  and Pb-Pb systematics that closed simultaneously (McKibbin et al., 2015), but the sample is severely contaminated with terrestrial lead, and shows evidence for disturbance of the  $^{87}\text{Rb}$ - $^{87}\text{Sr}$  system (Keil, 2012; Kleine et al., 2012). The remaining plutonic angrites are not suitable anchors because either they do not have concordant ages or they have not been measured for  $^{53}\text{Mn}$ - $^{53}\text{Cr}$ .

The isochron slopes determined here are anchored to the D'Orbigny uranium-isotope-corrected Pb-Pb age of  $4563.37 \pm 0.25$  Ma (Amelin, 2008; Brennecka and Wadhwa, 2012). We

use the revised D’Orbigny initial ( $^{53}\text{Mn}/^{55}\text{Mn}$ )<sub>0</sub> ratio of  $(3.54 \pm 0.18) \times 10^{-6}$  (McKibbin et al., 2015) instead of that from Glavin et al. (2004). McKibbin et al. (2015) measured manganese-chromium systematics using SIMS, where the isochron slope is dominated by the mineral kirschsteinite ( $\text{CaFe}(\text{SiO}_4)$ ). This mineral is argued to provide greater resistance to thermal resetting and to cation diffusion (McKibbin et al., 2015), as compared with the magnesium-iron-bearing olivine and pyroxene that dominated the isochrons from the TIMS measurements of Glavin et al. (2004). By assuming homogeneous distribution of  $^{53}\text{Mn}$  in the chondrite-forming region of the early Solar System, we can compare the relative initial ( $^{53}\text{Mn}/^{55}\text{Mn}$ )<sub>0</sub> ratios of the CR chondrite carbonates to that of D’Orbigny to obtain the absolute ages.

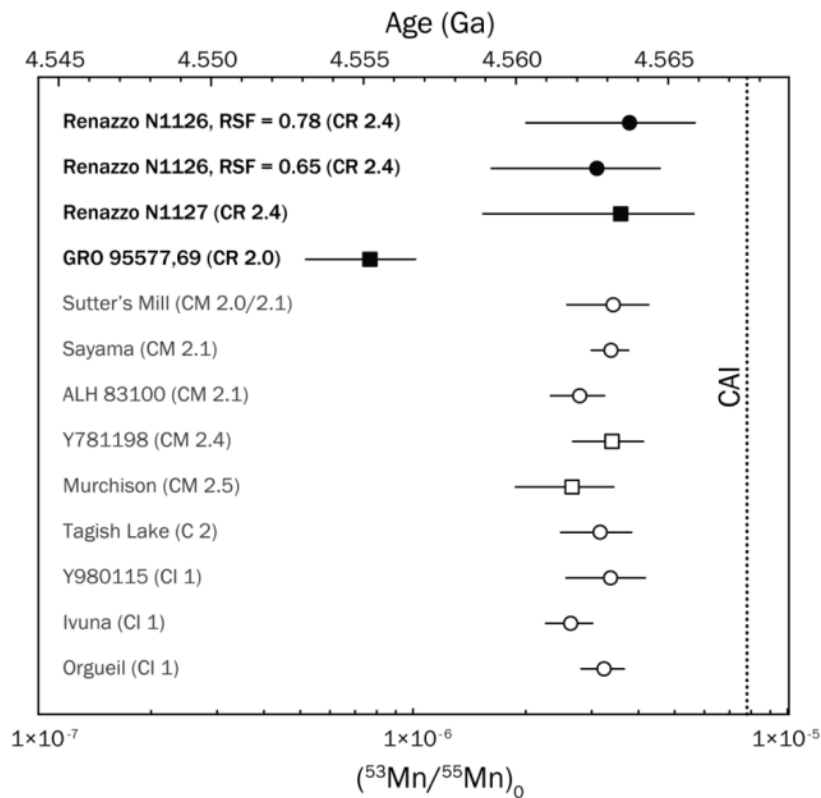


**Figure 3.10.** Plot depicting the absolute ages of carbonates measured by manganese-chromium. The age (Ga) is presented on the top axis, and the corresponding initial ( $^{53}\text{Mn}/^{55}\text{Mn}$ )<sub>0</sub> is presented on the bottom axis. The filled symbols represent data from this study. Circles represent dolomite analyses, and squares represent calcite. For the Renazzo dolomite, we present data for two different RSF values, since the correction factor is poorly constrained. Renazzo N1127 and GRO 95577 calcite uses the RSF value of 0.65. Sutter’s Mill datum is from Jilly et al. (2014), and the remaining data are from Fujiya et al. (2012; 2013). The CAI line represents the CV CAI formation age of  $4567.30 \pm 0.16$  Myr from Connelly et al. (2012). The Renazzo calcite and dolomite plots contemporaneously with previously measured carbonates in CI and CM chondrites, but GRO 95577 calcites were formed later. Error bars are  $2\sigma$ .

The isochron slopes yield ages of  $4563.4^{+2.2}/_{-4.3}$  Ma for the Renazzo N1127 calcite, and  $4555.2^{+1.3}/_{-1.9}$  Ma for GRO 95577,69 calcite (Fig. 3.10). These correspond to relative ages of ~3.9 Myr after CAI formation for Renazzo calcites, and ~12.1 Myr after CAI formation for GRO 95577 calcites (using the CAI formation age of  $4567.30 \pm 0.16$  Ma from Connelly et al., 2012). For the Renazzo dolomites, we obtain absolute ages of  $4562.7^{+1.8}/_{-3.2}$  (RSF = 0.65) or  $4563.7^{+1.8}/_{-3.2}$  (RSF = 0.78). This yields ages of ~4.6 or ~3.6 Myr after CAI formation for the RSF values of 0.65 and 0.78, respectively (Fig. 3.10). The errors are dominated by the  $2\sigma$  statistical uncertainty in the measurement, but also include the uncertainty in the RSF and the uncertainty in the manganese-chromium age of D'Orbigny.

The absolute ages of the Renazzo calcite and dolomite grains are in excellent agreement with carbonates (both calcite and dolomite) measured in Tagish Lake and CM and CI chondrites. However, GRO 95577 calcites are far younger and inconsistent with this general carbonate trend (see discussion below). Figure 3.10 shows that most carbonates have absolute ages between 3 and 5 Myr after CAI formation; the filled symbols in Figure 3.10 are from this study, and the open symbols are from the studies of Fujiya et al. (2012; 2013) and Jilly et al. (2014). Dolomite is designated by circle symbols, and calcite is designated by squares. We can compare our data to that of Fujiya et al. (2012; 2013), and Jilly et al. (2014), because they used the same matrix-matched synthetic calcite standards as we did in this study, and measured the RSF values independently using the methods, instruments, and conditions of the unknown. The large uncertainties in the measurements in the CR chondrites compared with those in the literature are due to the low count rates for manganese and chromium. It should be noted that Fujiya et al. (2013) reported one unresolved dolomite grain in a CI chondrite, but concluded that the isochron was either disturbed or had a different origin than the other grains.

Some previous  $^{53}\text{Mn}$ - $^{53}\text{Cr}$  studies of carbonates in carbonaceous chondrites are not included in Figure 3.10, as they have used silicate mineral or glass standards, or have used RSF values from literature to correct their data (Endreß et al., 1996; Hoppe et al., 2007; De Leuw et al., 2009; Petit et al., 2009; 2011; Blinova et al., 2012; Lee et al., 2012). These silicate RSF values range from 0.93 to 1.08 (or in some cases are not defined), and are much higher than the RSFs determined for carbonates here and in recent literature (Sugiura et al., 2010; Fujiya et al., 2012; 2013; Jilly et al., 2014; Steele et al., 2014; Ichimura and Sugiura, 2015). The higher RSF

overestimates the value of  $(^{53}\text{Mn}/^{55}\text{Mn})_0$ . We take caution when comparing inter-laboratory studies, as the RSF varies with instrument tuning and analytical setup, and therefore a systematic adjustment may not be suitable to obtain the correct RSF. Even small changes in the RSF can result in differences of millions of years in the inferred age. However, as an exercise, if a rough RSF correction factor of  $\sim 0.8$  is assumed for the initial  $(^{53}\text{Mn}/^{55}\text{Mn})_0$  of the silicate standardized literature data and the values are re-anchored to the same D'Orbigny angrite, the carbonate formation ages all fall between 2 and 5 Myr after CAI formation, broadly consistent with the data in Figure 10 (Endreß et al., 1996; Hoppe et al., 2007; De Leuw et al., 2009; Petitat et al., 2009; 2011; Blinova et al., 2012; Lee et al., 2012).

### 3.4.3 Aqueous alteration in the CR parent body

The mineral morphologies and petrographic textures observed in CR chondrites support formation on the CR parent body, rather than in a nebular environment. For example, mobile elements were transported by fluid water, resulting in elemental exchange between chondrules and matrix (e.g., Burger and Brearley, 2004; Brearley, 2006). This style of alteration is commonly observed in CR chondrites, where partially leached chondrules show evidence of elements having been transported from altered glassy mesostasis and deposited in the surrounding matrix as a secondary mineral (cf. Fig. 2.10 in Chapter 2). Pre-terrestrial calcite veins (Fig. 3.2) in the interchondrule matrix are particularly strong evidence for *in situ* alteration, as they are formed via small-scale fluid flow. Similarly, the framboidal and colloform magnetite and sulfide morphologies are indicative of formation from a fluid-rich environment (e.g., Ikeda and Prinz, 1993; Sawlowicz, 2000; Astafieva et al., 2003). These observations clearly show that most alteration occurred on the parent body. However, an earlier nebular history of hydration cannot be ruled out entirely, as it could have been overprinted by the subsequent parent body aqueous alteration. It has been argued that phyllosilicate rims and clasts may have formed by the reaction of primary silicates with nebular gas (Ikeda and Prinz, 1993; Ichikawa and Ikeda, 1995). This formation mechanism was invoked to explain sharp boundaries between chondrule phyllosilicates and matrix phyllosilicates that have different chemical compositions (Ichikawa and Ikeda, 1995). However, similar sharp boundaries seen in the heavily altered GRO 95577

suggest that water-rich parent-body replacement processes in CR chondrites can also preserve the textural integrity of the primary components (Weisberg and Huber, 2007).

Oxygen isotopes are further evidence for parent body alteration. The bulk oxygen-isotope array for CR chondrites has a slope of  $\sim 0.7$ , generally reflecting a progressive alteration trend (Clayton and Mayeda, 1999; Choi et al., 2009; Schrader et al., 2011). The oxygen isotopic compositions of magnetite and carbonates in all CR chondrites plot along parallel mass-independent fractionation arrays (Jilly-Rehak et al., 2015). These arrays have been interpreted as progressive alteration trends, where the calcite and magnetite grains form from a fluid that is constantly evolving. Both trends likely reflect the same phyllosilicate-dominated fluid evolution. This oxygen-isotope-evolution model is consistent with the closed-system parent body alteration models invoked for CM chondrite alteration trends (e.g., Clayton and Mayeda, 1984; 1999; Benedix et al., 2003; Bland et al., 2009). Furthermore, the oxygen compositions of magnetite and calcite in the GRO 95577 specimen all fall on a single mass-dependent fractionation line, indicating that they were formed locally from the same fluid (Jilly-Rehak et al., 2015). Such whole-rock and mineral oxygen-isotope relationships would be difficult to maintain in a pre-accretionary hydration environment where turbulence and disruption of planetesimals occurred prior to accretion (e.g., Brearley, 2006) and are most consistent with parent-body alteration models (e.g., Clayton and Mayeda, 1977; 1999).

#### *3.4.3.1 Early onset of alteration on the CR parent body*

The Renazzo  $^{53}\text{Mn}$ - $^{53}\text{Cr}$  carbonate ages ( $\sim 4$  Myr after CAI formation) provide evidence for the early onset of aqueous alteration on the CR parent body. Differences in the ages of calcite and dolomite cannot be resolved with our data, and therefore cannot distinguish the timing of alteration of the matrix as compared with dark inclusions. The old alteration ages are in good agreement with ages of carbonate formation in CI and CM chondrites, suggesting that rapid alteration after accretion on chondritic parent bodies was common in the early Solar System.

However, one main distinction between the CR chondrites and other chondrites may pose a problem for the parent body alteration model. When comparing the ages of alteration determined from  $^{53}\text{Mn}$ - $^{53}\text{Cr}$  and the chondrule ages determined from  $^{26}\text{Al}$ - $^{26}\text{Mg}$ , there is significant overlap.  $^{26}\text{Al}$ - $^{26}\text{Mg}$  dating of chondrules in CR chondrites has suggested that they are younger than chondrules from petrologic type 3.0 chondrites. Chondrules from the most

primitive CO and UOC chondrites range in age from ~ 1 to 3 Myr after CAI formation (Huss et al., 2001; Kita and Ushikubo et al., 2012), whereas the CR chondrule ages range from ~1 to  $\geq 4$  Myr with over 60% of measured CR chondrules showing no resolvable excess of  $^{26}\text{Mg}$  (Nagashima et al., 2007; 2008; 2015; Hutcheon et al., 2009; Kita and Ushikubo et al., 2012). If the majority of CR chondrules were indeed formed later than 3 or 4 Myr after CAI formation, then our  $^{53}\text{Mn}$ - $^{53}\text{Cr}$  data would suggest that parent body alteration occurred before there was even a CR parent body, unless the true age of secondary alteration occurred near the young end of the analytical uncertainties.

One study using the Pb-Pb system found that CR chondrules formed around  $2.5 \pm 1.2$  Myr after CAI formation (Amelin et al., 2002). This age is slightly older than the  $^{26}\text{Al}$ - $^{26}\text{Mg}$  ages determined for CR chondrules (Nagashima et al., 2008; 2014; Kita and Ushikubo, 2012; Schrader et al., 2013), and is in line with the parent-body model of alteration. If the Pb-Pb age of Amelin et al. (2002) is re-calculated with a  $^{238}\text{U}/^{235}\text{U}$  ratio of 137.79, a younger CR chondrule age of ~3.4 Myr after CV CAI formation is obtained that more closely reflects the  $^{26}\text{Al}$ - $^{26}\text{Mg}$  ages (Schrader et al., 2013; Nagashima et al., 2014). It is unclear if such a re-calculation of the Pb-Pb age with a different uranium-isotopic composition is valid, since the CR chondrules in the Amelin et al. (2002) study were not measured independently for uranium isotopes. However, there is no explicit evidence that uranium isotopes vary for bulk chondrites; rather, uranium isotope anomalies predominantly occur in CAIs (Connelly et al., 2012).

The CR chondrule age discrepancy may point to issues with the  $^{26}\text{Al}$ - $^{26}\text{Mg}$  dating system. The majority of chondrules that have yielded old aluminum-magnesium ages of ~2 Myr after CAI formation were from primitive type 3.0, UOC and CO chondrites that have not experienced extensive parent-body aqueous alteration. The CR chondrules measured are an exception; nearly all CR chondrites are type 2, and have been affected by aqueous alteration to some extent. No CM chondrules have ever been dated using the  $^{26}\text{Al}$ - $^{26}\text{Mg}$  system due to their heavily altered nature. The aqueous alteration process has a poorly understood effect on the aluminum-magnesium system. Recently, the  $^{26}\text{Al}$ - $^{26}\text{Mg}$  system has been called into question for dating chondrule glass and plagioclase, particularly for model isochrons where the intercept is forced through the origin (Alexander and Ebel, 2012). Thermal alteration has been shown to cause magnesium diffusion in feldspar at temperatures possibly as low as 400 to 500 °C (La Tourrette and Wasserburg, 1998; Van Orman et al., 2014), which can compromise the aluminum-

magnesium chronometer. Most CR chondrites have not experienced such high temperatures, but there is abundant evidence that chondrule mesostases (where glass and plagioclase reside) have exchanged mobile elements with the matrix during aqueous processing (cf. Fig. 2.10; Burger and Brearley, 2004; Jilly and Huss, 2012). Chondrule glasses in type 3 ordinary chondrites showed measurable excesses in  $^{26}\text{Mg}$ , despite considerable oxygen isotope exchange (Kita et al., 2010; Alexander and Ebel, 2012). Alexander and Ebel (2012) point out that there is a tendency for the  $^{26}\text{Al}$ - $^{26}\text{Mg}$  isochron slopes to decrease as the difference in oxygen isotopic compositions between chondrule minerals increases. If magnesium isotopic exchange occurred to some extent in CR chondrules while  $^{26}\text{Al}$  was still alive, then the ages may record the time of alteration, rather than the time of initial formation. The precision of the data is not high enough to tell the difference. In this scenario, the chondrules would have formed earlier than inferred from the disturbed isochrons (Alexander and Ebel, 2012). While studies of oxygen isotopes in CR chondrites show no clear evidence for oxygen isotope diffusion (e.g., Krot et al., 2006; Schrader et al., 2013; Tenner et al., 2015), more thorough studies of the aluminum-magnesium system in altered chondrules are needed to resolve these issues.

Clearly, one or more of the following scenarios must hold to reconcile the age issue for CR chondrites: 1. The  $^{26}\text{Al}$ - $^{26}\text{Mg}$  systematics measured in CR chondrules are disturbed, and do not represent true CR chondrule formation ages. The ages may have been partially or completely reset during subsequent parent body processing. 2. The  $^{53}\text{Mn}$ - $^{53}\text{Cr}$  ages presented here are disturbed, and do not represent the true ages of carbonate formation in CR chondrites. This conclusion can be avoided if true manganese-chromium ages of the carbonates reside near the young end of the  $2\sigma$  uncertainty, closer to 6-7 Myr after CAI formation, or if the manganese-chromium time anchor is not valid. 3. The carbonates represent alteration products that were formed from a previous generation of parent bodies that did not have chondrules; they might have been pre-altered clasts from early aqueous processing on a small protoplanetary body that was later disrupted and re-accreted into the final CR parent body (McSween, 1979; Browning et al., 1996; Brearley, 2006). This scenario does not seem likely as the carbonates measured in Renazzo were clearly formed from the same oxygen isotopic reservoirs as the other chondrule-bearing CR chondrites (c.f. Chapter 5), although CR chondrites have experienced complex alteration processes, as well as extensive brecciation and surface processing on the parent body.

Therefore, unraveling the specific history of each chondrule, mineral, or clast is a complicated task.

The  $\delta^{53}\text{Cr}^*$  versus  $1/^{52}\text{Cr}^+$  diagrams (Fig. 3.9) provide evidence of the temporal significance to the  $^{53}\text{Mn}$ - $^{53}\text{Cr}$  isochrons, as explained above. The purpose of measuring carbonates with the  $^{53}\text{Mn}$ - $^{53}\text{Cr}$  system is to provide age constraints on the secondary process of aqueous alteration, rather than the formation of primary minerals or components. Prolonged periods of alteration can theoretically disturb the  $^{53}\text{Mn}$ - $^{53}\text{Cr}$  isochron if there is incomplete dissolution and re-precipitation of the carbonate minerals. In this case, the slope of the isochron would become shallower, yielding younger ages of carbonate precipitation. The discrepancy here is the opposite: the ages of the Renazzo carbonates are old, indicating that they were formed early in the history of the CR parent body. Alternatively, the  $^{53}\text{Mn}$ - $^{53}\text{Cr}$  systematics theoretically could have been disturbed if manganese was somehow removed from the carbonates after they were formed. For both of these scenarios, the carbonates in Renazzo show no petrographic or textural evidence (such as layering, reaction rims, or embayment) that would be indicative of dissolution and re-precipitation, and no resolvable isochron disturbances. A detailed cathodoluminescence study may help to determine if multi-stage formation of carbonates occurred.

These observations suggest that the age discrepancy between  $^{26}\text{Al}$ - $^{26}\text{Mg}$  chondrule formation ages and  $^{53}\text{Mn}$ - $^{53}\text{Cr}$  parent body alteration ages is likely due to isochron disturbances. The arguments presented above suggest that the errors may lie with the  $^{26}\text{Al}$ - $^{26}\text{Mg}$  system rather than with the  $^{53}\text{Mn}$ - $^{53}\text{Cr}$  system, although there is no clear and simple resolution without more precise and accurate measurements.

#### *3.4.3.2 Late-stage alteration on the CR parent body*

The distinct ages of the Renazzo and GRO 95577 carbonates indicate that aqueous alteration on the CR parent body was either prolonged, or occurred in stages. Models of asteroidal accretion suggest that the carbonaceous chondrite parent bodies accreted near the snow line, a radial distance from the Sun ( $\sim 2$  to  $5$  AU) where the temperature was cold enough for water to condense into solid grains (e.g., Jewitt et al., 2007). The aqueous alteration process does not effectively occur between rock and ice; rather, water must exist as a fluid for alteration to proceed. Both the pressure and the temperature must be above the triple point of  $611$  Pa and

273.16 K for liquid water to be stable on the parent body. Very small bodies ( $r < 2$  km) can never sustain the triple-point pressure, and any heating of such bodies would cause sublimation of water-ice (Jewitt et al., 2007). Therefore, the aqueously altered chondritic parent bodies must have had radii  $\geq 2$  km (for average density  $\rho = 10^3$  g/m<sup>3</sup>) to have pressures above the triple point. Accretional heating (from the release of gravitational energy upon formation, also known as the gravitational binding energy) is an important heat source for large bodies, but is insufficient to melt ice on the smaller undifferentiated chondritic bodies studied here (Grimm and McSween, 1989; Jewitt et al., 2007; Melosh 2011). The dominant heat source for small bodies in the asteroid belt was likely <sup>26</sup>Al (MacPherson et al., 1995; Grimm and McSween, 1989; Jewitt et al., 2007), which is thought to be the heat source for not only aqueous alteration, but thermal metamorphism as well. The short half-life of  $\sim 0.7$  Myr for <sup>26</sup>Al leaves a relatively short window of time for parent body alteration to occur on small undifferentiated asteroids. Models of internal parent body heating confirm that carbonate forming temperatures (between  $\sim 10$  to  $60$  °C; Jilly-Rehak et al., 2015) should have easily been reached within 1 to 2 Myr after accretion on a parent body of radius  $> 20$  km, if <sup>26</sup>Al was distributed uniformly in the solar disk before rapid accretion (Grimm and McSween, 1989; Jewitt et al., 2007; Fujiya et al., 2013). For parent bodies of this scale, the water would be expected to refreeze within another  $\sim 5$  to  $20$  Myr, depending on the radius and time of accretion (Jewitt et al., 2007; Fujiya et al., 2013).

The late calcite age in GRO 95577 ( $\sim 12$  Myr after CAI formation) cannot be explained by the same early aqueous alteration processes as invoked for Renazzo and other carbonaceous chondrites. We propose two hypotheses for the late-stage alteration of GRO 95577 carbonates: internal heating on the CR parent body, or impact heating. If the CR parent body was sufficiently large to sustain temperatures above the triple point for  $\sim 8$  Myr, then carbonate formation may have occurred before water was lost or any remaining water was re-frozen. Oxygen isotopes have revealed that the GRO 95577 calcites were formed at temperatures between  $10$  to  $60$  °C (Jilly-Rehak et al., 2015). In the context of the Fujiya et al. (2013) <sup>26</sup>Al heating model, the parent body radius must have been greater than  $\sim 30$  km for the GRO 95577 calcite to have been formed at the given temperatures and times. This minimum radius would also require the GRO 95577 lithology to originate from a warmer, wetter region on the interior of the asteroid that sustained heating from <sup>26</sup>Al. If this scenario is correct, then all CR carbonate ages should span a continuum from  $\sim 3$  Myr to  $\sim 12$  Myr after CAI formation, reflecting the prolonged era of alteration.

Unresolved measurements of siderite in GRO 95577 suggest that alteration may have lasted for at least ~24 Myr after CAI formation (Tyra et al., 2010), when the  $^{53}\text{Mn}$  was no longer alive. This scenario would require an even larger parent body radius of ~50 km if heating was sustained by  $^{26}\text{Al}$ .

Alternatively, heat from impacts may have driven late-stage aqueous alteration. Models of post-accretional impacts show that they can easily melt ice to a depth of several kilometers (Grimm and McSween, 1989), allowing for aqueous alteration to occur sufficiently later than the alteration from  $^{26}\text{Al}$ -heating alone. If the impact scenario for late-stage carbonate formation is correct, then aqueous alteration would have occurred at discrete ages, reflecting the time of impact events large enough to melt ice. Three CR chondrites show extensive evidence of shock (MIL 07513, GRA 06100, and GRO 03116), confirming that large impacts occurred on the CR parent body (Abreu, 2012). Impact processes on the CR parent body have been invoked for the formation of high-temperature alteration products in the CR 2 chondrite Graves Nunataks (GRA) 06100, along with accessory carbonates and phosphates (Abreu and Bullock, 2013). Though GRA 06100 was not studied here, it would be interesting to measure the carbonates for  $^{53}\text{Mn}$ - $^{53}\text{Cr}$  to determine whether they formed contemporaneously with the GRO 95577 calcites.

Since the measurements here represent the only resolved  $^{53}\text{Mn}$ - $^{53}\text{Cr}$  ages for CR alteration products, it is difficult to distinguish which of the late-stage heating scenarios is correct. Though carbonates in CR chondrites are extremely common, they are difficult to measure with the  $^{53}\text{Mn}$ -Cr system as the minerals are often too small, and very pure. The low count rates of both manganese and chromium in the CR carbonates resulted in large uncertainties in the data, which interfere with the ability to resolve distinct alteration events. However, SIMS techniques are rapidly developing, and may soon be able to measure smaller grains with higher ion yields. Efforts to determine mineral relative sensitivity factors for the manganese-chromium system are currently underway (e.g., Steele and McKeegan, 2014; Ichimura and Sugiura, 2015) and will greatly improve the accuracy of measurements as well. Such advances will provide opportunities to resolve the unanswered questions about late-stage alteration processes.

### 3.5 CONCLUSIONS

We measured carbonates in the CR chondrites Renazzo and GRO 95577 for  $^{53}\text{Mn}$ - $^{53}\text{Cr}$ . Both dolomite and calcite show clear excesses of  $^{53}\text{Cr}$ , interpreted as the daughter product of  $^{53}\text{Mn}$  decay. The Renazzo dolomite and calcite grains have alteration ages between  $\sim 1.8$  to  $8.2$  Myr (including all  $2\sigma$  uncertainties) after the formation of CAIs, while the GRO 95577 calcite was younger, formed  $\sim 11.8$  to  $14.0$  Myr after CAIs. The distinct ages for the Renazzo and GRO 95577 suggest that aqueous alteration on the CR parent body did not occur in one instance, but instead was prolonged or occurred in stages. These data indicate that the calcite and dolomite in Renazzo formed during aqueous alteration early in the history of the CR parent body, likely as a consequence of internal heating from  $^{26}\text{Al}$  decay. For the carbonates in GRO 95577 to have been formed so late and at cool temperatures of  $10$ - $60$   $^{\circ}\text{C}$ , either the parent body was sufficiently large (at least  $30$  to  $50$  km radius) to retain heat, or late-stage impact events supplied heat to the GRO 95577 lithology. In the late-stage  $^{26}\text{Al}$ -decay heating scenario, GRO 95577 likely originated from a warmer, wetter region on the interior of the asteroid. If an impact scenario resulted in the formation of the calcites, the GRO 95577 lithology likely originated from a shallower depth that would have been heated substantially by shock. Our research has provided answers to key questions about the timing of aqueous alteration for the CR chondrites, but it also provides direction for future studies to better resolve events in the history of CR chondrites.

## CHAPTER 4

### **<sup>53</sup>Mn-<sup>53</sup>Cr DATING OF AQUEOUSLY FORMED CARBONATES IN THE CM2 LITHOLOGY OF THE SUTTER'S MILL CARBONACEOUS CHONDRITE**

Published as Jilly, C. E., Huss G. R., Krot A. N., Nagashima K., Yin Q.-Z., and Sugiura N. (2014) <sup>53</sup>Mn-<sup>53</sup>Cr dating of aqueously formed carbonates in the CM2 lithology of the Sutter's Mill carbonaceous chondrite. *Meteoritics & Planetary Science* 49, 2104-2117.

*Abstract*– Radiometric dating of secondary minerals can be used to constrain the timing of aqueous alteration on meteoritic parent bodies. Dolomite is a well-documented secondary mineral in CM chondrites, and is thought to have formed by precipitation from an aqueous fluid on the CM parent body within several million years of accretion. The petrographic context of crosscutting dolomite veins indicates that aqueous alteration occurred *in situ*, rather than in the nebular setting. Here we present <sup>53</sup>Mn-<sup>53</sup>Cr systematics for dolomite grains in Sutter's Mill section SM51-1. The Mn-Cr isotope data show well-resolved excesses of <sup>53</sup>Cr correlated with <sup>55</sup>Mn/<sup>52</sup>Cr ratio, which we interpret as evidence for the *in situ* decay of radioactive <sup>53</sup>Mn. After correcting for the relative sensitivities of Mn and Cr using a synthetic Mn- and Cr-bearing calcite standard, the data yield an isochron with slope corresponding to an initial <sup>53</sup>Mn/<sup>55</sup>Mn ratio of  $3.42 \pm 0.86 \times 10^{-6}$ . The reported error includes systematic uncertainty from the relative sensitivity factor. When calculated relative to the U-corrected Pb-Pb absolute age of the D'Orbigny angrite, Sutter's Mill dolomites give a formation age between 4564.8 and 4562.2 Ma (2.4 – 5.0 Myr after the birth of the solar system). This age is contemporaneous with previously reported ages for secondary carbonates in CM and CI chondrites. Consistent carbonate precipitation ages between the carbonaceous chondrite groups suggest that aqueous alteration was a common process during the early stages of parent body formation, likely occurring via heating from internal <sup>26</sup>Al decay. The high precision isochron for Sutter's Mill dolomite indicates that late stage processing did not reach temperatures that were high enough to further disturb the Mn-Cr isochron.

## 4.1 INTRODUCTION

Sutter's Mill, a witnessed meteorite fall, landed in the foothills of Sierra Nevada in northern California on April 22, 2012. Since its fall, nearly 100 specimens have been retrieved from the area. Initial characterization demonstrated that the meteorite is a carbonaceous chondrite regolith breccia with affinities to the CM group. Different lithologies exhibit varying degrees of thermal metamorphism, with inferred temperatures ranging from  $153 \pm 27$  °C to  $\sim 500$  °C in some lithologies (Jenniskens et al., 2012). The CM-like clasts are heavily aqueously altered, composed almost entirely of secondary minerals. These clasts apparently have not been heated significantly. The CM classification is confirmed by multiple studies, including geochemistry of light elements such as carbon and nitrogen (Grady et al., 2013), bulk chemistry, and whole-rock O and Cr isotopes (Jenniskens et al., 2012), which plot along CM trends. However, Jenniskens et al. (2012), Garvie (2013), and Ziegler and Garvie (2013) have identified clasts of different meteorite classes, possibly indicating that the Sutter's Mill parent body is a rubble-pile asteroid.

The  $^{53}\text{Mn}$ - $^{53}\text{Cr}$  radiochronometer is well suited for dating of materials formed within the first  $\sim 20$  Myr of Solar System formation (e.g., Lugmair and Shukolyukov, 1998; Shukolyukov and Lugmair, 2006).  $^{53}\text{Mn}$  decays into  $^{53}\text{Cr}$  via electron capture, with a half-life of 3.7 Myr. This half-life is sufficiently long to resolve ages for aqueous alteration, thought to range between 1–15 Myr after formation of calcium-aluminum-rich inclusions (CAIs), which are believed to be the earliest-formed Solar System objects (Krot et al., 2006). Secondary carbonate minerals are suitable targets for Mn-Cr dating as they fractionate Mn and Cr upon precipitation from an aqueous fluid. Mn acts as a compatible element and partitions into the carbonate crystal structure, while Cr remains incompatible (Pignatelli et al., 1988). Radioactive  $^{53}\text{Mn}$  leaves an excess of  $^{53}\text{Cr}$  in the carbonate mineral after decay, which can then be measured via secondary isotope mass spectrometry (SIMS). This method of Mn-Cr dating has been used to determine the ages of precipitation for secondary carbonates in a variety of carbonaceous chondrites (e.g., Endress et al., 1997; Hoppe et al., 2007; de Leuw et al., 2009; Petit et al., 2011; Lee et al., 2012; Fujiya et al., 2012; 2013). However, the accuracy of many previous measurements has been called into question due to the lack of proper standards and poorly constrained Mn/Cr relative sensitivity factors for carbonate minerals (Sugiura et al., 2010).

In this study, we present the *in situ* Mn-Cr isotope systematics from five secondary dolomite ( $\text{CaMg}(\text{CO}_3)_2$ ) grains in Sutter's Mill section SM51-1 to date the carbonate formation time. All Mn-Cr dating was performed by SIMS. We discuss the systematic effect that poorly constrained relative sensitivity factors have on Mn-Cr SIMS measurements. We compare our results to other Mn-Cr carbonate measurements in carbonaceous chondrites, and discuss implications for the formation mechanism of carbonates on the Sutter's Mill parent body.

## 4.2 SAMPLES AND ANALYTICAL METHODS

### 4.2.1 Sutter's Mill SM51-1

A polished, carbon-coated thin section of Sutter's Mill (SM51-1) from the UC Davis collection was used in this study, and in the previous work of Jenniskens et al. (2012). The sample was analyzed with backscattered- electron imaging on a JEOL JSM-5900LV scanning electron microscope (SEM) to confirm the mineralogy and petrography discussed in previous studies, and to locate suitable ion probe targets. The SEM was set to an accelerating voltage of 15 kV, and energy-dispersive X-ray spectroscopy (EDS) was used to identify minerals.

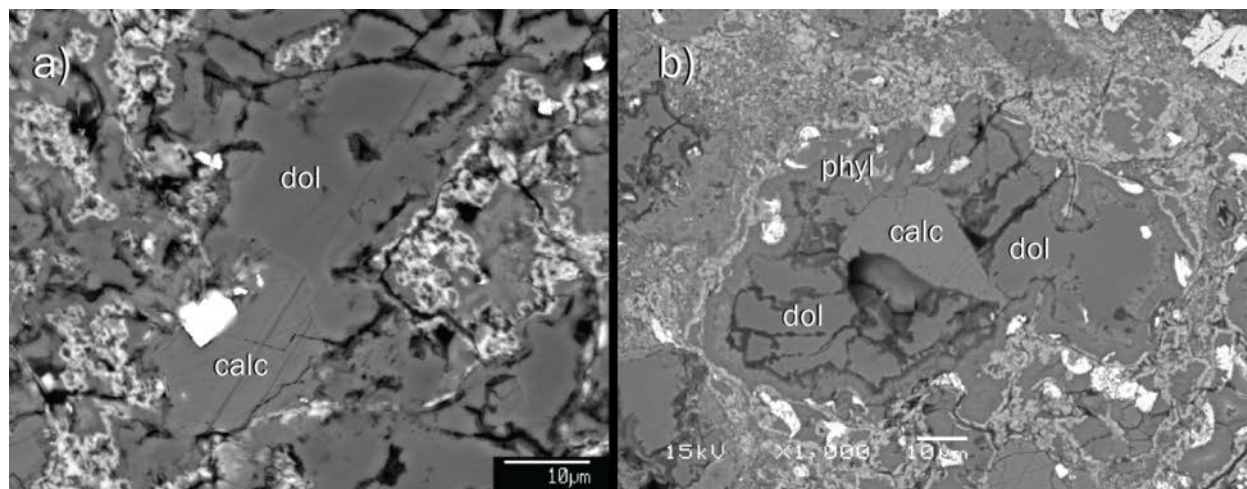


**Figure 4.1.** BSE images of intergrown calcite and dolomite grains in SM 51-1.

Sutter's Mill section SM51-1 contains two main lithologies, CM 2.0 and CM 2.1, both dominated by secondary minerals (Jenniskens et al., 2012). The lithologies are similar in composition, with the primary difference being a higher abundance of anhydrous silicate grains

(olivine and pyroxene) in the CM 2.1 clast. Both lithologies contain complete chondrule pseudomorphs embedded in an iron-rich phyllosilicate matrix; Mg-rich phyllosilicates also often display thin (~1  $\mu\text{m}$ ) Fe-rich rims. Magnetite occurs frequently in the matrix of both lithologies, mostly as subhedral grains of ~20  $\mu\text{m}$  in diameter. Small (~5  $\mu\text{m}$ ) Fe,Ni-sulfides occur in the matrix and are associated with carbonate minerals. Calcite and dolomite are common, both in the matrix and within altered chondrules, as 10–50  $\mu\text{m}$  sized equant grains. Dolomite crystals tend to be anhedral with many cracks, while calcite grains are often rounded, and are frequently intergrown with the dolomite (Fig. 4.1). Furthermore, dolomite veins crosscut the fine-grained rims of multiple chondrule pseudomorphs (Fig. 4.2), indicating that aqueous alteration occurred *in situ* (Jenniskens et al., 2012).

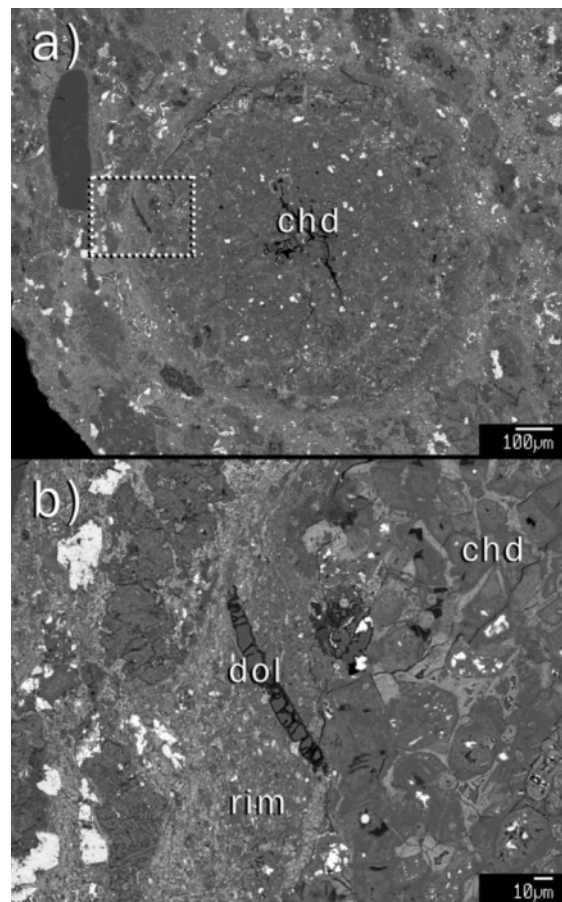


**Figure 4.2.** a) Backscattered electron image of a chondrule pseudomorph (chd) in SM 51-1, composed entirely of secondary minerals and phyllosilicates. The chondrule pseudomorph is surrounded by a fine-grained rim crosscut by dolomite veins, serving as evidence for *in situ* aqueous alteration on the CM parent body. The dotted square depicts the area of enlarged view b) of a dolomite vein (dol) crosscutting the chondrule rim (rim).

Jenniskens et al. (2012) reported on the compositions of representative calcite and dolomite in Sutter's Mill section 51-1. The calcite composition is nearly pure  $\text{CaCO}_3$ , containing < 1 mol% of trace Fe, Mg, Mn, and Si in the mineral. The dolomite compositions deviate from the Ca:Mg = 1:1 stoichiometry, all containing an excess of calcium relative to magnesium (Ca/Mg > 1) (Jenniskens et al., 2012). These values are consistent with the dolomite compositions in other CM chondrites, shown to have Ca excesses > 2 mol%  $\text{CaCO}_3$ , and dissimilar to the composition of CI dolomites, which tend to contain an excess of magnesium relative to calcium (Ca/Mg < 1) (de Leuw et al., 2010). The high abundance of dolomite and the relative lack of tochilinite in both the 2.0 and 2.1 lithologies of Sutter's Mill (Garvie et al., 2013) are consistent with their characterization as heavily altered CM material (Rubin et al., 2007). However, de Leuw et al. (2010) suggest that dolomites disappeared from the most aqueously altered CMs due to the lack of dolomites observed in MET 01070 (CM 2.0). This observation is inconsistent with the CM 2.0 SM51-1 clast that contains many dolomites, indicating a different alteration environment between MET 01070 and SM51. Dolomite and calcite grains for Mn-Cr analysis were identified by their characteristic EDS spectra. The grains chosen for this study were >15 $\mu\text{m}$  in diameter with uniform compositions.

#### 4.2.2 Secondary Ion Mass Spectrometry (SIMS)

SIMS analysis was carried out using the University of Hawai'i Cameca ims-1280 ion microprobe. An  $^{16}\text{O}^-$  primary beam with a total impact energy of 23 keV was used to sputter Mn and Cr isotopes from the sample. Masses  $^{50}\text{Cr}^+$  (including interferences from  $^{50}\text{V}^+$  and  $^{50}\text{Ti}^+$ ),  $^{52}\text{Cr}^+$ , and  $^{53}\text{Cr}^+$  were measured simultaneously in multicollection mode on electron multipliers (L2, C, and monocollection electron multipliers (EM)), followed by a peak jump to put  $^{55}\text{Mn}^+$  on the monocollector EM. The mass resolving power for  $^{50}\text{Cr}^+$  and  $^{52}\text{Cr}^+$  was ~4400, and for  $^{53}\text{Cr}^+$  and  $^{55}\text{Mn}^+$  was ~6200, sufficient to resolve the interference from the  $^{52}\text{CrH}^+$  ion on  $^{53}\text{Cr}^+$ . All samples and standards were pre-sputtered for 600 seconds with a 300 pA beam and  $5 \times 5 \mu\text{m}^2$  raster, followed by data collection at 100 pA with a beam spot size of 5  $\mu\text{m}$ . Each spot analysis ran for ~100 cycles, with a total measurement time ~1.5 hours. Automated centering of the secondary beam in the field aperture was applied before each measurement, and high voltage offset control to compensate charging in the sputtered area was applied before and during each

measurement. After the measurement, all ion probe pits were imaged to ensure that no cracks or impurities were included in the analysis.

All SIMS data were reduced using an in-house data reduction package. Isotope ratios were calculated from the summed total counts per run, rather than from the mean of the ratios in each cycle. The mean of the ratios method of calculating isotope ratios has been shown to introduce significant statistical bias, particularly for measurements with low count rates (Ogliore et al., 2011). The total counts method of calculating  $^{55}\text{Mn}/^{52}\text{Cr}$  minimizes the risk of interpreting biased data as an isochron.

To correct for instrumental mass fractionation, two standards were measured during analysis: San Carlos olivine, and synthetic Mn and Cr-bearing carbonates. The compositions of the two standards were measured with electron microprobe analysis, discussed in section 4.2.3 below. Instrumental mass fractionation (IMF) was corrected for externally by comparing the mean  $^{53}\text{Cr}^+ / ^{52}\text{Cr}^+$  ratio measured on the standards with the reference ratio, taken as  $^{53}\text{Cr} / ^{52}\text{Cr} = 0.113459 \pm 0.000005$  (Papanastassiou, 1986). We could not do an internal mass fractionation correction because the interferences ( $^{50}\text{V}$ ,  $^{50}\text{Ti}$ ) on  $^{50}\text{Cr}$  were too large. Over the course of the measurements, the instrument was re-tuned once, which can alter the IMF; therefore, two separate IMF corrections have been applied to measurements from before and after re-tuning.  $^{53}\text{Cr}$  excesses in the unknowns are reported as  $\delta^{53}\text{Cr}^*$ , representing the deviation of the IMF-corrected measurement ratios from the reference ratio in per mil (‰).

### 4.2.3 Relative Sensitivity Factors (RSF)

The fractionation of Mn and Cr in carbonates makes them difficult to standardize for Mn-Cr radiometric dating. An optimum standard should be a homogeneous crystal of the same carbonate mineral as the unknown, containing measurable amounts of both Mn and Cr. Mn and Cr-bearing carbonates do not occur commonly on Earth, and present a challenge to synthesize because Cr does not readily partition into the crystal structure. However, researchers at the University of Tokyo have recently successfully synthesized Mn and Cr-bearing calcite grains (Sugiura et al., 2010). We used some of these grains as a standard for carbonate Mn-Cr mass spectrometry in this study (Fig. 4.3).

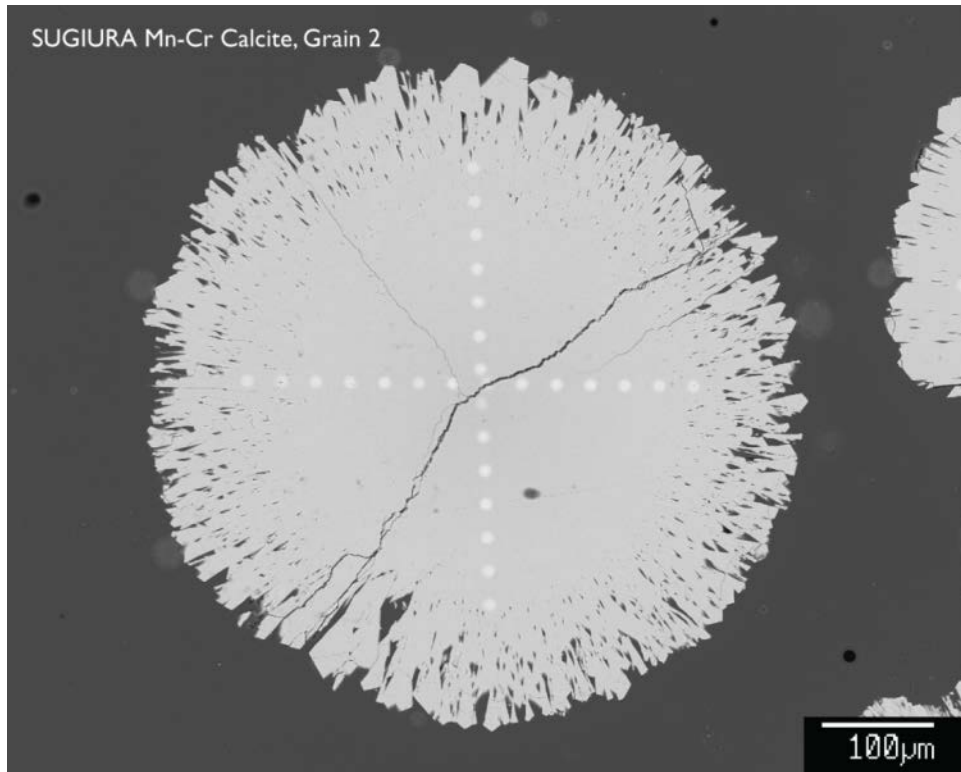


**Figure 4.3.** Synthetic Mn- and Cr-bearing calcite crystal used for standardization. The light spots across the vertical and horizontal profiles are electron microprobe beam damage from characterization.

The RSF – defined here as  $[(^{55}\text{Mn}^{+}/^{52}\text{Cr}^{+})_{\text{SIMS}} / (^{55}\text{Mn}/^{52}\text{Cr})_{\text{TRUE}}]$  – represents the isotopic ratio measured by SIMS relative to the true isotopic ratio of the sample (however, the inverse is sometimes used in literature). The RSF is dependent on a number of factors, the most important being the mineral composition and instrument tuning (McKibbin et al., 2013). Historically, the RSF for silicate minerals or glasses have been used as a proxy for carbonate RSF (e.g., Hoppe et al., 2007; de Leuw et al., 2009; Petit et al., 2011; Lee et al., 2012). However, recent studies have shown that the carbonate RSF differs significantly from that of olivine (Sugiura et al., 2010), therefore invalidating previously measured Mn-Cr carbonate isochrons. In this study, we have measured Mn and Cr isotopes in both San Carlos olivine and the synthesized Mn and Cr-bearing calcites to compare the effect of RSF on carbonate isochrons. It should be noted that the difference in RSF for calcite and dolomite is currently unknown. For the purpose of this study, we will construct our isochrons based on the assumption that the RSFs for calcite and dolomite

are indistinguishable. If the dolomite RSF is later found to differ from that of calcite, the data reported here should be corrected to the proper dolomite RSF,

To determine the value of  $(^{55}\text{Mn}/^{52}\text{Cr})_{\text{TRUE}}$  for both standards, elemental abundances were measured using the JEOL JXA-8500F electron microprobe at the University of Hawai'i. Because the synthetic calcite crystals are zoned in Mn and Cr, each synthetic calcite was characterized by two line profiles across the grain diameters, with measurements taken every 30  $\mu\text{m}$ . For the synthetic carbonates, Ca, Si, Mg, Mn, and Cr were measured at 15 keV accelerating voltage for 30 seconds each. The beam current was set to 10 nA, and a broad beam of 10  $\mu\text{m}$  was used to minimize damage to the calcite grains. Detection limits (in elemental weight percent) were 0.019, 0.013, 0.013, 0.041, and 0.027 for Ca, Si, Mg, Mn, and Cr, respectively. Carbonate measurements were standardized to rhodochrosite, chromite USNM 117075, San Carlos Olivine USNM 111312, and calcite standards. The carbon content was calculated stoichiometrically relative to cations by assuming there are 0.333 atoms of C per 1 atom of O. SIMS spot analyses for the calcite standards were then taken directly on the measured electron probe spots to avoid the small scale heterogeneity and zoning. For San Carlos olivine, electron microprobe analysis was conducted after the SIMS data collection. Seven points surrounding the ion probe pits were measured for Si, Mg, Fe, Mn, Ni, Cr, Al, and Ca with count times ranging from 20 to 90 seconds. Beam parameters were optimized for detecting Mn and Cr in olivine at 20 keV and 50 nA. San Carlos Olivine measurements were standardized to San Carlos olivine USNM 111312, Rockport MA fayalite USNM 85276, Verma garnet, and chromite USNM 117075. All EPMA data were routinely corrected using the ZAF method.

To calculate  $^{52}\text{Cr}$  concentrations from the EPMA data, the atomic Cr abundance was multiplied by the isotopic abundance of  $^{52}\text{Cr}$  (0.83789, Baum et al., 2002). No correction factor is needed for  $^{55}\text{Mn}$ , as it is the only stable isotope of Mn. RSF values for each standard were then obtained by dividing the measured SIMS  $^{55}\text{Mn}^+ / ^{52}\text{Cr}^+$  ratio with the  $^{55}\text{Mn} / ^{52}\text{Cr}$  EPMA ratio.

### 4.3 RESULTS

EPMA results are shown in Figure 4.4, plotting the variation in elemental abundance across the standard grain profile. All abundances are shown in atomic percent rather than weight percent for ease of comparison to the RSF. The calcite grain shows radial zoning in both Mn and

Cr, but variable  $^{55}\text{Mn}/^{52}\text{Cr}$  ratios. Combined errors are depicted on the Mn/Cr ratios, propagated from the total counts of the peak minus background for each point. Interior points had more stable Mn/Cr ratios due to higher Mn and Cr abundances, therefore SIMS standard measurements were preferentially taken around the center of the calcite crystal. Considering only the region between 90 – 300  $\mu\text{m}$  in the calcite standard (Fig. 4.4), the average value of  $^{55}\text{Mn}/^{52}\text{Cr}$  measured by EPMA is  $1.32 \pm 0.28$  ( $2\sigma$  standard deviation). However, since each individual SIMS spot was measured directly by EPMA, we use the  $^{55}\text{Mn}/^{52}\text{Cr}$  ratio measured for that spot, rather than the average value, to calculate the RSF. The time-averaged synthetic-calcite RSF was  $0.71 \pm 0.16$  ( $2\sigma$ ), compared with a higher RSF of  $0.86 \pm 0.06$  in San Carlos olivine (Fig. 4.5); all Sutter’s Mill data are corrected with the calcite RSF. Errors bars in Figure 4.5 represent the propagated errors from SIMS and EPMA data. The scatter in the RSF values for the synthetic calcite standard was found to exist regardless of whether EPMA measurements were taken before or after SIMS measurements.

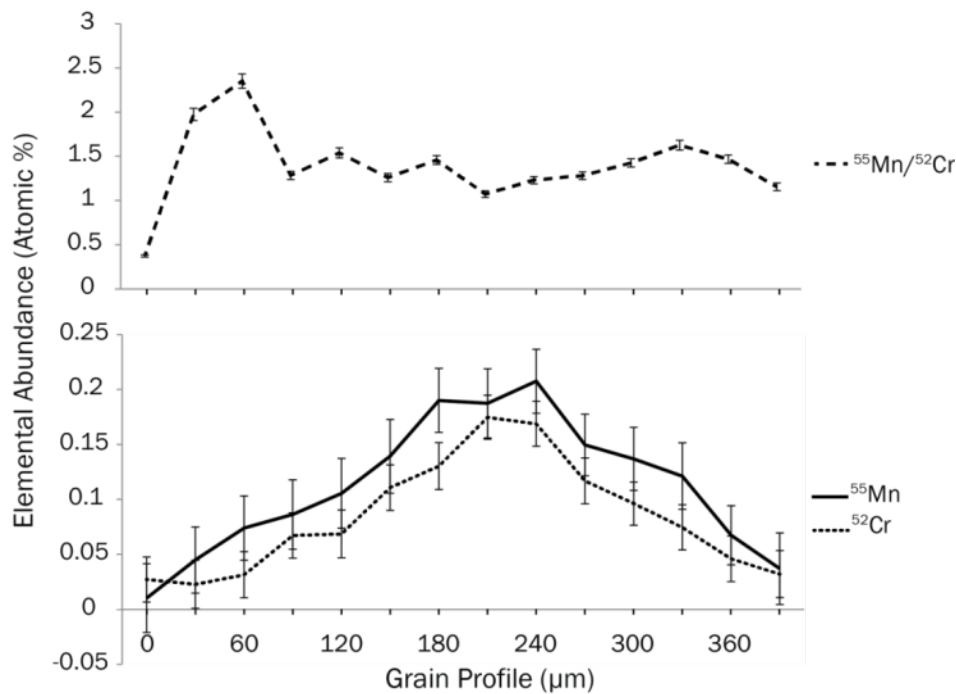


**Figure 4.4.** Graph depicting the heterogeneity of manganese and chromium in the synthetic calcite standards. Please note the different scales on the y-axes. Both manganese and chromium show radial zoning across the grain profile. However, the  $^{55}\text{Mn}/^{52}\text{Cr}$  does not display a predictable trend toward the grain edges. Elemental abundances are given in atomic %, measured by the electron microprobe.

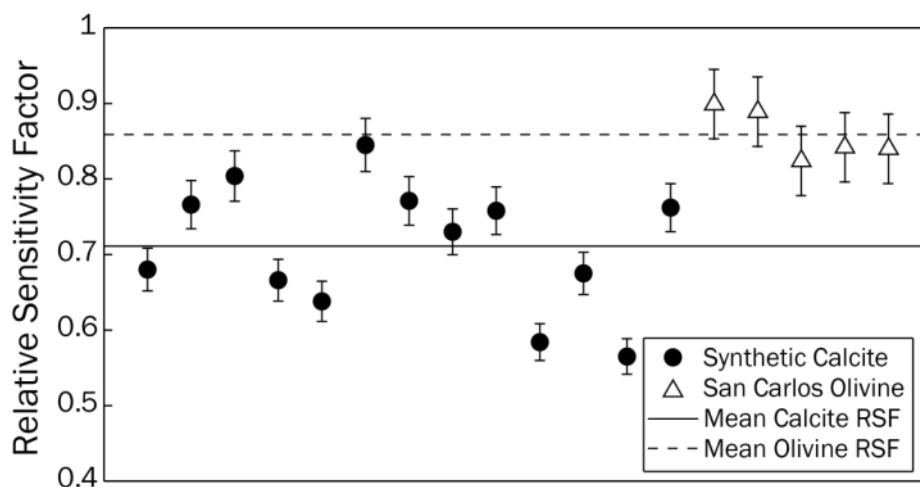


**Figure 4.5.** The relative sensitivity factors (RSF) of each standard measurement for both San Carlos olivine and a synthetic Mn- and Cr-bearing calcite. The RSF is defined as  $[(^{55}\text{Mn}+^{52}\text{Cr})_{\text{SIMS}} / (^{55}\text{Mn}/^{52}\text{Cr})_{\text{TRUE}}]$ , where the solid line represents an average value for the calcite RSF of  $0.71 \pm 0.16$ , and the dotted line represents the average value of the San Carlos olivine RSF of  $0.86 \pm 0.06$ . However, we stress that the average RSF value for calcite is significantly less than for olivine.

Seven points in five Sutter's Mill dolomite grains were measured for Mn-Cr. All but one of the grains were in the petrologic type 2.0 clast; the last grain was in the type 2.1 lithology (see Fig. 4.6). The analyzed dolomite grains ranged from 20 to 50  $\mu\text{m}$  in diameter, occurring in the phyllosilicate matrix either as isolated grains or within larger aggregates of carbonate minerals. Multiple calcite grains were targeted as well; however, due to mineral purity, the measurements yielded Mn and Cr count rates far too low for radiometric dating. Mn-Cr data from Sutter's Mill SM51-1 dolomites are listed in Table 4.1.  $\delta^{53}\text{Cr}^*$  in dolomite ranges up to  $1220.6 \pm 165.5$  ‰, and the  $^{55}\text{Mn}/^{52}\text{Cr}$  ranges up to  $38327 \pm 1260$  (after RSF correction). The errors reported are  $2\sigma$ . For  $^{55}\text{Mn}/^{52}\text{Cr}$  in Table 4.1, we report the  $2\sigma$  internal error on the measurements not including the systematic uncertainty from the RSF.

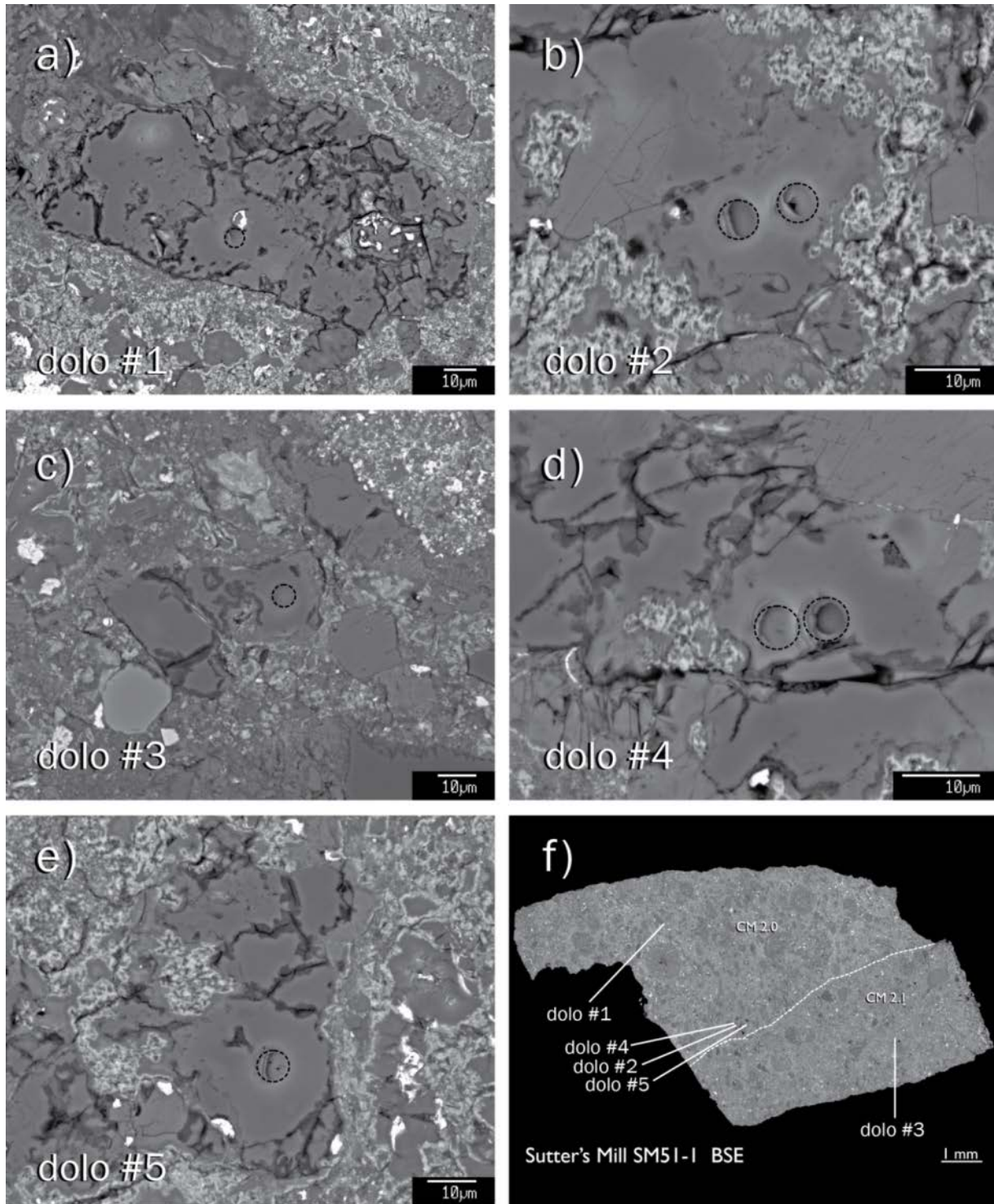


**Figure 4.6.** a–e) Backscattered-electron images of the five SM51-1 dolomite grains measured for Mn-Cr. Ion probe spots are designated by the black dashed circles. f) Backscattered-electron image of the SM51-1 thin section, showing the CM 2.0 / CM 2.1 clast boundary and dolomite grain locations.

**Table 4.1.** Mn-Cr isotope data from dolomite grains in Sutter's Mill SM 51-1.

Grain	$^{55}\text{Mn}/^{52}\text{Cr}$ <sup>a</sup>	$^{55}\text{Mn}$ total counts <sup>b</sup>	$^{53}\text{Cr}/^{52}\text{Cr}$ <sup>a</sup>	$\delta^{53}\text{Cr}^*$ <sup>a</sup>
dol #1	145.7 ± 0.4	67739	0.11494 ± 0.00088	13.0 ± 7.8
dol #2a	6620.5 ± 103.8	34213	0.13608 ± 0.00628	199.4 ± 55.3
dol #2b	38326.6 ± 1259.6	36134	0.25195 ± 0.01878	1220.6 ± 165.5
dol #3	3277.7 ± 62.3	11592	0.12489 ± 0.00720	100.8 ± 63.5
dol #4a	13864.4 ± 350.6	27534	0.15728 ± 0.01097	386.2 ± 96.6
dol #4b	2022.4 ± 19.8	33902	0.12203 ± 0.00363	75.6 ± 32.0
dol #5	8558.8 ± 154.3	33443	0.14366 ± 0.00739	273.8 ± 65.2

<sup>a</sup> Errors are 2 $\sigma$ , not including uncertainty in the RSF

<sup>b</sup> Sum of all counts per run, normalized by number of cycles per run

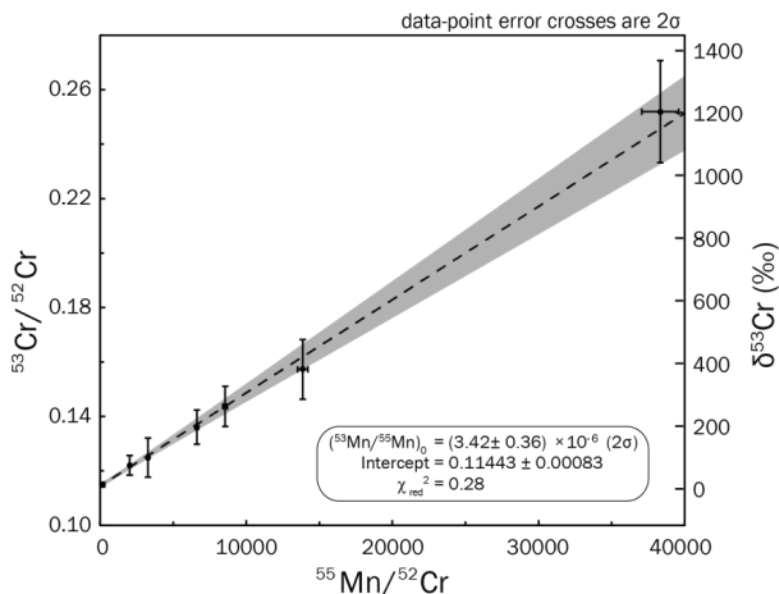


**Figure 4.7.**  $^{55}\text{Mn}/^{52}\text{Cr}$  versus  $^{53}\text{Cr}/^{52}\text{Cr}$  diagram for dolomites in Sutter's Mill SM51-1, corrected to an RSF value of 0.71.  $\delta^{53}\text{Cr}$  values are plotted on the right for reference. Error bars are 2 $\sigma$  internal error, not including systematic uncertainty in the RSF. Gray region indicates the 2 $\sigma$  error envelope.

A diagram of  $^{53}\text{Cr}/^{52}\text{Cr}$  versus  $^{55}\text{Mn}/^{52}\text{Cr}$  is displayed in Figure 4.7, showing clear evidence for excess  $^{53}\text{Cr}$  correlated with  $^{55}\text{Mn}/^{52}\text{Cr}$  ratio in the dolomites. The slope of the correlation trend corresponds to a  $^{53}\text{Mn}/^{55}\text{Mn}$  value of  $3.42 \pm 0.36 \times 10^{-6}$  during the precipitation of dolomite. The error bars in Figure 4.7 represent the 2 $\sigma$  statistical uncertainty in the measurements, not including the systematic uncertainty in the carbonate RSF. The low value of

$\chi_{\text{red}}^2 = 0.28$  (also equal to MSWD) indicates either that the errors are overestimated, or that the stochastic fluctuations in the data have led to a good agreement between the data and the fitted isochron. One major contribution to the low  $\chi_{\text{red}}^2$  is the propagation of the IMF standard error into the uncertainty in  $^{53}\text{Cr}/^{52}\text{Cr}$ . Although we did not witness a non-stochastic fluctuation in our standard measurements, we chose to be conservative with errors. Without the IMF error, the  $\chi_{\text{red}}^2$  value would double. Furthermore, the data do not show a strong correlated error that can commonly lead to a low  $\chi_{\text{red}}^2$  value. Other errors calculated are not likely overestimated, as they are dominated by the square root of the total counts, and do not include the error to the RSF.

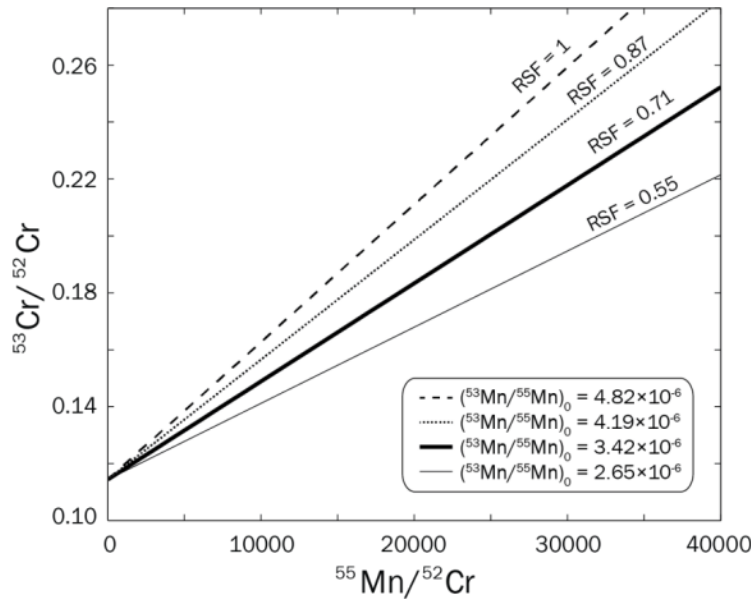


**Figure 4.8.** The Sutter’s Mill initial  $(^{53}\text{Mn}/^{55}\text{Mn})_0$  changes to a steeper or shallower slope depending on the value of the RSF used. In this study, we use an RSF for Mn-, Cr- bearing calcite of  $0.71 \pm 0.16$  ( $2\sigma$ ), as shown by the thick black line. Including the RSF uncertainty into the slope of the Mn-Cr correlation, we get  $(^{53}\text{Mn}/^{55}\text{Mn})_0 = 3.42 \pm 0.86 \times 10^{-6}$ .

Figure 4.8 demonstrates the effect of variable RSF on the isotope data. Although we use a value of 0.71 for the RSF, the slope of the correlation may be steeper or shallower when the error of  $\pm 0.16$  is taken into account. This error corresponds to a range of  $(^{53}\text{Mn}/^{55}\text{Mn})_0$  from  $4.19 \times 10^{-6}$  for an RSF of 0.87, to  $2.65 \times 10^{-6}$  for an RSF of 0.55. If we propagate the  $2\sigma$  standard deviation from the RSF into the dolomite  $^{53}\text{Cr}/^{52}\text{Cr}$  versus  $^{55}\text{Mn}/^{52}\text{Cr}$  trend, the uncertainty on the slope increases to  $3.42 \pm 0.86 \times 10^{-6}$ .

To determine the absolute ages of formation, Mn-Cr data are anchored to the U-isotope-corrected Pb-Pb ages of the D’Orbigny angrite. D’Orbigny is a quenched angrite (e.g.,

Mittlefehldt et al., 2002; Kleine et al., 2012) with an initial ( $^{53}\text{Mn}/^{55}\text{Mn}$ )<sub>0</sub> ratio of  $(3.24 \pm 0.04) \times 10^{-6}$  (Glavin et al., 2004) and absolute Pb-Pb age of  $4563.37 \pm 0.25$  Ma (Amelin 2010; Brennecka and Wadhwa, 2012). By assuming homogeneous  $^{53}\text{Mn}$  distribution in the chondrite-forming region of the early Solar System (Trinquier et al., 2008), we can compare the relative initial ( $^{53}\text{Mn}/^{55}\text{Mn}$ )<sub>0</sub> ratio of Sutter's Mill with that of D'Orbigny, to obtain an absolute age of  $4563.7^{+1.1}_{-1.5}$  Ma for the Sutter's Mill dolomite grains. This corresponds to a formation age between 2.4 and 5.0 Myr after the formation of CV CAIs (CAI formation age of  $4567.30 \pm 0.16$  Ma from Connelly et al. (2012)). Errors in the absolute age for the Sutter's Mill dolomites include the  $2\sigma$  statistical uncertainty in measurement and the systematic uncertainty in the RSF, and the uncertainty in the Mn-Cr age of D'Orbigny.

## 4.4 DISCUSSION

### 4.4.1 Aqueous alteration in the CM parent body

The excesses of  $^{53}\text{Cr}$  correlated with the Mn/Cr ratio in Sutter's Mill dolomites can, in principle, either be interpreted as an isochron, or as a mixing line of the carbonate mineral with a Cr-rich contaminant phase. The  $^{55}\text{Mn}$  contents in each measurement can be used to distinguish whether this trend is an isochron or not (e.g., Hoppe et al., 2007); total counts of  $^{55}\text{Mn}$  are presented in Table 4.1 and Figure 4.9. The counts of  $^{55}\text{Mn}$  vary from grain to grain, supporting a high time significance of our  $\delta^{53}\text{Cr}$  and  $^{55}\text{Mn}/^{52}\text{Cr}$  correlation. The Mn abundances in the dolomite grains are variable by a factor  $>2$ , suggesting that the observed correlation of  $\delta^{53}\text{Cr}$  with  $^{55}\text{Mn}/^{52}\text{Cr}$  likely represents zoning of Mn and Cr in the carbonate mineral during precipitation, rather than contamination from a Cr-bearing phase. Furthermore, plotting  $\delta^{53}\text{Cr}$  vs.  $1/^{52}\text{Cr}^+$  values yields a trend with a much larger MSWD of  $\sim 12$  (Fig. 4.9). A mixing line would result in a better correlation than the isochron, which is not the case for our data. Therefore, we take the well-resolved excesses of  $^{53}\text{Cr}$  to indicate the *in-situ* decay of live  $^{53}\text{Mn}$  at the time of carbonate precipitation.

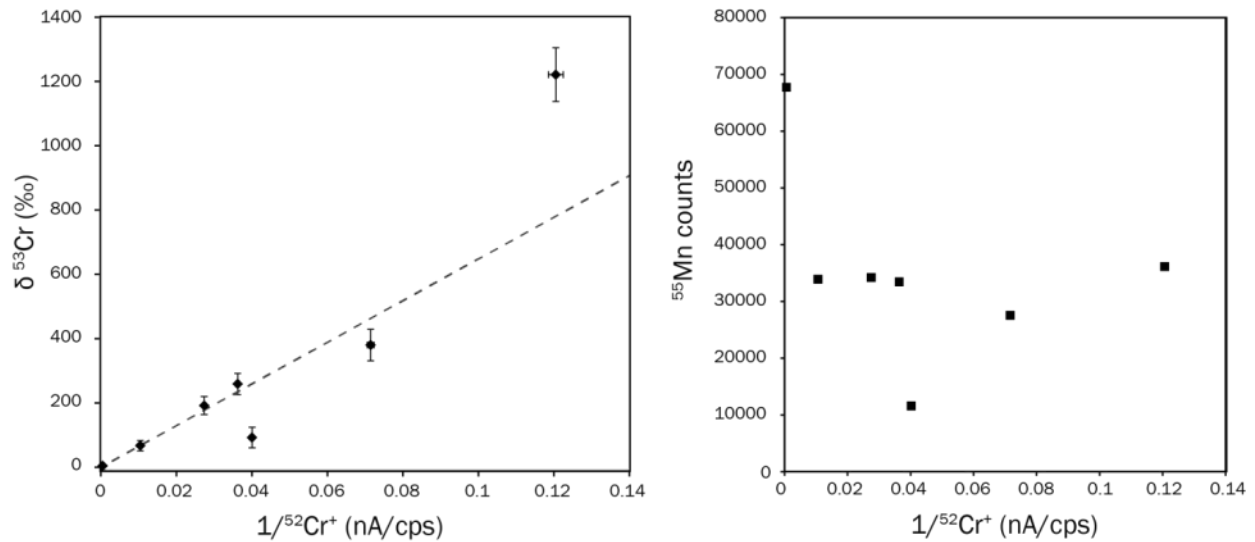


**Figure 4.9.** Graphs of  $\delta^{53}\text{Cr}$  vs.  $1/^{52}\text{Cr}^+$  and  $^{55}\text{Mn}$  vs.  $1/^{52}\text{Cr}^+$ . The  $1/^{52}\text{Cr}^+$  values are given in counts per second, normalized to beam current.  $^{55}\text{Mn}$  values are given as total counts, normalized to the number of cycles per run. The variability in  $1/^{52}\text{Cr}^+$  and  $^{55}\text{Mn}$  support the interpretation of our data as an isochron.

We interpret the  $^{53}\text{Mn}$ - $^{53}\text{Cr}$  trend as an isochron, providing evidence for the early onset of aqueous alteration on the Sutter's Mill parent body. Petrographically, the Sutter's Mill section SM 51-1 shows compelling evidence for *in situ* alteration in the formation of the secondary dolomite. Dolomite veins that cross-cut the rims of chondrule pseudomorphs are indicative of alteration on the parent body, rather than in the nebular setting (cf. Fig. 4.2). Hence, the aqueous alteration must have occurred after formation and accretion of the chondrules and matrix material. Possible sources of heating to drive aqueous alteration on the parent body include the internal decay of radioactive  $^{26}\text{Al}$ , and impact heating. Our age is consistent with the idea that aqueous alteration was driven by heating from radioactive  $^{26}\text{Al}$  in the Sutter's Mill parent body (e.g., Fujiya et al., 2012; 2013), soon after accretion. However, the impact-heating scenario cannot be entirely ruled out from this dataset alone.

Many previous studies have used the  $^{53}\text{Mn}$ - $^{53}\text{Cr}$  system to constrain the timing and duration of aqueous alteration in carbonaceous chondrites (e.g., Endress et al., 1996; Hoppe et al., 2007; de Leuw et al., 2009; Petit et al., 2011; Lee et al., 2012; Fujiya et al., 2012, 2013). In order to make accurate cross-laboratory comparisons with our results, there are two factors that must be addressed: absolute time anchors and relative sensitivity factors. Previous reports of absolute Pb-Pb ages assumed a constant  $^{238}\text{U}/^{235}\text{U}$  composition for solar system materials.

However, recent studies have shown that uranium-isotopes may vary, and therefore must be measured to obtain correct Pb-Pb ages (Amelin et al., 2010; Brennecka and Wadhwa, 2012). Brennecka and Wadhwa (2012) showed that angrite time anchors do contain deviations in uranium-isotopes, resulting in absolute age differences of >1 Myr from uncorrected measurements. The D'Orbigny angrite anchor used here has been extensively studied and corrected for such uranium-isotopic anomalies (Amelin 2008; Brennecka and Wadhwa, 2012). D'Orbigny is a favorable time anchor as it yields consistent Mn-Cr, Pb-Pb, and Hf-W ages, and well-behaved Al-Mg systematics (Glavin et al., 2004; Kleine et al., 2012). Furthermore, D'Orbigny is a quenched angrite, rather than plutonic (Keil, 2012), which means that closure times for the different systems are likely to be concordant, even for the short-lived radiochronometers.

As discussed earlier, the RSF for carbonates can change the slope of an isochron, and therefore should be independently measured on a carbonate standard under the same conditions as the unknowns. Prior studies have used silicate mineral or glass standards (Endress et al., 1996; Hoppe et al., 2007; Petit et al., 2011; Lee et al., 2012), or have used a previously determined RSF from literature to correct their data (e.g., de Leuw et al., 2009), introducing significant error into the results. However, the new RSF measurements for Mn- and Cr- bearing calcite grains have large uncertainties, as seen in Fig. 4.5. The uncertainty in our measured RSF is much larger than those for the electron probe data (Fig. 4.4), suggesting that there are small-scale heterogeneities in the calcite standards. While these standards are not perfect, they currently provide the best estimate of the true carbonate RSF.

We should be able to compare our Mn-Cr age in Sutter's Mill dolomite grains to ages obtained for other carbonaceous chondrite carbonates from the studies of Fujiya et al. (2012, 2013), as their measurements use the same synthetic calcite standards as in this study, with similar values determined independently for the RSF. Figure 4.10 shows the age range for Sutter's Mill carbonates compared with the *in-situ* Mn-Cr ages for carbonates in other CM and CI chondrites of varying petrologic type. Error bars for the Sutter's Mill age include the systematic error in the RSF. All data in Figure 4.10 are anchored to D'Orbigny angrite. Sutter's Mill dolomites give the largest  $^{53}\text{Mn}/^{55}\text{Mn}$  value, corresponding to the oldest age. However, within uncertainties, the ages are contemporaneous. Furthermore, to obtain a rough idea of how previous silicate-normalized measurements compare to this study, we can correct the published

$(^{53}\text{Mn}/^{55}\text{Mn})_0$  from literature using the difference in San Carlos olivine and carbonate RSF obtained in this study (this value is similar to that found by Fujiya et al., 2012). Assuming that the relative difference in RSF between silicate and carbonate is more or less independent of the lab, the isochron slopes can be corrected by the factor:  $\text{RSF}_{\text{calcite}}/\text{RSF}_{\text{olivine}} = 0.83$ , and re-anchored to D’Orbigny angrite. Carbonate data from the literature for CM and CI carbonates yield carbonate formation ages between 2.4 to 5.1 Myr after CAI formation, consistent with this study (Hoppe et al., 2007; deLeuw et al., 2009; Petit et al., 2009, 2011; and Lee et al., 2012). However, caution should be taken with these rough values as the magnitude of the RSF correction factor between San Carlos olivine (or other silicates) and carbonate is not necessarily the same for all instruments and studies.

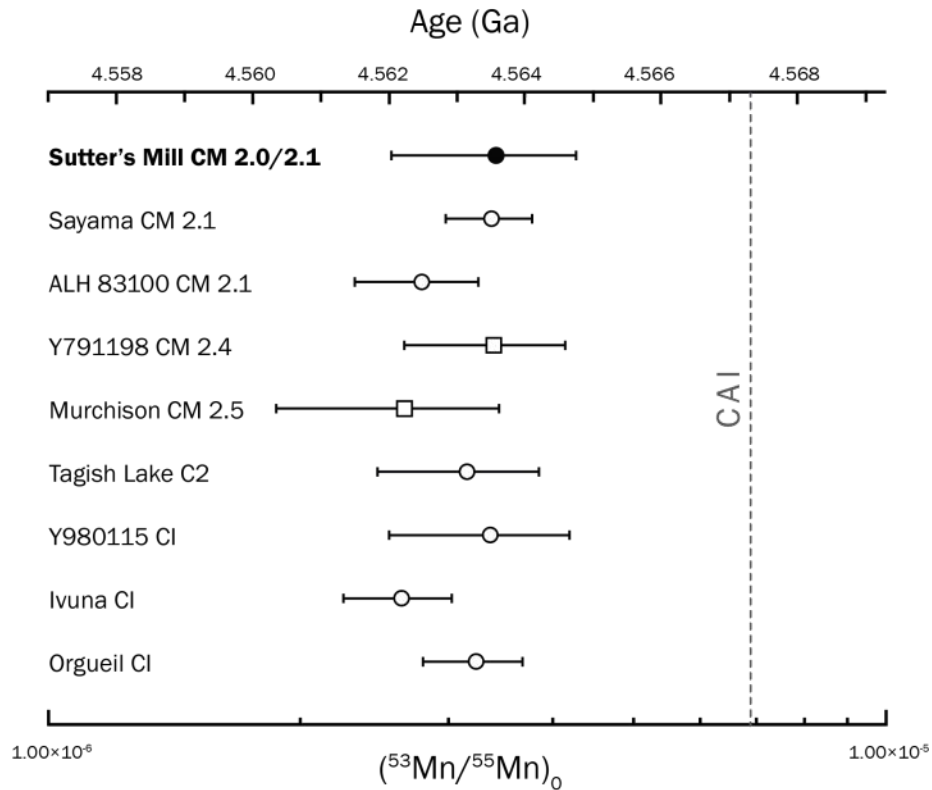


**Figure 4.10.** Mn-Cr ages and initial  $(^{53}\text{Mn}/^{55}\text{Mn})_0$  for carbonates in carbonaceous chondrites. All Mn-Cr ages are anchored to D’Orbigny angrite U-corrected Pb-Pb data (Brennecka and Wadhwa, 2012). The Sutter’s Mill dolomite age from this study is indicated by a closed symbol. CI, CM, and Tagish lake data are indicated in open symbols, where the data are from Fujiya et al. (2012, 2013), recalculated to the D’Orbigny anchor. Dolomites are indicated as circles, calcites as squares. The Pb-Pb age for CV CAIs is shown as a dashed line (Connelly et al., 2012). The age for carbonate formation in Sutter’s Mill SM51-1 is contemporaneous with carbonate formation in other carbonaceous chondrites.

The timing of carbonate formation in CM chondrites has been suggested to correlate with petrologic type (de Leuw et al., 2009). Their study measured the dolomite Mn-Cr ages in CM chondrites, and compared the results to previously measured carbonates in CI and CM chondrites, noting that the petrologic subtype correlates with carbonate age. De Leuw et al. (2009) conclude that alteration started contemporaneously throughout the CM parent body and that CM chondrites of lower petrologic subtype (more aqueously altered) experienced alteration over a longer period of time than CM chondrites of higher petrologic subtype (less aqueously altered). However, they did not independently measure the RSF for their instrumental setup, and compare literature data corrected to a variety of standards. In contrast to their results, our data, as well as data from Fujiya et al., (2012; 2013), do not show any observable correlation between the age of carbonates and the petrologic type. If such a correlation does exist, then the age differences occurred on a short timescale that is currently unresolvable by the Mn-Cr chronometer. Another possible scenario is that the differences in petrologic type on the CM parent body reflect heterogeneous accretion of water-ice to the parent body, where lower petrologic type corresponds to a larger amount of ice incorporated into the rock.

Previous measurements of carbonates in CM chondrites have suggested that aqueous alteration on the asteroidal parent body may have occurred nearly contemporaneously with CAI formation (de Leuw et al., 2009; Tyra et al., 2009). However, as mentioned in de Leuw (2009), these ages are anchored to the poorly constrained initial  $^{53}\text{Mn}/^{55}\text{Mn}$  ratio measured in bulk chondrites (Shukolyukov and Lugmair, 2006) and to the LEW 86010 plutonic angrite (Amelin, 2008), without taking into account an RSF measured on carbonate minerals. To consistently compare these ages to the Sutter's Mill data, we have re-anchored their data to the uranium-corrected Pb-Pb ages of D'Orbigny and compared it to the Pb-Pb ages of CAIs (Brennecka and Wadhwa, 2012; Connelly et al., 2012). The ages from de Leuw et al. (2009) are between ~1.3–2.5 Myr after CAI formation, and an RSF correction would make the age even younger. These ages are old compared with previously reported carbonate Mn-Cr ages of ~20 Myr in CI chondrites (Endress et al., 1996). Yet again, the young CI ages were anchored to Mn-Cr ages of CAIs from Birck and Allègre (1988), which have since been revised to lower values (Trinquier et al., 2008). When re-anchored to D'Orbigny, the age of CI carbonates measured by Endress et al. (1996) corresponds to ~6.4 Myr after CAI formation. Their measurements however did not include carbonate RSF analyses, and therefore the correction factor to the isochron is unknown.

Our results on SM51-1 show that aqueous alteration was occurring on the CM parent body by 2.4 to 5.0 Myr after CAI formation, consistent with the late accretion model of carbonaceous chondrites forming after differentiated parent bodies (Kleine et al., 2005). Hf-W ages of angrites and iron meteorites indicate that core formation in these bodies occurred no later than 2 Myr after CAI formation. Furthermore, thermodynamic modeling of planetesimals heated by  $^{26}\text{Al}$  reveals that there is a time gap between accretion and core formation, suggesting that differentiated meteorites accreted  $\sim 1.5$  Myr after CAI formation (Qin et al., 2008; Kleine et al., 2012). Pb-Pb and Al-Mg dating of chondrules from a variety of chondrites (including CV, CR, CO, and UOCs) show that most chondrules were formed within  $\sim 2$ -3 Myr of CAI formation (Kita and Ushikubo, 2012), after the suggested timing of core formation in differentiated bodies. Al-Mg ages of some chondrules in CR chondrites are shown to have formation ages  $> 3$  Myr (Nagashima et al., 2008). However, the Al-Mg system is currently under examination as to whether it has been disturbed from aqueous alteration or other parent body processes (Kita and Ushikubo, 2012; Alexander and Ebel, 2012). Chondrules in CM chondrites have not been dated due to their heavily altered nature, therefore other classes can be used as a proxy. If accurate, the chondrule formation timescale would allow for a span of 1–2 Myr for parent body accretion and the early onset of alteration; however, this would require aqueous alteration to occur nearly immediately after the accretion of the CM parent body. Secondary alteration would begin once temperatures became high enough to melt the accreted ice on the chondrite parent body, either occurring from internal heating due to the decay of radionuclides such as  $^{26}\text{Al}$ , or from other late-stage processes such as impact heating. Models of internal parent body heating from  $^{26}\text{Al}$  by Fujiya et al. (2012, 2013) confirm that optimum carbonate forming temperatures would easily be reached within 1–2 Myr, depending on the accretion time and radius of the CM parent body. Similar studies in CO and CV chondrites support the early accretion and aqueous alteration of carbonaceous chondrites (Krot et al., 2013; Doyle et al., 2013).

#### **4.4.2 Relative ages of dolomite and calcite**

Although the calcite and dolomite crystals in SM51-1 are intergrown (see Fig. 4.1a), they did not likely form in equilibrium from the same fluid (Riciputi et al., 1994). Petrographic observations show instances of dolomite encompassing calcite (Fig. 4.1b), suggesting a later

formation of dolomite. Furthermore, calcite formation temperatures in CM chondrites as estimated by clumped isotope thermometry (Guo and Eiler, 2007) and O-isotope fractionation (Clayton and Mayeda 1984) suggest formation at temperatures of 0–30°C. Dolomites in CM chondrites have been estimated to form at higher temperatures ~120°C, using an O-isotope dolomite-serpentine geothermometer (Nakamura et al., 2003). In the hypothesis of parent body alteration due to the heating from  $^{26}\text{Al}$  decay, the carbonate phases can be interpreted as calcite precipitating first, with dolomites forming afterwards under higher temperature conditions and progressive alteration (Rubin et al., 2007; Fujiya et al., 2012). However, Lee et al. (2012) have interpreted similar carbonate textures from the CM 2.1 chondrite QUE 93005 as forming in the reverse order, where breunnerite  $[(\text{Mg,Fe})\text{CO}_3]$  crystallizes first on pore margins, followed by dolomite, then calcite filling in as pore center.

O-isotopes in calcite and dolomite grains in Sutter's Mill SM51-1 were measured and reported in Jenniskens et al. (2012). The calcite grains appear to track fluid evolution, as the O-isotopes plot on an array with a slope nearly identical to calcites in other CM chondrites (Benedix et al., 2003). In contrast, dolomite grains from SM51-1 plot in a tightly clustered region near the lower  $\Delta^{17}\text{O}$  end of the calcite array, indicating stringent physico-chemical conditions upon formation (Jenniskens et al., 2012). If formed from the same fluid, dolomite formation may have occurred between (or simultaneous with) calcite precipitation events; otherwise, dolomite may have formed under distinct temperature and fluid chemistry altogether. Unfortunately, we were not able to locate any calcite crystals with Mn and Cr count rates high enough to use for radiometric dating to verify a relative formation timescale. Further analysis of calcites in SM51-1 could be of interest to see if one can distinguish the relative Mn-Cr ages of calcites and dolomites. However, considering the current level of uncertainty associated with the Mn-Cr chronometer, resolving the alteration ages between dolomite and calcite would require that the minerals precipitated in distinct events at least hundreds of thousands years apart.

#### **4.4.3 Relevance to other measured isotopic systems in Sutter's Mill**

Recent studies of the Sutter's Mill piece SM51 have suggested the disturbance of some isotopic systems. Walker et al. (2013) reported on  $^{187}\text{Re}$ - $^{187}\text{Os}$  systematics measured from whole rock powders taken from fresh interior portions of the meteorite. Their results show evidence for

a late stage disturbance to the highly siderophile elements (HSE), within the last ~1 Ga. However, our tight isochron shows that the Mn-Cr systematics was not affected by the HSE mobility that caused the Re-Os system to be disturbed. Our early alteration age of ~4564 Ma is contemporaneous with those of other CM chondrites (Fujiya et al., 2012), and can be reconciled if the dolomite was not the mineralogical carrier of the disturbances to the Re-Os system. Both rhenium and osmium are highly siderophile, and are likely sequestered in iron-rich secondary phases, rather than in the iron-poor carbonates measured here. Redistribution of the rhenium and osmium isotopes can occur on a scale of millimeters to centimeters in a sample, and may be due to aqueous alteration or shock on the parent body, or to later terrestrial weathering (Walker et al., 2002). Such a late stage disturbance suggests that the cause was likely terrestrial weathering or shock. A rainfall event was documented before the finding of SM51 (Jenniskens et al., 2012), and could have been sufficient to mobilize highly siderophile elements (Walker et al., 2013). Although no terrestrial weathering veins are seen in the section SM51-1 studied here, iron-bearing minerals are generally the most readily oxidized by the Earth's atmosphere (Bland et al., 2006). Minor terrestrial weathering due to the rainfall event could plausibly disturb the HSE elements, without affecting the iron-free dolomite grains, supporting the validity of our isochron.

The Mn-Cr system has been studied in SM51 in other capacities. Bulk Mn-Cr systematics from powders were investigated by Jenniskens et al. (2012). The isotopic data plot on a linear correlation with other carbonaceous chondrites, with a  $^{53}\text{Mn}/^{55}\text{Mn}$  ratio of  $(5.90 \pm 0.67) \times 10^{-6}$ ; a higher ratio than we obtain from Sutter's Mill dolomite ( $3.42 \pm 0.86 \times 10^{-6}$ ). Although many questions remain regarding the meaning of this bulk Mn-Cr carbonaceous chondrite array, it has been suggested that the bulk trend represents a large-scale fractionation of Mn and Cr in the early solar nebula, with the possibility of disturbance during planetesimal formation in the nebula (e.g. Shukolyukov and Lugmair, 2006; Scott and Sanders, 2009; Jenniskens et al., 2012). Regardless of the interpretation of the bulk isochron, Sutter's Mill dolomites record a younger age than the bulk trend, consistent with a later-stage Mn redistribution occurring on the CM parent body. Mn-Cr isotopes have also been measured in mineral leachates from SM51 (Yamakawa and Yin, 2013). The leaching was performed to identify the mineral phases containing distinct manganese and Cr isotopic signatures (Yamakawa and Yin, 2013). Leachate L1 in their study is comprised of easily soluble minerals that are dissolved by weak acids, including carbonates and sulfides. L1 carries a large excess of  $^{53}\text{Cr}$  compared with the other leachates, indicating that  $^{53}\text{Mn}$  was alive at

the time of formation of the L1 minerals. The L1 leachate plots below the bulk Mn-Cr isochron, suggesting that the leachate minerals were formed during a secondary process such as aqueous alteration post-accretion of the parent body of Sutter's Mill. Their carbonate leachate result is consistent with this study in that it demonstrates that  $^{53}\text{Mn}$  was alive at the time of aqueous alteration on the Sutter's Mill parent body.

## 4.5 CONCLUSIONS

The results of our investigation of Sutter's Mill SM51-1 are consistent with the CM 2.0/2.1 classification. The Mn-Cr radiometric dating of secondary dolomites from SM51-1 reveal ages contemporaneous with dolomite grains in other CM chondrites. In addition, the ages of dolomite in CI chondrites and Tagish Lake are also contemporaneous, suggesting that parallel aqueous alteration events occurred on the various parent bodies. We stress that inter-laboratory comparisons of Mn-Cr measurements in carbonates of carbonaceous chondrites are possible only if each measurement has been acquired self-consistently using the same standards to correct for RSF. We have used the same standard with similar relative sensitivity factors as used in Fujiya et al. (2012, 2013), and make comparisons to their dataset. Our SM51-1 dolomite age of  $4563.7^{+1.1}_{-1.5}$  Ma suggests that aqueous alteration occurred early in the parent body history, likely due to heating from  $^{26}\text{Al}$  decay. There is no observable correlation between the petrologic type for CM chondrites and the age of alteration, and any distinct carbonate forming events are currently unresolved. The well-defined isochron presented here suggests that any subsequent processing to SM51, whether thermal, impact, or terrestrial, did not disturb the Mn-Cr system in secondary dolomites.

## CHAPTER 5

### LOW TEMPERATURE AQUEOUS ALTERATION ON THE CR CHONDRITE PARENT BODY: IMPLICATIONS FROM *IN SITU* OXYGEN ISOTOPES

In preparation for submission to *Geochimica et Cosmochimica Acta*, as Jilly-Rehak C. E., Huss G. R., Nagashima K., and Schrader D. L. Low temperature aqueous alteration on the CR chondrite parent body: Implications from *in situ* oxygen isotopes.

*Abstract-* The process of aqueous alteration in chondritic meteorites is poorly understood. Type CR carbonaceous chondrites are particularly well-suited for the study of aqueous alteration. Samples range from being nearly anhydrous to fully altered, essentially representing snapshots of the alteration process through time. We studied secondary-mineral oxygen isotopes in six CR chondrites of varying hydration states to determine how aqueous fluid conditions (including composition and temperature) evolved on the parent body. Secondary minerals analyzed included calcite, dolomite, and magnetite. The oxygen composition of calcites ranged from  $\delta^{18}\text{O} \approx 9$  to 35‰, dolomites from  $\delta^{18}\text{O} \approx 23$  to 27‰, and magnetites from  $\delta^{18}\text{O} \approx -18$  to 5‰. The MIL 090292 magnetite diverges from this trend, possibly indicating an anomalous origin. The oxygen isotopic compositions of the secondary minerals do not correlate well with the assigned petrologic types from literature. Instead, they provide information about the degree of alteration for the different components (chondrules, matrices, rims, dark inclusions). In the context of a closed-system model of parent body alteration, the secondary oxygen isotopes reveal that water evolved from a heavier composition to a lighter composition as alteration progressed, likely dominated by phyllosilicate formation. The magnetite oxygen isotopes indicate that matrix magnetites formed first, followed by chondrule rims, dark inclusions, and then chondrule interiors. In contrast, the matrix carbonate oxygen-isotopes track the entirety of fluid evolution, indicating that carbonate formation was prolonged. The relative  $^{18}\text{O}$  fractionation between associated magnetite and calcite grains formed in equilibrium can be used to extract the temperature of co-precipitation. Isotopic fractionation in meteorites Al Rais and GRO 95577 both revealed low precipitation temperatures (< 60 °C). However, the two meteorite lithologies require fluids of different oxygen isotopic composition, supporting the idea that alteration conditions on the CR parent body evolved, or were chemically and spatially heterogeneous.

## 5.1 INTRODUCTION

The Renazzo-like carbonaceous chondrite (CR) sample suite records the process of aqueous alteration on chondritic parent bodies better than any other chondrite group. CR chondrites span the widest distribution of aqueous alteration, while experiencing only minor degrees of thermal metamorphism (e.g., Weisberg et al., 1993, 1995; Kallemeyn et al., 1994; Krot et al., 2002; Brearley, 2006; Rubin et al., 2007; Weisberg and Huber, 2007; Schrader et al., 2011; Harju et al., 2014). The degree of aqueous alteration is quantified by the petrologic type, where CR chondrites range from fully altered type 2.0 to nearly anhydrous type 2.8 (Weisberg and Huber, 2007; Abreu and Brearley, 2010; Harju et al., 2014). Most aqueous alteration literature is dominated by studies of Mighei-like (CM) and Ivuna-like (CI) chondrites. Yet unlike the CR chondrites, CM and CI chondrites have only experienced extensive aqueous alteration, with no samples that have had minimal exposure to water (CM chondrites range up to petrologic type 2.6; Rubin et al., 2007). The mineralogy of the precursor CM and CI material is therefore based upon many assumptions due to the relative lack of unaltered components. Other chondrite groups, such as Vigarano-like (CV), Ornans-like (CO) and Ordinary (OC) chondrites, have undergone minor amounts of aqueous alteration, but have also experienced extensive thermal metamorphism that overprints and obscures aqueous alteration signatures (e.g., Brearley et al., 2006; Weisberg et al., 2006).

CR chondrites are characterized by large (~0.7 mm) metal-rich type-I chondrules. Some chondrules are concentrically-layered, consisting of olivine- or pyroxene- rich cores surrounded by iron-nickel metal nodules, then another layer of finer-grained olivine and pyroxene, sometimes surrounded by more metal nodules, with a rim of fine-grained phyllosilicates or carbonates (Weisberg et al., 1993; Kallemeyn et al., 2014; Weisberg et al., 2006). In more aqueously altered samples, metal has been oxidized to magnetite and Fe,Ni-sulfides (pyrrhotite and pentlandite), and chondrule mesostasis and silicates have been altered to phyllosilicates (including serpentine, chlorite, and smectite). CRs consist of ~30-60 % matrix material, including fine-grained dark inclusions that exist as lithic clasts in the host meteorite (Weisberg et al., 1993; Kallemeyn et al., 1994; Weisberg et al., 2006). The matrix is primarily comprised of hydrous, anhydrous, and amorphous silicates in quantities that depend on the degree of alteration (Weisberg et al., 1993; Brearley, 2006; Abreu and Brearley, 2010). Fine-grained carbonates,

sulfides, and magnetite are also littered throughout the matrix. The dark inclusions are more hydrated than the interchondrule matrix, but are otherwise petrographically and compositionally very similar. Such dark inclusions typically contain small chondrules (<200  $\mu\text{m}$ ), as does the matrix (Weisberg et al., 1993).

*In situ* oxygen-isotope analyses of secondary mineral phases are crucial to understanding the aqueous alteration process. On an oxygen three-isotope plot, bulk samples and constituents of CR chondrites plot along a unique mixing line of slope  $\sim 0.7$ , that falls between the terrestrial fractionation line (TFL) and the carbonaceous chondrite anhydrous mineral line (CCAM) (e.g., Clayton and Mayeda, 1999; Choi et al., 2009; Schrader et al., 2011). This mixing line reflects the progressive alteration of a  $^{16}\text{O}$ -rich anhydrous reservoir by a more  $^{17,18}\text{O}$ -rich  $\text{H}_2\text{O}$  reservoir (Clayton and Mayeda, 1999; Schrader et al., 2011). The anhydrous reservoir is composed of primitive components that lie on the CCAM and/or the Young & Russell (Y&R) line, such as chondrules, calcium-aluminum inclusions (CAIs), and amoeboid olivine aggregates (AOAs; Young and Russell, 1998; Krot et al., 2006; Schrader et al., 2013). The heavy oxygen reservoir is thought to be the source of the altering fluid on the CR parent body, but may not necessarily represent the same heavy oxygen reservoir responsible for hydration of CI and CM chondrites (Clayton and Mayeda, 1984, 1999; Weisberg et al., 1995; Schrader et al., 2011). While the whole-rock mixing line serves as a broad generalization for progressive alteration, there are fine scale inconsistencies where the alteration states of some specimens do not perfectly correlate with their anticipated composition (Schrader et al., 2011). Such inconsistencies likely reflect the complex and heterogeneous nature of CR chondrites (Weisberg et al., 1993). *In situ* oxygen-isotope analyses are therefore needed to define the secondary mineral contributions to the CR trend.

Oxygen isotopic compositions of secondary minerals can also be used to constrain the temperatures of aqueous alteration on the CR parent body (e.g., Chiba et al., 1989; Zheng 1998; Choi et al., 2000). During secondary mineral precipitation, oxygen isotopes are partitioned between the water and the mineral phases. The degree of fractionation is highly dependent on temperature, and has been determined empirically for a variety of secondary minerals (including calcite, dolomite, and magnetite) under terrestrial conditions (e.g., Chiba et al., 1989; Zheng 1991, 1995, 1999, 2011; Kim and O'Neil, 1997). In the case that two secondary minerals are produced in equilibrium from a single fluid phase, the relative degree of oxygen-isotopic

fractionation can be used to determine the temperature of the fluid (Choi et al., 2000).

Equilibrium is determined using petrographic evidence and oxygen isotopic composition.

We measured *in situ* the oxygen isotopic compositions of secondary minerals in CR chondrites of varying petrologic type to address three main objectives: 1) To understand the evolution of fluid composition during progressive aqueous alteration. 2) To constrain the temperature of alteration on the CR parent body, and to discern whether the different petrologic types correspond to different alteration temperatures. 3) To measure the secondary mineral oxygen-isotope contributions to the whole-rock trend, and determine if these secondary signatures can explain bulk-trend inconsistencies.

## 5.2 EXPERIMENTAL TECHNIQUES

### 5.2.1 CR chondrite samples and petrography

We targeted calcite and magnetite grains in CR chondrites of varying petrologic type. A total of eight thin sections from six meteorites were used (Table 5.1), specifically made without water for the purpose of this study. The samples chosen for our study span a wide range of petrologic type, from minimally aqueously altered (type CR 2.0) to nearly completely hydrated (type CR 2.8; Harju et al., 2014). Specimens GRO 95577 and QUE 99177 were previously described as containing our desired target minerals within hydrated matrix material (Weisberg and Huber, 2007; Schrader et al., 2011). In addition, Renazzo (type CR 2.4) is a fall and has largely escaped terrestrial weathering, serving as a useful diagnostic tool to distinguish products of pre-terrestrial alteration from minerals formed via weathering.

Primary characterization of thin sections was conducted with optical microscopy. High-resolution optical maps were compiled using an automated mapping system (Ogliore and Jilly, 2013). The system employs focus stacking and high-dynamic-range imaging to create gigapixel images that can be viewed and magnified using a web-browser as a “virtual microscope”. After carbon-coating, element X-ray maps of each thin section were obtained using the JEOL JXA-8500F electron microprobe at the University of Hawai‘i. Calcium, iron, magnesium, aluminum, and sulfur were measured under conditions of 15.0 kV and 50 nA. Individual elemental maps were combined into multi-element pseudo-mineral maps used to identify potential carbonate and

magnetite-rich regions. Sections were then analyzed and imaged using backscattered-electron (BSE) imaging on a JEOL JSM 5900LV scanning electron microscope (SEM) set to an accelerating voltage of 15 kV. Calcite and magnetite grains for oxygen isotope analysis were identified using energy dispersive x-ray spectroscopy (EDX). The grains chosen for this study ranged from 5 – 50  $\mu\text{m}$  in diameter.

**Table 5.1.** List of meteorite thin sections used in this study.

Meteorite	Petrologic Type*	Find/Fall	Weathering Grade**
GRO 95577,69	CR 2.0	Find	B
MIL 090292,12	CR 2.0	Find	B
Al Rais USNM 6997	CR 2.3-an	Fall	N/A
Renazzo N1126	CR 2.4	Fall	N/A
Renazzo N1127	CR 2.4	Fall	N/A
EET 92159,20	CR 2.8	Find	B/C
QUE 99177,69	CR 2.8	Find	Be
QUE 99177,06	CR 2.8	Find	Be

\* Petrologic types from Harju et al., 2014. Petrologic types for CR chondrites range from 2.0 to 2.8. an = anomalous.

\*\* Weathering grades for Antarctic meteorites used by the Meteorite Working Group include categories “A,” “B,” and “C” to denote minor, moderate, and severe rustiness, respectively; “e” indicates the presence of evaporites. There is no weathering scheme for meteorite falls.

### 5.2.2 Secondary Ion Mass Spectrometry (SIMS)

Oxygen isotope compositions were measured *in situ* using the University of Hawai‘i Cameca ims-1280 ion microprobe. Two different analytical setups were used to measure the oxygen isotope compositions, based upon the methods of Makide et al. (2009). For both procedures, a  $\text{Cs}^+$  primary beam with total impact energy of 20 keV was used to sputter oxygen isotopes from the sample. Masses  $^{16}\text{O}^-$ ,  $^{17}\text{O}^-$ , and  $^{18}\text{O}^-$  were measured simultaneously in multicollection mode on a Faraday cup and two electron multipliers, respectively.

Mineral grains in Renazzo N1127 and GRO 95577,69 were presputtered for 90 s to remove carbon coating and surface contamination using a  $\sim 600$  pA primary beam focused to 10  $\mu\text{m}$  and a  $10 \times 10 \mu\text{m}^2$  raster. The raster size was then reduced to  $7 \times 7 \mu\text{m}^2$  for data collection. The mass resolving power was set to  $\sim 2000$  for  $^{16}\text{O}^-$  and  $^{18}\text{O}^-$ , and to  $\sim 5000$  for  $^{17}\text{O}^-$ , sufficient to resolve the interference from  $^{16}\text{OH}^-$ . Each run consisted of 30 cycles of 16 s each, for a total run time of  $\sim 10$  min. A second procedure was used for measuring mineral grains smaller than  $\sim 15$

$\mu\text{m}$ . A  $\text{Cs}^+$  primary beam current of 25 pA was used to obtain a spot size of  $\sim 3 \mu\text{m}$ . All grains were pre-sputtered for 180 s. Each run consisted of 30 cycles of 46 s each, with a total run time of  $\sim 25$  min. No raster was used for the reduced beam size procedure. After each run,  $^{16}\text{OH}^-$  peaks were measured. Values of  $^{17}\text{O}^-$  were corrected for the tail of  $^{16}\text{OH}^-$  using a tail/peak ratio of 20 ppm, with a typical contribution of  $\sim 0.6\%$ . To assure accuracy of the final results, data gathered by each method was reduced against standard data gathered in the same way. Terrestrial calcite, dolomite, and magnetite were used as standards.

All ion probe pits were imaged using the SEM after measurement to ensure that no cracks or different phases were included in the analysis. Any analyses that were clearly mixed or missed the target mineral were discarded. Data were collected over 30 cycles to permit monitoring of the ion signals with time and to evaluate their stability. The data were reduced using the method of total counts to minimize statistical bias (Ogliore et al., 2011). All measurement data were converted into delta notation with units of parts per mil (‰), where SMOW represents the oxygen isotopic composition of standard mean ocean water:

$$\delta^{17,18}\text{O} = [({}^{17,18}\text{O}/{}^{16}\text{O})_{\text{sample}}/({}^{17,18}\text{O}/{}^{16}\text{O})_{\text{SMOW}} - 1] \times 1000 \quad (1)$$

The  $^{17}\text{O}$  data were also expressed as  $\Delta^{17}\text{O}$ , representing the vertical displacement from the mass-dependent TFL, given in ‰:

$$\Delta^{17}\text{O} = \delta^{17}\text{O} - 0.52 \times \delta^{18}\text{O} \quad (2)$$

The IMS 1280 does not have sufficient abundance sensitivity to completely separate  $^{17}\text{O}^-$  from the tail of  $^{16}\text{OH}^-$ . After each measurement, the  $^{16}\text{OH}^-$  peak was measured, and the values of  $^{17}\text{O}^-$  were corrected for the tail of  $^{16}\text{OH}^-$  using a tail/peak ratio of 20 ppm; a typical correction was  $\sim 0.6\%$ . Instrumental mass fractionation (IMF) was corrected for via sample-standard bracketing using terrestrial calcite ( $\delta^{18}\text{O} = 23.36 \text{‰}$  and  $\delta^{17}\text{O} = 12.15 \text{‰}$ ), terrestrial magnetite ( $\delta^{18}\text{O} = -6.05 \text{‰}$  and  $\delta^{17}\text{O} = -3.20 \text{‰}$ ), and terrestrial dolomite ( $\delta^{18}\text{O} = -21.61 \text{‰}$  and  $\delta^{17}\text{O} = 11.24 \text{‰}$ ) standards. Reported uncertainties reflect the propagation of both the internal analytical precision and the external reproducibility of the standards. Standard reproducibility ranged from 0.4–2.0 ‰ for  $\delta^{18}\text{O}$ , and 0.5–1.9 ‰ for  $\delta^{17}\text{O}$  ( $2\sigma$  standard deviation), and is the dominant source of error.

## 5.3 RESULTS

### 5.3.1 Thin section mineralogy and petrography

Both calcite and magnetite are present in seven of the eight thin sections studied. Only magnetite was found in MIL 090292,12, with no carbonates present. Dolomite was found in dark inclusions from two thin sections, Renazzo N1126 and EET 92159,20.

Although GRO 95577 (CR 2.0) is a breccia (Weisberg et al., 1993; Tyra et al., 2011), the section studied here consists of one heavily hydrated lithology that contains abundant small ( $< 200 \mu\text{m}$ ) chondrules, and a small  $\sim 2$  mm clast of a similar, but more Fe-rich and Ca-depleted lithology. The main hydrated lithology likely represents the dark inclusion lithology described by Weisberg and Huber (2007) and Tyra et al. (2011). Calcite grains are ubiquitous within the magnesium-rich phyllosilicate matrix, typically occurring as individual  $10\text{-}30 \mu\text{m}$  wide anhedral grains (Fig. 5.1a), and as submicron framboidal aggregates (Fig. 5.1b). Additionally, some calcite grains occur within chondrules as pseudomorphs of chondrule mesostasis, though most chondrule mesostasis has been altered to an Al-rich phyllosilicate (likely chlorite; Weisberg and Huber, 2007). Matrix calcite is commonly associated with Fe-sulfides, including pyrrhotite ( $\text{Fe}_{(1-x)}\text{S}$ ; Fig. 1a) and pentlandite ( $\text{Fe,Ni}_9\text{S}_8$ ). Magnetite in GRO 95577,69 occurs in the same lithology as the calcite, although they are rarely in contact. There are two main magnetite morphologies: small framboidal aggregates within the matrix and replacement products for round metal nodules in chondrules (Fig. 5.2). The matrix magnetite grains were too small (typically  $< 5 \mu\text{m}$ ) to be measured with SIMS, and were not included in this study. However, the chondrule magnetite grains averaged about  $100 \mu\text{m}$  in diameter, and are reported here. GRO 95577 has experienced moderate terrestrial weathering, which manifests as gypsum ( $\text{CaSO}_4 \cdot 2\text{H}_2\text{O}$ ; Bland et al., 2006) evaporite grains in the weathered fusion crust and in large cracks in the thin section.

The thin section MIL 090292,12 (CR 2.0) is highly brecciated, and is composed of at least three clasts of similar chondrule-bearing lithologies. Phyllosilicate pseudomorphs of chondrules and matrix are the dominant phase, with only a few relict pyroxene grains in the section. Magnetite is pervasive throughout the section replacing altered chondrule metal nodules.

Small relict nickel-metal grains (~88 wt% Ni, 12 wt% Fe) remain unoxidized within most chondrule magnetite grains. Magnetite is also abundant in the matrix, where the crystal morphology varies with each the lithologic clast. In two clasts, matrix magnetite is abundant as ~5  $\mu\text{m}$  euhedral to subhedral grains. The magnetite is less abundant in the other lithologies, and occurs as spherules and anhedral grains. No carbonates were found in MIL 090292,12. Calcium instead resides in secondary Ca-rich silicates and occasional phosphates. The thin section examined here has experienced substantial terrestrial weathering. Large cracks in the thin section are filled with epsomite ( $\text{MgSO}_4 \cdot 7\text{H}_2\text{O}$ ) evaporites, and gypsum veins litter the entire thin section, in cracks and along chondrule boundaries.

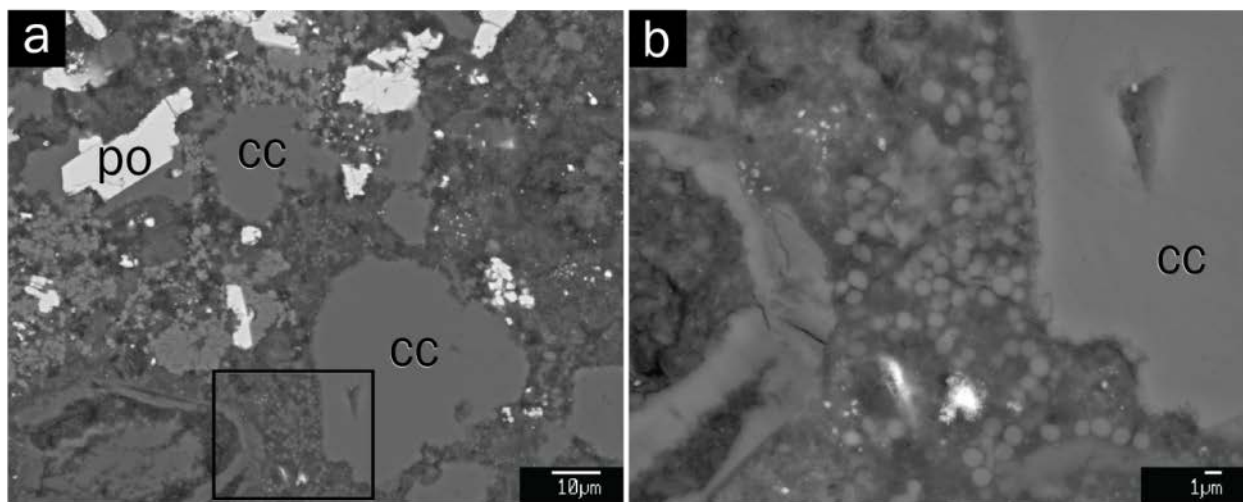


**Figure 5.1.** BSE images of calcite in the GRO 95577,69 matrix. (a) Calcite (cc) and associated pyrrhotite (po) in a phyllosilicate-rich hydrated matrix. (b) Close up of the inset square from image a, showing small framboidal calcite. cc = calcite, po = pyrrhotite.

Al Rais is an anomalous CR 2.3, in that it contains an unusually high matrix plus dark inclusion abundance (>70%) compared with other CR chondrites. The Al Rais USNM 6997 section in this study is relatively chondrule-rich. The matrix is composed of phyllosilicates, and chondrule mesostases are completely altered to phyllosilicate material. Most chondrule phenocrysts remain unaltered as olivine or pyroxene. Nearly all chondrule Fe,Ni metal has been oxidized to either magnetite or sulfides. Magnetite is abundant in the matrix, existing as rounded spherules (~10  $\mu\text{m}$ ) and as framboidal clusters. Magnetite framboids are frequently associated with calcite in assemblages where the calcite appears to cement the magnetite framboids. Calcite-rich material also occurs in mottled intergrowths within the phyllosilicate matrix, similar to carbonate morphologies seen in CM chondrites (Tyra et al., 2007). Al Rais is one of only two

CR falls and is minimally terrestrially weathered, having minor rust halos on a few remaining Fe,Ni metal grains.

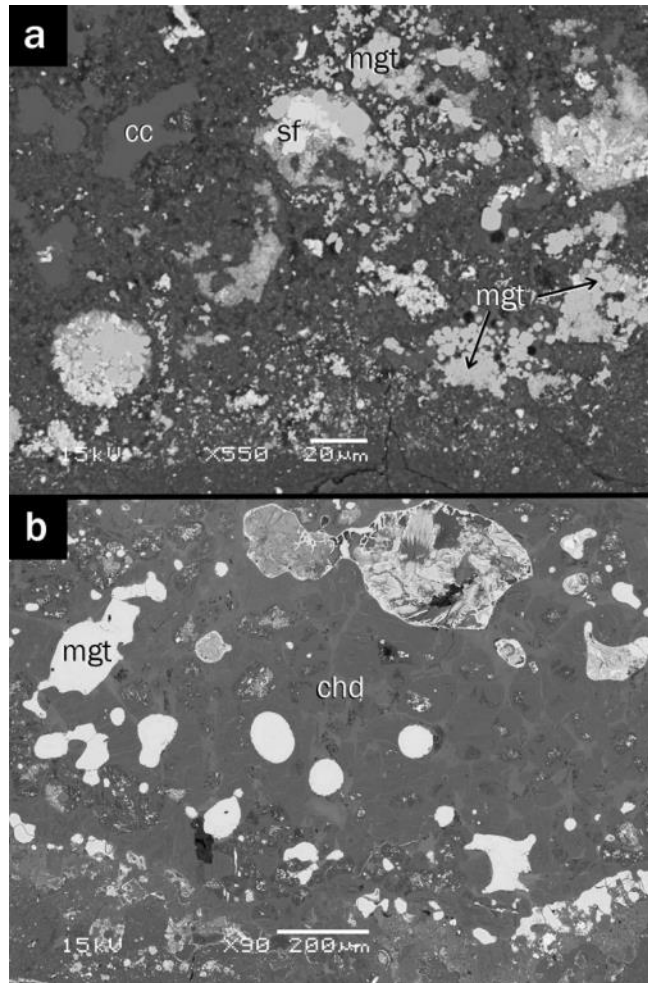


**Figure 5.2.** BSE images of magnetite in GRO 95577,69. (a) Spherule and framboidal magnetite set in the phyllosilicate matrix. (b) Magnetite pseudomorphically replacing metal grains in this completely altered type-I chondrule. cc = calcite, chd = chondrule pseudomorph, mgt = magnetite, sf = sulfide.

The Renazzo sections N1126 and N1127 are brecciated, and consist of a CR 2.4 lithology and at least two mm-sized clasts of a more altered lithology (dark inclusions). Numerous fine-grained aggregates containing submicron carbonates and silicates occur in the matrix and chondrule rims; however, the grain size is too small and not suitable for ion-probe study. Coarse-grained calcites are less abundant in Renazzo, and occasional calcite veins exist in the matrix. The calcite veins are thin ( $< 15 \mu\text{m}$ ) and extend up to  $100 \mu\text{m}$  in length (e.g., Fig. 5.3a). Some magnetite occurs as a replacement of altered metal nodules in chondrules and chondrule rims.

However, magnetite in Renazzo is more prevalent in the hydrated clasts, occurring as small framboids ( $< 10 \mu\text{m}$ ) embedded within fine-grained phyllosilicate material. The dark inclusions mainly consist of abundant magnetite, calcite, and sulfides. Dolomite only exists in one dark inclusion, as anhedral grains ranging from 5-50  $\mu\text{m}$  in width. Terrestrial weathering in Renazzo is very minor, with only a few instances of rusting of chondrule metal.

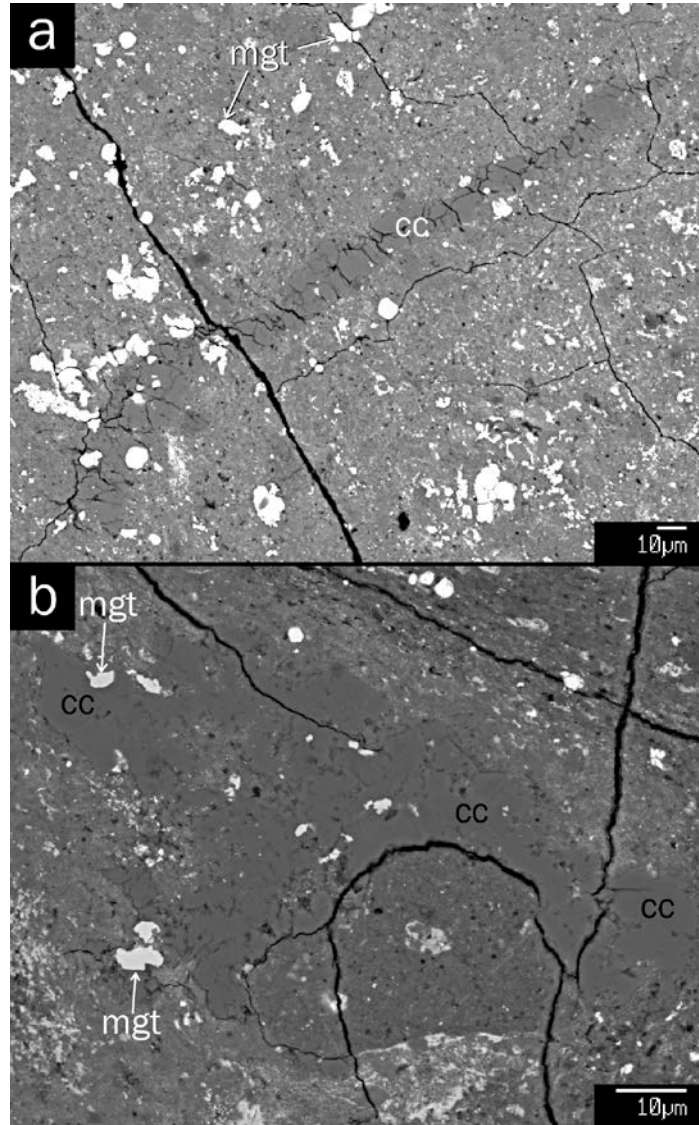


**Figure 5.3.** BSE image of a calcite and magnetite. (a) Magnetite grains and a calcite vein in the matrix of Renazzo N1127. The bright minerals in the matrix are magnetite grains. (b) Calcite and magnetite in the matrix of QUE 99177,06. Magnetite and calcite are associated phases, usually existing in the same lithologies. In this instance, the two minerals are in contact cc = calcite, mgt = magnetite.

The thin section of EET 92159,20 (CR 2.8) contains one chondrule-rich lithology, and one dark inclusion ~2 mm wide. The host lithology contains a small abundance of interchondrule matrix, composed of phyllosilicates and possibly some primary silicate material. The matrix is sulfide-rich, but magnetite and carbonates are rare. Some chondrule rims are decorated with magnetite spherules along their peripheries. In the dark inclusion, both calcite and magnetite occur in framboidal assemblages similar to those seen in Al Rais. Magnetite in the dark inclusion also exists as ~10  $\mu\text{m}$  spherules. One dolomite grain (~20  $\mu\text{m}$  in diameter) was found in the dark inclusion near a relict type-II chondrule. EET 92159 has been extensively weathered. Fe-hydroxides fill cracks in the thin sections and form large systems of veins surrounding clast and grain boundaries. Nearly all metal nodules display rust halos, with some rusted areas extending for nearly 100  $\mu\text{m}$ . The sample displays pervasive limonitic staining common to weathered Antarctic meteorites.

The chondrules in both sections of QUE 99177 (CR 2.8) display minimal evidence for aqueous alteration, retaining glassy mesostasis and Fe,Ni metal nodules. The matrix has been altered to a varying extent, with some regions containing more secondary minerals than other regions. Hydrated dark inclusions are present in both sections. The boundaries for these inclusions are not well defined, obscuring the distinction between dark inclusion and matrix. Parts of the fine-grained matrix and dark inclusions are composed of hydrated phyllosilicates, and contain embedded calcite and sulfides. Magnetite grains occur mostly in dark inclusions. Magnetite is also found on the peripheries of fine-grained chondrule rims, similar to those in EET 92159, and as observed by Abreu and Brearley (2010). The vast majority of these secondary mineral grains are ~10  $\mu\text{m}$  in diameter. Calcite and magnetite often occur in the same lithologies in QUE 99177, and in some instances in contact (Fig. 5.3b). The sections exhibit limonitic staining, Fe-hydroxide veining, and many chondrules contain rust halos around metal, particularly for chondrules located near the fusion crust and cracks. No sulfates or evaporites were observed in either thin section (Table 5.1).

### **5.3.2 Oxygen isotopes in calcite**

Oxygen isotopes were obtained for 51 calcite grain analyses among six thin sections (Table 5.2). While calcite is present in EET 92159,20, the grain sizes were too small for SIMS

**Table 5.2.** Secondary calcite oxygen isotope results from CR chondrites. All values reported in permil deviation from SMOW (‰). Measurements are shown in order of increasing  $\delta^{18}\text{O}$ .

Thin Section	$\delta^{18}\text{O}^*$	$\delta^{17}\text{O}^*$	$\Delta^{17}\text{O}^*$	Grain	Lithology
GRO 95577,69 (CR 2.0)	17.4 ± 0.9	7.8 ± 0.8	-1.3 ± 1.0	C22	Chondrule mesostasis
	18.3 ± 0.9	10.0 ± 1.1	0.5 ± 1.2	C10	Matrix
	18.3 ± 0.9	9.5 ± 0.9	0.0 ± 1.0	C05	Matrix
	18.8 ± 0.9	8.9 ± 0.8	-0.9 ± 0.9	C21	Chondrule mesostasis
	19.0 ± 0.9	10.4 ± 0.9	0.5 ± 1.0	C11	Matrix
	19.1 ± 0.8	9.3 ± 0.8	-0.6 ± 0.9	C01	Matrix
	19.1 ± 0.7	10.3 ± 0.9	0.4 ± 1.0	C20	Chondrule mesostasis
	19.1 ± 0.9	9.7 ± 1.0	-0.3 ± 1.1	C12	Matrix
	19.1 ± 1.0	9.0 ± 0.9	-0.9 ± 1.1	C13a	Matrix
	19.1 ± 0.9	9.8 ± 1.1	-0.1 ± 1.2	C13b	Matrix
	19.1 ± 0.9	10.0 ± 0.9	0.1 ± 1.0	C06	Matrix
	19.2 ± 0.9	10.2 ± 1.1	0.2 ± 1.2	C08	Matrix
	19.2 ± 1.0	9.2 ± 0.9	-0.8 ± 1.1	C14	Matrix
	19.3 ± 0.9	10.1 ± 0.8	0.1 ± 0.9	C16	Chondrule mesostasis
	19.3 ± 0.8	10.4 ± 1.0	0.4 ± 1.1	C18	Chondrule mesostasis
	19.4 ± 0.9	10.1 ± 0.9	0.0 ± 1.0	C09	Matrix
	19.5 ± 0.9	9.5 ± 0.9	-0.7 ± 1.0	C17	Chondrule mesostasis
	19.6 ± 0.9	10.2 ± 0.9	0.0 ± 1.0	C03	Matrix
	19.6 ± 0.9	10.5 ± 1.0	0.4 ± 1.1	C04	Matrix
	19.6 ± 1.0	10.2 ± 0.9	0.0 ± 1.0	C07	Matrix
	19.6 ± 0.9	10.2 ± 0.8	0.0 ± 0.9	C23	Matrix
	19.6 ± 0.9	10.3 ± 1.0	0.0 ± 1.1	C02	Matrix
	19.6 ± 1.0	10.9 ± 0.8	0.7 ± 1.0	C19	Chondrule mesostasis
20.1 ± 0.9	10.1 ± 0.8	-0.3 ± 0.9	C15	Chondrule mesostasis	
20.2 ± 0.8	9.6 ± 0.9	-0.9 ± 1.0	C24	Matrix	
Al Rais USNM 6997 (CR 2.3)	28.8 ± 0.5	15.2 ± 1.6	0.2 ± 1.6	C02	Matrix
	32.0 ± 0.5	17.0 ± 1.6	0.4 ± 1.6	C03b	Matrix
	32.3 ± 0.5	18.3 ± 1.6	1.5 ± 1.6	C03a	Matrix
	34.3 ± 0.4	19.4 ± 1.6	1.5 ± 1.6	C04	Matrix
	34.8 ± 0.6	18.4 ± 1.6	0.3 ± 1.7	C01	Matrix
Renazzo N1126 (CR 2.4)	16.2 ± 0.6	7.5 ± 1.6	-1.0 ± 1.7	C03b	Matrix
	17.8 ± 0.6	7.4 ± 1.7	-1.9 ± 1.7	C01a	Matrix
	19.3 ± 0.6	9.8 ± 1.6	-0.2 ± 1.7	C01b	Matrix
	19.4 ± 0.6	9.4 ± 1.7	-0.7 ± 1.7	C03a	Matrix
	20.7 ± 0.6	9.9 ± 1.7	-0.8 ± 1.7	C04b	DI
21.4 ± 0.6	9.9 ± 1.7	-1.3 ± 1.7	C04a	DI	
Renazzo N1127 (CR 2.4)	23.9 ± 0.7	12.7 ± 0.9	0.2 ± 1.0	C02	Matrix
	27.9 ± 1.3	14.9 ± 1.0	0.4 ± 1.2	C04a	Matrix
	28.4 ± 0.7	15.7 ± 0.9	0.9 ± 1.0	C04b	Matrix
	30.3 ± 1.1	17.0 ± 0.9	1.3 ± 1.1	C01	Matrix
QUE 99177,06 (CR 2.8)	8.5 ± 1.1	1.5 ± 1.7	-2.9 ± 1.7	C07	Matrix
	8.9 ± 1.1	1.6 ± 1.7	-3.1 ± 1.8	C06	Matrix
	14.7 ± 1.1	8.1 ± 1.7	0.4 ± 1.8	C02b	Matrix
	15.4 ± 1.1	8.6 ± 1.7	0.6 ± 1.8	C02c	Matrix
	18.6 ± 1.1	9.9 ± 1.7	0.3 ± 1.8	C01b	Matrix
	18.6 ± 1.1	10.2 ± 1.8	0.5 ± 1.9	C02a	Matrix
	18.8 ± 1.1	10.6 ± 1.7	0.9 ± 1.8	C01a	Matrix
20.6 ± 1.1	12.0 ± 1.7	1.3 ± 1.8	C08	DI	
QUE 99177,69 (CR 2.8)	16.1 ± 2.2	8.3 ± 1.1	-0.1 ± 1.6	C01c	DI
	17.8 ± 2.2	8.6 ± 1.1	-0.7 ± 1.6	C01b	DI
	25.2 ± 2.3	15.9 ± 1.2	2.8 ± 1.7	C04	Chondrule rim/Matrix

\*All reported uncertainties are  $2\sigma$ .

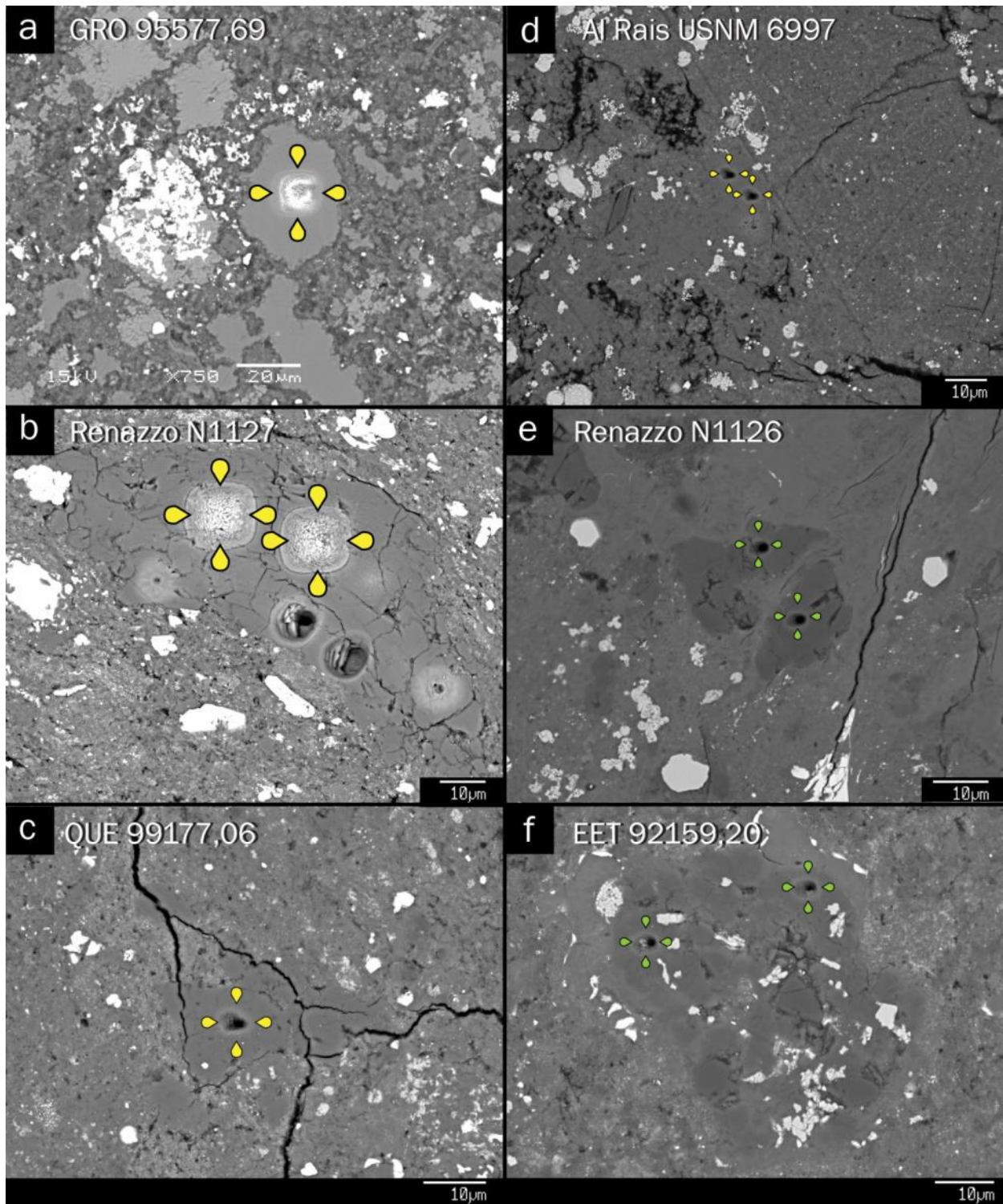


**Figure 5.4.** BSE images of characteristic ion probe pits in carbonates. Calcites indicated in yellow, dolomite in green. (a) Analysis C09 from GRO 95577,69. (b) Analyses C04a,b from Renazzo N1127. Other holes are from Mn and Cr measurements in a separate study. (c) Analysis C08 from QUE 99177,06. (d) Analyses C03a,b from Al Rais USNM 6997. (e) Analyses D01a,b from Renazzo N1126. (f) Analyses D01a,b from EET 92159,20.

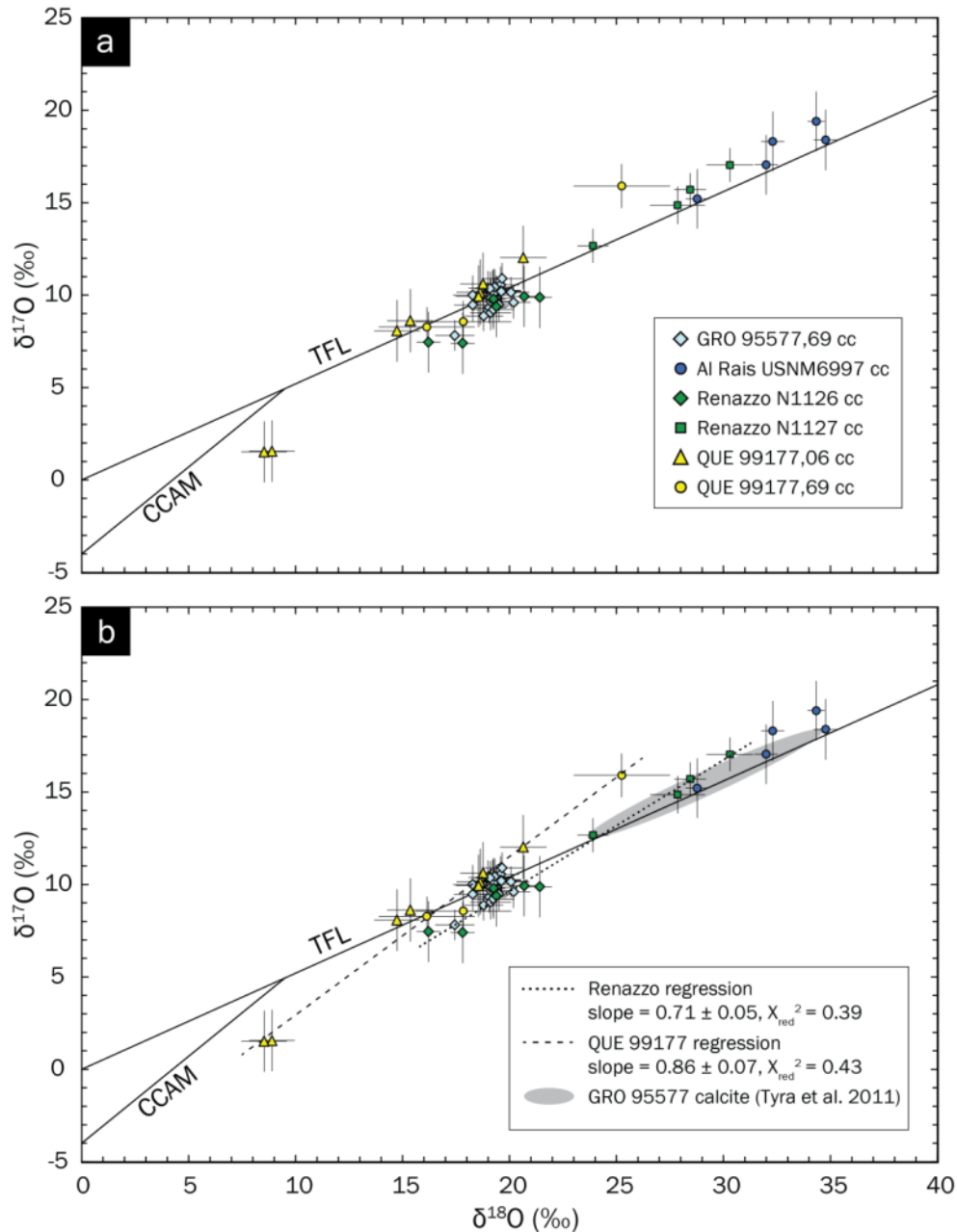


**Figure 5.5.** (a) Calcite oxygen isotopes from GRO 95577,69, Al Rais USNM 6997, Renazzo N1126, Renazzo N1127, QUE 99177,06, and QUE 99177,69. Plotted for reference are the terrestrial fractionation line (TFL) and the carbonaceous chondrite anhydrous mineral line (CCAM). The majority GRO 95577 calcites plot in a tightly clustered area of the graph, Al Rais calcites spread along a mass-dependent trend, and the Renazzo and QUE 99177 calcites plot along mass-independent arrays, crossing over the TFL. Uncertainties are  $2\sigma$ . (b) Weighted linear regressions for QUE 99177 and Renazzo mass independent trends, showing the correlation between  $\Delta^{17}\text{O}$  and  $\delta^{18}\text{O}$ .

analysis. No calcite is present in MIL 090292. All ion probe pits were imaged by SEM (characteristic ion probe pits for each meteorite are shown in Fig. 5.4). The calcite measurements are all fractionated toward positive values of  $\delta^{18}\text{O}$ , with a range in  $\delta^{18}\text{O}$  from 9 ‰ to 35 ‰ (Fig. 5.5a). Calcite from each meteorite defines a distinct trend. The GRO 95577 (CR 2.0) analyses are tightly clustered around  $\delta^{18}\text{O} \approx 19$  ‰, and  $\Delta^{17}\text{O} \approx 0$  ‰. In contrast, calcite in Al Rais (CR 2.3), Renazzo (CR 2.4) and QUE 99177 (2.8) plot on arrays of variable  $\delta^{18}\text{O}$ . The Al Rais calcites have the heaviest oxygen isotopic compositions of all minerals measured here, with  $\delta^{18}\text{O}$  ranging from 30 ‰ to 35 ‰. The average  $\Delta^{17}\text{O} = 0.8$  ‰ for Al Rais, and there is no resolved correlation between  $\delta^{18}\text{O}$  and  $\Delta^{17}\text{O}$ . For Renazzo N1126 and N1127,  $\delta^{18}\text{O}$  ranges from approximately 24 ‰ to 30 ‰. The  $\Delta^{17}\text{O}$  values correlate with  $\delta^{18}\text{O}$ , forming an array of slope  $\sim 0.71$  (Fig. 5.5b). This array has a low  $\chi_{\text{red}}^2$  of 0.39 due to conservative estimates of the uncertainties and high degree of correlation in the small dataset. The majority of the QUE 99177 calcite grains plot on a linear array ranging from  $\delta^{18}\text{O} = 14$  ‰ to 26 ‰. Two calcite grains from a single lithology have distinctly lower  $\delta^{18}\text{O}$  values of about 9 ‰. The values of  $\Delta^{17}\text{O}$  are variable and correlate with  $\delta^{18}\text{O}$ , forming an array of slope 0.86 ( $\chi_{\text{red}}^2 = 0.43$ ).

### 5.3.3 Oxygen isotopes in dolomite

**Table 5.3.** Secondary dolomite oxygen isotope results from CR chondrites. All values reported in permil deviation from SMOW (‰). Measurements are shown in order of increasing  $\delta^{18}\text{O}$ .

Thin Section	$\delta^{18}\text{O}^*$	$\delta^{17}\text{O}^*$	$\Delta^{17}\text{O}^*$	Grain	Lithology
Renazzo N1126 (CR 2.4)	24.2 ± 0.8	11.7 ± 1.1	-0.9 ± 1.1	D01a	DI
	23.5 ± 0.8	11.5 ± 1.1	-0.7 ± 1.1	D01b	DI
	23.3 ± 0.8	10.6 ± 1.1	-1.5 ± 1.2	D02b	DI
EET 92159,20 (CR 2.8)	26.8 ± 0.8	12.4 ± 1.1	-1.5 ± 1.2	D01a	DI
	25.7 ± 0.8	13.5 ± 1.0	0.2 ± 1.1	D01b	DI

\*All reported uncertainties are  $2\sigma$ .

Dolomite grains are rare in CR chondrites, and were only found in two chondrites, Renazzo N1126 and EET 92159. Five oxygen-isotope analyses were made in dolomite grains in the two thin sections (Table 5.3; Fig. 5.4d-e). Dolomite grains are clustered near the terrestrial fractionation line, with the data averaging  $\delta^{18}\text{O} = 23.7$  ‰ for Renazzo, and  $\delta^{18}\text{O} = 26.3$  ‰ for EET 92159 (Fig. 5.6). The average of the data for both meteorites plots below the terrestrial

fractionation line. There is no resolvable correlation between  $\Delta^{17}\text{O}$  and  $\delta^{18}\text{O}$  for dolomites in either thin section.

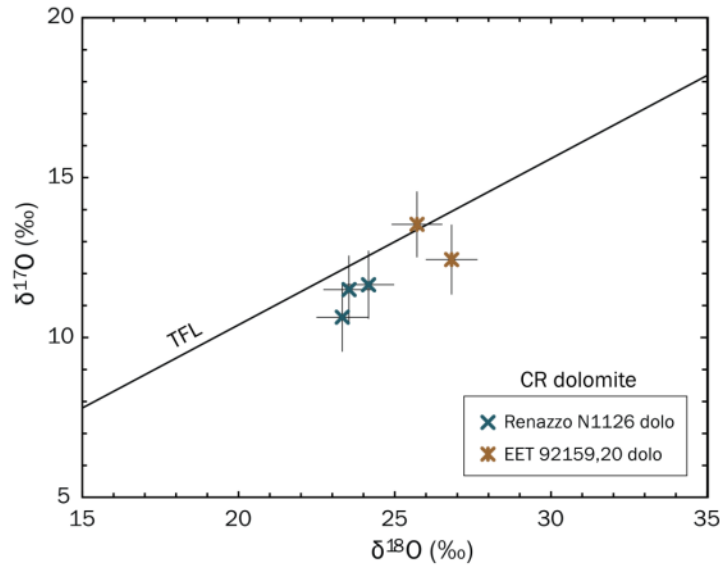


**Figure 5.6.** Dolomite oxygen isotopes from Renazzo N1126 and EET 92159,20. The terrestrial fractionation line is plotted for reference. Uncertainties are  $2\sigma$ .

### 5.3.4 Oxygen isotopes in magnetite

A total of 50 oxygen isotope analyses were taken from magnetite grains in the eight thin sections (Table 5.4). All ion probe pits were imaged by SEM, with characteristic images shown in Fig. 5.7. Most magnetite measurements were fractionated toward negative values on the oxygen three-isotope diagram, with the total  $\delta^{18}\text{O}$  ranging from -17 to 5 ‰ (Fig. 5.8). Each meteorite exhibits a distinct array, with some overlapping regions. The GRO 95577 magnetite array ranges from  $\delta^{18}\text{O} = -11$  to  $-17$ ‰, with a  $\Delta^{17}\text{O}$  value of  $\sim -0.5$  ‰. Matrix spherules from Al Rais are the isotopically heaviest magnetite grains, and the only grains with positive  $\delta^{18}\text{O}$  values (from 1 ‰ to 5 ‰). The average  $\Delta^{17}\text{O}$  is 1.3 ‰, slightly above the terrestrial fractionation line. Renazzo magnetites are variable, depending on the clast measured. The magnetite from Renazzo N1127 is represented by one grain from a dark inclusion ( $\delta^{18}\text{O} = -10.1$  ‰) and one altered metal nodule from a chondrule ( $\delta^{18}\text{O} = -12.3$  ‰). Both grains have  $\Delta^{17}\text{O} \sim 0$  ‰. Magnetite from a fine-grained layered chondrule rim in a distinct clast in Renazzo N1126 forms an array from  $\delta^{18}\text{O} = -2.5$  to  $-4$  ‰, and  $\Delta^{17}\text{O} \sim 0$  ‰. Five magnetite analyses from a dark inclusion in Renazzo N1126 fall slightly below the CR trend at  $\Delta^{17}\text{O} \approx -1.9$ ‰. In EET 92159,20, magnetite from the dark

**Table 5.4.** Secondary magnetite oxygen isotope results from CR chondrites. All values reported in permil deviation from SMOW (‰). Measurements are shown in order of increasing  $\delta^{18}\text{O}$ .

Thin Section	$\delta^{18}\text{O}^*$	$\delta^{17}\text{O}^*$	$\Delta^{17}\text{O}^*$	Grain	Lithology
GRO 95577,69 (CR 2.0)	-17.9 ± 1.6	-9.7 ± 1.3	-0.4 ± 1.6	M01b	Chondrule nodule
	-17.2 ± 1.6	-9.4 ± 1.4	-0.5 ± 1.6	M15	Chondrule nodule
	-14.0 ± 1.7	-8.7 ± 1.3	-1.4 ± 1.6	M01a	Chondrule nodule
	-13.3 ± 1.6	-7.1 ± 1.4	-0.3 ± 1.6	M04	Chondrule nodule
	-13.2 ± 1.6	-7.7 ± 1.3	-0.8 ± 1.5	M06a	Chondrule nodule
	-13.2 ± 1.6	-7.5 ± 1.2	-0.7 ± 1.5	M06b	Chondrule nodule
	-13.0 ± 1.7	-6.4 ± 1.4	0.4 ± 1.6	M02	Chondrule nodule
	-12.5 ± 1.6	-7.0 ± 1.3	-0.5 ± 1.5	M14	Chondrule nodule
	-12.3 ± 1.7	-6.8 ± 1.3	-0.4 ± 1.6	M11z	Chondrule nodule
	-11.2 ± 1.7	-6.5 ± 1.3	-0.6 ± 1.5	M11b	Chondrule nodule
MIL 090292,12 (CR 2.0)	-11.2 ± 1.6	-6.1 ± 1.2	-0.3 ± 1.5	M08	Chondrule nodule
	-8.2 ± 1.2	-7.6 ± 1.4	-3.3 ± 1.5	M03	Chondrule nodule
	-7.6 ± 1.2	-6.5 ± 1.4	-2.5 ± 1.6	M02b	Chondrule nodule
	-6.9 ± 1.2	-7.4 ± 1.4	-3.9 ± 1.5	M04	Chondrule nodule
	-6.4 ± 1.2	-7.7 ± 1.5	-4.4 ± 1.6	M01b	Chondrule nodule
	-4.2 ± 1.2	-5.2 ± 1.4	-3.0 ± 1.5	M02a	Chondrule nodule
	-3.8 ± 1.2	-6.1 ± 1.4	-4.1 ± 1.5	M01a	Chondrule nodule
Al Rais USNM 6997 (CR 2.3)	-3.7 ± 1.2	-5.3 ± 1.4	-3.4 ± 1.5	M05	Chondrule nodule
	1.1 ± 1.2	1.8 ± 1.4	1.2 ± 1.5	M04	Matrix
	3.2 ± 1.2	3.8 ± 1.4	2.1 ± 1.5	M03	Matrix
	3.2 ± 1.2	3.0 ± 1.4	1.3 ± 1.5	M01	Matrix
Renazzo N1126 (CR 2.4)	4.9 ± 1.2	3.2 ± 1.4	0.7 ± 1.5	M02	Matrix
	-7.2 ± 2.0	-6.0 ± 1.6	-2.2 ± 1.9	M03	DI
	-7.0 ± 2.0	-5.7 ± 1.6	-2.0 ± 1.9	M02	DI
	-6.1 ± 2.0	-6.0 ± 1.6	-2.9 ± 1.9	M01	DI
	-5.3 ± 2.0	-4.5 ± 1.6	-1.8 ± 1.9	M04b	DI
	-4.8 ± 2.0	-3.1 ± 1.6	-0.6 ± 1.9	M04a	DI
	-4.0 ± 2.0	-1.4 ± 1.6	0.7 ± 1.9	M06	Chondrule rim (in clast)
	-3.3 ± 2.0	-1.2 ± 1.6	0.5 ± 1.9	M08	Chondrule rim (in clast)
	-2.4 ± 2.0	-1.0 ± 1.6	0.3 ± 1.9	M05	Chondrule rim (in clast)
Renazzo N1127 (CR 2.4)	-2.3 ± 2.0	-1.0 ± 1.6	0.3 ± 1.9	M07	Chondrule rim (in clast)
	-12.3 ± 1.7	-7.2 ± 1.3	-0.9 ± 1.5	M01	Chondrule nodule
EET 92159,20 (CR 2.8)	-10.1 ± 1.7	-5.3 ± 1.4	-0.1 ± 1.6	M05	DI
	-2.9 ± 2.0	0.0 ± 1.6	1.5 ± 1.9	M03	Chondrule rim
	-2.3 ± 2.0	-0.6 ± 1.6	0.6 ± 1.9	M01	Chondrule rim
	-2.1 ± 2.0	0.0 ± 1.6	1.1 ± 1.9	M04	Chondrule rim
QUE 99177,06 (CR 2.8)	-1.6 ± 2.0	-0.5 ± 1.6	0.3 ± 1.9	M02	Chondrule rim
	-9.8 ± 2.1	-4.7 ± 2.0	0.4 ± 2.3	M04a	DI
	-9.4 ± 2.1	-5.0 ± 1.9	-0.1 ± 2.2	M03	DI
	-9.0 ± 2.1	-5.3 ± 1.9	-0.6 ± 2.2	M02b	DI
	-8.9 ± 2.1	-4.3 ± 2.0	0.4 ± 2.3	M04d	DI
	-8.1 ± 2.1	-4.3 ± 1.9	-0.1 ± 2.2	M01	DI
QUE 99177,69 (CR 2.8)	-6.3 ± 2.1	-3.5 ± 1.9	-0.2 ± 2.2	M04b	DI
	-5.4 ± 2.1	-2.3 ± 1.9	0.5 ± 2.2	M02a	DI
	-11.2 ± 2.1	-5.6 ± 1.9	0.2 ± 2.2	M03a	DI
	-10.5 ± 2.1	-4.0 ± 1.9	1.5 ± 2.2	M03b	DI
	-9.4 ± 2.1	-6.0 ± 1.9	-1.1 ± 2.2	M01	DI
QUE 99177,69 (CR 2.8)	-7.7 ± 2.1	-4.1 ± 1.9	-0.1 ± 2.2	M02a	DI
	-7.0 ± 2.1	-2.5 ± 1.9	1.1 ± 2.2	M02b	DI
	-6.8 ± 2.1	-3.0 ± 1.8	0.6 ± 2.1	M02c	DI

\*All reported uncertainties are  $2\sigma$ .

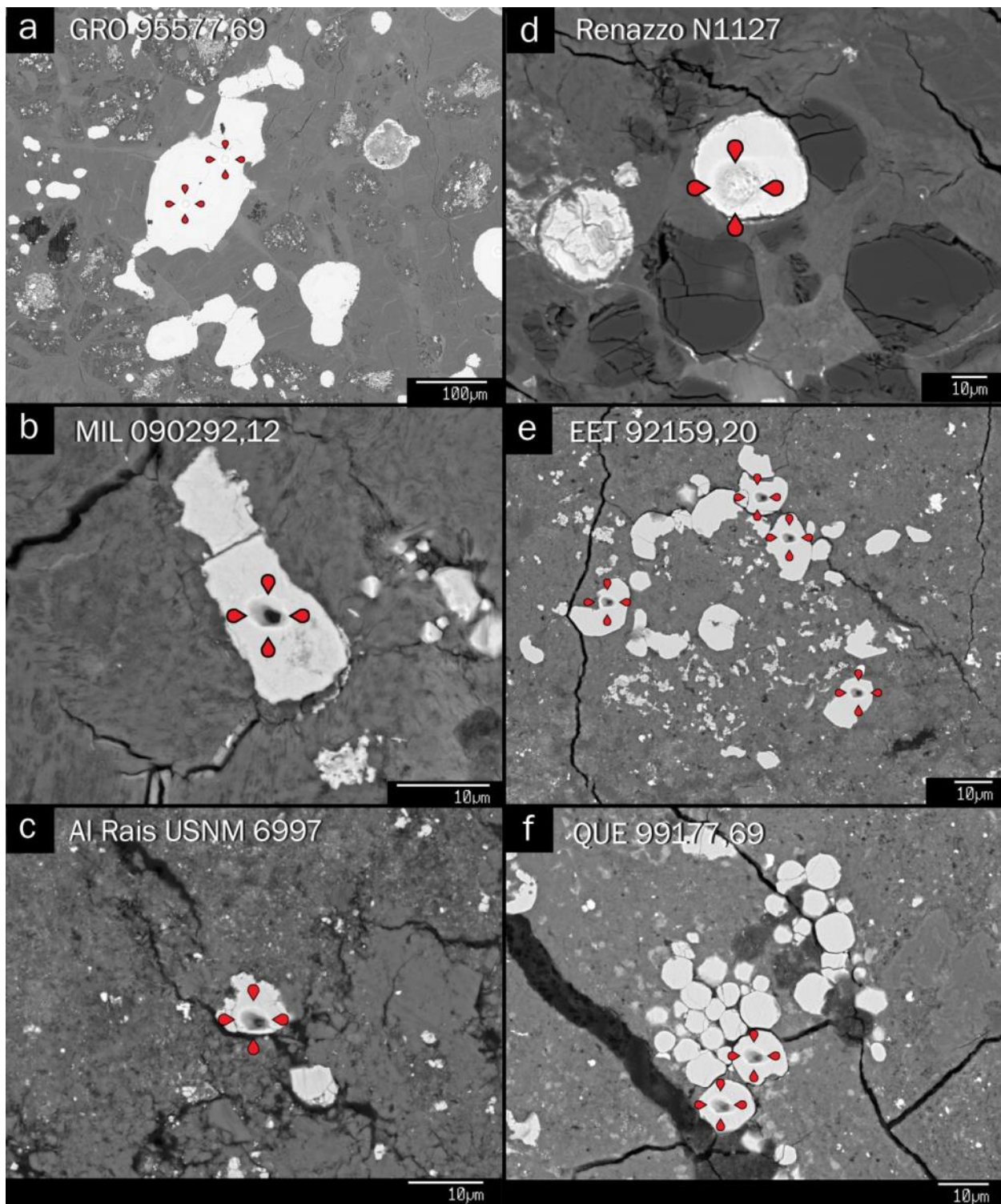


**Figure 5.7.** BSE images of characteristic ion probe pits in magnetite (red). (a) Analyses M06a,b from GRO 95577,69. (b) Analysis M05 in MIL 090292,12. (c) Analysis M04 from Al Rais USNM 6997. (d) Analysis M01 from Renazzo N1127. (e) Analyses M01, M02, M03, M04 from EET 92159,20. (f) Analyses M03a,b from QUE 99177,69.

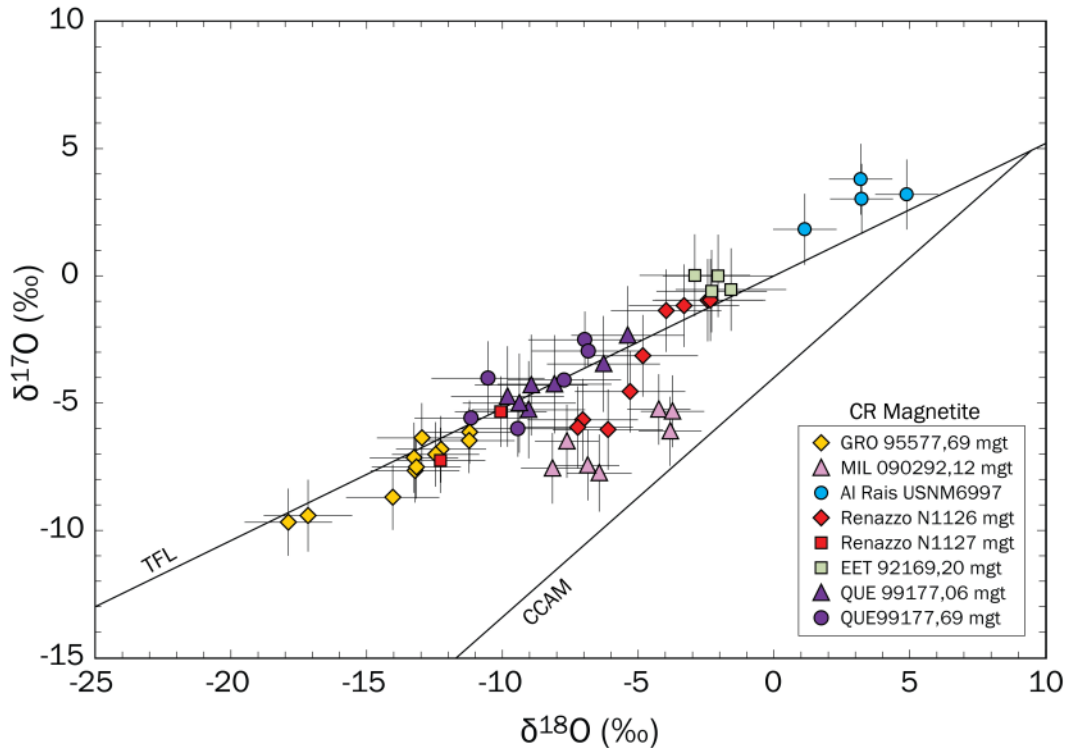


**Figure 5.8.** Magnetite oxygen isotopes from all eight thin sections in this study. Each meteorite forms a separate array with a spread of 3-6 ‰. While most magnetite grains plot on an array near the TFL, magnetite grains from MIL 090292,12 define a distinctly low  $\Delta^{17}\text{O}$  array. Uncertainties are  $2\sigma$ .

inclusion lithology was measured, as no large magnetite grains were found in the host matrix. Values cluster near  $\delta^{18}\text{O} \sim -6$  ‰ and  $\Delta^{17}\text{O} \sim 1$  ‰. In both sections of QUE 99177, the magnetite plots on a trend along the terrestrial fractionation line, ranging from  $\delta^{18}\text{O} = -5$  ‰ to  $-11$  ‰. Magnetite in MIL 090292,12 has a composition that falls off of the trend defined from the other CR chondrites. The  $\Delta^{17}\text{O}$  value is significantly lower at  $\sim -3$  ‰, falling below even the magnetite in the Renazzo N1126 dark inclusion. The  $\delta^{18}\text{O}$  values range from  $-3.7$  ‰ to  $-8.2$  ‰. For all meteorites, there is no resolvable correlation between  $\Delta^{17}\text{O}$  and  $\delta^{18}\text{O}$ .

## 5.4 DISCUSSION

The aqueous alteration of chondritic meteorites is a well-known but poorly understood process. The bulk oxygen isotopic compositions of CR chondrites are generally considered to reflect the mixing of an  $^{16}\text{O}$ -depleted  $\text{H}_2\text{O}$  reservoir with an  $^{16}\text{O}$ -enriched anhydrous reservoir

through progressive alteration. In this work, we aim to deconvolve the aqueous alteration signatures in the bulk oxygen isotope trend by measuring the compositions of secondary-minerals *in situ*. Calcite, dolomite, and magnetite were measured in CR chondrites of different petrologic type to examine alteration conditions, fluid evolution, and the compositions of oxygen reservoirs.

Oxygen isotopes of calcite, dolomite, and magnetite plot on trends near the terrestrial fractionation line, with the exception of MIL 090292, which we interpret as an anomalous specimen (see below). We find, surprisingly, that the average oxygen isotopic compositions of secondary minerals do not correlate with the petrologic type of the host specimen. Instead, the oxygen isotopic composition of individual mineral grains is shown to depend on the lithology being measured. This lithologic diversity of CR chondrites can account for inconsistencies in the bulk oxygen trend, as the bulk oxygen isotopes represent an amalgamation of different generations of alteration, scattered by impacts as lithic clasts, and in some cases overprinted by additional *in situ* alteration. Equilibrium oxygen isotope partitioning in calcite and magnetite indicates that alteration temperatures were low ( $< 60$  °C) and that the fluid composition evolved significantly on the CR parent body.

#### **5.4.1 Influence of terrestrial weathering**

Before discussing oxygen trends, we need to point out issues associated with the terrestrial weathering of meteorites. Terrestrial weathering is of great concern for studies of aqueous alteration, as many of the secondary products produced by weathering on Earth are similar to minerals that formed during parent body alteration (Bland et al., 2000, 2006; Tyra et al., 2007). Renazzo and Al Rais, both witnessed falls, are particularly important to this study as they have escaped the harsh weathering that is common for North African and Antarctic meteorites. Such falls provide a baseline for distinguishing parent body and terrestrial alteration products.

CR chondrites have terrestrial residence ages of less than a few hundred thousand years, as determined by cosmic ray dating (Nishiizumi et al., 1989; Bland et al., 2006). For the majority of their Antarctic residence, the meteorites remain trapped in glacial ice sheets, preserving the stone in its original state (Cassidy et al., 1992). However, once the meteorites were exhumed

from the ice by the Antarctic winds, freeze-thaw cycling subjected the meteorites to liquid water that causes terrestrial weathering. Antarctic glacial ice and melt-water has extremely negative values of  $\delta^{18}\text{O} \sim -35$  to  $-50$  ‰ (Gooding, 1986; Aharon, 1988; Faure et al., 1988), suggesting that even small contamination could lead to changes in the measured oxygen isotopes. Yet surprisingly, a significant amount of Antarctic weathering ( $>25\%$  oxidation of iron) is required before any significant isotopic effect is observed in the bulk oxygen isotopic compositions (Bland et al., 2000, 2006). A similar finding has been established for hydrogen, carbon, and nitrogen compositions of CM and CR meteorites, where falls and weathered finds show similar ranges with no correlation between weathering grade and bulk composition (Alexander et al., 2012, 2013).

Iron oxidation products are the most obvious signs of terrestrial weathering for CR chondrites. Most Antarctic CR chondrites contain networks of iron-oxyhydroxide veins that fill in cracks, fractures, and follow grain boundaries in chondrules (Abreu and Brearley, 2010). TEM studies of weathering vein cross-sections have shown that although weathering can be significant, it remains restricted to the alteration veins with minimal effects on the surrounding material (Abreu and Brearley, 2010). Some metal grains in Renazzo and Al Rais exhibit minor rust halos, but the sections are otherwise free of iron oxide veins. Most metal grains display pre-terrestrial oxide rims composed of magnetite, rather than the common weathering products ferrihydrite or goethite (Bland et al., 2006). Magnetite has been noted as being extremely uncommon alteration product in Antarctic samples (Bland et al., 1998; 2006) supporting a pre-terrestrial origin for the magnetite measured here.

Carbonates have been noted as a common product of terrestrial weathering, usually occurring as hydrous magnesium carbonates (Velbel et al., 1991; Bland et al., 2006) and possibly calcium carbonates (Abreu and Brearley, 2005). Carbonates formed from Antarctic waters have  $\delta^{18}\text{O}$  values ranging from  $-47$  ‰ to  $4.5$  ‰ (Hays and Grossman, 1991; Rao et al., 1998). Low  $\delta^{18}\text{O}$  values in carbonates reflect the formation from glacial melt water with highly negative  $\delta^{18}\text{O}$  at low temperatures (Hanshaw and Hallet, 1978; Faure et al., 1988; Hays and Grossman, 1991; Zheng, 2011). The calcite and dolomite measured in GRO 95577, EET 92159, and QUE 99177 do not exhibit a large depletion of  $^{18}\text{O}$  and have compositions outside of the range of what would be expected for Antarctic precipitates (e.g., Gooding et al., 1986; Hays and Grossman, 1991; Tyra et al., 2011; Zheng, 2011). A lack of highly negative carbonates may not necessarily stand

as proof against weathering; some Antarctic CM chondrites contain carbonates that have exchanged oxygen isotopes, thus forming a unique array that intersects the trend for carbonate in CM falls and the terrestrial fractionation line (Tyra et al., 2007). No similar trend exists for the Antarctic CR carbonates in this study. The magnetite and carbonate oxygen isotopes plot on the same general trend as Al Rais, and in arrays that overlap the Renazzo secondary mineral compositions.

Instances of terrestrial calcite have been reported in some meteorite falls, suggesting that carbonate formation can occur even within months of exposure (Abreu and Brearley, 2005). Such terrestrial calcites may manifest as long veins extending up to hundreds of microns. However, some key characteristics of the Renazzo veins set them apart from terrestrially formed veins. First, the oxygen isotopic compositions of some Renazzo calcite veins do not lie on the terrestrial fractionation line, indicating formation from an oxygen reservoir that was clearly not terrestrial. Renazzo veins do not cross cut the meteorite components; they are only found in hydrated matrix. The calcite veins in Renazzo are compositionally homogeneous, and do not show elemental zoning or co-precipitation with terrestrial iron oxides, as seen in terrestrial carbonate veins (Abreu and Brearley, 2005). Finally, the Renazzo calcite veins do not fill in cracks in the meteorite, nor are carbonates found in the pore space of the fusion crust or on the exterior of the meteorite.

While these petrographic observations provide ample evidence for pre-terrestrial alteration, perhaps the most convincing evidence lies in radiometric dating.  $^{53}\text{Mn}$ - $^{53}\text{Cr}$  dating of carbonate grains in Renazzo and GRO 95577 indicates that  $^{53}\text{Mn}$  ( $t_{1/2} = 3.7$  Myr) was still present at the time of calcite formation. The resolvable manganese-chromium isochrons are evidence that the carbonates formed between ~2–14 Myr after the formation of the Solar System, at  $> 4.55$  Ga (c.f. Chapter 3). The Renazzo and GRO 95577 carbonates measured in the manganese-chromium study were the same grains measured here for oxygen isotopes.

#### **5.4.2 Distinct properties of MIL 090292**

Many properties of MIL 090292 suggest that this sample is anomalous, or possibly unrelated to the CR chondrite group. MIL 090292 has been classified as a CR 2.0 based upon its high abundance of secondary minerals, including phyllosilicates, magnetite, and sulfides

(Satterwhite and Righter, 2012; Harju et al., 2014). Magnetite-bearing chondrule pseudomorphs indicate that the precursor chondrules were metal-rich, similar to the chondrules in CR chondrites. However, an important mineralogical difference is that the chondrule magnetite in MIL 090292 contains abundant small 1-6  $\mu\text{m}$  grains of metallic Ni-rich metal (~ 88 wt.% Ni, 12 wt.% Fe). This Ni-rich metallic phase is not seen in other CR chondrites, suggesting that the alteration conditions or oxygen fugacity for MIL 090292 were unique. Similarly, the MIL 090292,12 section does not contain calcium-carbonates, a very common phase in all other CR chondrites. Rather, calcium resides in secondary calcium-rich silicates and phosphates (c.f. Chapter 2). The lack of carbonate phases may be indicative of different alteration conditions such as lower pH, higher silicon activity, or higher temperatures (e.g., Krot et al., 1998; 2000; Jilly and Huss, 2012)

Oxygen isotopes from MIL 090292 consistently diverge from established CR trends (e.g., Harju et al., 2014; Schrader et al., 2014). Magnetite oxygen isotopes reported here (with  $\Delta^{17}\text{O} \sim -3.5 \text{‰}$ ) plot outside of the array defined by all other CR chondrite magnetite. This low  $\Delta^{17}\text{O}$  value is similar to magnetite in some CV and CK chondrites (Choi et al., 1997; Choi and Wasson, 2003; Hsu et al., 2006; Davidson et al., 2014). The whole-rock oxygen isotopic composition of MIL 090292 measured by Harju et al. (2014) fell off of the slope-0.7 CR mixing line, near the CCAM. Similar whole-rock and matrix-separate analyses from Schrader et al., (2014) show that MIL 090292 plots distinctly lower on the bulk CR trend than would be expected for an extensively altered CR. These observations suggest an anomalous origin for MIL 090292; either the specimen comes from a distinct parent body, or alteration occurred under unique fluid conditions. It would be interesting to compare the oxidation buffers for iron, nickel, and sulfur phases in MIL 090292 to other CR chondrites to investigate such differences in oxygen fugacity, and what that means for the origin of MIL 090292.

### **5.4.3 Carbonate oxygen isotopes: A proxy for fluid evolution on the CR parent body**

In any water-rock reaction, there are four main influences on the isotopic composition: the temperature, the water/rock (W/R) ratio, the original composition of the fluid, and the original composition of the rock (Taylor, 1977; Agrinier and Cannat, 1997). For terrestrial minerals, all of these influences result in oxygen fractionation along the terrestrial fractionation

line, which has a slope of 0.52 on the oxygen three-isotope diagram. Oxygen isotopic fractionation in extra-terrestrial materials is more complicated, as the interaction between materials from distinct oxygen reservoirs can lead to arrays that do not follow a slope-0.52 trend. Mass-dependent fractionation trends in secondary minerals can be attributed to variation in temperature or variation in fluid composition during equilibrium fractionation (e.g., Clayton and Mayeda, 1984; Young et al., 1999). Mass-independent trends (i.e., variable  $\Delta^{17}\text{O}$ ) arise from processes that do not depend on mass, such as oxygen isotope exchange between, or mixing of two different oxygen reservoirs. The slope of a data array on the oxygen three-isotope diagram can therefore reveal information about fluid chemistry and conditions of aqueous alteration (e.g., Clayton and Mayeda 1984; 1999; Benedix et al., 2003; Schrader et al., 2011).

The calcite oxygen-isotope arrays differ for each meteorite in this study (Fig. 5.5). All GRO 95577,69 calcite grains were taken from the hydrated lithology, where 21 analyses were of matrix grains and 11 analyses were from pseudomorphed chondrule mesostasis. All calcite grains in GRO 95577,69 have the same compositions (within error), suggesting that they were formed under uniform physico-chemical conditions (e.g., Schrader et al., 2011). These oxygen isotopes are dissimilar to calcite measured in other sections of GRO 95577 (Tyra et al., 2011), which spanned an array near the TFL from  $\delta^{18}\text{O} \sim 25\text{--}35\text{‰}$  (see Fig. 5.5). The calcite measurements in Tyra et al. (2011) were taken from three lithologies across two thin sections. Their data showed that the oxygen isotopic composition of carbonates varied between the different lithologies. The different GRO 95577 results from these two studies likely reflect the heterogeneity of lithologic components in this meteorite. The clustered oxygen isotopic compositions of calcite in GRO 95577,69 suggest that fluids were locally uniform during carbonate precipitation in the region surrounding GRO 95577,69. On a larger spatial and/or temporal scale, the oxygen isotopes were fractionated mass-dependently ( $\Delta^{17}\text{O} \sim 0\text{‰}$ ) where each lithology was altered under different fluid conditions on the parent body and was subsequently transported via impact processes. This is in clear contrast to calcite from Al Rais, Renazzo, and QUE 99177, which all showed evidence for evolving fluid conditions in a single lithology.

Al Rais calcite grains measured here were all located in the fine-grained matrix of a single lithology. They plot along a mass-dependent trend with no resolvable variation in  $\Delta^{17}\text{O}$ , and no evidence for isotopic exchange between the primary minerals. This may indicate that

isotopic exchange was minimal within the locality sampled in the thin section, or that isotopic exchange was complete. Al Rais calcite grains do, however, plot above the terrestrial fractionation line and have the most positive average  $\Delta^{17}\text{O}$ . In a model where the fluid has a higher  $\Delta^{17}\text{O}$ , this might indicate a low degree of exchange with the solids prior to carbonate precipitation. The variation in  $\delta^{18}\text{O}$  is interpreted as changing temperature during progressive alteration or variable fluid composition due to equilibrium fractionation during the precipitation of calcite. In the case of variable composition, the fluid would evolve towards  $^{16}\text{O}$ -enriched values as carbonates precipitate from fluid.

Calcite in Renazzo was measured from two distinct lithologies: eight analyses within the fine-grained interchondrule matrix, and two analyses from a dark inclusion. The data form a single array with a slope of  $\sim 0.7$  (Fig. 5.5b), indicating that both lithologies were altered by a single evolving fluid on the CR parent body. Endreß et al. (1994) suggested that the dark inclusions may have originated from an exogenous source outside of the CR parent body. Our oxygen isotopes indicate that the dark inclusions come from a nearby region on the CR parent body, transported by impacts, rather than being foreign clasts from an exogenous source (e.g., Weisberg et al., 1993). The varying  $\Delta^{17}\text{O}$  likely reflects the isotopic exchange between heavy water and a lighter solid material during progressive alteration, while some variation in  $\delta^{18}\text{O}$  is probably due to changes in temperature. The dolomite oxygen isotopes from a dark inclusion in Renazzo N1126 plot within the calcite array. However, in contrast to the calcite array, the dolomite grains show no indication of chemical or temperature evolution during formation. However, the dolomite data represent a statistically small sample set due to the rarity of dolomite (c.f., Chapter 2).

The widest calcite array belongs to QUE 99177, plotting along a trend with slope  $\sim 0.9$ . Calcite grains were analyzed from multiple lithologies, including the host inter-chondrule matrix and from dark inclusions. Similar to Renazzo, the variation in both  $\delta^{18}\text{O}$  and  $\Delta^{17}\text{O}$  reflects progressive fluid evolution during aqueous alteration, possibly coupled with mass-dependent fractionation processes.

#### **5.4.4 Magnetite oxygen isotopes: Orientation effects in SIMS or fluid evolution?**

The magnetite oxygen isotopes from CR chondrites do not exhibit the same fractionation trends as the carbonates, and they display distinctly low  $\delta^{18}\text{O}$  values compared with other chondrite groups (UOC, CV, CI, CM, CK; Rowe et al., 1994; Choi et al., 1998; 2001; Davidson et al., 2014). Magnetite analyses from each meteorite plot along mass-dependent arrays, with no resolvable mass-independent trend (Fig. 5.8). The lack of variation in  $\Delta^{17}\text{O}$  indicates that the magnetite grains did not track oxygen isotopic exchange in a single meteorite. The fluid composition may vary along the mass-dependent trend if carbonates or other oxygen-bearing minerals contemporaneously formed from the altering fluid, or if temperature was changing. The magnetite oxygen isotope arrays in Al Rais, Renazzo, EET 92159, and QUE 99177 can be explained in this manner, where the magnetite measurements represent frambooids or spherules that had precipitated from an aqueous fluid. In Renazzo, the spread in  $\delta^{18}\text{O}$  is  $\sim 10$  ‰, larger than seen in other samples. This is explained by the range in lithologies sampled for Renazzo: dark inclusions, chondrule interiors, and chondrule rims (see section 5.4.5 below).

The oxygen isotopic compositions of magnetite from replaced metal nodules in GRO 95577,69 are particularly interesting; they show a  $\sim 6$  ‰ mass-dependent spread that contrasts with the tightly clustered calcite oxygen isotopes. This spread likely indicates changes in fluid temperature or composition during magnetite formation. The petrographic context of the magnetite (replacing metal nodules) and calcite (replacing mesostasis) in GRO 95577 chondrule interiors suggests that they were formed contemporaneously. However, a layered structure in the altered nodules that is not observed in the calcite may indicate that the magnetite formed at a slower rate, explaining why the calcite grains do not show this same oxygen isotopic trend.

Possible crystal orientation effects in oxygen-isotope measurements of magnetite may complicate interpretations. The isotope spread of  $\sim 3$  to  $6$  ‰ along the slope-0.52 trend seen in magnetite from GRO 95577, Al Rais, EET 92159, and QUE 99177 may be an artifact from crystal-orientation effects for magnetite during SIMS analysis (Lyon et al., 1998; Huberty et al., 2010; Kita et al., 2011). Single-crystal SIMS analyses of magnetite have been shown to vary in  $\delta^{18}\text{O}$  between  $3$  to  $6$  ‰, depending on the orientation of the crystal lattice at the time of measurement. One possible explanation of this phenomenon is that the secondary ions may be preferentially selected for the light isotope if the crystal planes are near perpendicular to the incident angle of the primary ion beam (Huberty et al., 2010). The magnetite grains measured in

our meteorites are all randomly oriented, with some grains being spherules and framboids, and others being layered aggregate pseudomorphs of primary metal nodules.

For randomly oriented magnetite grains, we would expect to see a spread in the data reflecting the various orientations. We analyzed magnetite grains in MIL 090292,12 and Renazzo N1126 using electron backscatter diffraction (EBSD) on a JEOL 5900 LV SEM. Thin sections were polished with 0.3 and 0.05  $\mu\text{m}$  alumina powder and 200 proof ethanol to avoid  $\text{H}_2\text{O}$  exposure. Sections were analyzed at 25 keV, 70° tilt, and 16mm working distance. EBSD analyses showed no Kikuchi bands for magnetite grains in Renazzo N1126 or MIL 090292, although bands for silicates were visible. The absence of visible magnetite Kikuchi bands is likely a result of low spatial resolution. The spatial resolution of EBSD analysis is related to the resolution of the SEM and the working distance (Maitland and Sitzman, 2007), on the order of  $\sim 5 \mu\text{m}$  for our instrumental setup. The pseudomorphed nodules are indicative of sub-micron intergrown crystal aggregates, much smaller than the resolution for EBSD. Furthermore, these measurements suggest that the spherule morphologies may also be colloform masses of small magnetite crystallites, rather than being a single individually-oriented crystal. The absence of bands can reflect inadequate polishing or too large a working distance, but these explanations are difficult to reconcile since Kikuchi bands were detected from silicate minerals in the samples and in a silicon wafer standard.

Questions remain regarding whether or not the SIMS crystal orientation effect would occur for a series of aggregate crystals (such as the ones measured here). However, according to probability theory and the central limit theorem, we would not expect to see the same 3 to 6 ‰ spread as in the case of a randomly oriented single crystal. For an aggregate grain containing thousands of randomly oriented sub-micron crystals, a single SIMS measurement represents the convolution of those thousands of crystal orientation effects. Multiple measurements of the aggregate would produce a normal distribution around the expectation value of the measurement. Therefore, it seems likely that the variations in oxygen isotopes are not due to crystal orientation effects. A preliminary study has found that oxygen isotopic variation in magnetite during SIMS may instead represent defects or fractures in the crystal structure, rather than orientation (Caplan et al., 2015). In this case, it remains unclear whether the spreads in oxygen isotopic compositions reflect true mass-dependent fractionation trends or artifacts during SIMS measurement

#### 5.4.5 Models of asteroidal fluid evolution

Interpretations of the progressive alteration trends in oxygen isotopes are highly model-dependent. Progressive alteration can either shift the oxygen isotopic composition of carbonates toward lighter or heavier values, depending on the model. The two prevalent schools of thought for asteroidal fluid evolution rely upon the assumption of either open-system or closed-system fluid-rock interaction. Both models can produce the oxygen isotopic compositions observed in carbonaceous chondrites, but with different implications for the alteration process.

Open-system models describe large-scale fluid flow driven by pressure or temperature gradients in the asteroidal parent body (Young et al., 1999; Cohen and Coker, 2000; Young, 2001). Earlier thermal models predicted that icy planetesimals would have broken up due to vapor overpressure once the ice began to melt (e.g., Grimm and McSween, 1989; Wilson et al., 1999; Young, 2001). Fluid flow has been invoked to reconcile the existence of aqueously altered chondrites with these thermal models and oxygen isotopic studies. The altering liquid flows over 10's of km on the parent body, releasing water at the surface in the form of vapor, and therefore relieving built up pressure. This vapor release and fluid flow over large distances transports water out of a local alteration system.

The open-system models of asteroidal alteration (Young et al., 1999; Young, 2001) describe the oxygen isotopic exchange between a heavy water reservoir (assumed to have  $\Delta^{17}\text{O} \sim 16 \text{‰}$ ) and a lighter solid (represented by bulk rock compositions of  $\Delta^{17}\text{O} \sim -3 \text{‰}$ ). The asteroidal fluid-flow models propose a region of intense alteration on the parent body, between the center of the asteroid and the frozen outer crust. In this region, the oxygen compositions of alteration products evolve towards heavier  $\delta^{17}\text{O}$ ,  $\delta^{18}\text{O}$ , and  $\Delta^{17}\text{O}$  as the alteration process proceeds. The altering fluid decreases in  $\Delta^{17}\text{O}$  with progressive alteration, but the effects of fluid evolution on the solid compositions are mitigated due to the evaporation of the evolved water and the influx of heavier water from an interior source. Oxygen isotopic exchange between the light rock and the heavy water would have led to an increase in  $\delta^{17}\text{O}$ ,  $\delta^{18}\text{O}$ , and  $\Delta^{17}\text{O}$  in the solids as the lighter evolved water escaped the system (Young et al., 1999; Young, 2001).

The closed-system model also documents the interaction between an isotopically heavy fluid with a lighter anhydrous rock (e.g., Clayton and Mayeda, 1984; 1999; Leshin et al., 1997; Benedix et al., 2003; Bland et al., 2009). One main difference between the models is that fluid

flow is confined to small scales (~ a few 100  $\mu\text{m}$ ) in a closed-system, and water is not lost from the alteration environment during the timescales considered here; rather, it is either fully consumed during alteration, or lost at a later stage as vapor when liquid later was no longer stable. During progressive alteration, the anhydrous rock reacts with water to form secondary minerals, with the dominant alteration products being phyllosilicates and carbonates (e.g., Weisberg et al., 1993; Brearley, 2006). In the process, the  $\Delta^{17}\text{O}$  of the water decreases as the fluid exchanges oxygen with the solids. The phyllosilicates are formed by the replacement and hydration of primary silicates, incorporating oxygen isotopes from both the water and the primary silicates into the final phyllosilicate composition. This process helps to modify the  $\Delta^{17}\text{O}$  oxygen composition of the fluid, as well as fractionating  $\delta^{18}\text{O}$  toward higher values (Clayton and Mayeda, 1984; Zheng, 1993). Carbonates and magnetite are precipitated from fluid, with the majority of the oxygen atoms inherited from the aqueous fluid. The carbonate and magnetite compositions are therefore fractionated along a mass-dependent fractionation line relative to the water. Carbonate minerals are fractionated towards higher  $\delta^{18}\text{O}$  relative to the fluid composition, while magnetite is fractionated towards lower  $\delta^{18}\text{O}$  (Zheng, 1991; 1999; 2001). However, depending on the formation mechanism of the carbonate minerals, some oxygen may be inherited from dissolved  $\text{CO}_2$  or from organics in the matrices. Since no fluid leaves the system, the combined effect causes water to become progressively lighter as more secondary phases are formed. Through a combination of reaction and exchange, the  $\delta^{17}\text{O}$ ,  $\delta^{18}\text{O}$ , and  $\Delta^{17}\text{O}$  of the aqueously formed minerals all decrease during fluid evolution on the parent body (Clayton and Mayeda, 1984; 1999; Leshin et al., 1997; Benedix et al., 2003; Bland et al., 2009).

Petrographic and compositional observations favor the closed-system model over the open-system model for alteration of CR chondrites. A number of problems exist when considering the open-system model of alteration. Large-scale fluid flow will mobilize and fractionate elements over large distances (Bland et al., 2009). However, mineralogical maps show that element mobility in CR chondrites is limited to short distances (~ 100  $\mu\text{m}$ ) before redeposition (e.g., elements leached from chondrule components and re-precipitated in the surrounding matrix). The CR chondrites show no evidence for an interconnected network of fractures that would allow for such vigorous fluid flow such as that described in the open-system models. Veining is rare in CR chondrites, and the few carbonate veins in Renazzo do not extend for regions greater than ~200  $\mu\text{m}$  in apparent length. The bulk elemental compositions of CR

chondrites indicate that most CRs are chemically similar (Kallemeyn et al., 1994), with little indication that elements or species were fractionated between meteorite samples. Further evidence for isochemical alteration in CR chondrites lies in the nearly identical elemental compositions of the hydrated matrix from Renazzo compared with the primitive matrices of QUE 99177 and MET 00426 (cf. Fig. 2.7 in Chapter 2; Zolensky et al., 1993). The oxygen isotopic compositions for minerals in the most heavily altered GRO 95577 can also clarify the direction of fluid evolution. The GRO 95577 magnetite and calcite compositions fall near the  $^{16}\text{O}$ -enriched ends of the oxygen isotope trends, indicating that the water was the lightest at the end of fluid evolution.

Lastly, the open-system models neglect to account for the observed sub-micron grain size of the matrix material. The open-system models assume that the fine-grained matrix is analogous in permeability and porosity to Lunar soils (Grimm and McSween, 1989; Young et al., 1999; Cohen and Coker, 2000; Young, 2001). Bland et al. (2009) revised estimates for grain- and pore-size distributions in primitive chondrite matrices to be substantially lower, with the effect of decreasing the modeled permeability of the rock and restricting the flow of water on the parent body. Under these revised conditions, thermal models more closely reflect the chemical observations of chondrite samples, and suggest that alteration occurred in a closed-system with small length-scales of liquid water transport (Clayton and Mayeda, 1984; 1999; Benedix et al., 2003; Bland et al., 2009). In reality, both open- and closed-system processes may have occurred to different extents on the CR parent body. However, the evidence presented here dominantly supports a closed system, which we will consider to be the main environment for simplicity. In the context of the closed system model, the magnetite and carbonate arrays presented here would reflect the precipitation of progressively lighter ( $^{16}\text{O}$ -enriched) minerals from an isotopically evolving fluid.

### 5.4.6 Lithologies and mineral contributions to the CR whole-rock mixing line

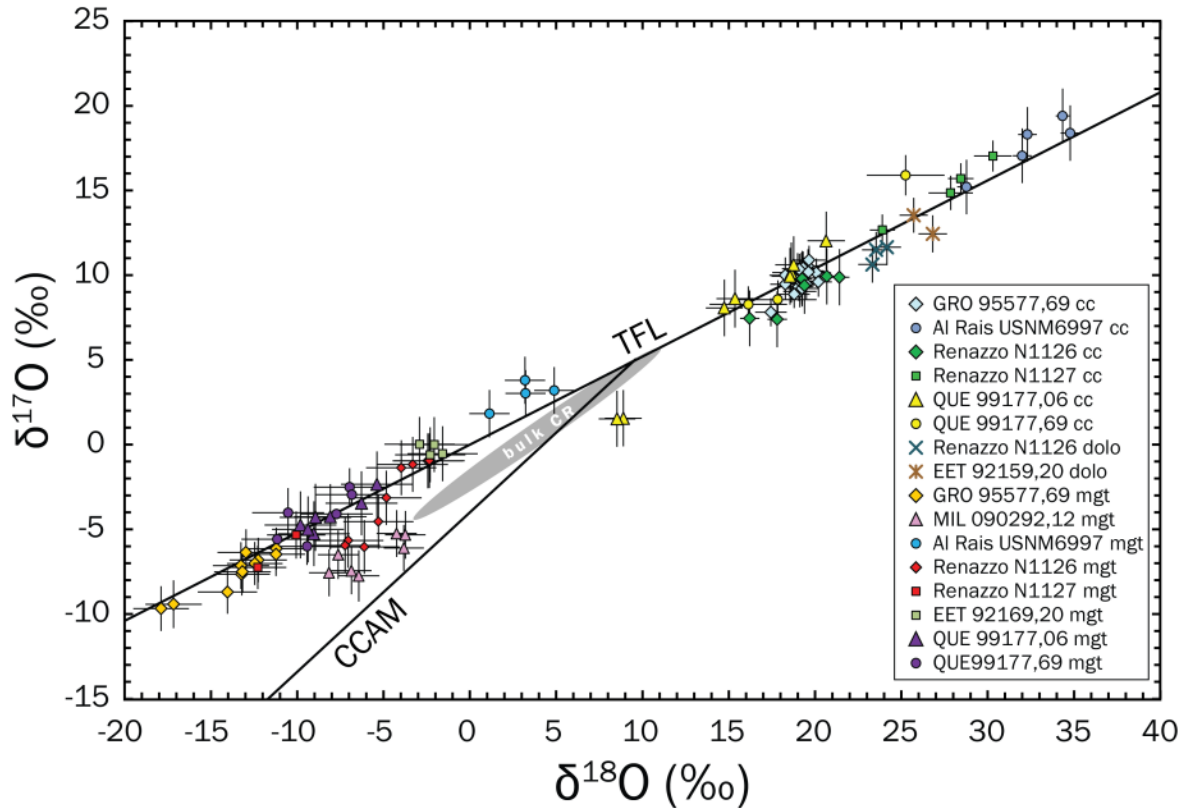


**Figure 5.9.** Comparison of carbonate and magnetite oxygen isotopes from CR chondrites. The shaded region represents the whole-rock oxygen isotope trend for CR chondrites. Uncertainties are  $2\sigma$ .

The whole-rock oxygen-isotope trend for CR chondrites (Fig. 5.9) is generally interpreted as a progressive alteration trend, representing a two-component mixture between an  $^{16}\text{O}$ -enriched solid reservoir, and a heavy  $\text{H}_2\text{O}$  reservoir (Clayton and Mayeda, 1984; 1999; Rowe et al., 1994; Young 1999; Schrader et al., 2011). However, there are some fine-scale inconsistencies, particularly for the more heavily-altered samples, where the relative position in the progressive alteration trend is inconsistent with the petrologic type (Schrader et al., 2011). The *in situ* compositions of secondary minerals document the compositional evolution of the fluid during alteration, and may help to determine the source of such inconsistencies.

In the context of the closed system model of progressive alteration (Clayton and Mayeda, 1984; 1999; Leshin et al., 1997; Benedix et al., 2003; Bland et al., 2009), the *in situ* oxygen isotopes for secondary minerals should display a progressive alteration trend that corresponds with the petrologic type. The progressive alteration trend in a closed system model arises from

the mixing of a  $^{16}\text{O}$ -enriched solid reservoir with a heavy water reservoir. As the material incorporates more and more water, the bulk solid compositions would become heavier, while the water becomes lighter. In the case of single mineral oxygen compositions, the minerals formed first would have come from heaviest water composition, and later minerals would be progressively lighter if formed under the same temperatures and conditions. Therefore, the magnetites and carbonates from the least altered sample QUE 99177 would be expected to have heavier oxygen compositions than those in GRO 95577, and the remaining samples would fall in between the two extremes (e.g., Benedix et al., 2003). Surprisingly, the *in situ* compositions of secondary minerals do not demonstrate a correlation between composition and petrologic type (Fig. 5.10a). For example, the CRs of lowest petrologic type, GRO 95577 (CR 2.0) and Al Rais (CR 2.3) plot at the lightest and heaviest ends of the magnetite trend. All higher petrologic types plot between these two heavily altered samples.

The lack of correlation between the petrologic type and the *in situ* mineral oxygen isotopes suggests that either the simple two-component hydration model is not sufficient to explain the progressive alteration of CR chondrites, or the petrologic type characterizations do not adequately represent the specimens. The extreme lithologic heterogeneity in CR samples has led to difficulties in establishing a consistent petrologic type classification scheme that fully describes the alteration states of the samples. Alternative methods for classifying the CR petrologic types have recently been proposed (Alexander et al., 2013; Harju et al., 2014; Schrader et al., 2014; Abreu, 2015; Howard et al., 2015), but no scheme can fully account for the complex variations in clast, component, and dark inclusion abundances across the CR spectrum.

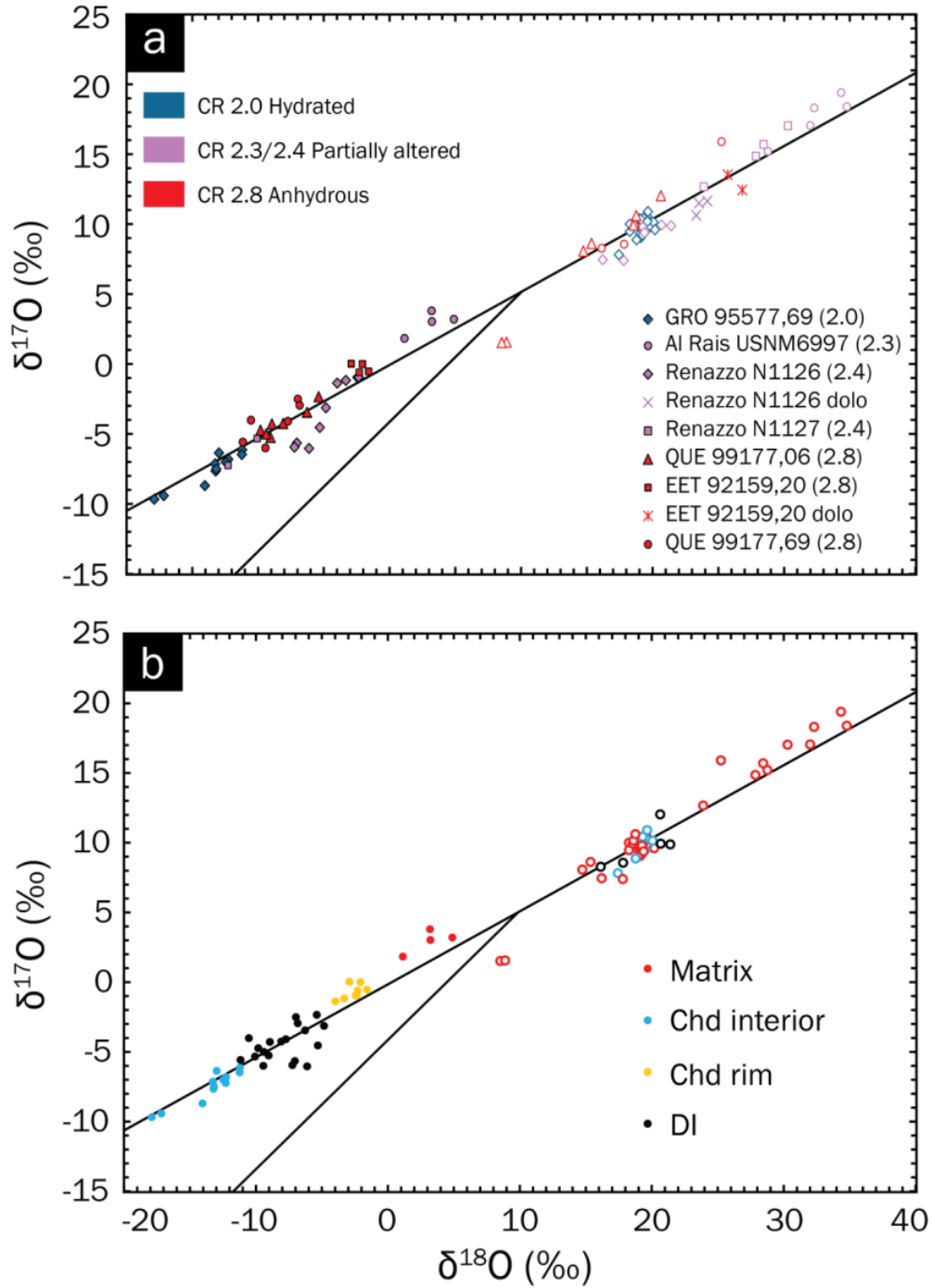


**Figure 5.10.** (a) Secondary mineral oxygen isotopes color-coded by petrologic type. Uncertainties have been removed for clarity. Sample data points are color-coded by the degree of alteration, ranging from heavily hydrated (blue) to minimally altered (red). There is no correlation between the oxygen isotope trend and petrologic type. The analyses given as x's represent dolomite (b) Secondary mineral oxygen isotopes color-coded by lithology, not including dolomite data. Uncertainties have been removed for clarity. Open symbols are carbonate analyses, closed symbols are magnetite.

To understand why secondary mineral compositions do not correlate with petrologic type, we looked at the oxygen isotopes in terms of their lithologies. The main lithologic components of CR chondrites are metal-rich chondrules, fine-grained matrix, fine-grained chondrule rims, and dark inclusions. We have measured magnetite and carbonates from each of these lithologies across the different samples. When plotted in terms of lithology, an interesting pattern emerges for the magnetite grains. The different lithologies plot in distinct clusters on the three oxygen-isotope diagram. In order of increasing  $^{16}\text{O}$  (toward the lower left of the diagram), they define the following order: matrices, chondrule rims, dark inclusions, chondrule interiors (Fig. 5.10b). This pattern is exemplified also in a single meteorite, Renazzo, where we measured magnetite from multiple dark inclusions, a chondrule interior, and a chondrule rim. Magnetite from each different Renazzo lithology plots near similar lithologies from other CR chondrite samples.

This trend indicates the order of formation from an evolving fluid in the context of the closed-system progressive alteration model. The *in situ* oxygen isotopes reveal that magnetite in the matrix formed first, followed by fine-grained chondrule rims, then dark inclusions, and then chondrule interiors. This progressive alteration trend is supported by petrographic evidence that the matrix is the first material to become altered, and that the alteration of chondrule interior metal occurs during more advanced states of alteration (Weisberg et al., 1993; Brearley 2006; Abreu and Brearley, 2010). In this scenario, the fluid evolution is dominated by phyllosilicate or carbonate formation, which progressively shifts the fluid toward a lighter oxygen composition (e.g., Choi et al., 1998). The reverse trend would be expected if magnetite were the only mineral forming from the fluid, since magnetite oxygen isotopes are fractionated towards negative  $\delta^{18}\text{O}$  relative to the composition of the altering fluid. Petrographic observations support the assumption that phyllosilicate formation dominates the aqueous alteration process.

Phyllosilicates and clays are formed throughout all stages of alteration; first they form during the alteration of fine-grained matrices and chondrule mesostasis, and later during the alteration of chondrule silicates (Weisberg et al., 1993; Brearley, 2006, Abreu and Brearley, 2010).

Calcite does not show a similar trend with lithology (Fig. 5.10b). Rather, the matrix carbonates track fluid evolution. The large spread in matrix calcites may indicate a prolonged period of carbonate formation, with precipitation throughout various stages of fluid evolution. Calcites in dark inclusions plot near the chondrule and matrix carbonates from GRO 95577. We interpret the similar compositions of the dark inclusion calcites to indicate that these hydrated

lithic clasts are indeed related to the CR parent body. When compared with this calcite trend, magnetite appears to have been formed under a more limited set of conditions. One possible explanation may be variations in fluid chemistry during alteration. Iron is rapidly oxidized and precipitated as magnetite upon interaction with water, and is primarily sequestered in iron-metal nodules. Once the metal has been exhausted, magnetite no longer forms, but instead iron-bearing phyllosilicates form as replacement products for primary silicates. In contrast, calcium is sequestered in multiple minerals with variable dissolution rates. Calcite may form at the initial stages of alteration as calcium is leached from the glassy mesostasis, through the final stages of alteration when calcium is released into the fluid during the replacement of pyroxene crystals by magnesium-iron silicates. Other calcium-bearing secondary phases in CR chondrites, such as phosphates and smectites, may also form, but require additional cations in the solution and have higher relative energy barriers to begin nucleation.

The spread in oxygen isotopes for matrix calcites may also reflect the varying water/rock (W/R) ratios for the host lithology of each meteorite. In terms of mass-balance, the amplitude of  $\delta^{18}\text{O}$  isotopic evolution in minerals would be less in a water-rich system than in a system with low W/R ratio (Agrinier and Cannat, 1997). The W/R ratio has been estimated for a variety of CR chondrite samples (Clayton and Mayeda, 1999; Schrader et al., 2011). These values are highly model-dependent, based on a number of assumptions regarding the nature of the water and rock oxygen reservoirs and the oxygen isotope fractionation factors. For the conceptual purpose of this discussion however, we will refer to these W/R values as an indicator of the degree of alteration and petrologic type. CR specimens of lower petrologic type have higher W/R ratios than the less altered samples (Clayton and Mayeda, 1999; Schrader et al., 2011). We show that the matrix calcites in low petrologic type (and high W/R) samples show less evidence for fluid evolution than the high petrologic type samples (Fig. 5.11). The extent of fluid evolution in the matrix calcites is quantified by the spread in measured  $\delta^{18}\text{O}$  and  $\Delta^{17}\text{O}$  for a given meteorite. In terms of increasing  $\delta^{18}\text{O}$  isotopic evolution, GRO 95577 < Al Rais < Renazzo < QUE 99177. A similar trend is apparent for  $\Delta^{17}\text{O}$ , but the uncertainty in  $\Delta^{17}\text{O}$  is too large to distinguish small variations at high W/R ratios. This suggests that the extent of local fluid evolution may be controlled by the W/R ratio. The heterogeneous distribution of ice during parent body accretion may contribute to local variations in W/R.

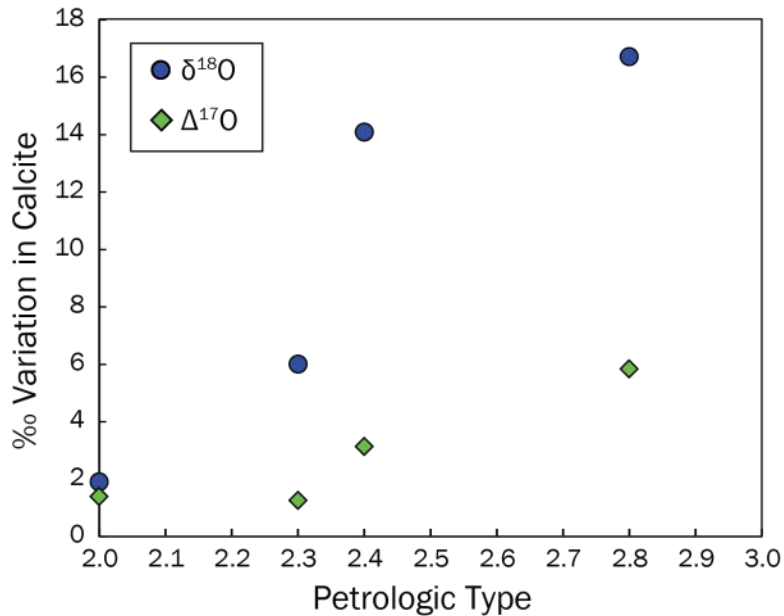


**Figure 5.11.** Graph depicting the variation of oxygen isotopes for matrix calcite (%) versus the petrologic type for four CR chondrites: GRO 95577, Al Rais, Renazzo, QUE 99177 (left to right across the plot). This plot shows a strong correlation for  $\delta^{18}\text{O}$ . The correlation for  $\Delta^{17}\text{O}$  is weaker due to the small fractionation and large uncertainty in analyses.

The accuracy of these observed lithologic patterns is limited by the extreme heterogeneity of CR chondrites. For instance, not all magnetite and carbonate-containing lithologies were found in each sample. Carbonates from fine-grained rims were not large enough to be measured, no magnetite grains were measured from dark inclusions in GRO 95577, and the only matrix magnetites measured here were from Al Rais. Furthermore, oxygen isotopes in magnetite from a petrographically unique dark inclusion in Renazzo (Fig. 5.12) plot at slightly lower  $\Delta^{17}\text{O}$ , close to the anomalous magnetite in MIL 090292. This variation may support the idea that some dark inclusions (but not all) have an exogenous origin (Endreß et al., 1994).

The inconsistencies in the whole-rock trend can be explained by lithologic heterogeneity and fluid evolution. Particularly for the most altered samples, fluid evolution will drag the isotopic composition of secondary minerals towards a lighter oxygen composition, in the opposite direction of the simple two-component whole-rock mixing line. Abundant  $^{16}\text{O}$ -enriched magnetite in GRO 95577 may pull the bulk composition towards the less-altered end of the CR trend, while the  $^{16}\text{O}$ -poor matrix magnetite and calcite in Al Rais shift the bulk values towards the altered end of the CR mixing trend. These data indicate that not all clasts were altered *in situ*, but that some were incorporated as pre-altered lithologies from elsewhere on the CR parent body

(or possibly from an exogenous source), complicating the whole-rock signature. Our research highlights the need for a better measure of CR petrologic types, one that considers the alteration contribution from every lithology.

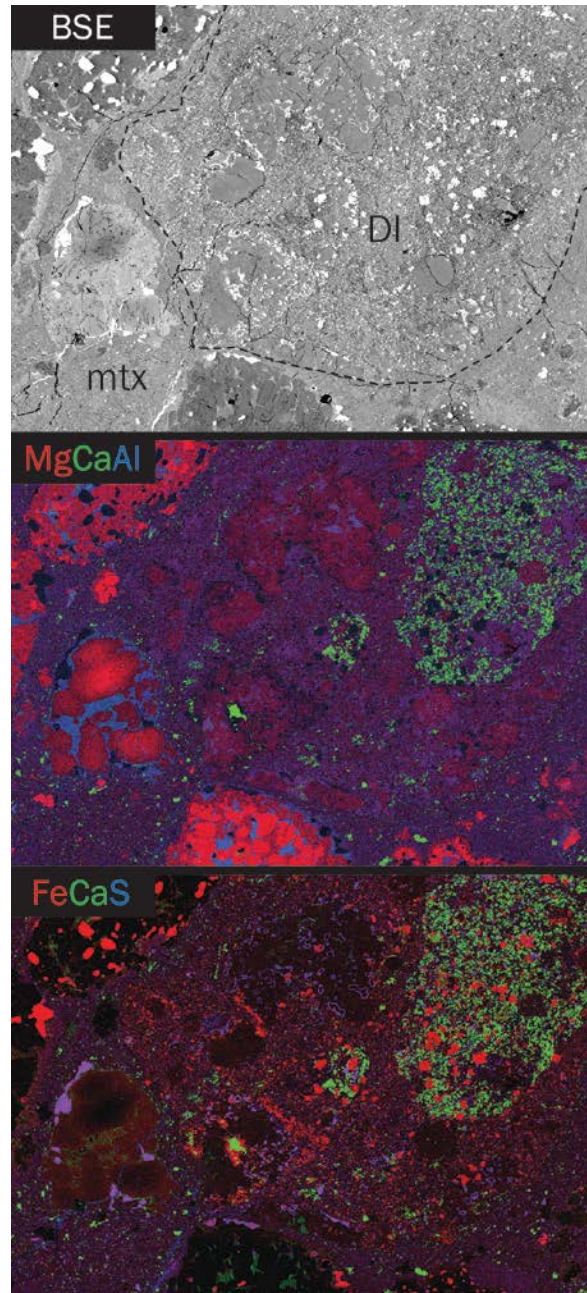


**Figure 5.12.** Unique dark inclusion (DI) in Renazzo N1126. This inclusion contains abundant magnetite and calcite, but the crystal habits are tabular and dissimilar to other DI clasts. This DI also contains a region rich in Ca-Fe silicate material (possibly kirschteinite)

### 5.4.7 Oxygen isotope geothermometry

The relative oxygen-isotope fractionation between carbonate and magnetite can be used as a geothermometer for aqueous alteration (Zheng 1991; Choi et al., 2000; Zheng 2011). Fractionation factors have been empirically derived for calcite-water (Eqn. 3; Zheng, 2011), dolomite-water (Eqn. 4; Zheng 2011) and magnetite-water (Eqn. 5; Zheng 1991) systems at low temperatures, where T = temperature (in K), and  $\alpha = [({}^{18}\text{O}/{}^{16}\text{O})_{\text{mineral}} / ({}^{18}\text{O}/{}^{16}\text{O})_{\text{water}}]$ .

$$10^3 \ln \alpha = 4.01 \times 10^6/T^2 - 4.66 \times 10^3/T + 1.71 \quad (3)$$

$$10^3 \ln \alpha = 4.06 \times 10^6/T^2 - 4.65 \times 10^3/T + 1.71 \quad (4)$$

$$10^3 \ln \alpha = 3.02 \times 10^6/T^2 - 12.00 \times 10^3/T + 3.31 \quad (5)$$

At temperatures of interest for minimally-metamorphosed chondrites (< ~400 °C), the magnetite and calcite fractionation curves show different trends (Fig. 5.13). Oxygen isotopes for calcite are fractionated towards positive values relative to water. Fractionation is greatest at near-freezing temperatures, and exponentially decreases with rising temperature. By ~500 °C, the fractionation factor has plateaued near zero (Zheng, 2011). The dolomite oxygen-partitioning curve for dolomite is nearly identical to that for calcite, with a ~1 ‰ offset towards higher values near 0 °C, so for clarity it is not pictured in Fig. 13. The magnetite fractionation pattern is more complicated. Oxygen in magnetite is fractionated to negative values between 0-500 °C. The fractionation curve reaches a minimum of  $10^3 \ln \alpha \sim -8$  at around 250 °C, and then gradually approaches zero fractionation at high temperatures (Zheng, 1991).

The fluid composition must be known to extract temperature information from a single mineral composition. In the case that two minerals are formed at the same time from a uniform fluid, the relative equilibrium fractionation factors can provide temperature information without knowledge of the water composition (Chiba et al., 1989; Choi et al., 2000). While it is petrographically difficult to determine equilibrium assemblages for such sedimentary matrix material, we assume that local fluid equilibrium and co-precipitation are valid if the following criteria are met: 1. The two secondary minerals must occur in the same clast/lithology. 2. The

minerals should be associated or frequently in contact, but with no evidence that one was clearly formed before the other. 3. The minerals lie on the same mass-dependent fractionation line (indistinguishable  $\Delta^{17}\text{O}$  values), consistent with formation in equilibrium from a common reservoir (Clayton and Mayeda, 1984; 1999; Choi et al., 2000).

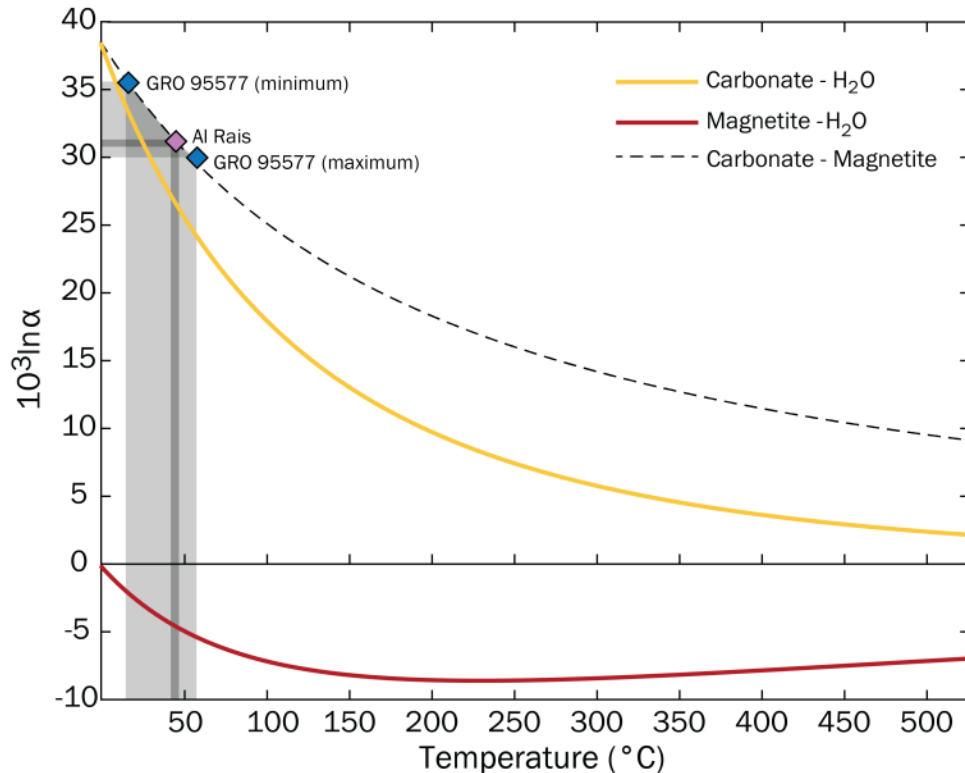


**Figure 5.13.** Diagram of fractionation curves for precipitation of magnetite and calcite from an aqueous solution at varying temperature. The degree of fractionation is given in units of  $10^3 \ln(\alpha)$ , where  $\alpha = [({}^{18}\text{O}/{}^{16}\text{O})_{\text{mineral}} / ({}^{18}\text{O}/{}^{16}\text{O})_{\text{water}}]$ . The magnetite-water curve is shown in red (Zheng, 1991) and the calcite-water curve is in yellow (Zheng, 2011). The dolomite-water curve is not shown, as it is nearly identical to the calcite-water curve. The dashed black line represents the relative fractionation between calcite and magnetite. If produced from a fluid in local thermodynamic equilibrium, calcite-magnetite assemblage in Al Rais was formed at  $\sim 44^\circ\text{C}$ , while GRO 95577 chondrule pseudomorphs range from  $\sim 12$  to  $59^\circ\text{C}$ , indicated by the shaded regions.

Since the composition of water on the CR parent body is unknown (e.g., Clayton and Mayeda, 1999; Schrader et al., 2011), the calcite-magnetite and dolomite-magnetite fractionations can provide insight into both the temperature and water composition at the time of alteration. The black dashed line in Fig. 5.13 represents the relative fractionation between calcite

and magnetite precipitated from a uniform fluid at varying temperatures (Eqn. 6). The curve for dolomite and magnetite fractionation curve is nearly identical (Eqn. 7).

$$10^3 \ln \alpha = 0.99 \times 10^6/T^2 + 7.34 \times 10^3/T - 1.60 \quad (6)$$

$$10^3 \ln \alpha = 1.04 \times 10^6/T^2 + 7.35 \times 10^3/T - 1.60 \quad (7)$$

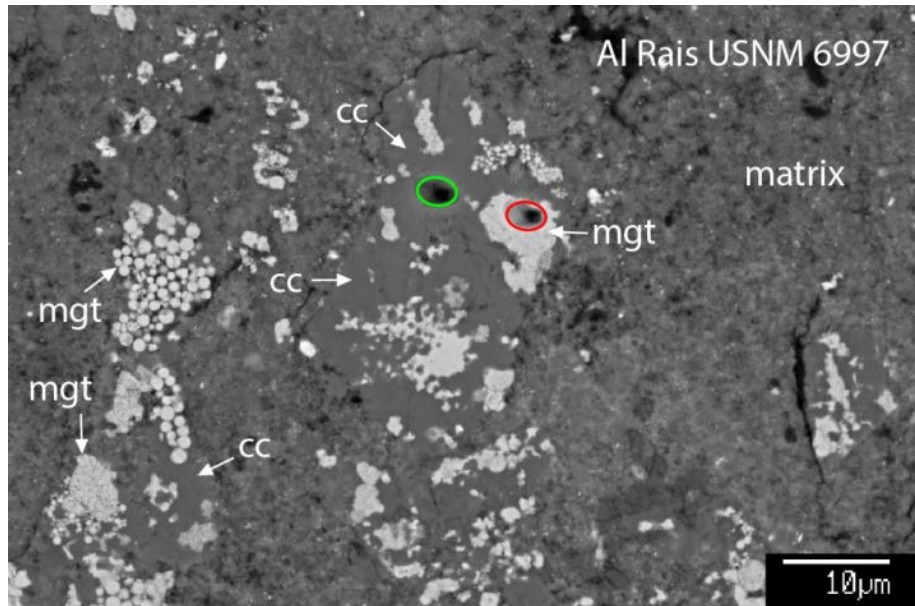


**Figure 5.14:** BSE image of a calcite (cc) and magnetite (mgt) assemblage in Al Rais. Ion probe pits are indicated in green for cc, and red for mgt.

A characteristic carbonate-magnetite assemblage in Al Rais USNM 6997 (Fig. 5.14) is a good candidate for co-precipitation. This assemblage contains abundant magnetite spherules and framboids, intergrown with calcite. Both minerals were measured for oxygen isotopes, yielding a relative fractionation of 31 ‰ on a single mass-dependent fractionation line (Fig. 5.15). This large fractionation implies a low formation temperature of ~ 44 °C (Fig. 5.13). A similar exercise may be done for chondrule alteration products in GRO 95577,69. Magnetite and calcite in GRO 95577 chondrules all plot along the same mass-dependent fractionation line (Fig.5.15), and are products of chondrule alteration. The relative fractionation ranges from ~ 30 to 36 ‰, yielding a fluid temperature between 12 to 59 °C (Fig. 5.13). The alteration temperatures for equilibrium assemblages in Al Rais and GRO 95577 are similar, but require fluids of significantly different O isotopic composition:  $\Delta^{17}\text{O} \sim 1\text{‰}$  and  $\delta^{18}\text{O} \sim 10\text{‰}$  for Al Rais, and a maximum of  $\Delta^{17}\text{O} \sim -0.5$

$\text{‰}$  and  $\delta^{18}\text{O} \sim -6 \text{‰}$  for GRO 95577. These alteration temperatures are cooler than previously estimated for CR chondrites (50-150 °C; Zolensky et al., 1993), but are similar to some estimated temperatures for CM and CO chondrite alteration (e.g., Clayton and Mayeda, 1984; 199; Zolensky et al., 1993; Brearley 2006; Guo and Eiler, 2007).

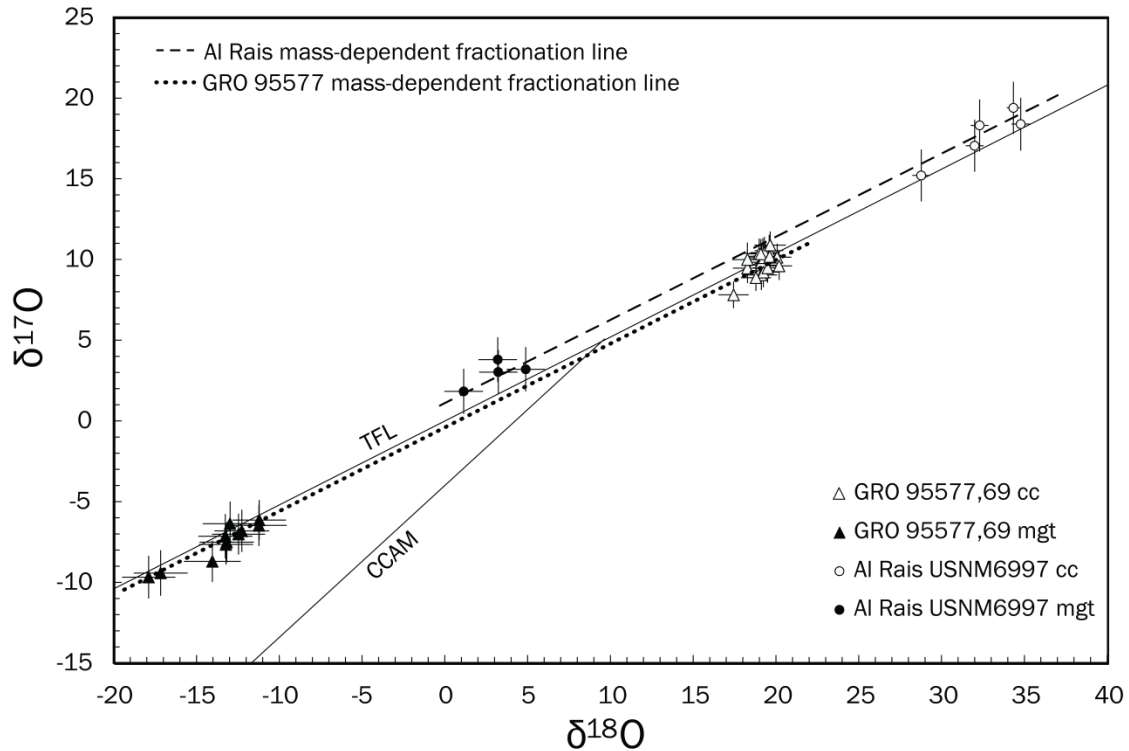


**Figure 5.15.** Diagram showing the magnetite and calcite analyses for Al Rais and GRO 95577. For each meteorite, the calcite and magnetite plot on a mass-dependent fractionation line parallel to the TFL, supporting formation from an equilibrium fluid.

#### 5.4.8 The evolving oxygen-isotope composition of fluid on the CR parent body

All calcite data may be interpreted as a single progressive alteration trend that represents the formation of calcite at various stages of fluid evolution. A linear least-squares regression through all calcite yields a slope of  $0.64 \pm 0.02$  ( $\chi_{\text{red}}^2 = 1.1$ ). Similarly, a regression through the magnetite data from CR chondrites (not including MIL 090292) yields a slope of  $0.63 \pm 0.02$  ( $\chi_{\text{red}}^2 = 0.9$ ). The calcite and magnetite minerals show identical fluid evolution trends (within uncertainty). These trends indicate that fluid evolution was dominated by mass-dependent fractionation processes, and that oxygen isotopic exchange between water and phyllosilicates

during alteration on the CR parent body was comparatively minor. In the case that both trends are reflecting the same phyllosilicate-dominated fluid evolution on the CR parent body, then some inferences about the water composition can be made. For the equilibrium calcite-magnetite assemblages described above, the matrix phases in Al Rais would have represented some of the earliest stages of alteration of CR chondrites, and GRO 95577 chondrules would represent late-stage alteration by an evolved,  $^{17,18}\text{O}$ -depleted fluid. The initial documented fluid composition determined from the Al Rais assemblage above was at  $\Delta^{17}\text{O} \sim 1\text{‰}$  and  $\delta^{18}\text{O} \sim 10\text{‰}$ . The evolution of the fluid can then be interpreted to follow the same slope-0.63 line as the magnetite and calcite trends, ending near the final fluid composition of  $\Delta^{17}\text{O} \sim -0.5\text{‰}$  and  $\delta^{18}\text{O} \sim -6\text{‰}$  determined from GRO 95577 chondrules (Fig. 5.16). While this interpretation is likely a simplification of many combined processes, it provides a first-order estimate of both the composition and evolution of fluid on the CR parent body.

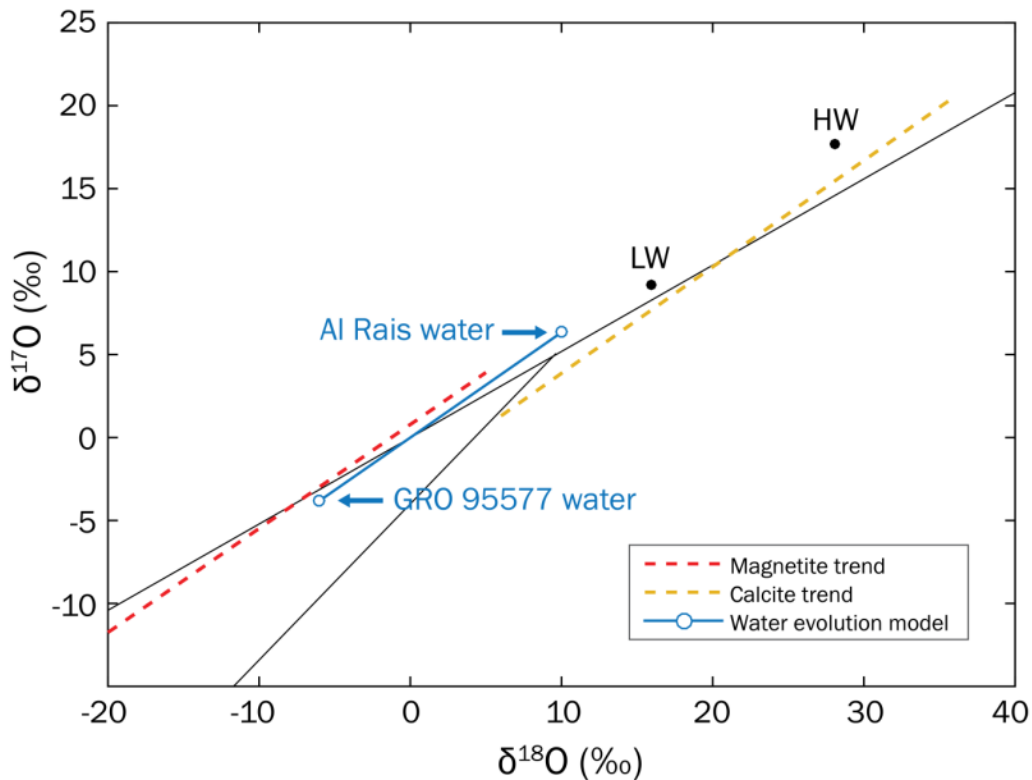


**Figure 5.16.** Model for the evolution of CR water during progressive alteration. Depicted are the oxygen isotope trends for magnetite (red dashed line), and calcite (yellow dashed line). Also on the plot are the compositions of the light (LW) and heavy (HW) water compositions from Clayton and Mayeda (1999). We show that the CR water evolved from the composition labeled “Al Rais water”, down toward  $^{16}\text{O}$ -enriched values near “GRO 95577 water”.

## 5.5 CONCLUSIONS

We successfully measured oxygen isotopes *in situ* for secondary calcite, dolomite, and magnetite in a variety of components for six CR chondrites of different petrologic type. In this study, we find:

1. The oxygen isotopic compositions of secondary minerals are highly variable among CR chondrites. In general, the oxygen composition of calcites ranged from  $\delta^{18}\text{O} \approx 9$  to 35‰, dolomites from  $\delta^{18}\text{O} \approx 23$  to 27‰, and magnetites from  $\delta^{18}\text{O} \approx -18$  to 5‰. Both the calcite and magnetite oxygen compositions plot in arrays of slope 0.63. These parallel arrays may reflect the evolution of the altering fluid in a phyllosilicate-dominated and closed-system environment.

2. The isotopic compositions of secondary minerals do not correlate with the specimen's petrologic type, likely due to the heterogeneity of lithologies in each meteorite. This observation can explain inconsistencies in whole-rock O isotopic progressive alteration trend. The high abundance of  $^{16}\text{O}$ -depleted magnetite and calcite in Al Rais matrices as compared with  $^{16}\text{O}$ -enriched compositions in GRO 95577 can shift the bulk isotopic compositions away from progressive alteration trends.

Models of progressive alteration for CR chondrites can only be reconciled if the relative abundance of components and clasts in each sample is quantified. Our magnetite measurements show that different lithologies may record various stages in the alteration process. In the context of phyllosilicate-dominated alteration model, our data would suggest that the matrices were altered first, followed by chondrule rims, then dark inclusions, and lastly the chondrule interiors. Progressive alteration trends have been suggested for bulk oxygen isotopes, but do not hold up due to the complex heterogeneity of CR chondrites and the extreme variation in component abundances.

3. Calcite oxygen isotopes in the host matrices of each CR chondrite track fluid evolution. This indicates that carbonates were likely formed over longer timescales than magnetite. The oxygen isotopic evolution of the fluid may have been more rapid in samples with a lower W/R ratio, such as QUE 99177, reflected in the large spread in oxygen isotopic compositions for calcite. The extensively hydrated GRO 95577 experienced little to no fluid evolution during carbonate precipitation, which may reflect late-stage alteration in a water-saturated system. A variety of W/R ratios previously quantified for CR samples supports the idea

that aqueous alteration was spatially heterogeneous, with some regions accreting more water-ice than others.

4. Magnetite oxygen isotopes from MIL 090292,12 fall off of the general trend for CR other CR chondrites. The secondary mineralogy is also different than typical CR chondrites, with no evidence of Ca-carbonates. Instead, Ca resides in secondary Ca-silicates, often Ca-pyroxene or an unidentified Ca,Fe-bearing silicate phase. These differences in composition may suggest an anomalous origin for MIL 090292 or relation to a different chondrite group.

5. Alteration temperatures estimated for a calcite-magnetite assemblage in Al Rais and chondrule alteration in GRO 95577 are  $\sim 44$  °C and 12 to 59 °C, respectively. These temperatures are relatively low compared with previous temperature estimates in CR chondrites. Though Al Rais and GRO 95577 were altered at similar temperatures, they require altering fluids of different O-isotopic composition, supporting the hypothesis of significant fluid evolution between these two alteration events. The unique oxygen compositions of secondary minerals in CR chondrites suggest a water reservoir of different composition than CM and CI chondrites.

## CHAPTER 6

### CONCLUDING REMARKS AND FUTURE STEPS

This dissertation presents new insights into the timing and conditions of aqueous alteration in chondrites. Detailed petrographic studies were presented that documented the process of alteration in CR chondrites. The mobilization of elements during alteration was documented in X-ray maps and optical photomicrographs. As matrices and chondrule mesostases were altered, calcium was leached from the chondrules and precipitated as calcite in the matrix. Sulfur from primary troilite was mobilized into the surrounding matrix and into chondrule interiors, where it reacted with iron to form pyrrhotite and pentlandite. Iron was mobilized into the matrix, precipitating magnetite framboids and spherules. Despite small-scale elemental transport, bulk matrix samples are essentially isochemical. Using such petrographic observations, secondary assemblages were modeled in simple geochemical systems. Conditions for aqueous alteration in the CR chondrites were found to be spatially variable, and highly dependent on the local microenvironment. The alteration pH for all modeled assemblages indicates that the fluid was neutral to alkaline, with pH ~7-9. This finding is in agreement with theoretical models of CR chondrite fluids (Zolotov et al., 2015). For the formation of secondary sulfides, the partial pressure of H<sub>2</sub>S must have been much greater than O<sub>2</sub>.

Using the <sup>53</sup>Mn-<sup>53</sup>Cr radiometric dating system, we determined the first resolved ages for carbonate formation in CR chondrites, providing constraints on the timescales for aqueous alteration on the CR parent body. Calcite and dolomite in Renazzo was found to have formed quickly after the accretion of the CR parent body, ~4 Myr after CAI formation. Calcite from the more heavily altered GRO 95577 was formed later, ~12 Myr after CAI formation. These results indicate that aqueous alteration on the CR parent body was prolonged, or occurred in stages. These results have further implications regarding the source of heat on the CR parent body. While the carbonates in Renazzo were likely formed during alteration as the result of internal heating from <sup>26</sup>Al, the GRO 95577 calcite may have been formed by the same process of a large parent body, or by impact heating. In the case of prolonged heating on a large parent body, the sample would have originated in a warmer interior region of the asteroid, while late-stage impact heating would likely only affect the outer few kilometers. Dolomite in the CM fall Sutter's Mill was also measured to have formed ~4 Myr after CAI formation, contemporaneous with

carbonates measured in other CM chondrites. These consistent results strengthen the case for the early onset of aqueous alteration on chondritic parent bodies, fueled by heating from  $^{26}\text{Al}$ .

In Chapter 5, we discussed new insights into the fluid evolution on the CR parent body during alteration. The oxygen isotopic compositions of magnetite reveal that the different CR chondrite lithologies reflect the progression of alteration, while carbonates were formed throughout the entire process, independent of the lithology. This likely reflects a prolonged era of carbonate formation, and suggests that magnetite was formed over shorter periods of time, and required stricter alteration conditions. The relative oxygen isotopic fractionation between magnetite and calcite reveals low temperatures of alteration, below  $\sim 60$  °C.

This work has revealed some additional areas of study that would improve the understanding of the questions asked in this research. Directions for future work in the study of aqueous alteration are described below.

## **6.1 Classification of MIL 090292**

Chapters 2 and 5 lay out petrographic and isotopic evidence that MIL 090292 is not a CR chondrite. The mineral assemblages suggest that it was altered under conditions different than those of the other CR chondrites, and mineral morphologies are not typical. The magnetite oxygen isotopes stray from the general CR trend in a way that cannot be explained by terrestrial weathering. While the oxygen isotopes are similar to magnetite from CV and CK chondrites, this observation alone cannot categorize the sample. Detailed studies of the MIL 090292 mineralogy and petrography are needed to determine the proper classification.

## **6.2 Methods for more precise and accurate $^{53}\text{Mn}$ - $^{53}\text{Cr}$ dating**

As outlined in Chapter 3, the  $^{53}\text{Mn}$ - $^{53}\text{Cr}$  radiometric dating system can be incredibly useful for the dating of secondary minerals in chondrites. However, the secondary minerals often have low count rates of both manganese and chromium, which results in large uncertainties. Furthermore, the issue of mineral relative sensitivity factors has recently been identified as a large source of error as well. These large measurement errors diminish the ability for distinct alteration events to be resolved. In the case of this dissertation, we were not able to distinguish

the ages of calcite and dolomite formation, or between the ages of CR alteration compared with CM alteration. Luckily, SIMS techniques are rapidly developing and may soon be able to measure smaller grains with higher ion yields. Efforts to determine mineral relative sensitivity factors for minerals measured by the manganese-chromium system would greatly improve the accuracy of data. Such advances will provide opportunities to resolve the unanswered questions about late-stage alteration processes.

### **6.3 $^{26}\text{Al}$ - $^{26}\text{Mg}$ chondrule-forming ages in CR chondrites**

As described in Chapter 3, the chondrule ages for CR chondrites pose a problem for the ages of parent body alteration determined from  $^{53}\text{Mn}$ - $^{53}\text{Cr}$ . There is significant overlap between the secondary alteration ages determined from  $^{53}\text{Mn}$ - $^{53}\text{Cr}$  in carbonates, with the primary chondrule ages determined by  $^{26}\text{Al}$ - $^{26}\text{Mg}$  dating. In the literature, chondrules in CR chondrites are measured as being younger than chondrules from petrologic type 3.0 chondrites. The CR chondrule ages range from  $\sim 1$  to  $\geq 4$  Myr with over 60% of measured CR chondrules showing no resolvable excess of  $^{26}\text{Mg}$ . If the majority of CR chondrules were indeed formed later than 3 or 4 Myr after CAI formation, then our  $^{53}\text{Mn}$ - $^{53}\text{Cr}$  data would suggest that parent body alteration occurred before there was even a CR parent body. With more precise manganese-chromium ages, the alteration ages may be resolved if the true values were near the young-end of the uncertainties. However, some of the issues may lie with the aluminum-magnesium chronometer. The aqueous alteration process has a poorly understood effect on the aluminum-magnesium system. If diffusive isotopic exchange occurred to some extent in CR chondrules while  $^{26}\text{Al}$  was still alive, then the ages may not record the timing of initial formation. The system may be disturbed, recording some signature of the isotopic compositions at the time of alteration as well. Further studies of the  $^{26}\text{Al}$ - $^{26}\text{Mg}$  system in aqueous environments are needed to assess whether the chronometer is easily compromised.

### **6.4 SIMS crystal orientation effects in magnetite**

The measured oxygen isotopic data in magnetite are affected to an unknown extent by crystal orientation effects during SIMS analysis. As stated in Chapter 5, single-crystal SIMS

analyses of magnetite have been shown to vary in  $\delta^{18}\text{O}$  between 3 to 6 ‰, depending on the orientation of the crystal lattice at the time of measurement. One possible explanation of this phenomenon is that the secondary ions may be preferentially selected for the light isotope if the crystal planes are near perpendicular to the incident angle of the primary ion beam. However, others have hypothesized that remnant magnetization of the grains may be to blame. Preliminary studies at the University of Hawai‘i have suggested that crystal defects or fractures may be responsible for the variation in oxygen isotopic compositions of magnetite. However, the cause and full extent of this issue are not known, and deserves further study.

## **6.5 Investigations into oxygen isotope trends for CR lithologies**

The oxygen isotopes presented in Chapter 5 suggest that the magnetite in different CR chondrite lithologies may record the timing and progression of alteration. However, one limitation to this study is that not all lithologies in all CR were evaluated. A comprehensive study of the oxygen isotopes of all secondary minerals in every CR lithology would be of interest to either corroborate or invalidate the hypothesis.

## APPENDIX A

### METHODS FOR DETERMINING THE CARBONATE MINERAL RELATIVE SENSITIVITY FACTORS

The timing of aqueous alteration can be determined in secondary carbonates from CR chondrites using the  $^{53}\text{Mn}$ - $^{53}\text{Cr}$  radiochronometer ( $t_{1/2} = 3.7$  Myr; Shukolyukov and Lugmair, 2006). Carbonate minerals are good targets for  $^{53}\text{Mn}$ - $^{53}\text{Cr}$  dating, as they fractionate manganese and chromium during formation from aqueous fluids. The  $\text{Mn}^{2+}$  ion has a distribution coefficient,  $K_D$ , of  $\sim 1$  to 15 in carbonates such as calcite and dolomite, while  $\text{Cr}^{2+}$  has  $K_D < 1$  (Pingitore et al., 1988). A distribution coefficient greater than one indicates that trace amounts of manganese are incorporated into the carbonate, either substituting for cations in the crystal structure or occurring interstitially. A carbonate mineral would have acquired a non-zero initial ( $^{53}\text{Mn}/^{55}\text{Mn}$ )<sub>0</sub> abundance if it formed while  $^{53}\text{Mn}$  was still alive during the first few Myr of Solar System formation. As the  $^{53}\text{Mn}$  decayed over time, it would have left a small excess of  $^{53}\text{Cr}$  trapped in the crystal. Since carbonates do not naturally incorporate large amounts of chromium in their crystal structures, the  $^{53}\text{Cr}$  excess can be easily detected and measured using mass spectrometry.

The accuracy of manganese-chromium measurements has recently been questioned due to inadequate standards and poorly constrained relative sensitivity factors (RSF) for carbonate minerals (Sugiura et al., 2010). We have attempted to address this problem in two experiments detailed here: laboratory synthesis of manganese and chromium bearing carbonates, and manganese-chromium ion implantation studies. Ultimately, the methods described here were not used for the  $^{53}\text{Mn}$ - $^{53}\text{Cr}$  studies in this dissertation, but are nonetheless documented for future development.

#### A.1 Experiments on the synthesis of manganese and chromium bearing calcite

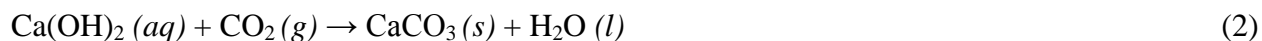
*Purpose:* We have attempted to precipitate manganese- and chromium- bearing carbonates from solution to use as secondary ion mass spectrometry standards for manganese-chromium radiometric dating. We tried two experiments of varying parameters. Though the efforts were unsuccessful, the experiments are summarized here for reference.

*Hypothesis:* The basic idea behind these experiments is to precipitate calcite from a solution in the presence of  $\text{Mn}^{2+}$  and  $\text{Cr}^{2+}$ , thus incorporating trace amounts of manganese and chromium upon formation. If  $\text{Ca}^{2+}$  and  $\text{CO}_3^{2-}$  are present in solution at super-saturated levels and neutral to basic pH, carbonates will precipitate.  $\text{Mn}^{2+}$  is compatible with the carbonate structure, and should readily become incorporated if present in the solution. Manganese is provided to the solution at saturation as  $\text{MnCO}_3$ . Chromium poses a unique challenge, as  $\text{Cr}^{2+}$  is extremely unstable at STP, and is readily oxidized into  $\text{Cr}^{3+}$  (trivalent) or  $\text{Cr}^{6+}$  (hexavalent). Carbonates will not incorporate an oxidized  $\text{Cr}^{3+}$  ion due to charge restrictions in the carbonate salt (the cation must balance  $\text{CO}_3^{2-}$ ). Hexavalent chromium is highly toxic and a known carcinogen. We use  $\text{CrCl}_2$ , a chromium II salt that is highly soluble in water and stable at neutral and slightly basic pH, but quickly becomes oxidized upon prolonged exposure to air.

In order to keep the solution from preferentially precipitating calcium or manganese halide salts, the concentration of  $\text{CrCl}_2$  must be kept to levels under saturation. Since it is highly soluble, a concentration of  $\sim 0.07$   $\text{CrCl}_2$  is enough where calcite has the highest saturation state over other ionic compounds. The solution cannot become acidic, or the chromium will quickly oxidize via the following reactions:



We conducted two experiments. In the first, we used  $\text{Na}_2\text{CO}_3$  as a pH buffer. In the second experiment, the addition of hydroxylamine hydrochloride ( $\text{NH}_2\text{OH} \cdot \text{HCl}$ ) was used to keep the solution mildly reducing, encouraging chromium to remain in the 2+ state. The hydroxyl-ammonium anion is a reducing agent, and can be added to solutions to maintain lower valence state and more reducing conditions. However, this may substantially lower the pH of the solution due to the HCl. For this reason, we attempted to buffer the solution in experiment #2 to neutral or slightly basic conditions through carbonate equilibrium using  $\text{Ca}(\text{OH})_2$ . If the mixture becomes too basic (i.e.  $\text{pH} > 11$ ), there is a risk of precipitating portlandite (the solid form of calcium hydroxide  $\text{Ca}(\text{OH})_2$  rather than calcite. However, portlandite will completely dissociate in solutions of less than 0.01 M, and will drive carbonate precipitation in the presence of  $\text{CO}_2$  (Eqn. 2).



*Apparatus:* Under a fume hood, a large hot plate is set up with a water bath. The temperature of the hot plate is kept at a constant  $T=75^\circ\text{C}$ , monitored using a surface thermometer. Solutions are placed in an Erlenmeyer flask, and suspended in the water bath using a clamp and stand such that the fluid in the flask is entirely submerged (Fig. A1a). Experiments are to be conducted in an open container to drive water evaporation. Evaporation will increase the salinity, hence forcing crystal growth. The water bath should be at a dynamic equilibrium temperature (in our case  $T = 44^\circ\text{C}$ ). One seed crystals are added, the temperature of the hotplate will be lowered to  $T=70^\circ\text{C}$  to drive precipitation. A simultaneous experiment will be run in at room temperature under the fume hood, in an identical Erlenmeyer flask.

**Table A1.** Reagents (experiment #1):

Reagent	Molecular Mass (g/mol)	Saturation (g/100mL)	Experimental Concentration (g/250mL)	Solution Molarity (mol/L)	Saturation
CrCl <sub>2</sub>	122.902	60	0.215	0.007 M	Undersaturated
MnCO <sub>3</sub>	114.946	0.00004877	0.00015	0.0000052 M	Just Saturated
CaCO <sub>3</sub>	100.088	0.0047	0.02	0.0008 M	Supersaturated
Na <sub>2</sub> CO <sub>3</sub>	105.988	21.5	2.6	0.1 M	Undersaturated

**Table A2.** Reagents (experiment #2):

Reagent	Molecular Mass (g/mol)	Saturation (g/100mL)	Experimental Concentration (g/250mL)	Solution Molarity (mol/L)	Saturation
CrCl <sub>2</sub>	122.902	60	0.215	0.007 M	Undersaturated
MnCO <sub>3</sub>	114.946	0.00004877	0.00015	0.0000052 M	Just Saturated
CaCO <sub>3</sub>	100.088	0.0047	0.02	0.0008 M	Supersaturated
Ca(OH) <sub>2</sub>	74.094	0.189	0.1	0.005 M	Undersaturated
Na <sub>2</sub> CO <sub>3</sub>	105.988	21.5	2.6	0.1 M	Undersaturated
NH <sub>2</sub> OH- HCl	69.49	83	2.55	0.01 M	Undersaturated

*Procedure:*

1. Prepare water bath and set on top of heating unit. Heat until both water and unit read  $75^\circ\text{C}$ , using surface thermometer and thermocouple.

2. (Experiment #2 only) Prepare 0.1M Hydroxylamine hydrochloride solution: add 0.6949g NH<sub>2</sub>OH-HCl to a small beaker. Fill with 100 mL of DI water, stir.
3. Fill Erlenmeyer flask with 250mL DI water
4. Attach neck of flask to a ring stand using ring clasps, such that the flask sits comfortably in the water bath without touching the base. Water bath level should be higher than the solution in the flask. Allow temperature of solution to equilibrate.
5. Add 0.02 g CaCO<sub>3</sub> (supersaturated) to warm water, stirring to encourage dissolution.
6. Add 2.6 g Na<sub>2</sub>CO<sub>3</sub> to solution to assist in buffering at pH~9. Stir. Solution is under saturated with respect to sodium carbonate, should not precipitate crystals.
7. To the flask, add 0.215 g CrCl<sub>2</sub> (~0.007 M), 1.5\*10<sup>-4</sup> g MnCO<sub>3</sub>, and 0.1 g Ca(OH)<sub>2</sub> (experiment #2 only; under-saturated such that is completely dissociated, ~ 0.005M). Stir well for a few minutes to encourage dissolution.
8. (Experiment #2) Using disposable pipette, add about 10mL of hydroxylamine-HCl solution to the flask, resulting in a solution of about 0.004 M.
9. Reduce heat to 70°C, hold constant.
10. If necessary, add a small amount of CaCO<sub>3</sub> to act as nucleation seeds for calcite crystal growth.
11. Observe, and test pH every 12 hours. Let precipitate for 48 hours.
12. Run simultaneous experiment at room temperature.

*Results:* The first experiment was conducted without the use of hydroxylamine HCl or Ca(OH)<sub>2</sub>. We set up two flasks of the same chemical composition. The first flask was kept at room temperature, while the second flask was kept at an elevated temperature of ~44°C. In the second experiment, we used additional compounds in an effort to stabilize Cr<sup>2+</sup> in the solution. In experiment #1, during solution mixing, the sodium carbonate was the last chemical added to the solution. As soon as it was added, the solution quickly precipitated a blue phase, leaving a layer of yellowish liquid. It is likely that the precipitated material is chromium (II) hydroxide through the reaction:



Chromous hydroxide is yellow, yet rapidly oxidizes in the presence of air. This may account for the initial yellow color seen in the solution as soon as the sodium carbonate was added. The denser precipitate is likely chromic hydroxide. Chromic hydroxide is occurs as a blueish green colloidal precipitate. After a total of 48 hours, the solution did not appear to be precipitating any calcite crystals, but instead retained a gel-like hydrated chromium substance that sunk to the bottom of both experiments (Fig. 1b). Samples were filtered and saved for future reference.

In experiment #2, the solution suffered a similar fate. As soon as sodium carbonate was added, there was some precipitation. In this trial, the precipitation was a murky blue-purple color, rather than the vivid blue-green substance (Fig. 1c). Regardless, the byproduct was again a hydrated substance, rather than calcium-carbonate, and remained in a non-crystalline form, even after filtering and drying.

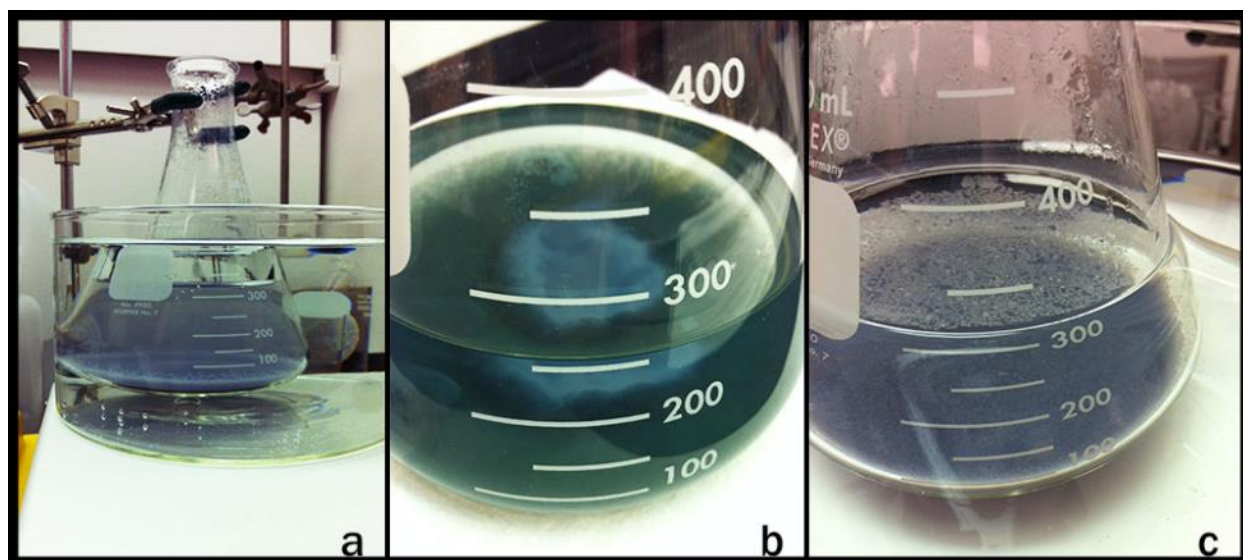


**Figure A1.** Precipitation experiments.

### **A.2 Manganese and chromium ion implantation studies**

As shown above and in literature (Sugiura et al., 2010; Ichimura and Sugiura, 2015), synthetic manganese- and chromium- bearing carbonate minerals are difficult to synthesize in a laboratory setting. Furthermore, the samples that have successfully been synthesized tend to be heterogeneous and zoned, with small scale variations that lead to large uncertainties in the RSF.

Ion implantation of manganese and chromium are a promising solution. A variety of silicate and carbonate minerals and glasses were implanted with  $\text{Cr}^+$  ions through a commercial vendor.  $\text{Mn}^+$  was not implanted, as all of the carbonate minerals contained minor manganese. The samples included two terrestrial calcite crystals, one terrestrial dolomite, one terrestrial magnesite, one terrestrial rhodochrosite crystal, one Si-wafer, and two NIST standard glasses: NIST 612 and NIST 614, which are synthetic glasses that have been doped with known quantities of various trace elements. The samples were provided by B. Jacobsen, J. Matzel, and I.D. Hutcheon at the Lawrence Livermore National Laboratory. All minerals were mounted in an epoxy plug and carbon-coated before ion-implantation (Figure A2). The  $\text{Cr}^+$  ions were implanted at an energy of 180 KeV and 22  $\mu\text{A}$  current, for a total dose of  $1.50 \times 10^{14}$  atoms/ $\text{cm}^2$ .

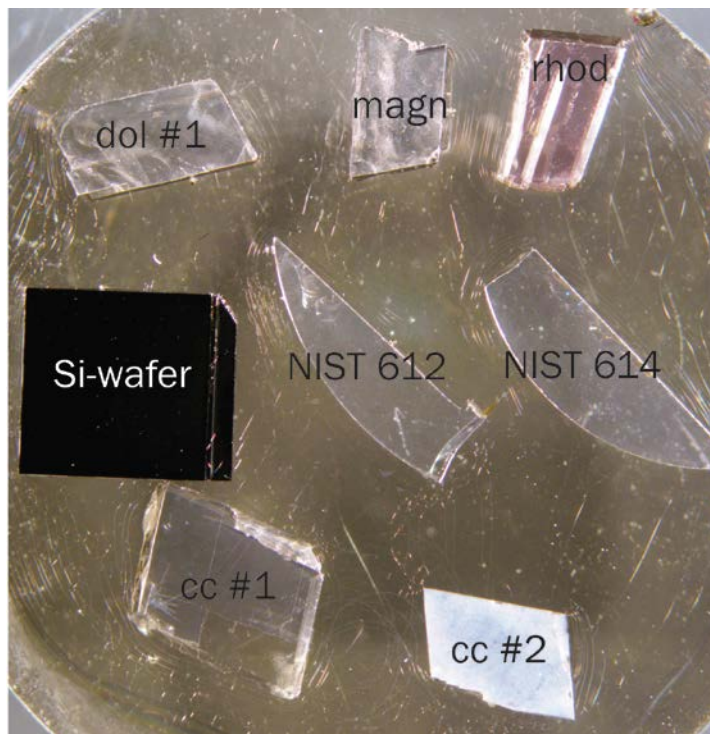


**Figure A2.** Implanted carbonate samples.

To determine the RSF of the implanted minerals, we measured  $^{43}\text{Ca}^+$ ,  $^{52}\text{Cr}^+$ ,  $^{53}\text{Cr}^+$ , and  $^{55}\text{Mn}^+$  using the Cameca 1280 IMS ion microprobe at the University of Hawai'i. We measured calcite #1, calcite #2, dolomite #1, and the NIST-612 glass. The calcium was measured for the purpose of normalizing the measurements to the known abundances in the NIST glass standards.

$^{43}\text{Ca}^+$  was measured on the mono EM for 2 s, followed by a peak jump to  $^{52}\text{Cr}^+$ ,  $^{53}\text{Cr}^+$ , and  $^{55}\text{Mn}^+$ , which were collected in multicollecion mode on the L1 electron multiplier (EM), and C EM, and mono EM, respectively, for a duration of 10 s. The mass resolving power for  $^{55}\text{Mn}^+$  and  $^{43}\text{Ca}^+$  was  $\sim 5800$ , and  $\sim 1800$  for  $^{52}\text{Cr}^+$  and  $^{53}\text{Cr}^+$ . Measurements were taken using the  $^{16}\text{O}^-$  duoplasmatron source set to 23 kV impact energy and 10 nA primary beam current. Analyses used a  $50\ \mu\text{m} \times 50\ \mu\text{m}$  raster with an electronic gate (e-gate) set to 50% to reduce edge effects, for a total analyzed region of  $25\ \mu\text{m} \times 25\ \mu\text{m}$ . Each carbonate was analyzed for 140 cycles, and the NIST-glass was analyzed for 160 cycles. Automated mass calibration occurred at cycle 120, when the measurement had reached the background plateau. Mass calibrations were not conducted at the beginning of the measurement, as they would drill into to the ion-implantation profile. Fig. 3 shows typical depth profiles for each standard. Depth profiles are presented as counts versus cycle for the carbonates, and as  $\log(\text{counts})$  versus cycle for the NIST standard to illustrate the typical shape of the  $^{53}\text{Cr}^+$  profile (Fig. A3).

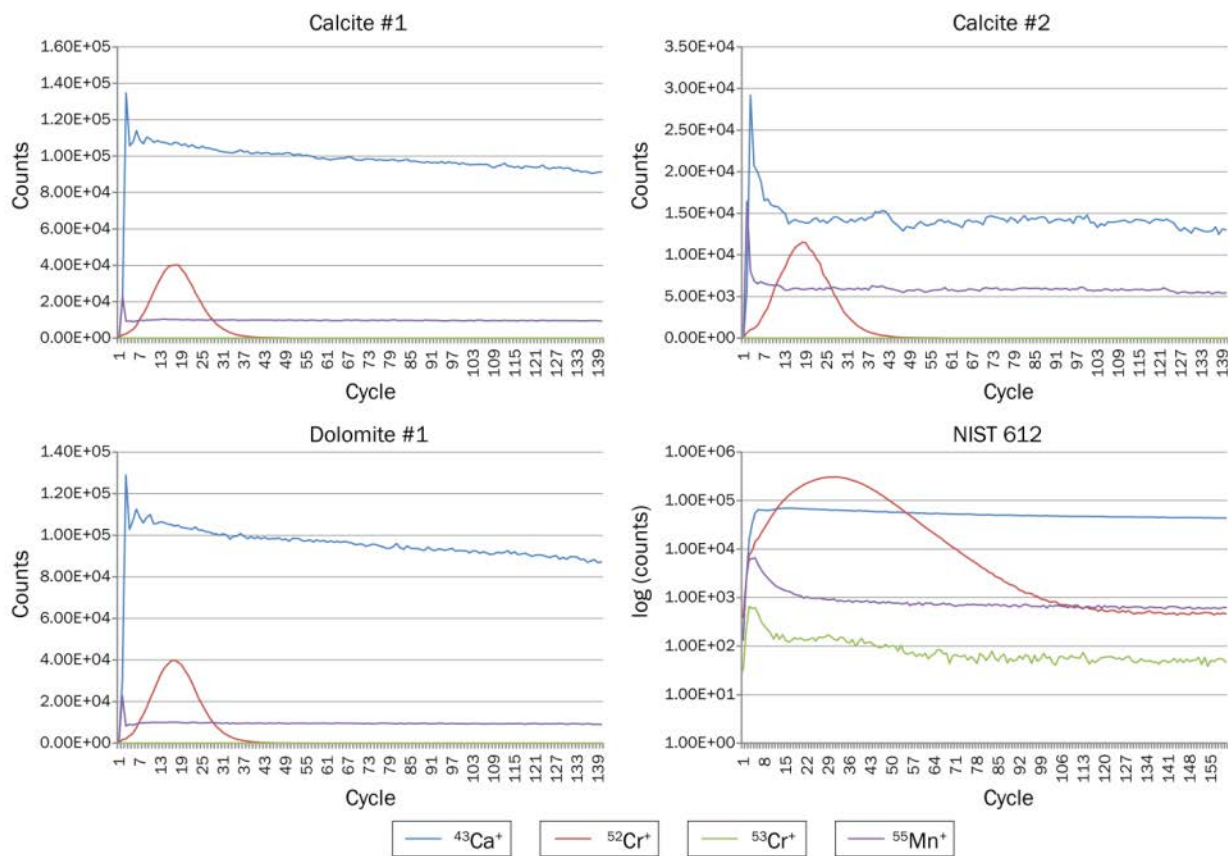


**Figure A3.** Characteristic ion implant profiles.

The implant profiles for  $^{52}\text{Cr}^+$  showed expected Gaussian peaks with measurement depth. Despite being implanted in unison, the profiles did not show identical peaks for the two calcite crystals, although similar peaks were obtained for calcite #1 and dolomite #1. Calcite #2 had a smaller quantity of  $^{52}\text{Cr}$  implanted, though the implant depth was approximately the same. For the NIST-612 glass,  $^{52}\text{Cr}^+$  was implanted to greater depths and in a higher quantity than the carbonate minerals.

To accurately use these implants to assess the RSF, two additional quantities must be known. First, the depth of the ion implant must be known. This can be roughly estimated using monte-carlo simulation programs such as SRIM. For a more accurate depth analysis, the ion probe pits will be measured by profilometer with collaborators B. Jacobsen and J. Matzel at the Lawrence Livermore National Laboratory. This RSF research is currently at this stage. Second, the true amount of implanted ions in the sample must be quantified. The implant dose has been estimated at  $1.50 \times 10^{14}$  atoms/cm<sup>2</sup>, however these quantities are highly uncertain (they can be an order of magnitude off), and may vary on a mineral-by-mineral basis, depending on the insulating properties of the substrate. To quantify the implant dose, a method such as Rutherford Backscattering Spectrometry (RBS) can be used. Once these values are confirmed, the RSF can be determined by taking the integrals of the  $^{52}\text{Cr}^+$  Gaussian profile relative to the  $^{55}\text{Mn}^+$  flat profile, and comparing that ratio to the true amount of implanted and native  $^{55}\text{Mn}$  and  $^{52}\text{Cr}$ , as measured by RBS and EPMA. Measurements similar to these have been conducted by Steele and McKeegan (2014), where they find that the dolomite RSF is indeed larger than the calcite RSF, dependent on the amount of magnesium in the carbonate.

## APPENDIX B

### PETROGRAPHY AND CLASSIFICATION OF NWA 7402: A NEW SULFIDE-RICH UNEQUILIBRATED ORDINARY CHONDRITE

In review for publication in *Chemie der Erde* as Jilly-Rehak, C. E., Huss G. R., Bonal L., and Twelker E., Petrography and classification of NWA 7402: A new sulfide-rich unequilibrated ordinary chondrite.

*Abstract-* We studied a new chondritic find Northwest Africa (NWA) 7402 for classification purposes. Initial observations showed that this meteorite is highly unequilibrated, and therefore potentially significant for the study of primitive Solar System materials. Using optical microscopy, we observed the modal abundances of petrographic components and the abundance of metal within the specimen, and determined that the sample is most likely an L chondrite. However, the specimen contains a higher abundance of sulfide than commonly seen in ordinary chondrites. Raman spectroscopy and electron microprobe analysis were used to determine the petrologic type. The structural order of organic matter in the matrix and the chromium content of olivine grains indicate that the sample is type 3.1, having largely escaped thermal metamorphism on the meteorite parent body. Furthermore, secondary phases formed by aqueous alteration are rare to absent. Minor recrystallization of matrix and undulatory extinction of olivine grains suggest that NWA 7402 experienced shock up to stage 2. Terrestrial weathering is heterogeneous in the specimen; much of the stone's exterior shows substantial iron oxidation (weathering grade 2), while some parts of the interior remain relatively fresh (weathering grade 1). The large sample size and pristine nature of NWA 7402 make this meteorite a valuable resource for the study of early Solar System processes. Not only is NWA 7402 of low petrologic type, but it has unusual features (including anomalous chromium composition and elevated sulfide abundance) that deserve further study.

Keywords: Meteorite Classification; Unequilibrated Ordinary Chondrites; Meteoritics; Cosmochemistry; Early Solar System; Petrography

## B.1 INTRODUCTION

A new chondritic meteorite find Northwest Africa (NWA) 7402 displays rare features suggesting that it could be highly primitive, warranting detailed study for classification purposes. NWA 7402 is a 4013.4 g individual stone, purchased on August 26, 2010 by Eric Twelker of the Meteorite Market from a meteorite trader in Morocco (Fig. B1). Its history—including finder and location—remain unknown, as is the case with many NWA meteorites. Two large slabs and one thin section of NWA 7402 were supplied to the University of Hawai‘i at Mānoa for classification purposes. The largest mass of 25.5 g was set aside as the type sample for later study, while a smaller slab of approximately 12 g was cut into one thick section and three thin sections. We have employed optical microscopy, scanning electron microscopy (SEM), electron microprobe analysis (EPMA), and Raman spectroscopy to determine the chemical group of NWA 7402 and to examine the petrologic type, stage of shock, terrestrial weathering grade, and composition.



**Figure B1.** (a) NWA 7402 whole rock. Reference cube edges are 1 cm in length. (b) The sliced edge shows variation in chondrule diameter. Heterogeneous weathering is apparent, where the less weathered interior is visibly lighter than the weathered rusty outer edges of the rock.

## B.2 PETROGRAPHY

Naked-eye examination of the cut slab reveals heterogeneity in the NWA 7402 samples. Rust-colored, apparently weathered areas with orange-brown chondrules surround less-

weathered regions containing light gray chondrules set within a darker gray groundmass. The meteorite is a breccia, with occasional lithic clasts of impact melt present. The transition from weathered to unweathered lithology is abrupt, and does not correlate with clast boundaries. Further observations of weathering grade will be discussed below.

Transmitted and reflected light optical microscopy reveal a high abundance of chondrules embedded in a clastic, sulfide-rich matrix. Chondrules span a large size range, from ~0.2 - 2 mm in apparent diameter (apparent chondrule sizes measured from thin sections may differ from the true sizes due to random sectioning of the chondrule spheres (Hughes, 1978; Eisenhour, 1996)). A melt inclusion of approximately 4 mm in length is present in the thick section, and an anomalously large barred olivine chondrule of 8 mm in apparent diameter exists in one thin section. Chondrule types found in the meteorite include porphyritic olivine, barred olivine, porphyritic pyroxene, radial pyroxene, and cryptocrystalline. The porphyritic olivine chondrules comprise both type I (Fa <2%) and type II (Fa 10-25%) (Brearley and Jones, 1998).

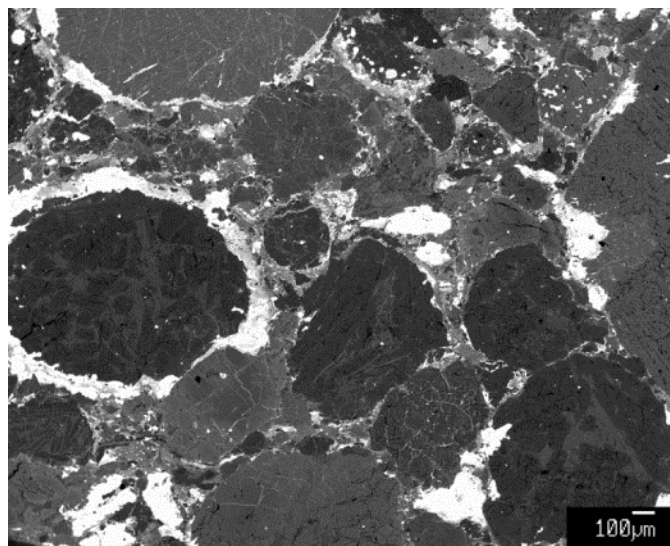


**Figure B2.** BSE image of NWA 7402 thin section showing variation in chondrule size and fragmented matrix. Low-FeO silicates appear darker than the FeO-rich silicates, and the bright grains and chondrule rims consist primarily of Fe-sulfides and Fe,Ni metal.

NWA 7402 was analyzed with backscattered-electron imaging and energy-dispersive x-ray spectroscopy (EDS) on a JEOL JSM-5900LV scanning electron microscope (SEM) to observe the sample mineralogy. Chondrule silicates exhibit a large range in contrast in backscattered electrons due to variation of Fe content, suggesting that the chondrite is

unequilibrated (Fig. B2). Fine-grained FeO-rich silicate rims are observed surrounding some (but not all) chondrules. The rims are typically embedded with micron-sized Fe sulfides. The matrix of NWA 7402 contains abundant Fe,Ni metal and sulfides, as well as chondrule fragments and isolated silicate grains (Fig. B2). Large opaque assemblages (~300  $\mu\text{m}$  in diameter) occur in the matrix, containing both kamacite and taenite (Fe,Ni metal minerals), Fe sulfides, and Fe oxides. Some Fe oxides appear in veins surrounding the metal or sulfide, and are likely products of terrestrial weathering. The studied sections do not contain any calcium-aluminum inclusions (CAIs), although one aluminous chondrule was found (Fig. B3).

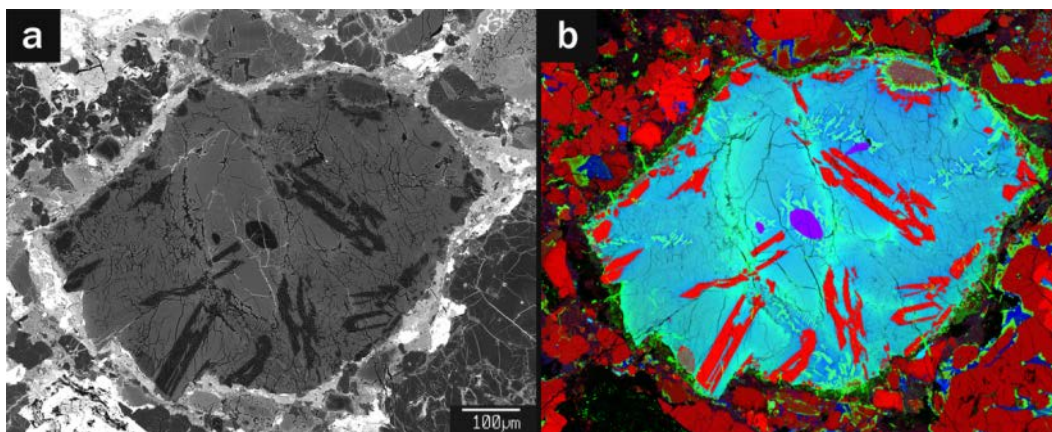


**Figure B3.** (a) Backscattered electron image of aluminous chondrule. (b) Elemental x-ray mapping, depicted in RGB where red=Mg, green=Ca, blue=Al. Red skeletal crystals are olivine, purple is spinel, and the blue-green regions are plagioclase.

### B.3 TECHNIQUES AND SAMPLE CLASSIFICATION

#### B.3.1 Compositional classification.

Modal abundances of the various components in chondrites can be valuable indicators for group classification. The modal abundance of fine-grained matrix and rim material in NWA 7402 is approximately 14 vol%, and chondrule abundance is around 66 vol% (as determined by point counting), within the range seen in ordinary chondrites (e.g., Weisberg et al. 2006). The remaining volume consists mostly of metals, sulfides, and silicate fragments. In contrast, carbonaceous chondrites (CI, CM, CO, CV, CK, CR) generally have high abundances of fine-grained matrix (>30 vol%). CH chondrites are an exception, where fine-grained matrix

abundance is about 5 vol%. However, we may rule out the possibility of NWA 7402 being a CH chondrite, as the average chondrule size in NWA 7402 is much larger than the small ~20  $\mu\text{m}$  cryptocrystalline chondrules typical of the CH chondrite group. Furthermore, the wide variety of chondrule types seen in NWA 7402 is inconsistent with the highly reduced enstatite chondrites or the highly oxidized R-type chondrites (Kallemeyn et al., 1996; Weisberg et al. 2006). Petrographically, NWA 7402 is most consistent with ordinary chondrites; they both have high chondrule to matrix ratios, few CAIs, and exhibit a variety of chondrule types.

Ordinary chondrites are further categorized into subgroups H, L, and LL according to the abundance of total Fe and the distribution of Fe between metal and FeO in silicates (Van Schmus and Wood, 1967). To determine the average FeO content of chondrule silicates, we measured the elemental composition of chondrule olivine and pyroxene grains with the JEOL Hyperprobe JXA-8500F Electron Microprobe at the University of Hawaii. Over the course of two sessions, a total of 265 grains were chosen at random to obtain an unbiased bulk characterization of the chondrules. Elements measured were Al, Ti, Na, Fe, K, Si, Cr, Mg, Mn, and Ca, calculated in oxide wt%. Standards included San Carlos olivine, sphene glass, Amelia albite, orthoclase, Verma garnet, and USNM 117075 chromite. We calculated the fayalite (Fa) content for each olivine, where  $\text{Fa} = 100 \times (\text{FeO}/(\text{FeO}+\text{MgO}))$  in atomic units, and the ferrosilite (Fs) content of each pyroxene, where  $\text{Fs} = 100 \times (\text{FeO}/(\text{FeO}+\text{MgO}+\text{CaO}))$  in atomic units (Table B1).

Equilibrated ordinary chondrites show characteristic fayalite content (in mol%) as follows: H 16–20; L 23–26; LL 27–32 (Weisberg et al., 2006). Unequilibrated ordinary chondrites (UOCs) do not necessarily follow these trends, as the FeO is dispersed. The Fa content of NWA 7402 olivine is highly variable, with the Fa distribution ranging from <1 up to ~36 mol% (Fig. 4). The average calculated Fa contents of the session one and two olivines are  $11.8 \pm 7.8$  mol% and  $12.9 \pm 8.7$  mol%, respectively. The pyroxene analyses yield average Fs contents of  $10.8 \pm 10.2$  mol% and  $8.4 \pm 7.6$  mol% for sessions one and two, respectively. The values are consistent between measurement sessions, and well within error. Clearly, the average values that we obtain for Fa content are lower than what would be expected in an equilibrated ordinary chondrite, and most closely resembles the wide Fa distributions seen in UOCs. However, the FeO content of the silicates does not establish the UOC subgroup for NWA 7402.

The modal abundance of native metal in NWA 7402 may help to determine the UOC subgroup. Over 650 points were counted in reflected optical light and distinguished either as

silicate, Fe,Ni metal, sulfide, or weathering product, using the methods of Boeck et al. (2009). Modal abundances (in vol%) gave 79.0 silicates, 14.4 sulfides, 3.8 metallic Fe,Ni, and 2.8 weathering products. This is equivalent to abundances (in wt%) of 71.2 silicates, 18.1 troilite, 7.8 metallic Fe,Ni, and 2.9 weathering products. We can roughly estimate the pre-weathering metal abundance by assuming that all weathering products were formed from the oxidation of primary Fe,Ni metal. If the weathering products are assumed to be goethite (FeOOH), then by mass balance the pre-weathering metal abundance could have been up to 10.7 wt% (Table B2). Under classification of equilibrated ordinary chondrites, this would place the meteorite into the L-chondrite range of 4.4 – 11.7 wt% Fe,Ni (Keil, 1962; Gomes and Keil, 1980), or about 4 vol% metal (Weisberg et al., 2006).

**Table B1.** (a) Elemental abundance averages, and average fayalite (Fa) content for chondrule olivines, in mol%. (b) Elemental abundance averages and average enstatite (En), wollastonite (Wo), and ferrosilite (Fs) content for chondrule pyroxenes, in mol%.

A)	Session 1	Session 2	B)	Session 1	Session 2
<b>SiO<sub>2</sub></b>	39.6 ± 1.63	39.7 ± 1.5	<b>SiO<sub>2</sub></b>	56.9 ± 2.7	58.6 ± 2.3
<b>Al<sub>2</sub>O<sub>3</sub></b>	0.05 ± 0.06	0.05 ± 0.05	<b>Al<sub>2</sub>O<sub>3</sub></b>	0.40 ± 0.32	0.77 ± 2.11
<b>FeO</b>	11.1 ± 6.9	11.8 ± 7.2	<b>FeO</b>	7.17 ± 6.33	5.78 ± 4.93
<b>MgO</b>	47.7 ± 6.0	47.0 ± 7.3	<b>MgO</b>	33.8 ± 5.3	34.6 ± 5.7
<b>CaO</b>	0.17 ± 0.08	0.19 ± 0.11	<b>CaO</b>	0.48 ± 0.48	0.90 ± 1.93
<b>K<sub>2</sub>O</b>	0.00 ± 0.00	0.00 ± 0.00	<b>K<sub>2</sub>O</b>	0.00 ± 0.00	0.01 ± 0.02
<b>Na<sub>2</sub>O</b>	0.01 ± 0.01	0.01 ± 0.02	<b>Na<sub>2</sub>O</b>	0.03 ± 0.04	0.09 ± 0.58
<b>TiO<sub>2</sub></b>	0.01 ± 0.02	0.02 ± 0.02	<b>TiO<sub>2</sub></b>	0.06 ± 0.06	0.08 ± 0.13
<b>MnO</b>	0.27 ± 0.17	0.30 ± 0.17	<b>MnO</b>	0.35 ± 0.24	0.28 ± 0.19
<b>Cr<sub>2</sub>O<sub>3</sub></b>	0.40 ± 0.14	0.38 ± 0.13	<b>Cr<sub>2</sub>O<sub>3</sub></b>	0.71 ± 0.24	0.67 ± 0.22
<b>TOTAL</b>	99.3 ± 0.96	99.4 ± 1.57	<b>TOTAL</b>	99.9 ± 1.51	101.7 ± 1.26
<b>Fa [Fe]</b>	11.88 ± 7.68	12.70 ± 8.08	<b>En [Mg]</b>	87.06 ± 10.93	86.90 ± 12.40
<b>Fa [Mg]</b>	11.67 ± 7.93	13.06 ± 9.35	<b>Wo [Ca]</b>	0.92 ± 0.93	1.68 ± 3.61
<b>Fa [Avg.]</b>	11.77 ± 7.79	12.88 ± 8.71	<b>Fs [Fe]</b>	10.81 ± 10.16	8.43 ± 7.60
<b>PMD</b>	66.6%	67.6%	<b>PMD</b>	94.0%	90.2%

**Table B2.** Modal abundances of metal, sulfide, silicates, and weathering in NWA 7402, expressed in vol% and wt%. To calculate weight percent, sulfide is assumed to be troilite (FeS), and weathering products are assumed to be goethite (FeOOH).

	Point count	vol. %	wt. %
<b>Sulfide</b>	98	14.37	18.09
<b>Fe,Ni</b>	26	3.81	7.81
<b>Weathering</b>	19	2.79	2.89
<b>Silicates</b>	539	79.03	71.21
<b>TOTAL</b>	682	100.00	100.00

### B.3.2 Petrologic type.

Meteoritic petrologic types range from 1 to 6, reflecting different degrees of parent body processing. Type 3 is considered to be the most unaltered, while values greater than 3 represent increasing degrees of thermal metamorphism, and values less than 3 indicate increasing aqueous alteration (e.g., Weisberg et al., 2006). The unequilibrated FeO content of NWA 7402 silicates suggests that the sample has largely escaped thermal metamorphism, an observation supported by the lack of recrystallization in the thin sections. In addition, there are few secondary minerals indicative of aqueous alteration processes. Pre-terrestrial aqueous alteration could have been involved in the formation of some Fe oxides in the metal-sulfide assemblages, but most of the Fe-oxides have textures and veining structures suggestive of terrestrial weathering. Sulfides are all Ni-poor, primarily troilite. Readily altered material such as chondrule mesostasis retains a glassy or quenched texture. The matrix is primarily composed of submicron crystals of Fe-rich olivine, but may also contain amorphous silicates and phyllosilicate material; transmission electron microscopy (TEM) studies are needed to further determine whether aqueous phases are present in the fine-grained matrix. No carbonates or carbide assemblages occur in the sections studied. NWA 7402 therefore falls into the type 3 category, having largely escaped both thermal metamorphism and aqueous alteration.

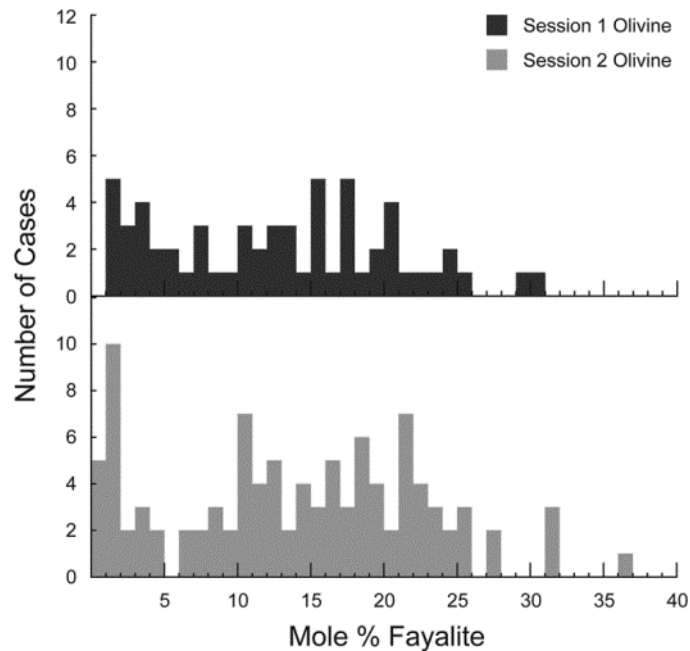


**Figure B4.** Histograms of fayalite content in chondrule olivines in the unclassified meteorite from sessions 1 and 2. The percent mean deviations (PMD) for these distributions are 66.6% and 67.6%, respectively.

Type 3 chondrites are further delineated into subtypes ranging from 3.0-3.9. The large percent mean deviation (PMD) of ~67% for the fayalitic distributions (Fig. B4) labels the meteorite as petrologic type <3.4 (Van Schmus and Wood, 1967; Huss et al., 2006). Various tracers may be used to further constrain the chondrite subtype, including chromium abundance and distribution in olivine grains, thermoluminescence, structural order of organic matter, and recrystallization of matrix material, among others (Sears et al., 1980, 1991; Grossman and Brearley, 2005; Bonal et al., 2006, 2007; Huss et al., 1981, 2006). For the purpose of classification of NWA 7402, we will compare chromium abundances of olivine and the structural order of organic matter.

The chromium abundance in olivine grains is particularly variable for UOC subtypes 3.0-3.2. This correlation is valid for chondrules with FeO > 2 wt%; below 2 wt%, FeO and Cr<sub>2</sub>O<sub>3</sub> are instead correlated by volatility control over minor elements. Meteorites that are type 3.0 generally have the highest Cr<sub>2</sub>O<sub>3</sub> contents in olivine, whereas the 3.1 subtypes have the broadest distributions (Grossman and Brearley, 2005). We measured Cr<sub>2</sub>O<sub>3</sub> in a total of 140 olivine grains with FeO > 2.0 wt% during the two EPMA sessions described earlier. Semarkona (LL3.00) and Bishunpur (LL3.15) were also measured under the same analytical setup to assess the accuracy of the analyses. Olivine grains (56 in Semarkona and 43 in Bishunpur) were selected from outside of the visible extent of the fusion crust, as the heat upon entry may have altered the Cr<sub>2</sub>O<sub>3</sub> composition of exposed olivine.

In both NWA 7402 sessions, the Cr<sub>2</sub>O<sub>3</sub> abundance consistently ranges from about 0.2-0.7 wt%, with an average of 0.41 wt% (Fig. B5). The relatively high modal value and broad distribution of Cr<sub>2</sub>O<sub>3</sub> in olivine suggests that NWA 7402 is near type 3.0-3.1. When the mean Cr<sub>2</sub>O<sub>3</sub> value is plotted against the standard deviation of Cr<sub>2</sub>O<sub>3</sub> (Fig. 6), NWA 7402 falls off of the general trend defined for typical UOCs (Grossman and Brearley, 2005). However, the analyses of the control specimens Semarkona and Bishunpur generally agree with the literature values, as both fall within 0.05 wt% of the mean Cr<sub>2</sub>O<sub>3</sub> values and within 0.006 wt% of  $\sigma$ - Cr<sub>2</sub>O<sub>3</sub> (Fig. B6) as given in Grossman and Brearley (2005). This anomalous Cr<sub>2</sub>O<sub>3</sub> composition in NWA 7402 is an unusual feature that deserves further study.

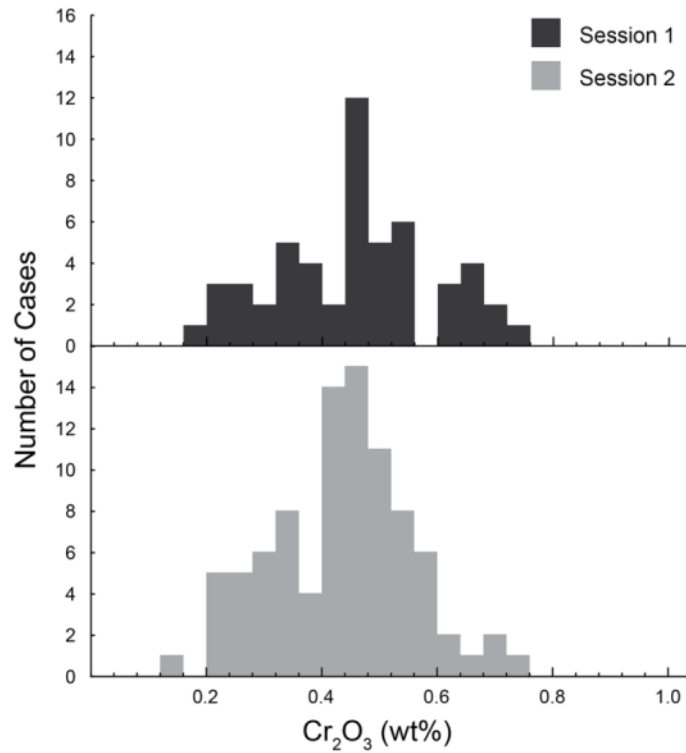


**Figure B5.** Histograms for the chromium content in chondrule olivine grains with FeO > 2 wt% from sessions 1 and 2. The mean values are  $0.41 \pm 0.14$  and  $0.41 \pm 0.12$  wt%, respectively.

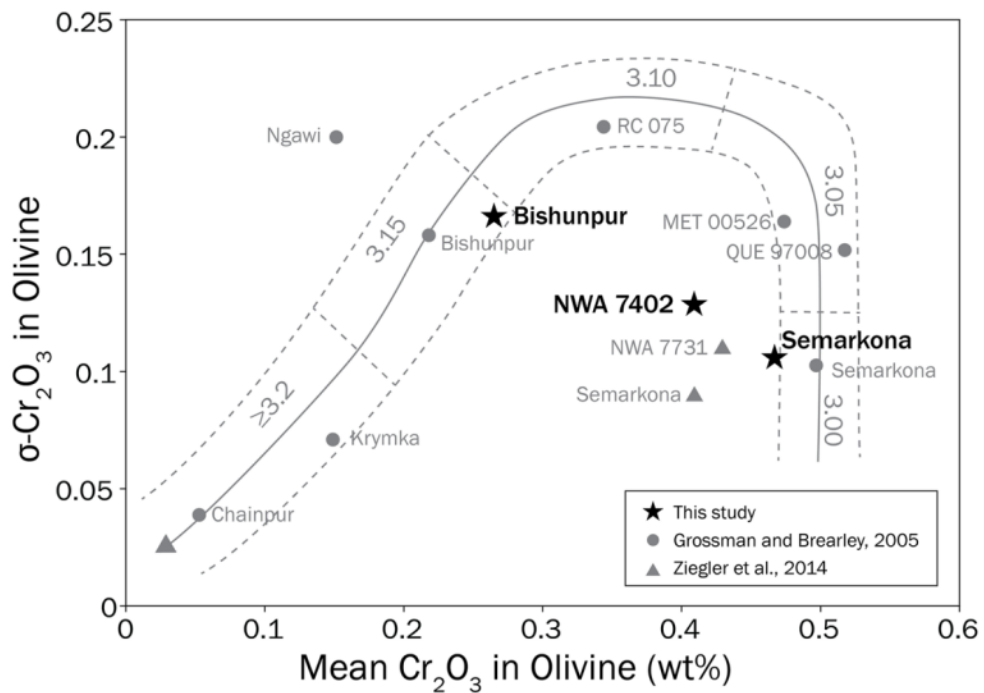


**Figure B6.** A plot of the standard deviation versus the mean of the Cr<sub>2</sub>O<sub>3</sub> content of ferroan olivine (FeO > 2 wt%) for NWA 7402. Semarkona and Bishunpur ordinary chondrites were also

measured to determine relative accuracy. The data in this study are shown as bold stars. Previously measured UOCs from Grossman and Brearley (grey circles; 2005) and Ziegler et al. (grey triangles; 2014) are plotted for reference. The solid grey line represents the approximate UOC trend, while the dashed lines represent the approximate spread for UOC samples (Grossman and Brearley, 2005). NWA 7402 plots away from the typical UOC trend (see text).

To further constrain petrologic type, Raman spectroscopy measurements have been conducted at Laboratoire de Géologie de Lyon (Université Claude Bernard - Ecole Normale Supérieure de Lyon, France). Multiple studies (e.g. Quirico et al., 2003; Bonal et al., 2006, 2007) have shown that the structural order of the polyaromatic organic matter reflects the thermal history experienced by the host meteorite, particularly for low type 3 chondrites. The principle behind this approach is that thermal metamorphism causes irreversible structural, textural, and compositional transformations to organic matter. Raman spectroscopy is sensitive to the degree of structural order of polyaromatic organic matter, with transformations reflected in the spectral parameters of the Raman bands of the polyaromatic organic matter, the so-called D and G bands. (e.g., Bonal et al., 2006). For type 3 chondrites of low-metamorphic grades, the most sensitive spectral parameters are the width and the relative intensity of the D-band and its relative intensity. By comparing these parameters to reference samples, a relative petrologic type can be assigned. This method has successfully been applied to CV, CO, and unequilibrated ordinary chondrites. Using similar experimental methods to those employed by Bonal et al. (2006, 2007), matrix material was separated (<50 mg) and measured via Raman spectroscopy. Spectral parameters for the D and G bands were fit with Lorentzian and Breit-Wigner Fano mathematical profiles, respectively. Fig. B7 depicts the full width at half-max (FWHM) of the D band versus the ratio of the peak intensities (I) for the D and G bands. NWA 7402 is plotted in black, with other classified chondrites plotted in gray to be used as petrologic anchors. The proximity of NWA 7402 to Bishunpur (LL3.15) indicates that NWA 7402 should be considered petrologic type 3.1.

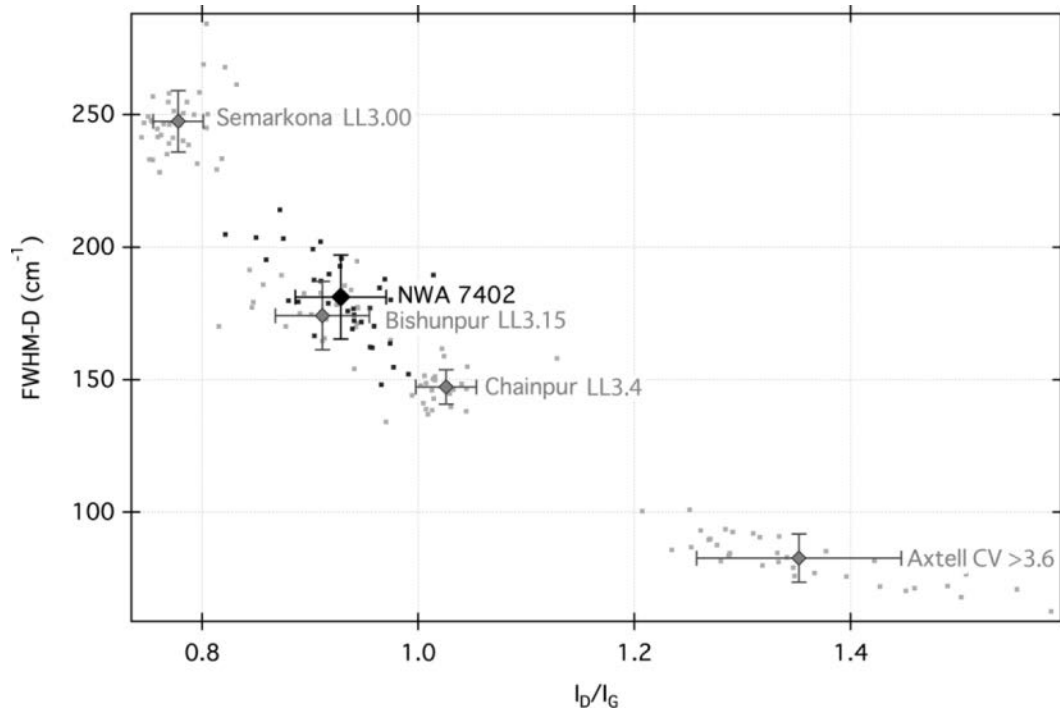


**Figure B7.** To characterize the maturity of the matrix carbonaceous material in NWA 7402, we compare Raman spectral parameters. Plotted are the FWHM of the Raman D band ( $\text{cm}^{-1}$ ) versus the ratio of peak intensities for the D and G bands,  $I_D/I_G$ . Small dots represent the individual data points, while the large points with error bars represent the weighted averages of all measurements and  $2\sigma$  standard deviation. The point in black is NWA 7402, plotting close to Bishunpur (LL3.15) shown in gray. Gray points are well-known petrologic type 3 chondrites. Lower petrologic types trend toward the upper left of the diagram; down and to the right are higher metamorphic grade type 3's.

### B.3.3 Weathering grade.

The degree of weathering is heterogeneous in all samples of NWA 7402. Highly weathered portions can be distinguished by the rust-colored staining of the sample (Fig. B1), and by Fe-oxide veins easily seen in the SEM or in reflected light. Highly weathered sections show some replacement of metal to Fe oxides and widespread veining along grain boundaries. Less weathered portions do not exhibit extensive veining and nearly all metal grains remain unoxidized. Weathering is most severe approaching the fusion crust, but also occurs in large rusty patches on the meteorite interior, presumably due to fractures exposing the interior to the oxidizing terrestrial conditions.

To assess the terrestrial weathering stage of the meteorite, polished thin sections were examined using the optical microscope employing the methods of Wlotzka (1993). The less altered regions on the interior of the meteorite show minor oxide veins and alteration of Fe-rich phases, particularly around the edges of large metal-sulfide assemblages, consistent with W1 classification. However, the more weathered portions of the meteorite show at least moderate oxidation of metal with about 20-60% being affected, consistent with W2 grade.

#### **B.3.4 Shock classification.**

The methods proposed by Stöffler et al. (1991) were used to assess the degree of shock in NWA 7402. Most olivines studied showed undulatory extinction and irregular fractures, and a few rare instances of planar fractures and mosaicism exist. To classify the stage of shock for a breccia with a complicated history, Stöffler et al. (1991) suggest that the assigned stage should be the best estimate of the peak shock pressure experienced by the whole rock. For this reason we suggest that the chondrite be classified as shock stage S2 (weakly shocked). While one ~ 4mm impact melt inclusion occurs in the NWA 7402 breccia, the remainder of the specimen does not have extremely shocked lithologies, implying that the material is not part of a polymict breccia lens formed after impact (Stöffler et al., 1991). The variety of shock phases present in the samples suggests that the meteorite may be a fragmental or regolith breccia that incorporated spalled fragments from an impact. This classification has some uncertainty due to the heterogeneity of a type 3 brecciated chondrite.

### **B.4 DISCUSSION**

NWA 7402 has experienced little thermal metamorphism and aqueous alteration, making it a valuable meteorite for studying early Solar System processes. However, NWA 7402 also displays attributes that are unusual for unequilibrated ordinary chondrites. The elevated sulfide abundance and anomalous chromium content of olivines suggests NWA 7402 may have an anomalous origin.

#### **B.4.1 Sulfide abundances in Ordinary Chondrites.**

The high abundance of sulfides (18.1 wt%) in NWA 7402 is well beyond the norm for ordinary chondrites, which typically have 5-7 wt% sulfides (e.g., Gomes and Keil, 1980). However, elevated abundances of approximately 9 wt% troilite have been reported for the low petrologic type ordinary chondrites Moorabie (L3.8-an) and Suwahib Buwah (H3.8-an; McCoy et al., 1994), and some equilibrated L chondrites contain up to 10.3 wt% troilite (Dunn et al., 2010). Although these samples are not as sulfide-rich as NWA 7402, there appears to be more variability in ordinary chondrite sulfide abundances than is generally appreciated.

Most of the sulfides observed in NWA 7402 occur in sulfide-rich chondrule rims, or in metal-sulfide assemblages. Fine-grained sulfides found in the chondrule rims and matrix of NWA 7402 are characteristic of primitive type 3 ordinary chondrites (Allen et al., 1980; Nagahara, 1984; Agee et al., 2013). Upon heating and increasing petrologic type, S is mobilized and sulfide grains coalesce and grow larger (Lauretta et al., 1997; Grossman and Brearley, 2005; Huss et al., 2006). The kamacite-taenite-troilite assemblages in NWA 7402 are common in UOCs such as Semarkona and Bishunpur (e.g., Rubin et al., 1999). These assemblages may represent the unaltered precursors of rarer carbide-magnetite and Ni-sulfide assemblages described in aqueously altered type 3 UOCs, such as Semarkona (Krot et al., 1997; Brearley and Jones, 1998; Rubin et al., 1999; Huss et al., 2006). No carbide-magnetite assemblages were found in NWA 7402. The retention of such primary Fe-sulfide features and lack of Ni-sulfides reflect the extremely unaltered nature of NWA 7402, and may help to explain the high S abundance.

#### **B.4.2 Anomalous chromium composition of iron-bearing olivines.**

While NWA 7402 shares many traits with other UOCs, the anomalous Cr<sub>2</sub>O<sub>3</sub> composition sets it apart. Descriptions of another new African find, NWA 7731, are very similar to NWA 7402 (Agee et al., 2013; Ziegler et al., 2014; Ziegler and Agee, 2014). Both contain abundant sulfur-rich opaque matrix, are highly primitive, and NWA 7731 plots within 0.02 wt% Cr<sub>2</sub>O<sub>3</sub> of NWA 7402 in Fig. B6. While the Cr content may suggest that these two stones are related, we note that the Cr<sub>2</sub>O<sub>3</sub> obtained for Semarkona in the Ziegler et al. (2014) study are

shifted by nearly 0.1 wt % from the Grossman and Brearley (2005) values (Fig. B6). If this shift indicates a systematic calibration issue for EPMA analyses, then the NWA 7731 data would also be affected, and may not be in proximity to NWA 7402 after all.

## B.5 CONCLUSION

We utilized a variety of micro-analytical methods for classification of the previously unclassified NWA 7402. The abundance and variety of components suggests that NWA 7402 is an unequilibrated ordinary chondrite. The modal metal abundance (7.8-10.7 wt% Fe,Ni metal) further suggests that NWA 7402 is a member of the L chondrites. FeO contents of olivine and pyroxene revealed the highly unequilibrated nature of the sample, suggesting low petrologic type. Raman spectroscopy of organic matter in the fine-grained matrix indicates that the sample has undergone little thermal metamorphism, and should be considered of petrologic type similar to Bishunpur (3.15). Electron microprobe measurements of chromium contents in olivine generally agree that NWA 7402 lies between types 3.00 and 3.15, but falls off the trend for typical UOCs. Such anomalous chromium content complicates the petrologic type classification, and therefore NWA 7402 remains an L3.1 until additional observations can justify a more accurate petrologic type. Optical microscopy reveals that the sample has experienced moderate shock and weathering, corresponding to maximum stages S2 and W2, respectively. The largest inconsistency with this classification is the elevated sulfide abundance in NWA 7402 (>15 wt%), which may be a reflection of the minimal aqueous alteration. We therefore suggest that the meteorite is categorized as a sulfide-rich L3.1 UOC, weathering grade W1-W2, and shock stage S2. However, the unusual chromium and sulfide abundances suggests that there may be more to its history than meets the eye, making it a good target for further study.

APPENDIX C  
THIN SECTION IMAGES

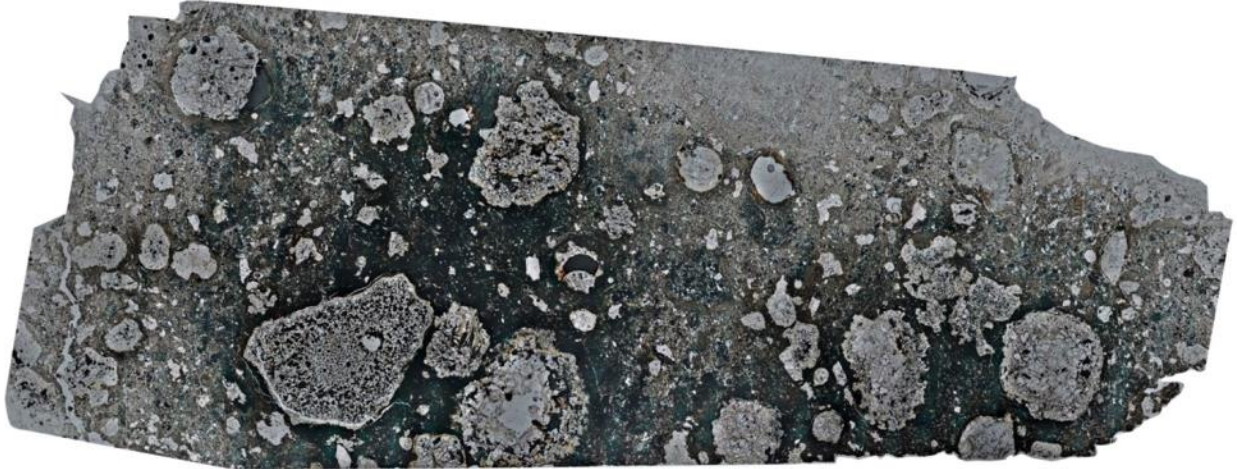


**Figure C1.** Al Rais USNM 6997 Optical microscope (transmitted light) mosaic

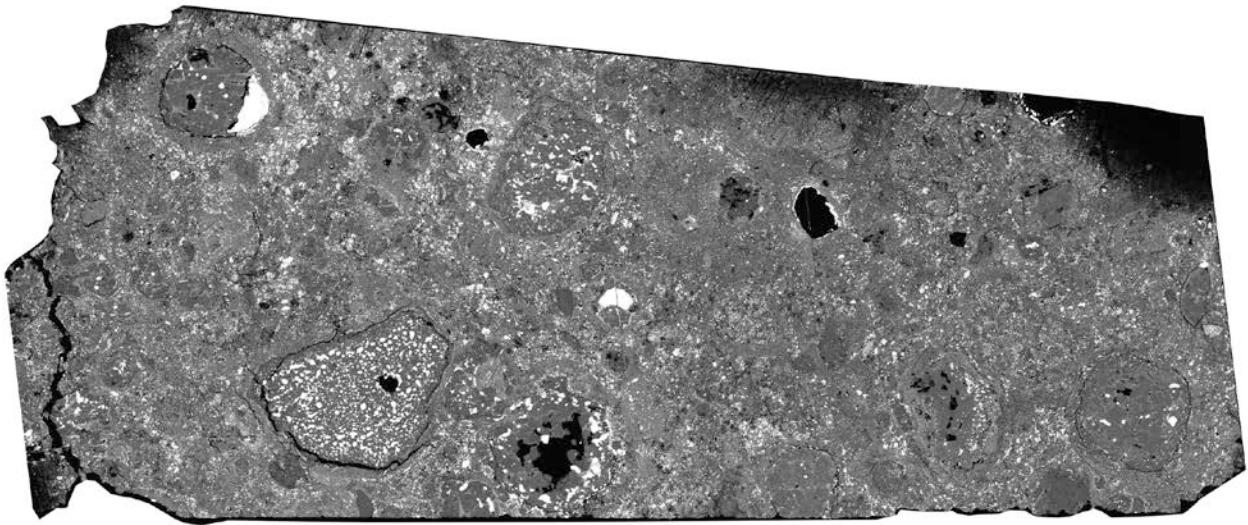


**Figure C2.** Al Rais USNM 6997 Backscattered electron map

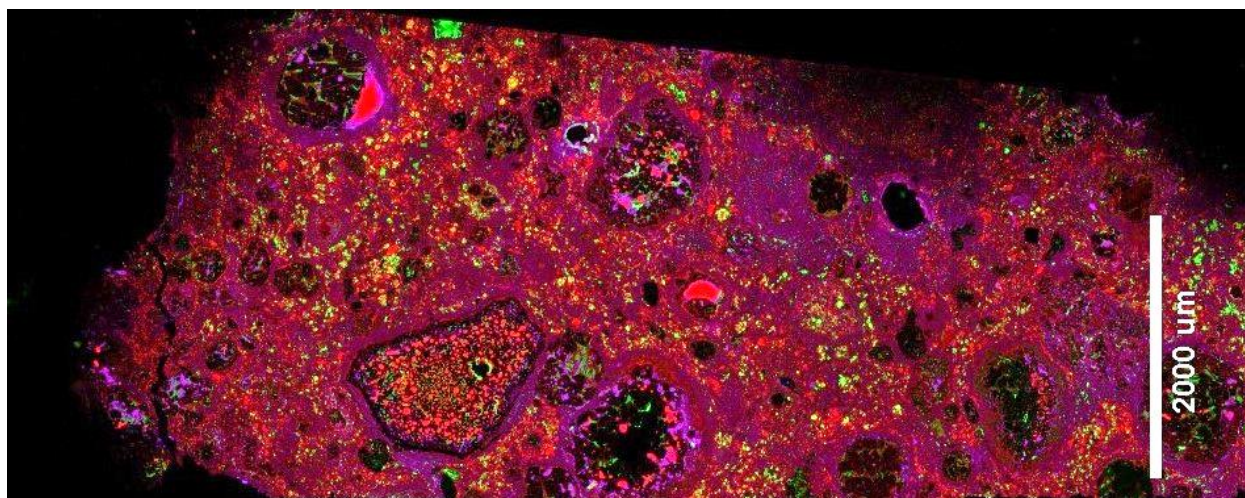


**Figure C3.** Al Rais USNM 6997 X-ray map (RGB = FeCaS)

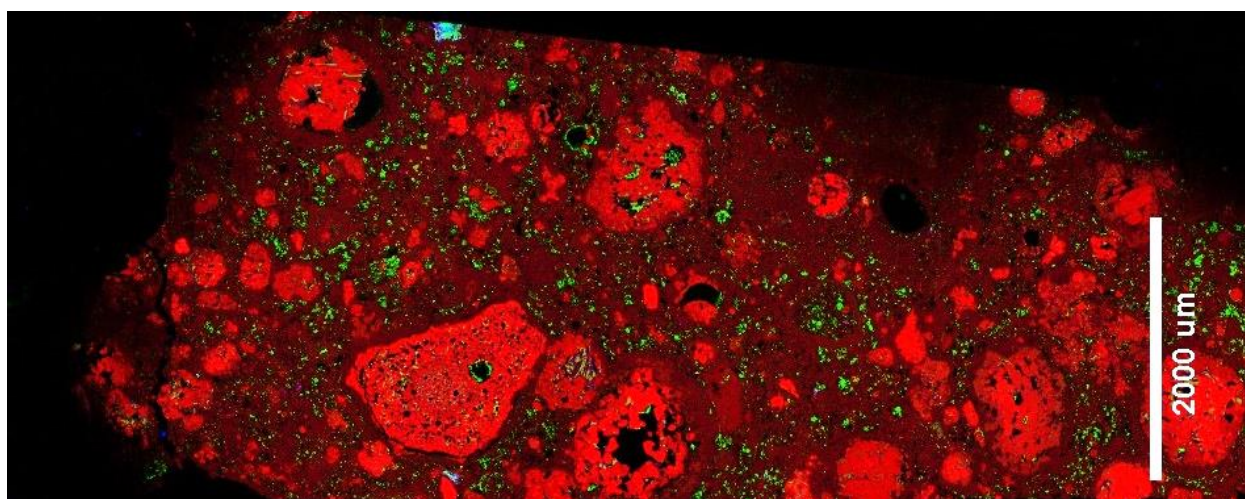


**Figure C4.** Al Rais USNM 6997 X-ray map (RGB = MgCaAl)

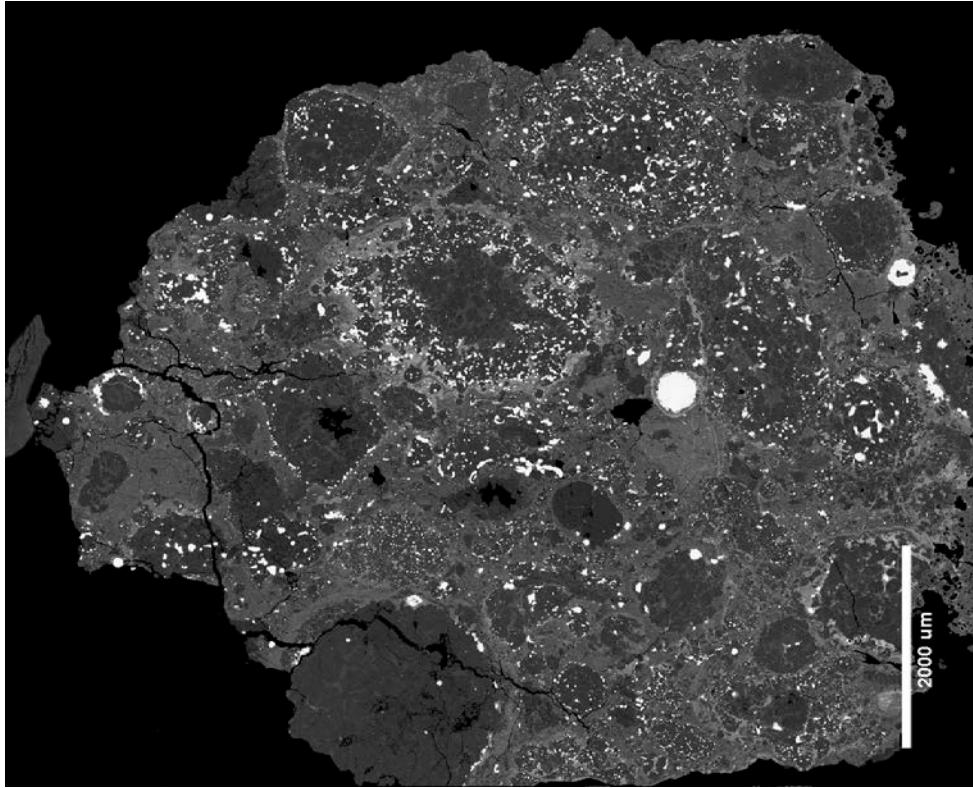


**Figure C5.** EET 87770,30 Backscattered electron map

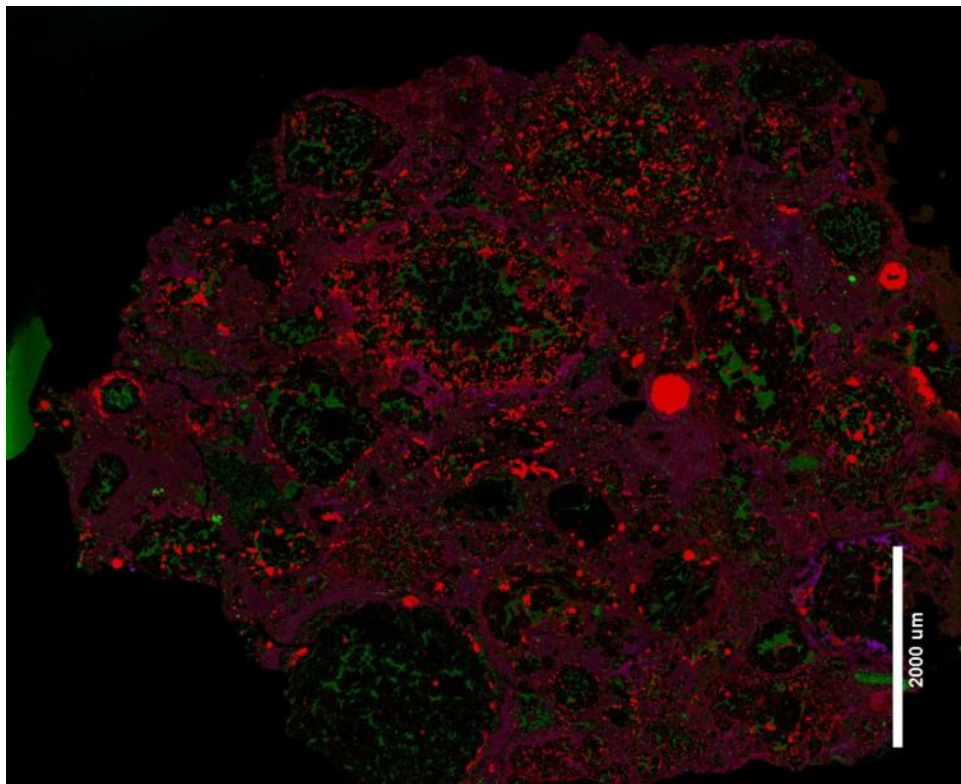


**Figure C6.** EET 87770-30 X-ray map (RGB = FeCaS)

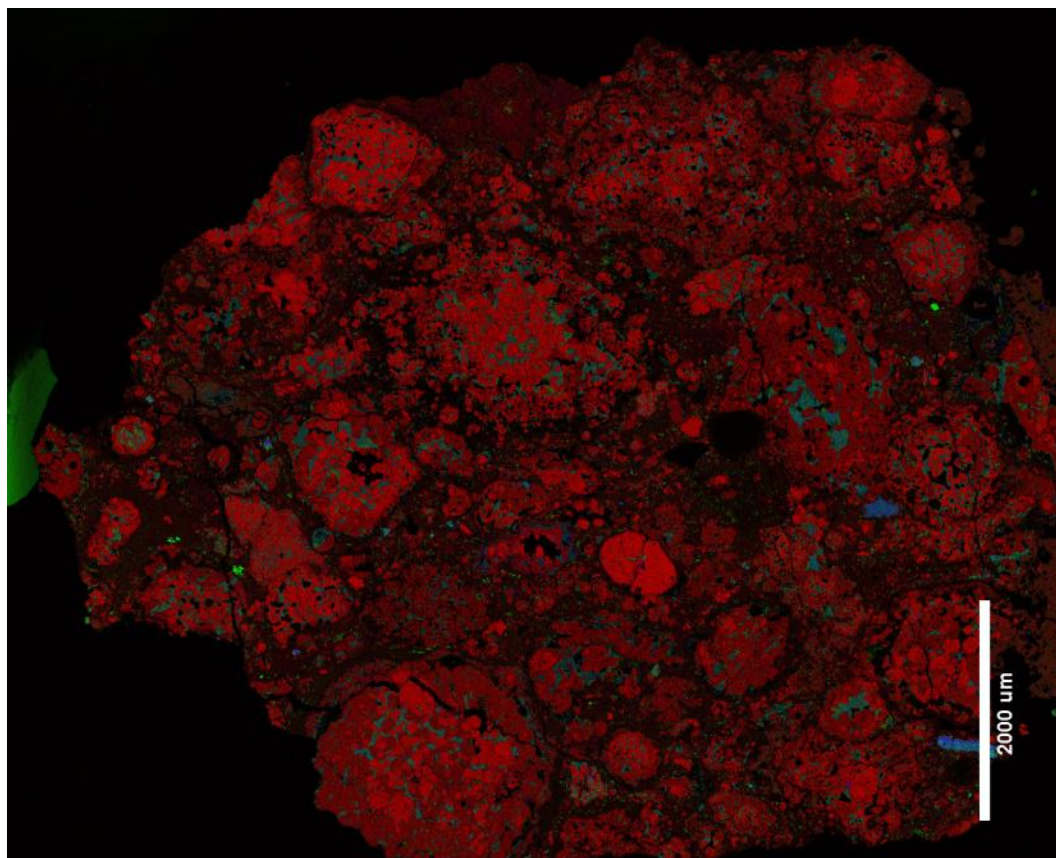


**Figure C7.** EET 87770-30 X-ray map (RGB = MgCaAl)

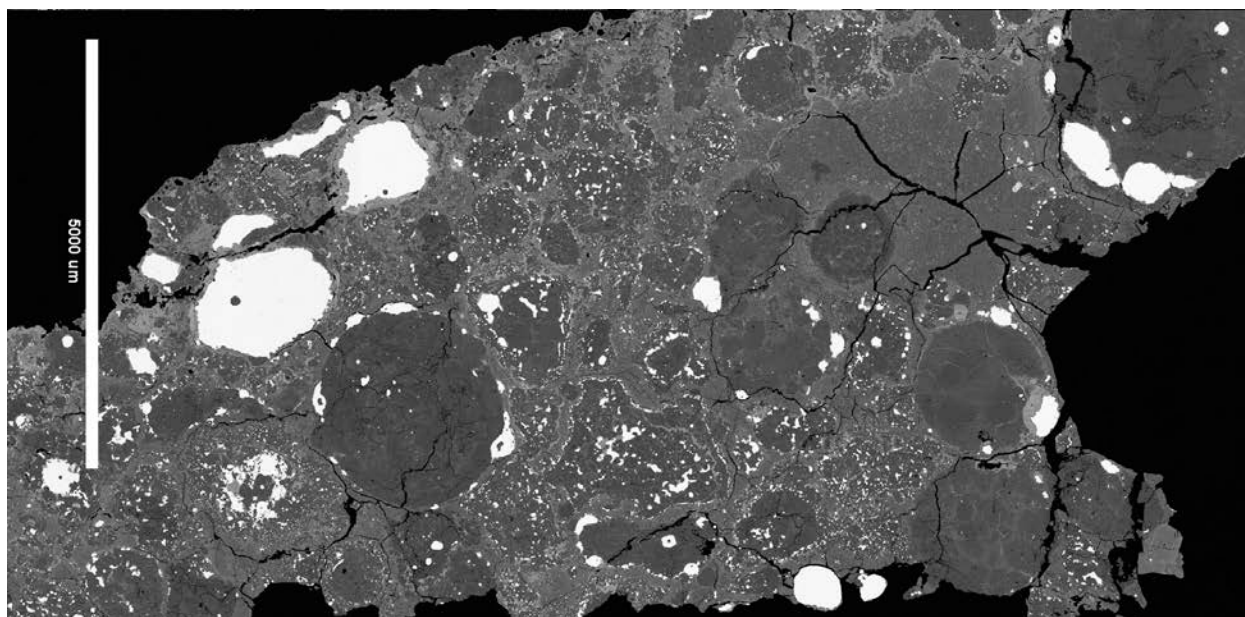


**Figure C8.** EET 92159,20 Backscattered electron map

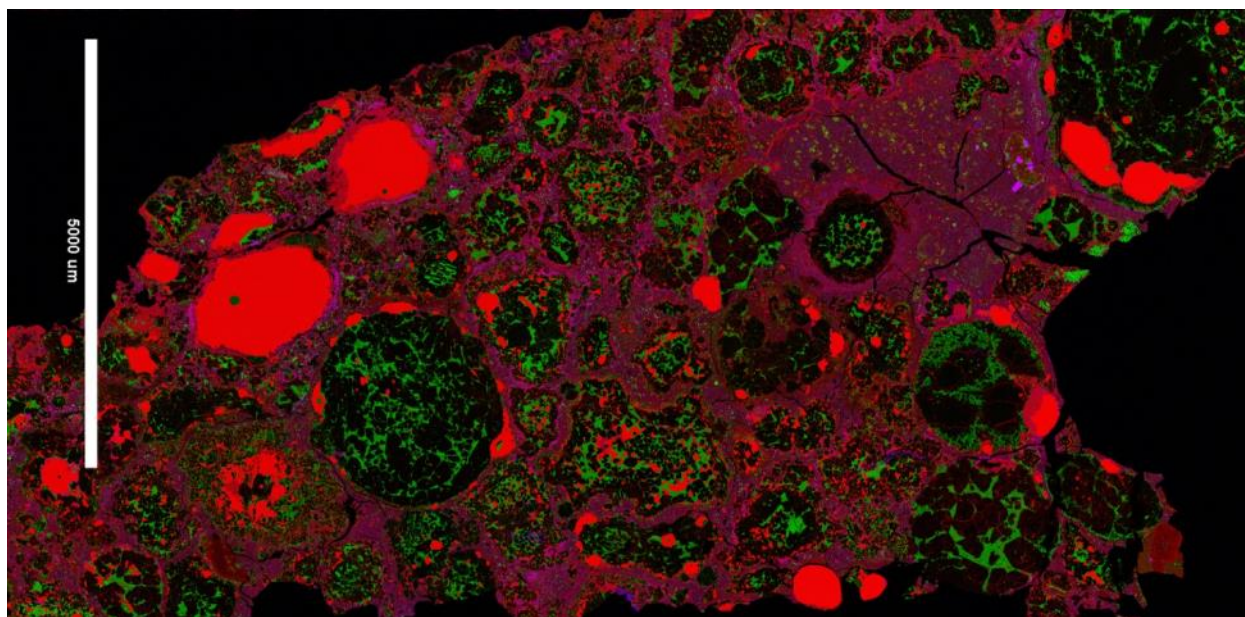


**Figure C9.** EET 92159,20 X-ray map (RGB = FeCaS)

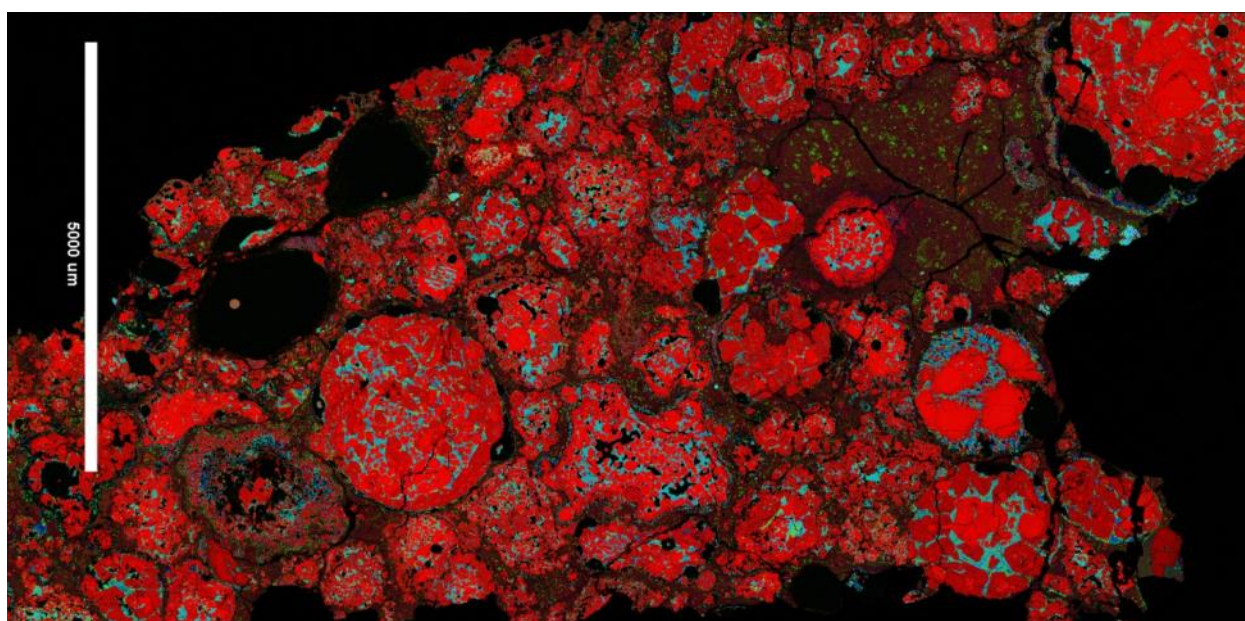


**Figure C10.** EET 92159,20 X-ray map (RGB = MgCaAl)

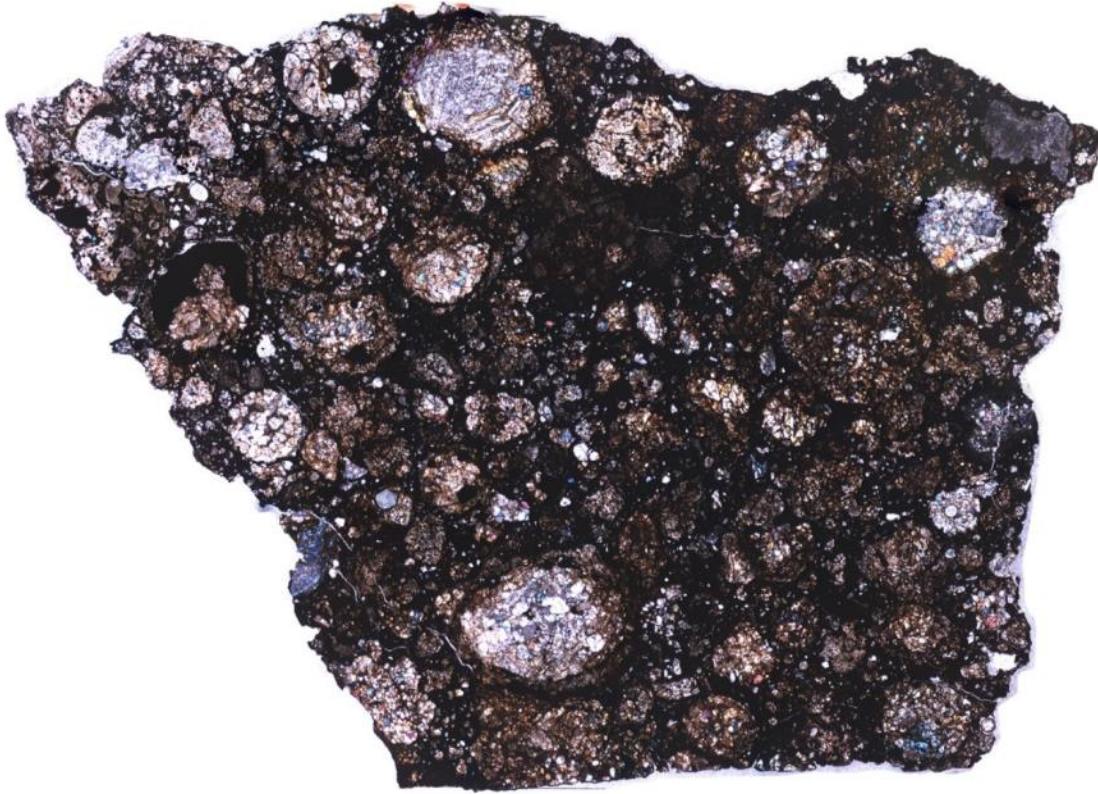


**Figure C11.** GRA 95229,18 Optical microscope (cross-polarized light) mosaic



**Figure C12.** GRA 95229,18 Optical microscope (reflected light) mosaic



**Figure C13.** GRO 95577,69 Optical microscope (reflected light) mosaic



**Figure C14.** GRO 95577,69 Optical microscope (stereo microscope) mosaic

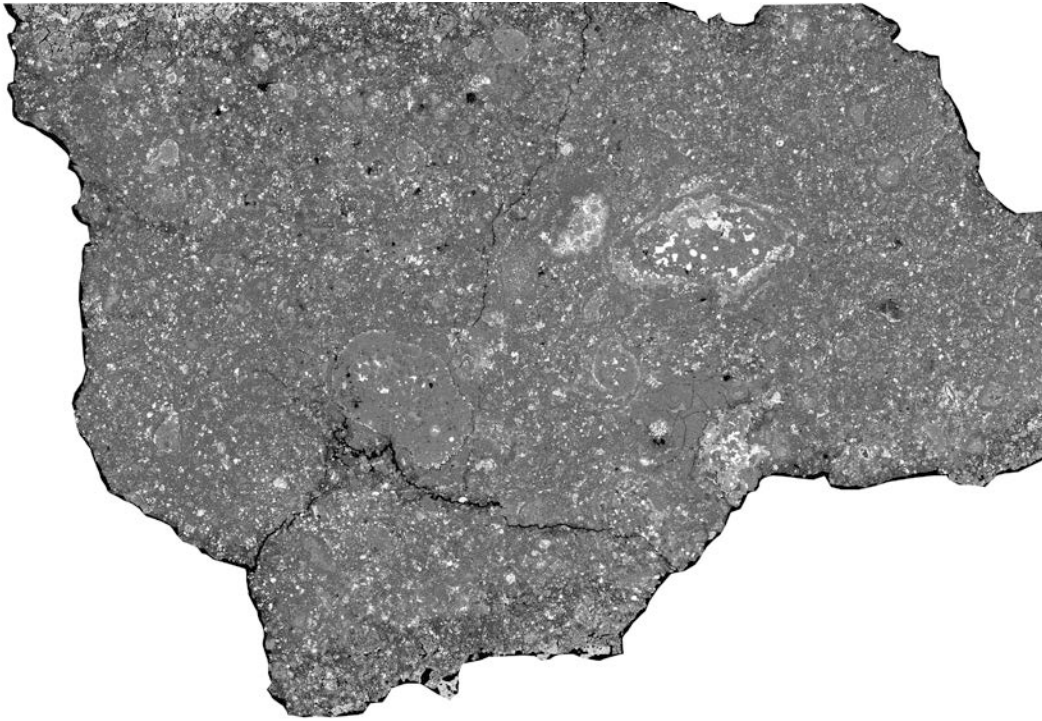


**Figure C15.** GRO 95577,69 Backscattered electron map

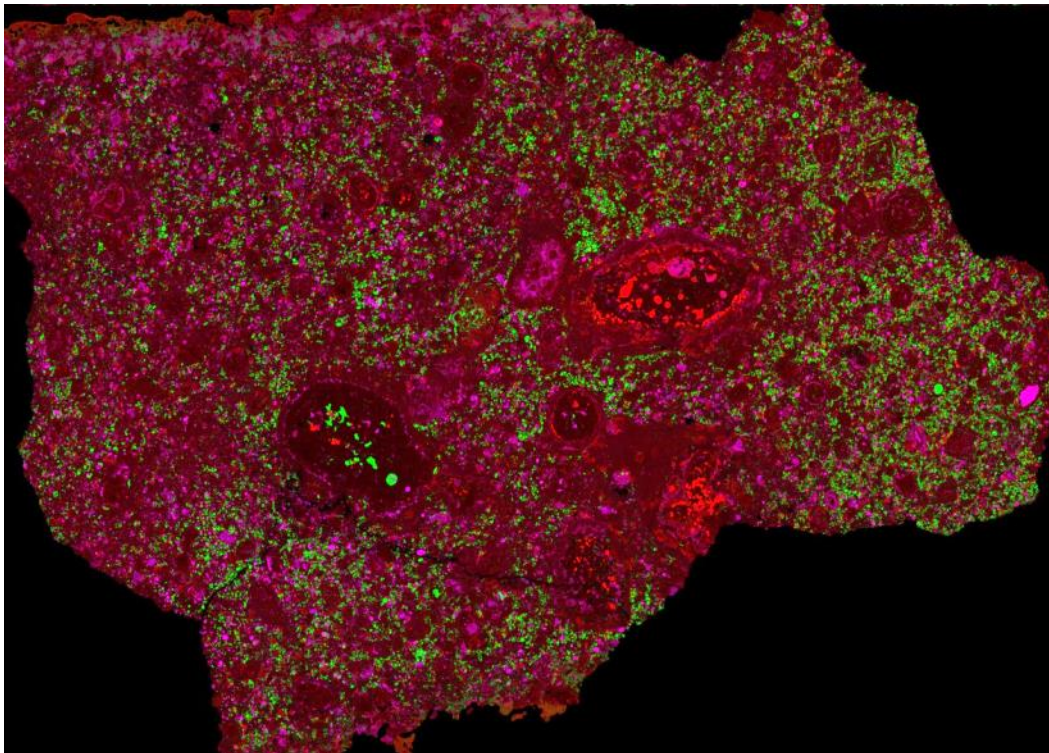


**Figure C16.** GRO 95577,69 X-ray map (RGB = FeCaS)

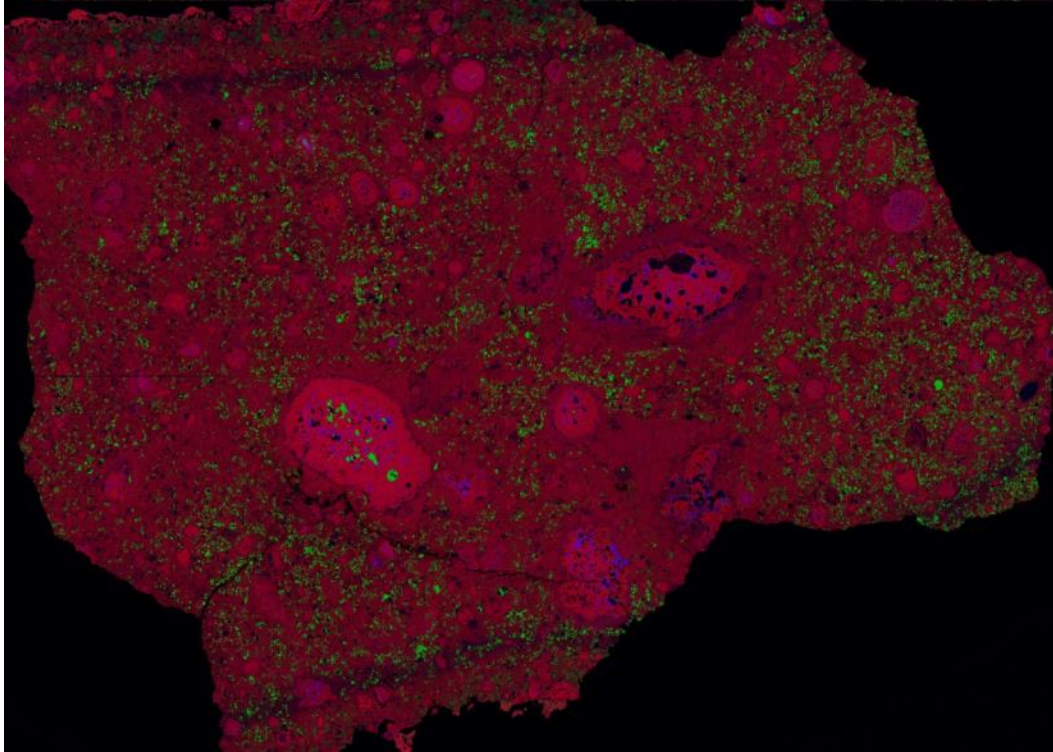


**Figure C17.** GRO 95577,69 X-ray map (RGB = MgCaAl)

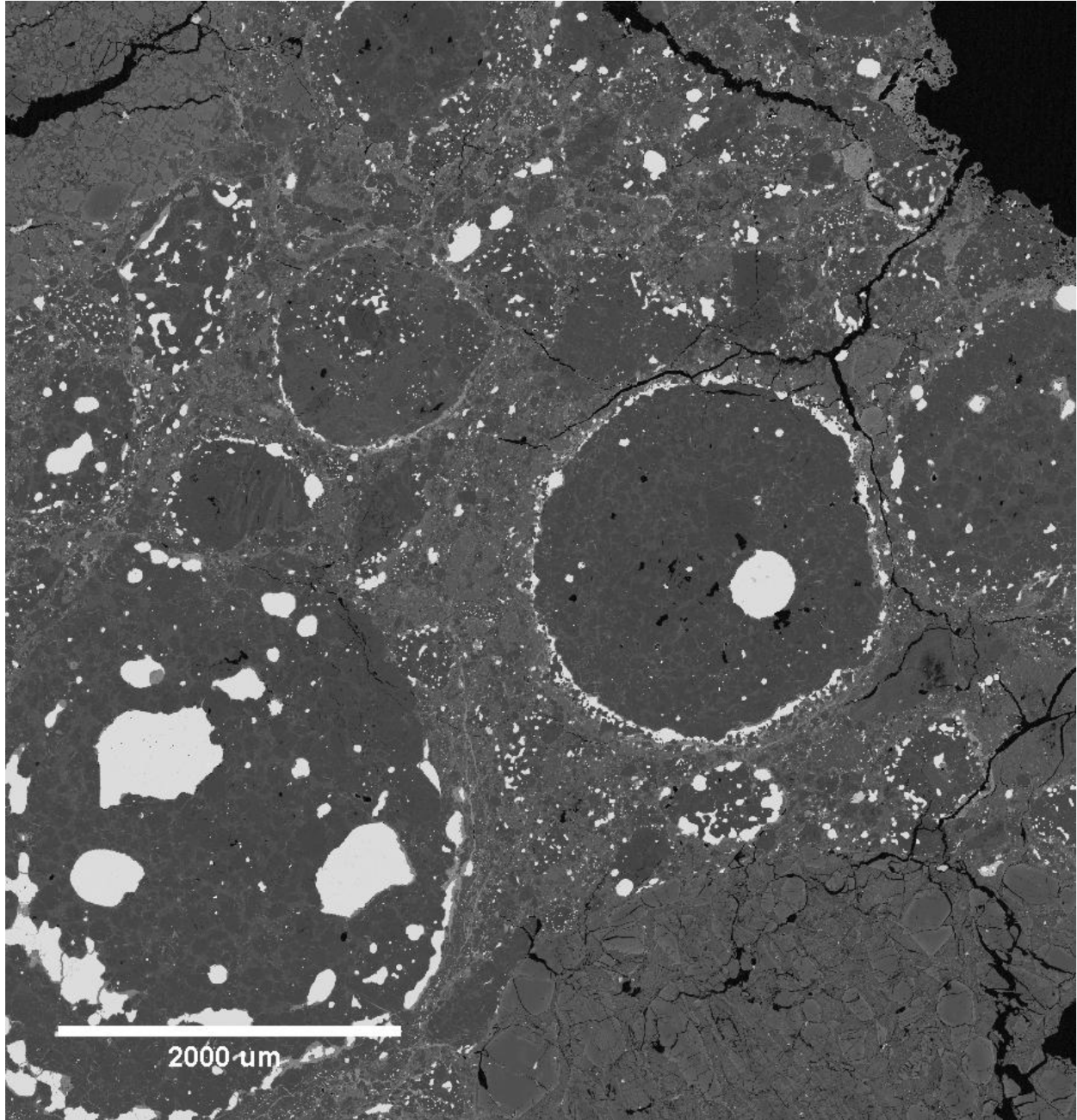


**Figure C18.** MAC 87320,9 Backscattered electron map

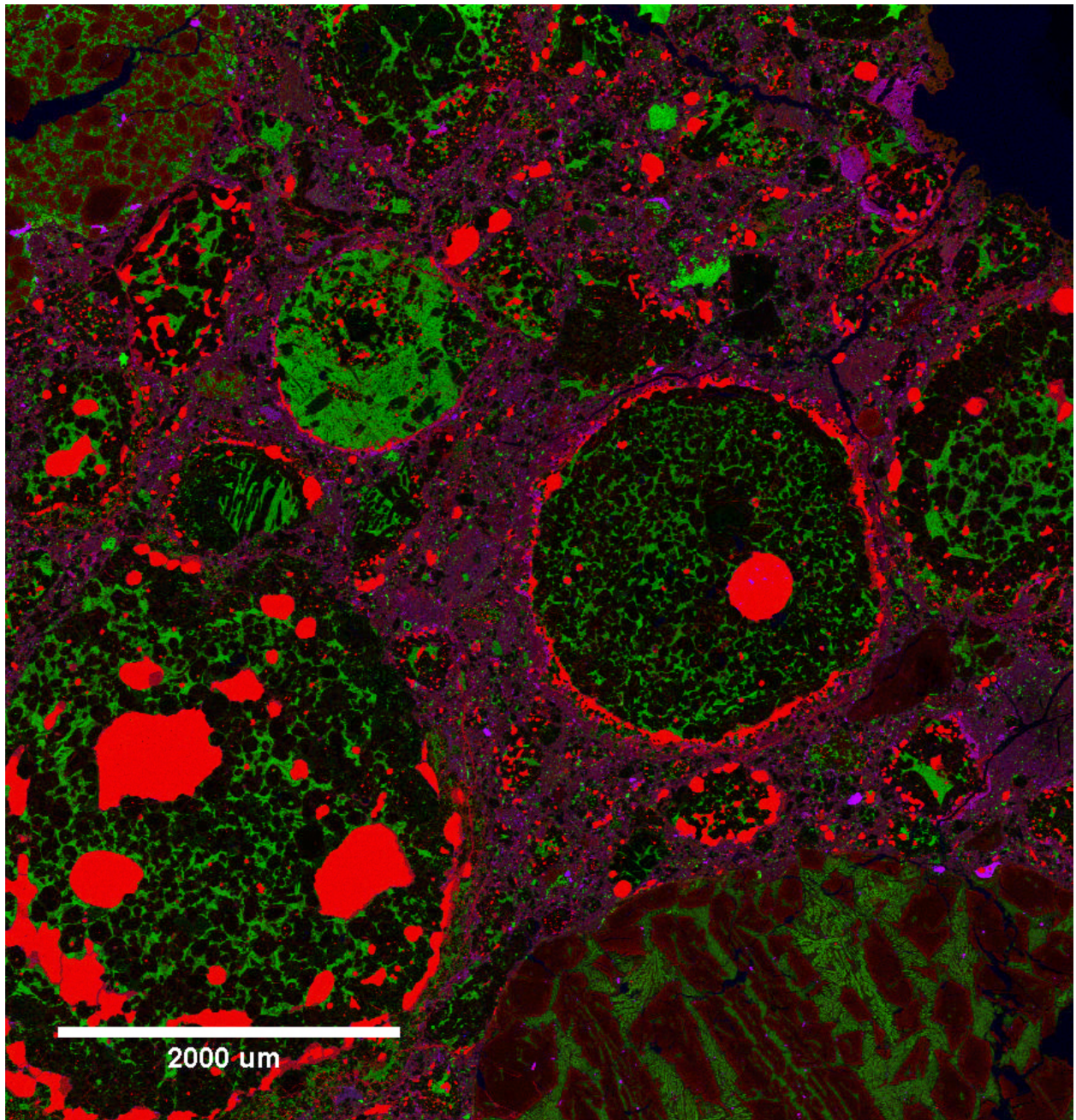


**Figure C19.** MAC 87320,9 X-ray map (RGB = FeCaS)

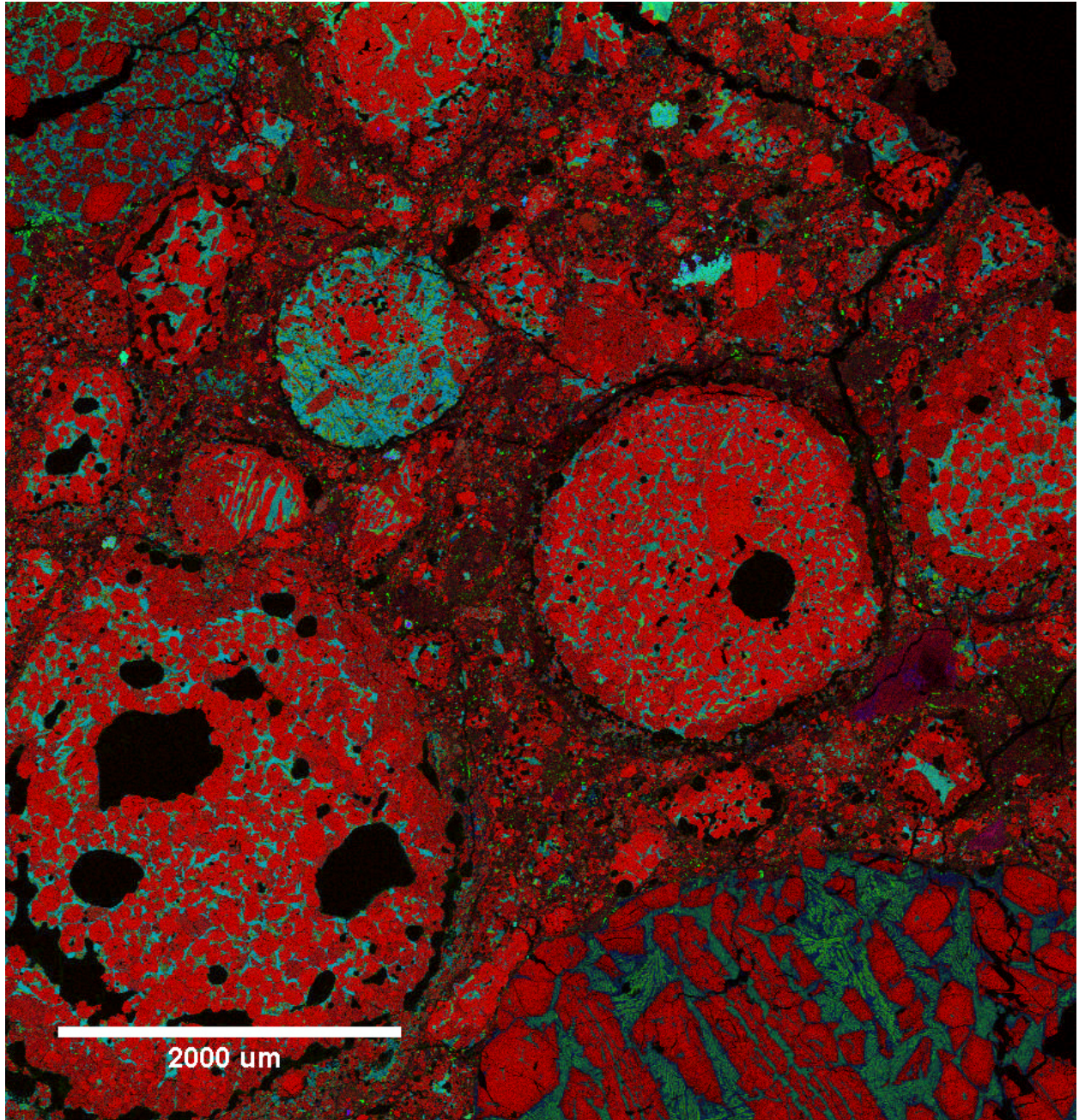


**Figure C20.** MAC 87320,9 X-ray map (RGB = FeCaS)

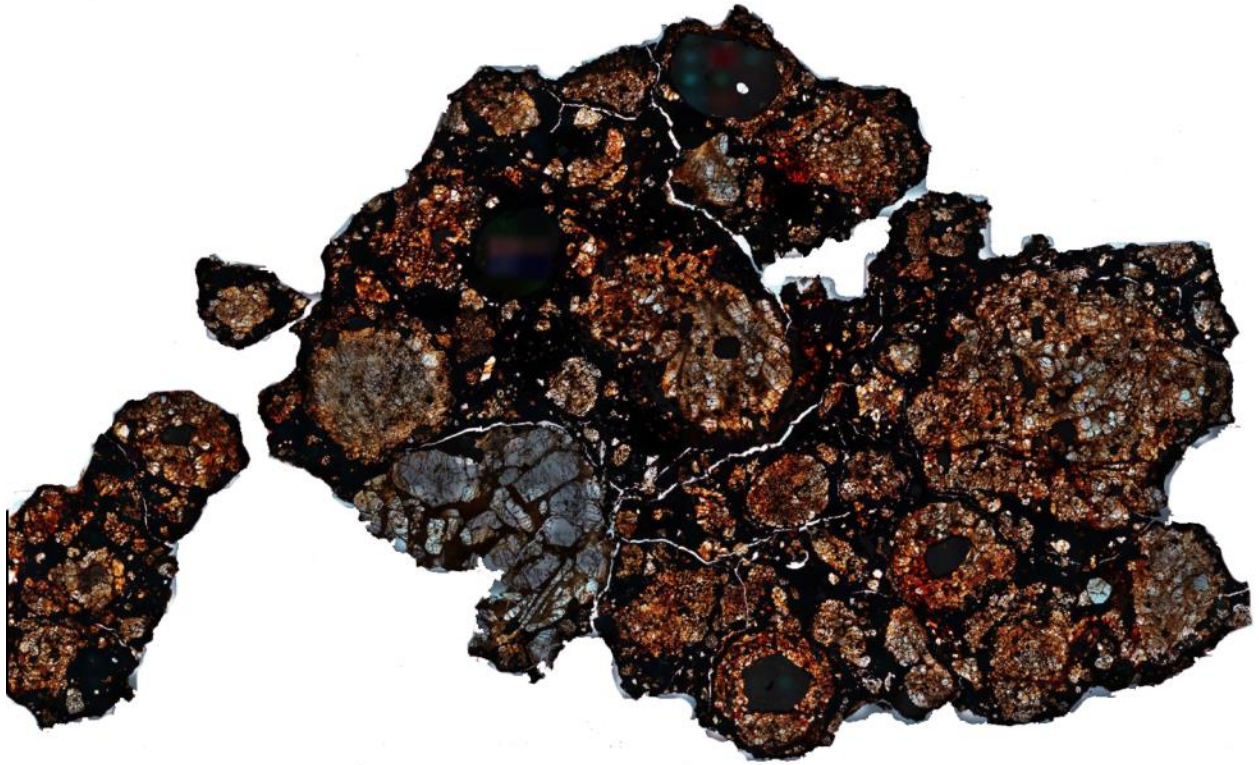


**Figure C21.** MET 00426,60 Optical microscope (transmitted light) mosaic



**Figure C22.** MET 00426,60 Optical microscope (reflected light) mosaic

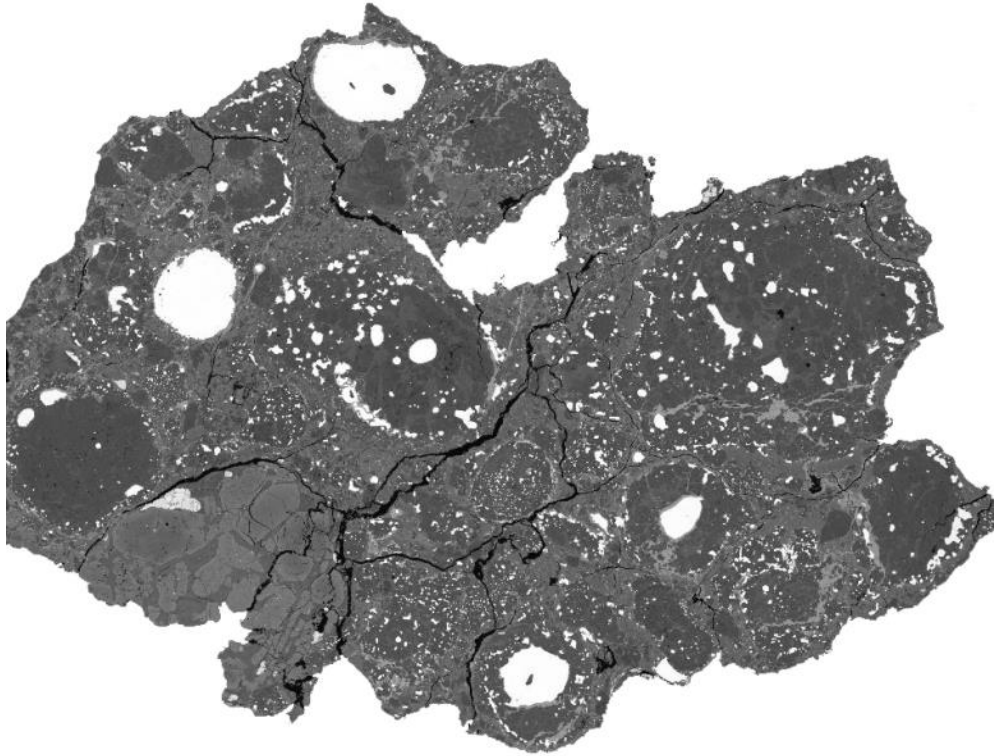


**Figure C23.** MET 00426,60 Backscattered electron map

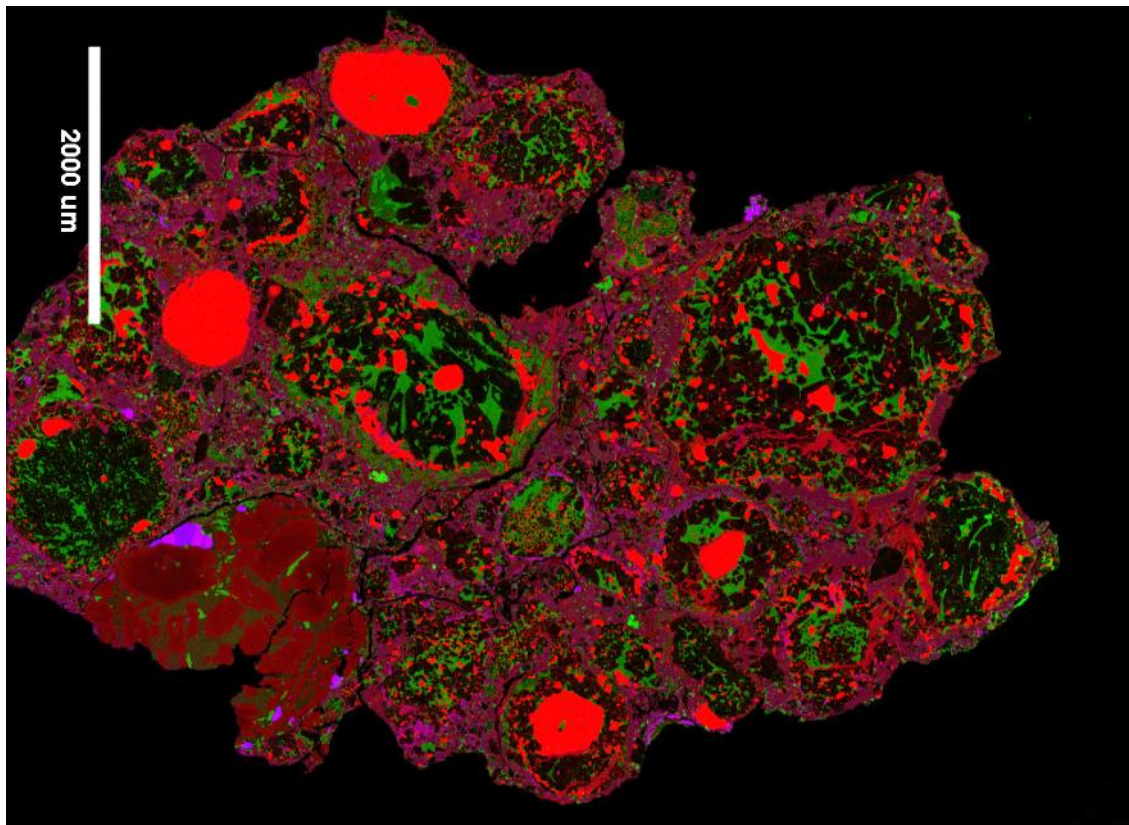


**Figure C24.** MET 00426,60 X-ray map (RGB = FeCaS)

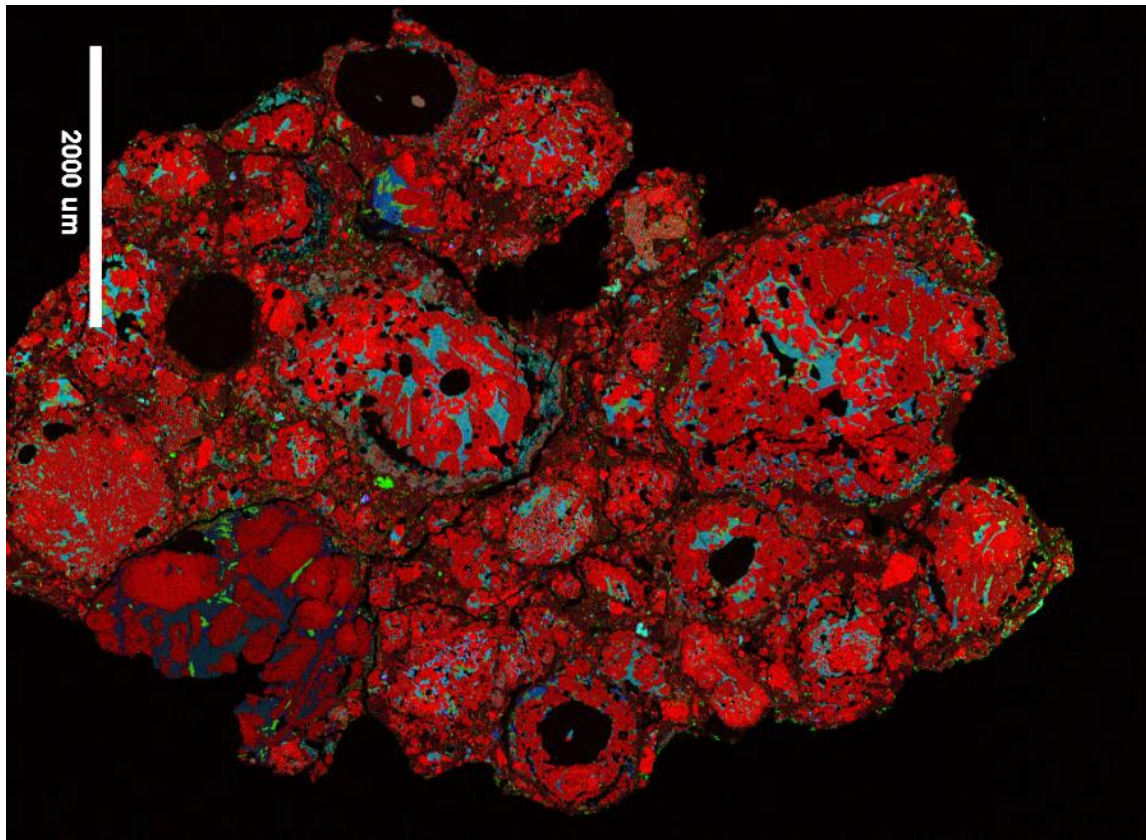


**Figure C25.** MET 00426,60 X-ray map (RGB = MgCaAl)

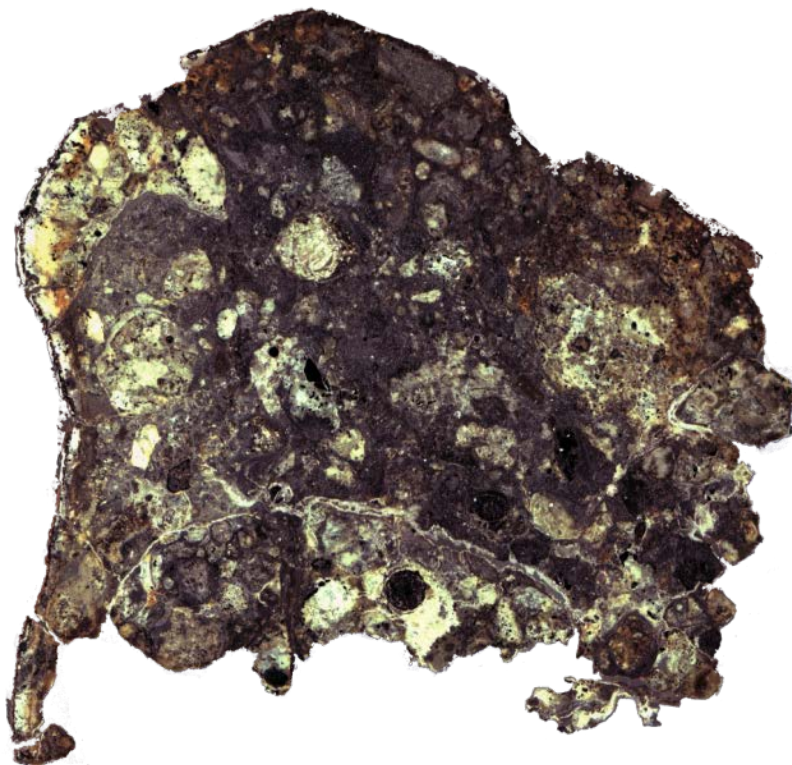


**Figure C26.** MIL 090292,12 Optical microscope (stereo microscope) mosaic

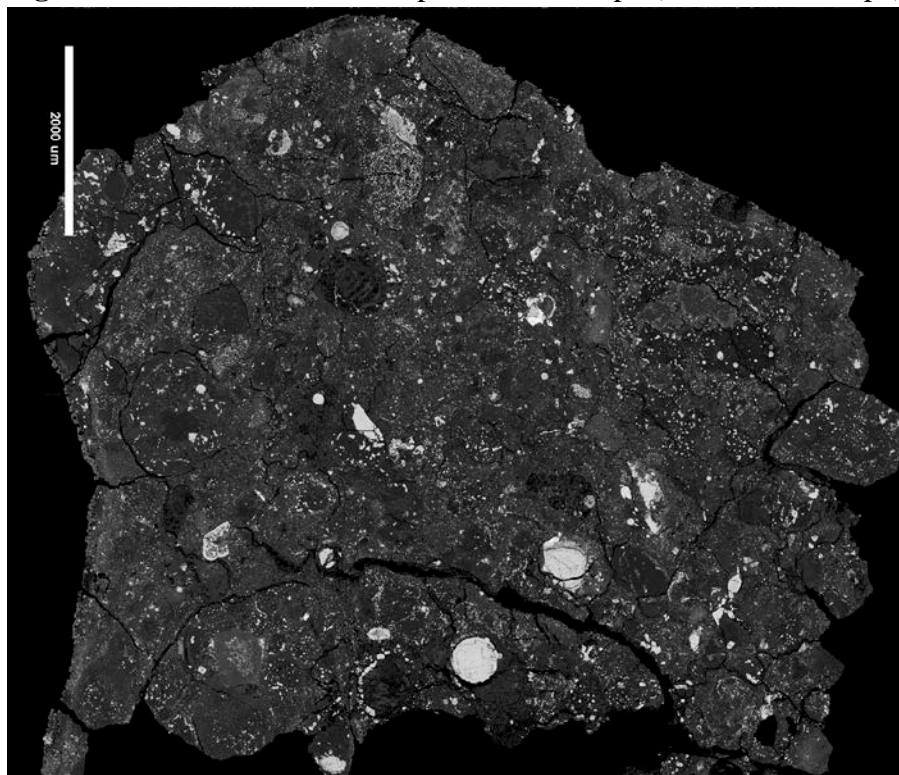


**Figure C27.** MIL 090292 Backscattered electron map

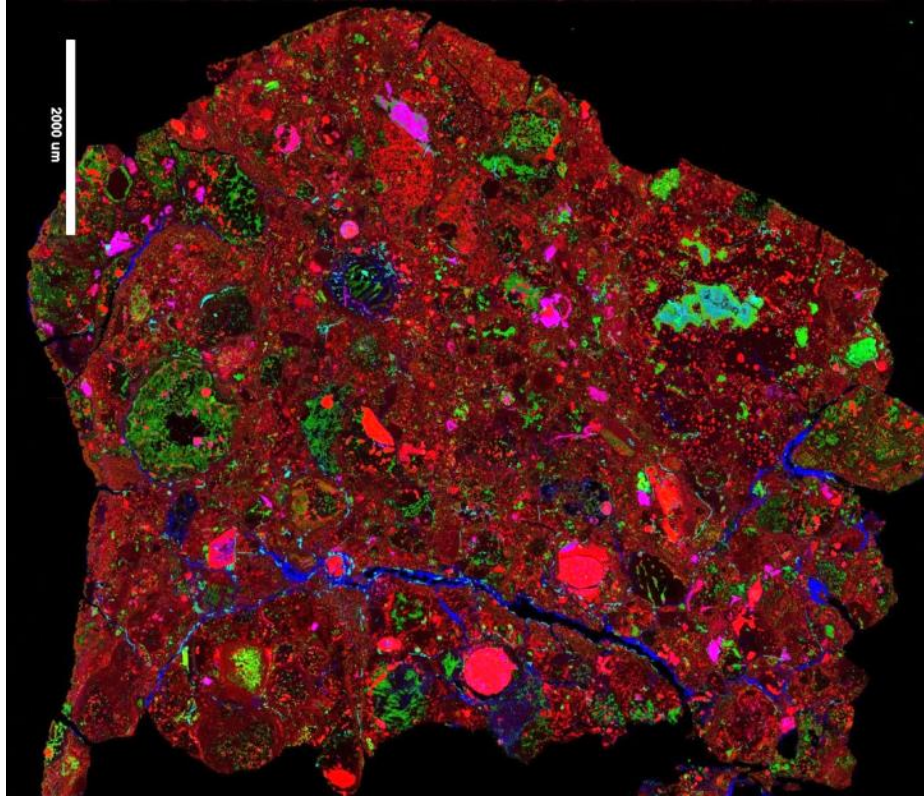


**Figure C28.** MIL 090292,12 X-ray map (RGB = FeCaS)

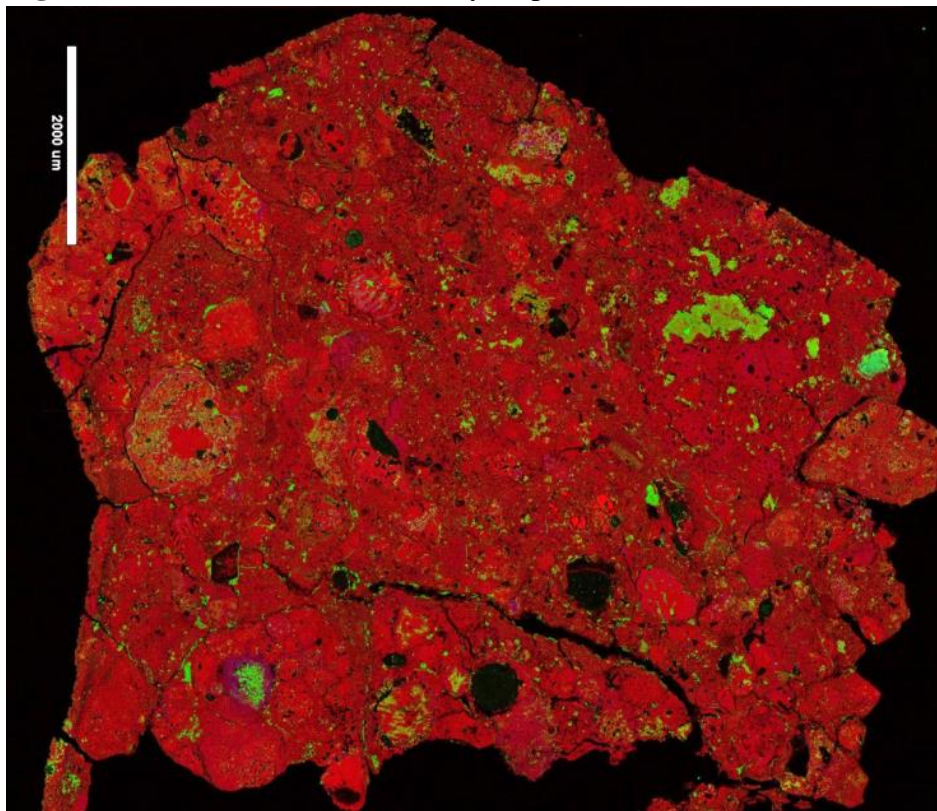


**Figure C29.** MIL 090292,12 X-ray map (RGB = MgCaAl)

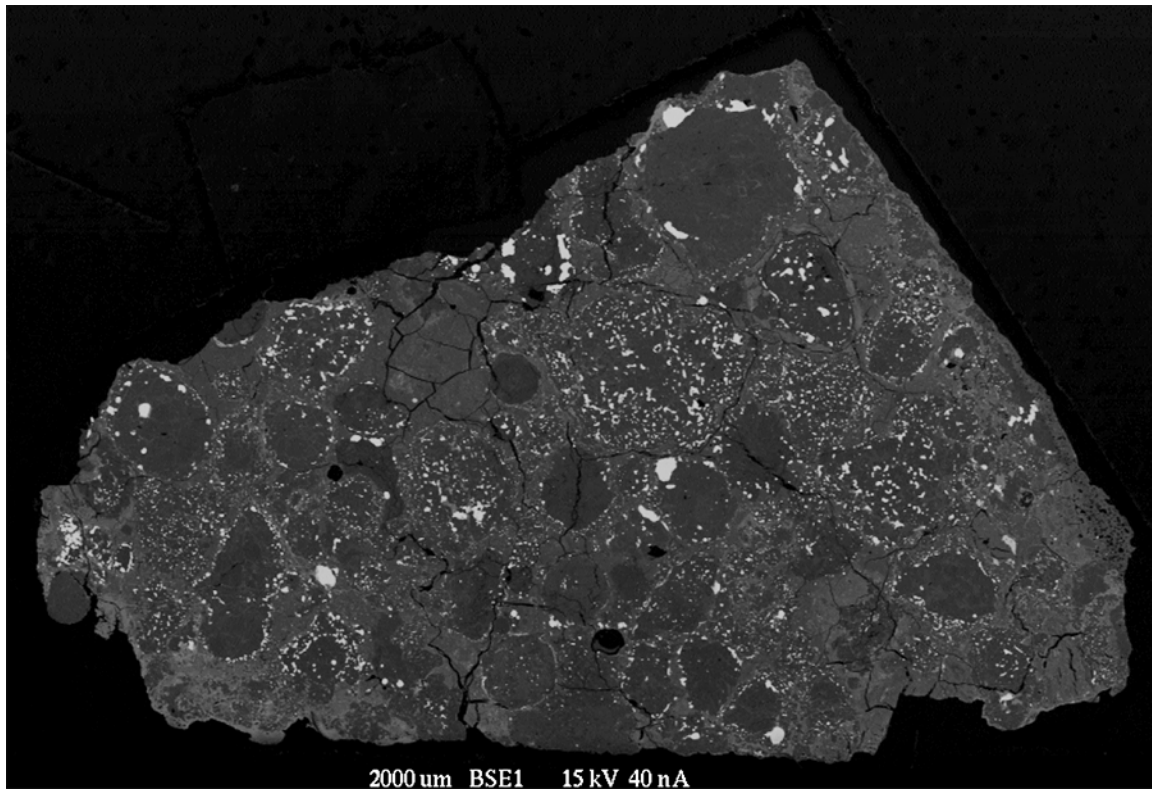


**Figure C30.** QUE 99177,06 Backscattered electron map (image provided by D. Schrader)



**Figure C31.** QUE 99177,69 Optical microscope (reflected light) mosaic

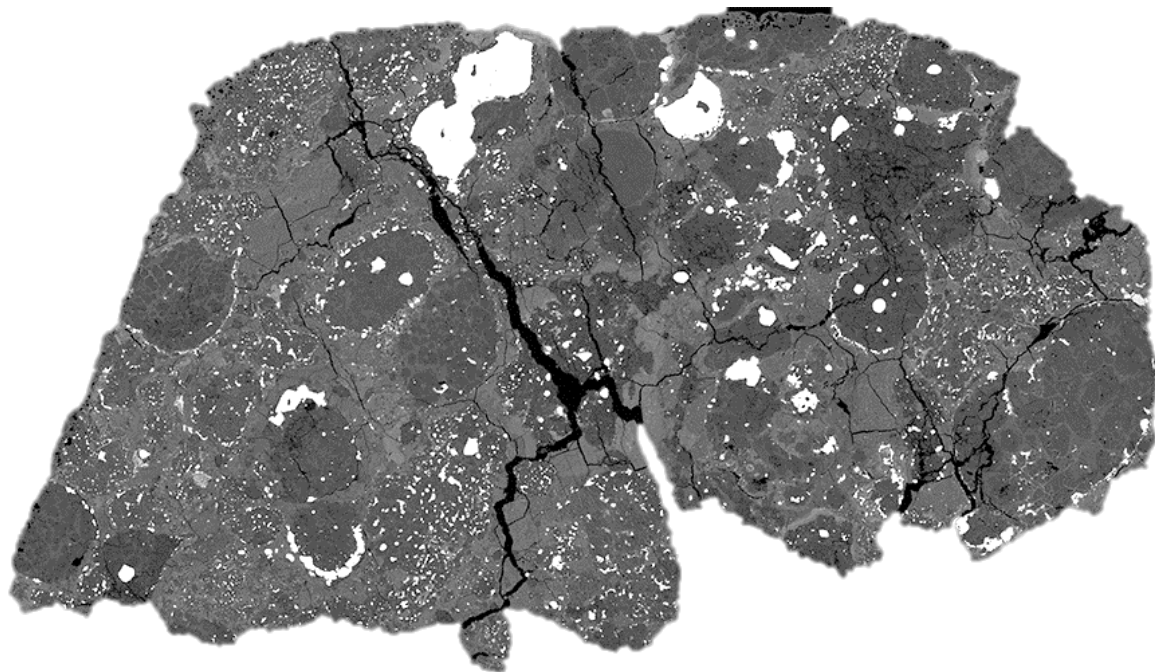


**Figure C32.** QUE 99177,69 Backscattered electron map

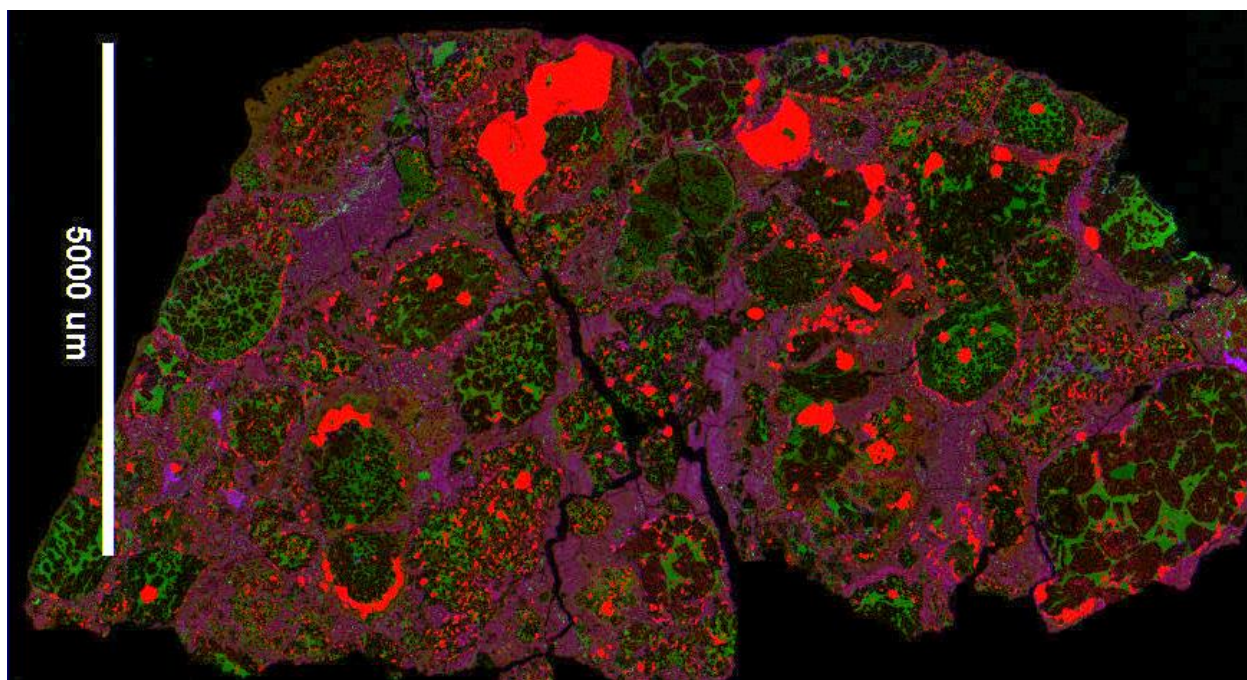


**Figure C33.** QUE 99177, 69 X-ray map (RGB = FeCaS)

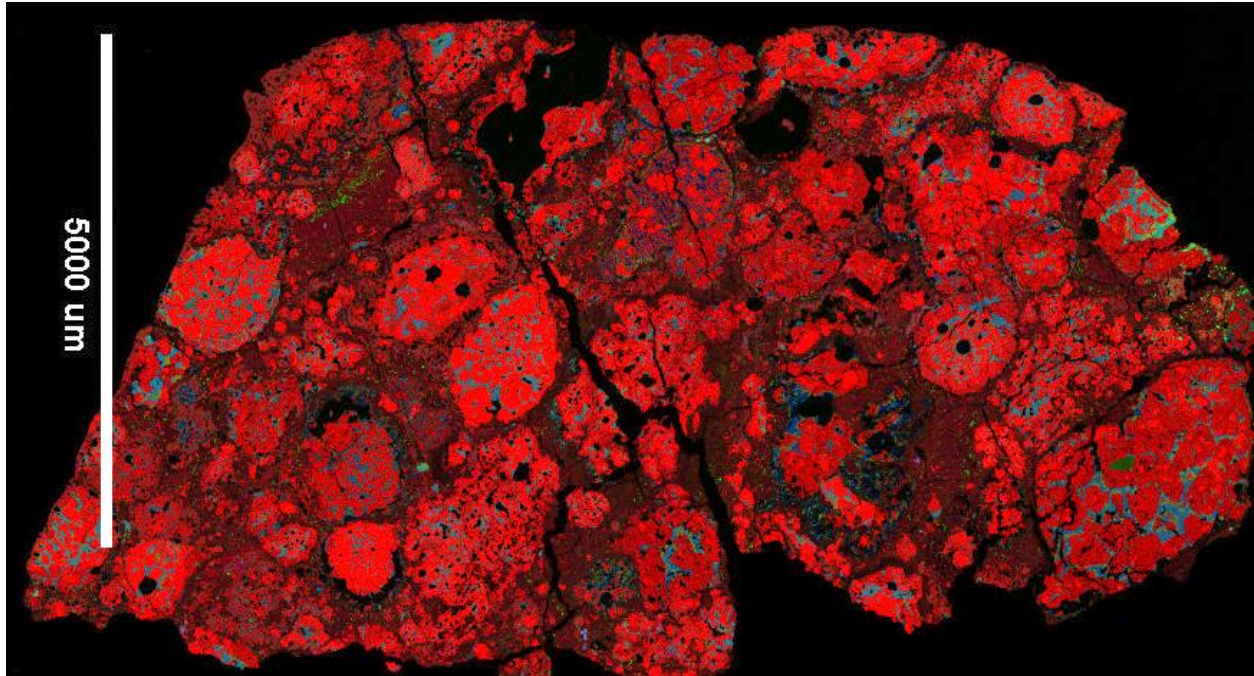


**Figure C34.** QUE 99177, 69 X-ray map (RGB = MgCaAl)

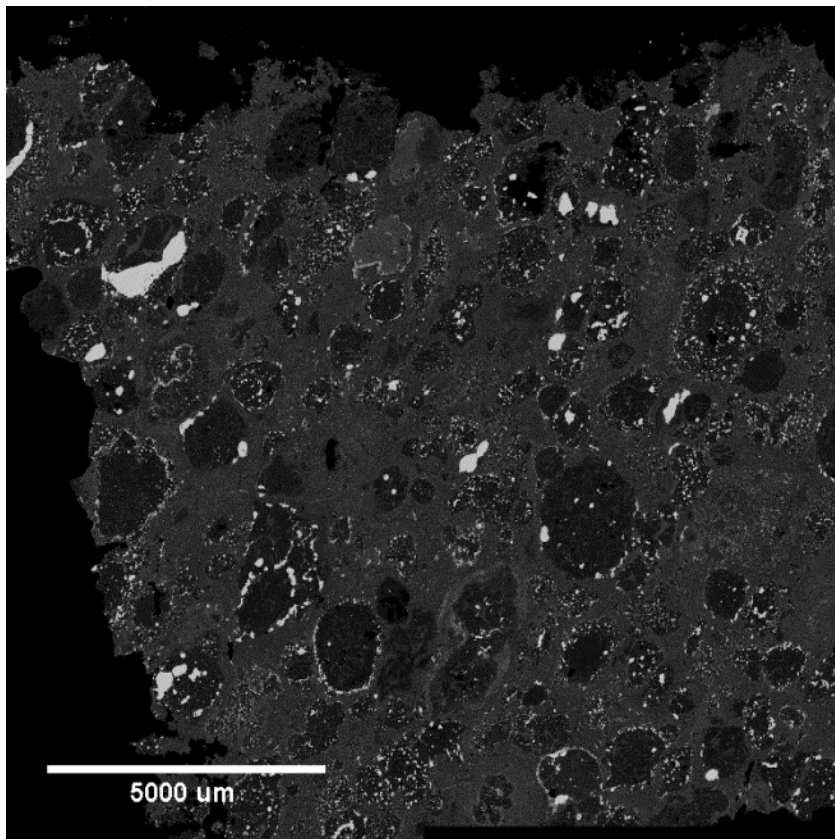


**Figure C35.** Renazzo N1126 Backscattered electron map

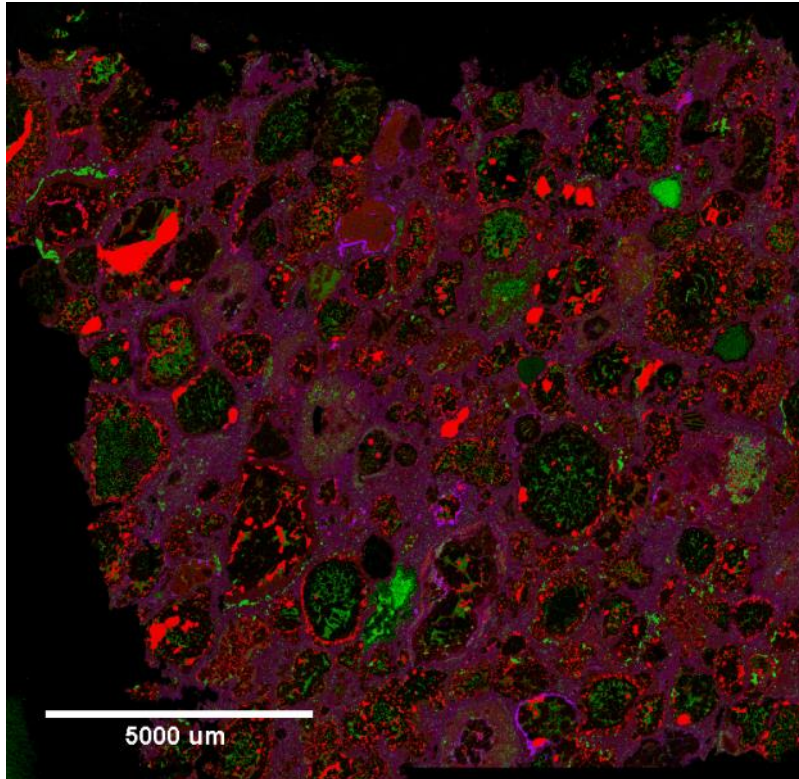


**Figure C36.** Renazzo N1126 X-ray map (RGB = FeCaS)

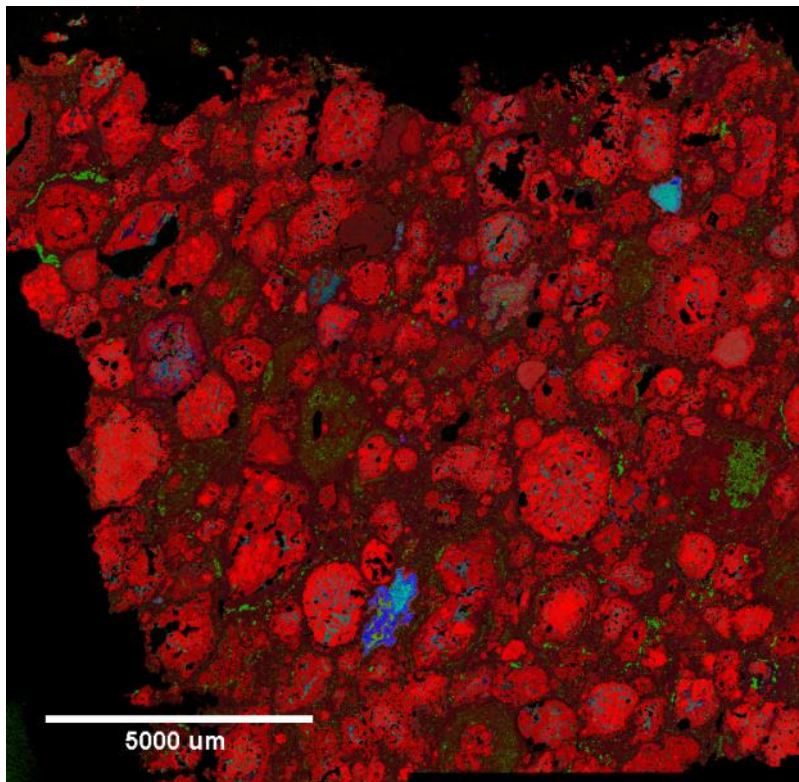


**Figure C37.** Renazzo N1126 X-ray map (RGB = MgCaAl)

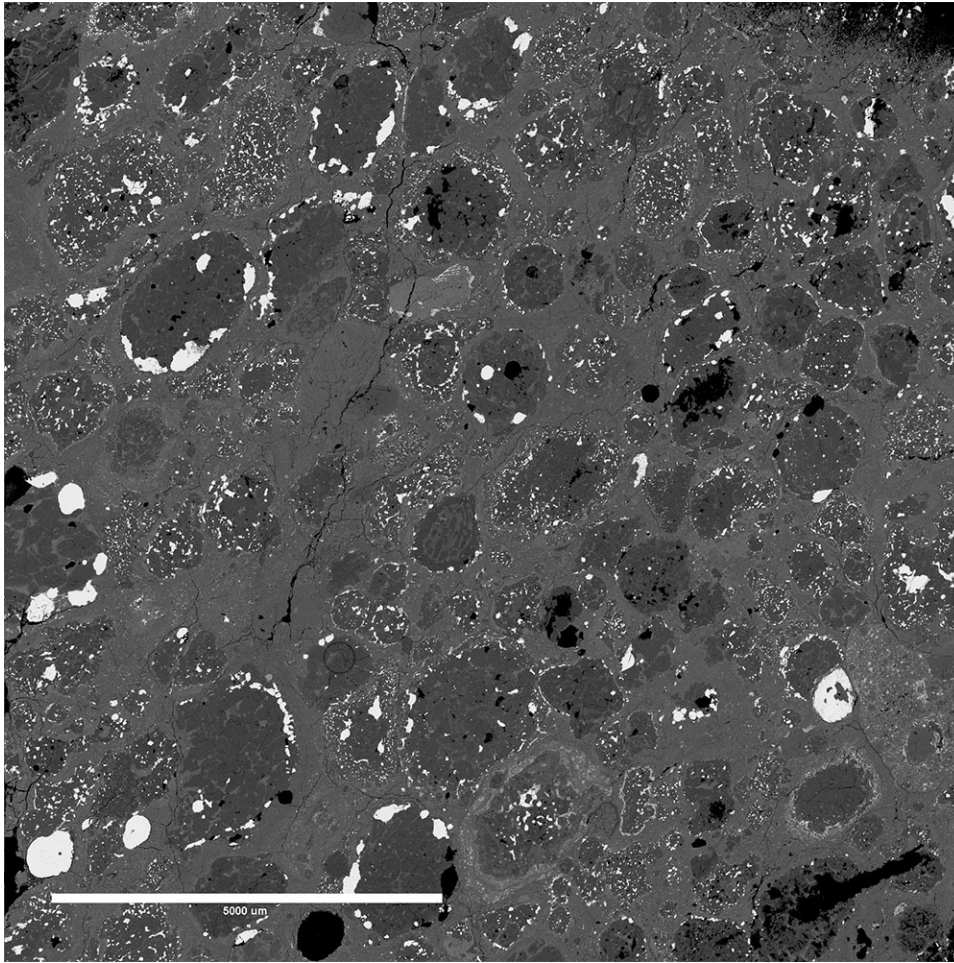


**Figure C38.** Renazzo N1126 Backscattered electron map

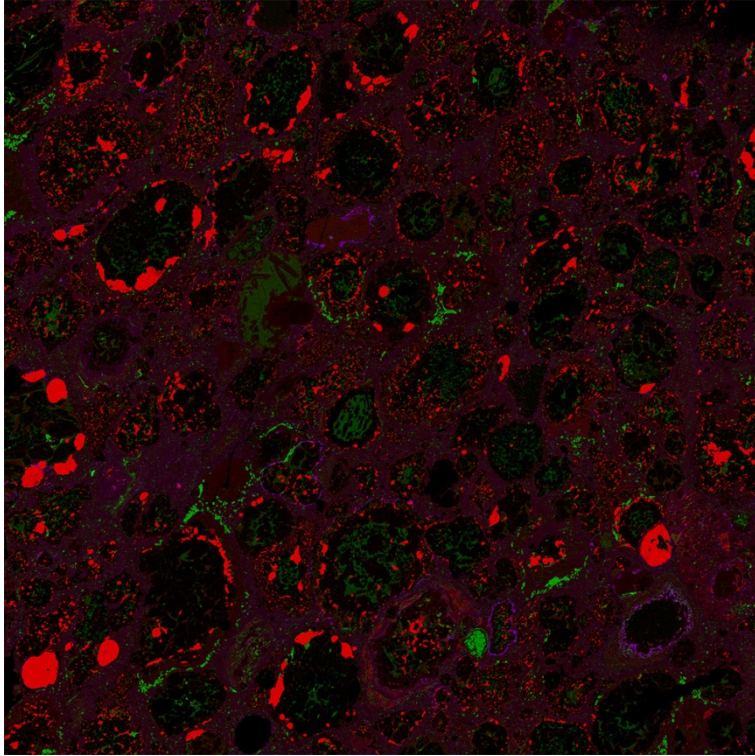


**Figure C39.** Renazzo N1127 X-ray map (RGB = FeCaS)

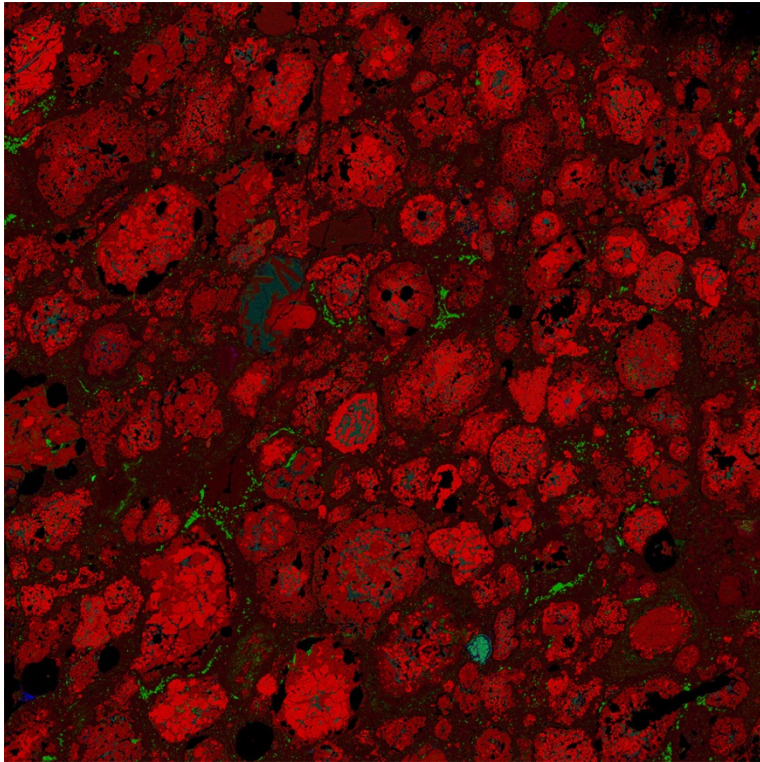


**Figure C40.** Renazzo N1127 X-ray map (RGB = MgCaAl)

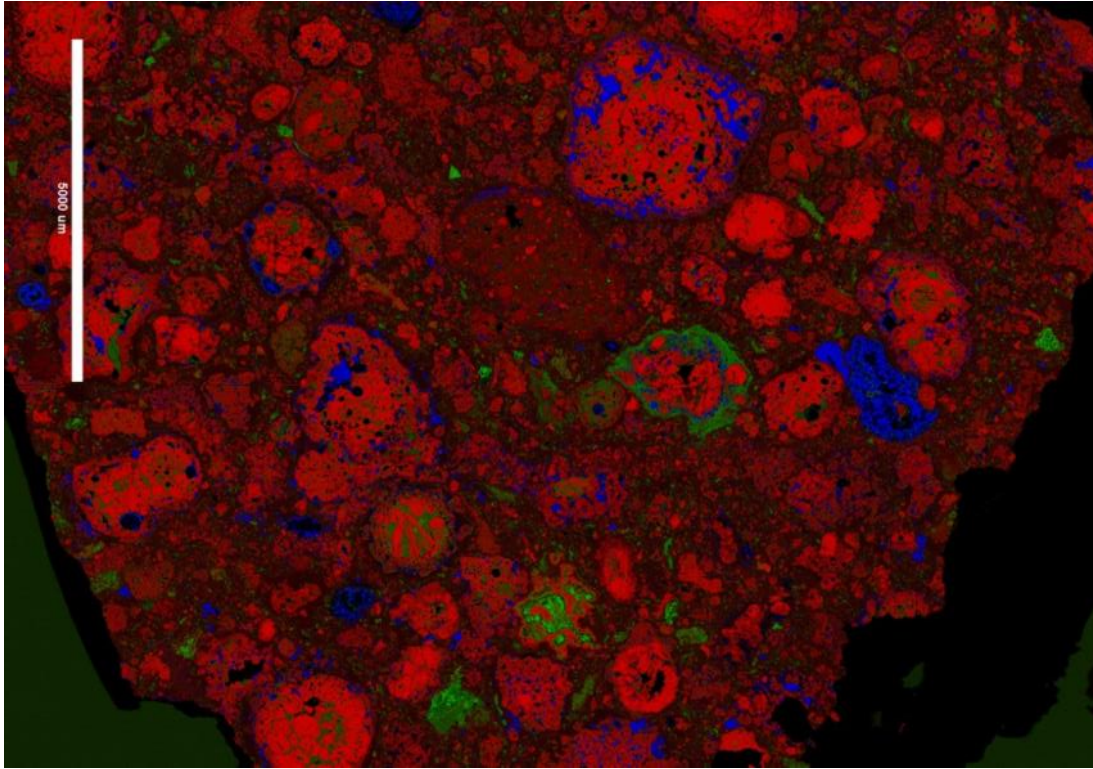


**Figure C41.** Renazzo UH 1 X-ray map (RGB = MgCaS)

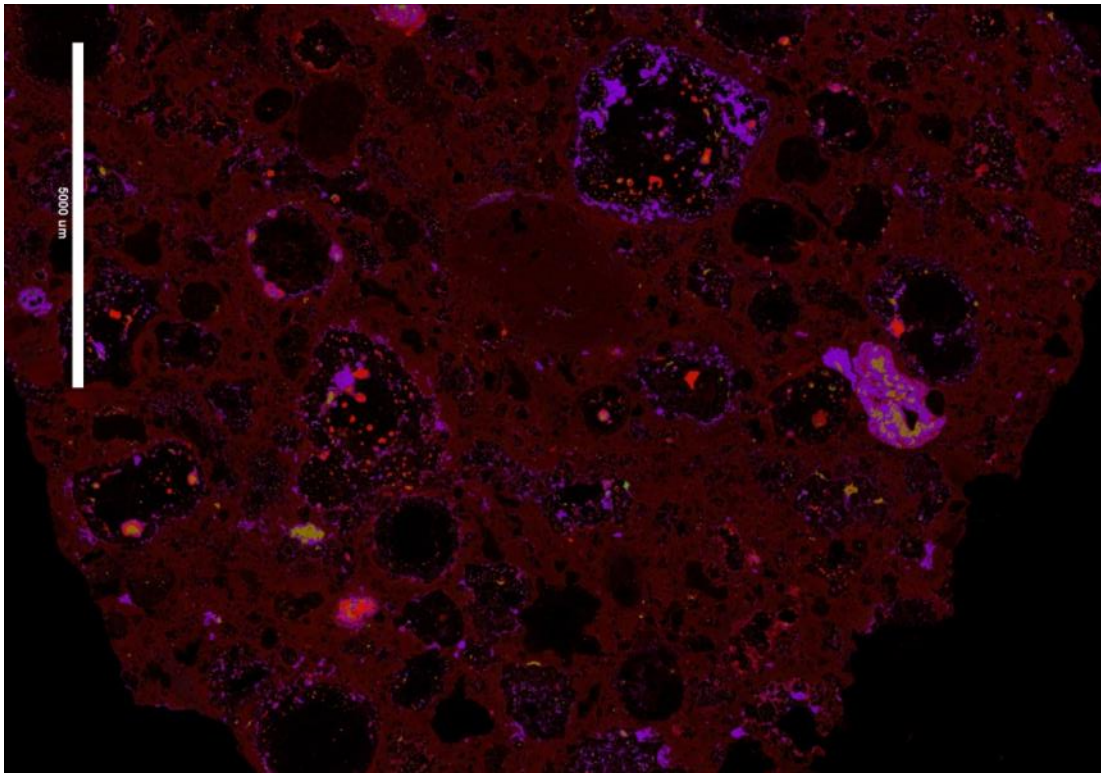


**Figure C42.** Renazzo UH 1 X-ray map (RGB = FeNiS)

## REFERENCES

- Abreu N. M. (2012) CR chondrites: Shock, aqueous alteration and terrestrial weathering. In *AGU Fall Meeting Abstracts*, 1909 (Abstract).
- Abreu N. M. (2015) Processes affecting the CR chondrites parent body: Petrology, mineralogy and chemical composition of the matrices of Antarctic CR carbonaceous chondrites. *Lunar and Planetary Science Conference XLVI*, #2561 (Abstract).
- Abreu N. M., and Brearley A. J. (2005) Carbonates in Vigarano: Terrestrial, preterrestrial, or both? *Meteoritics & Planetary Science* 40, 609-625.
- Abreu N. M., and Brearley A. J. (2010) Early solar system processes recorded in the matrices of two highly pristine CR3 carbonaceous chondrites, MET 00426 and QUE 99177. *Geochimica et Cosmochimica Acta* 74, 1146-1171.
- Abreu N. M., and Bullock E. S. (2013) Opaque assemblages in CR2 Graves Nunataks (GRA) 06100 as indicators of shock-driven hydrothermal alteration in the CR chondrite parent body. *Meteoritics & Planetary Science* 48, 2406-2429.
- Agee, C. B., Burkemper, L. K., Muttik, N., Spilde, M. N., (2013) New Primitive Ordinary Chondrite: Northwest Africa 7731 (L3. 00). *Meteoritics & Planetary Science Supplement* 76, #5130 (Abstract).
- Agrinier P. and Cannat M. (1997) Oxygen-isotope constraints on serpentinization processes in ultramafic rocks from the Mid-Atlantic Ridge (23°N). In *Proceedings of the Ocean Drilling Program, Scientific Results*, Vol.153. College Station, TX. pp. 381-388.
- Aharon P. (1988) Oxygen, carbon and U-series isotopes of aragonites from Vesfold Hills, Antarctica: Clues to geochemical processes in subglacial environments. *Geochimica et Cosmochimica Acta* 52, 2321-2331.
- Airieu S. A., Farquhar J., Thiemens M. H., Leshin L. A., Bao H., and Young E. (2005) Planetesimal sulfate and aqueous alteration in CM and CI carbonaceous chondrites. *Geochimica et Cosmochimica Acta* 69, 4166-4171.
- Alexander C. M. O'D., and Ebel D. S. (2012) Questions, questions: Can the contradictions between the petrologic, isotopic, thermodynamic, and astrophysical constraints on chondrule formation be resolved? *Meteoritics & Planetary Science* 47, 1157-1175.

- Alexander C. M. O'D., Bowden R., Fogel M. L., Howard K. T., Herd C. D. K., and Nittler L. R. (2012) The provenances of asteroids, and their contributions to the volatile inventories of the terrestrial planets. *Science* 337, 721–723.
- Alexander C. M. O'D., Howard K. T., Bowden R., and Fogel M. L. (2013) The classification of CM and CR chondrites using bulk H, C, and N abundances and isotopic compositions. *Geochimica et Cosmochimica Acta* 123, 244-260.
- Allen, J. S., Nozette, S., Wilkening, L. L., (1980) A study of chondrule rims and chondrule irradiation records in unequilibrated ordinary chondrites. *Geochimica Cosmochimica Acta* 44, 1161-1175.
- Amelin Y. (2008) U-Pb ages of angrites. *Geochimica et Cosmochimica Acta* 72, 221-232.
- Amelin Y., Krot A. N., Hutcheon I. D., and Ulyanov A. A. (2002) Lead isotopic ages of chondrules and calcium-aluminum-rich inclusions. *Science* 297, 1678-1683.
- Amelin Y., Kaltenbach A., Iizuka T., Stirling C. H., Ireland T. R., Petaev M., Jacobsen S. B. (2010) U-Pb chronology of the Solar System's oldest solids with variable  $^{238}\text{U}/^{235}\text{U}$ . *Earth and Planetary Science Letters* 300, 343–350.
- Astafieva M. M., Rozanov A. Y., and Hoover R. B. (2003) Framboidal structures in Earth rocks and in Astromaterials. In *Proceedings-SPIE The International Society For Optical Engineering*, 36-47.
- Baum, E.M., Knox H.D., Miller, R.T. (2002) *Nuclides and Isotopes* Sixteenth Edition, p. 47.
- Benedix G. K., Leshin L. A., Farquhar J., Jackson T., and Thiemens, M. H. (2003) Carbonates in CM2 chondrites: Constraints on alteration conditions from oxygen isotopic compositions and petrographic observations. *Geochimica et Cosmochimica Acta* 67, 1577-1588.
- Birck J.-L., and Allègre C. J. (1988) Manganese-chromium isotope systematics and the development of the early Solar System. *Nature* 331, 579–584.
- Bland P. A., Sexton A., Jull A. J. T., Bevan A. W. R., Berry F. J., Thornley D., Astin T., and Pillinger C. T. (1998) Climate and rock weathering: A study of terrestrial age dated ordinary chondritic meteorites from hot desert regions. *Geochimica et Cosmochimica Acta* 62, 3169–3184.
- Bland P. A., Zolensky M. E., Benedix G. K., Sephton M. A. (2006) Weathering of Chondritic Meteorites. In *Meteorites and the Early Solar System II*. 853–867.

- Bland P. A., Jackson M. D., Coker R. F., Cohen B. A., Webber J. B. W., Lee M. R., Duffy C.M., Chater R.J., Ardakani M.G., McPhail D.S., McComb D.W., and Benedix, G. K. (2009) Why aqueous alteration in asteroids was isochemical: High porosity≠ high permeability. *Earth and Planetary Science Letters* 287, 559-568.
- Blinova A., Alexander C. M. O'D., Wang J., and Herd C. D. K. (2012) Mineralogy and Mn-Cr extinct radionuclide dating of a dolomite from the pristine Tagish Lake meteorite. *43<sup>rd</sup> Lunar and Planetary Science Conference*, #1188 (Abstract).
- Boeck, L., Keil, K., Huss, G.R., and Wilson, I.E. (2009) Description and classification of RC 110, a new ordinary chondrite from Roosevelt County, New Mexico, USA. *Chemie der Erde* 69, 287-290.
- Bonal, L., Quirico, E., Bourot-Denise, M., and Montagnac, G. (2006) Determination of the petrologic type of CV3 chondrites by Raman spectroscopy of included organic matter. *Geochimica Cosmochimica Acta* 70, 1849-1863.
- Bonal L., Bourot-Denise M., Quirico E., Montagnac G., and Lewin E. (2007) Organic matter and metamorphic history of CO chondrites. *Geochimica Cosmochimica Acta* 71, 1605-1623.
- Bonal L., Alexander C. M. O'D., Huss G. R., Nagashima K., Quirico E., and Beck P. (2013) Hydrogen isotopic composition of the water in CR chondrites. *Geochimica et Cosmochimica Acta* 106, 111-133.
- Bouvier A., and Wadhwa M. (2010) The age of the Solar System redefined by the oldest Pb–Pb age of a meteoritic inclusion. *Nature Geoscience* 3, 637–641.
- Brearley A. J. (2006) The Action of Water. In *Meteorites and the Early Solar System II* (eds. Lauretta D. S. and McSween H. Y.), pp. 584–624.
- Brearley A. J., and Chizmadia L. J. (2005) On the behavior of phosphorous during the aqueous alteration of CM2 carbonaceous chondrites. *36<sup>th</sup> Lunar and Planetary Science Conference*, #2176 (Abstract).
- Brearley A. J., and Jones R. H. (1998) Chondritic Meteorites. *Reviews in Mineralogy and Geochemistry* 36, 3-1.
- Brennecka G. A. and Wadhwa M. (2012) Uranium isotope compositions of the basaltic angrite meteorites and the chronological implications for the early Solar System. *Proceedings of the National Academy of Sciences* 109, 9299-9303.

- Browning L. B., McSween H. Y., and Zolensky M. E. (1996) Correlated alteration effects in CM carbonaceous chondrites. *Geochimica et Cosmochimica Acta* 60, 2621-2633.
- Burger P. V., and Brearley A. J. (2004) Chondrule glass alteration in type IIA chondrules in the CR2 chondrites EET 87770 and EET 92105: Insights into elemental exchange between chondrules and matrices. *Lunar and Planetary Science XXXV*, #1966 (Abstract).
- Caplan C. E., Huss G. R., Hammer J. E., Oglione R. C., and Nagashima K. (2015) Crystal orientation effects for oxygen-isotope measurements of magnetite and chromite. 78<sup>th</sup> *Annual Meteoritical Society Meeting*, #5333 (Abstract).
- Cassidy W., Harvey R., Schutt J., Delisle G., and Yanai K. (1992) The meteorite collection sites of Antarctica. *Meteoritics* 27, 490-525.
- Chiba H., Chacko T., Clayton R. N., and Goldsmith J. R. (1989) Oxygen isotope fractionations involving diopside, forsterite, magnetite, and calcite: Application to geothermometry. *Geochimica et Cosmochimica Acta* 53, 2985-2995.
- Choi B.-G., and Wasson J. T. (2003) Microscale oxygen isotopic exchange and formation of magnetite in the Ningqiang anomalous carbonaceous chondrite. *Geochimica et Cosmochimica Acta* 67, 4655-4660.
- Choi B.-G., McKeegan K. D., Leshin L. A., and Wasson J. T. (1997) Origin of the magnetite in oxidized CV chondrites: In situ measurement of oxygen isotopic compositions of Allende magnetite and olivine. *Earth and Planetary Science Letters* 146, 337-349.
- Choi B.-G., McKeegan K. D., Krot A. N., and Wasson, J. T. (1998) Extreme oxygen-isotope compositions in magnetite from unequilibrated ordinary chondrites. *Nature* 392, 577-579.
- Choi B.-G., Krot A. N., and Wasson, J. T. (2000) Oxygen isotopes in magnetite and fayalite in CV chondrites Kaba and Mokoia. *Meteoritics & Planetary Science* 35, 1239-1248.
- Choi B.-G., Ahn I., Ziegler K., Wasson J. T., Young E. D. and Rubin A. E. (2009) Oxygen isotopic compositions and degree of alteration of CR chondrites. *Meteoritics & Planetary Science* 44 (Supplement), A50 (Abstract).
- Ciesla F. J., Lauretta D. S., Cohen B. A., and Hood L. L. (2003) A Nebular origin for chondritic fine-grained phyllosilicates. *Science* 299, 549-552.
- Clayton R. N. and Mayeda T. K. (1977) Oxygen isotopic compositions of separated fractions of the Leoville and Renazzo carbonaceous chondrites. *Meteoritics* 12, A199.

- Clayton R. N. and Mayeda T. K. (1984) The oxygen isotope record in Murchison and other carbonaceous chondrites. *Earth and Planetary Science Letters* 67, 151–161.
- Clayton R. N. and Mayeda T. K. (1999) Oxygen isotope studies of carbonaceous chondrites. *Geochimica et Cosmochimica Acta* 63, 2089–2104.
- Cohen B. A. and Coker R. F. (2000) Modeling of liquid water on CM meteorite parent bodies and implications for amino acid racemization. *Icarus* 145, 369-381.
- Connelly J. N., Bizzarro M., Krot A. N., Nordlund A., Wielandt D., and Ivanova M. A. (2012) The absolute chronology and thermal processing of solids in the solar protoplanetary disk. *Science* 338, 651-655.
- Cyr K. E., Sears W. D., Lunine J. I. (1998) Distribution and evolution of water ice in the solar nebula: Implications for Solar System body formation. *Icarus* 135, 537-548.
- Davidson J., Krot A. N., Nagashima K., Hellebrand E., and Lauretta, D. S. (2014) Oxygen isotope and chemical compositions of magnetite and olivine in the anomalous CK3 Watson 002 and ungrouped Asuka-881595 carbonaceous chondrites: Effects of parent body metamorphism. *Meteoritics & Planetary Science* 49, 1456-1474.
- De Leuw S., Rubin A. E., Schmitt A. K., and Wasson J. T. (2009)  $^{53}\text{Mn}$ - $^{53}\text{Cr}$  systematics of carbonates in CM chondrites: Implications for the timing and duration of aqueous alteration. *Geochimica et Cosmochimica Acta* 73, 7433-7442.
- De Leuw S., Rubin A. E., and Wasson J. T. (2010) Carbonates in CM chondrites: Complex formational histories and comparison to carbonates in CI chondrites. *Meteoritics and Planetary Science* 45, 513–530.
- Doyle P. M., Krot A. N., Nagashima K. (2013) Oxygen-isotopes of fayalite, magnetite and chondrule olivine in the CO (Y-81020, EET 90043) and CO-like (MAC 88107) chondrites. *76<sup>th</sup> Annual Meteoritical Society Meeting*, #5135 (Abstract).
- Doyle P. M., Nagashima K., Jogo K., and Krot A. N. (2013)  $^{53}\text{Mn}$ - $^{53}\text{Cr}$  chronometry reveals secondary fayalite in Asuka 881317 (CV) and MacAlpine Hills 88107 (Co/Cm-like) formed 4-5 Ma after CV CAIs. *44<sup>th</sup> Lunar and Planetary Science Conference*, #1793 (Abstract).
- Doyle P. M., Jogo K., Nagashima K., Krot A. N., Wakita S., Ciesla F., and Hutcheon I. D. (2015) Early aqueous activity on the ordinary and carbonaceous chondrite parent bodies recorded by fayalite. *Nature Communications* 6:7444..

- Drake M. J. (2005) Origin of water in the terrestrial planets. *Meteoritics & Planetary Science* 40, 519-527.
- Drake M. J. and Righter K. (2002) Determining the composition of the Earth. *Nature* 416, 39-44.
- Dunn T. L., Cressey G., McSween H. Y., and McCoy T. J. (2010) Analysis of ordinary chondrites using powder X-ray diffraction: 1. Modal mineral abundances. *Meteoritics & Planetary Science* 45,123-134.
- Eisenhour D. D. (1996) Determining chondrule size distributions from thin-section measurements. *Meteoritics & Planetary Science* 31, 243-248.
- Endreß M., Keil K., Bischoff A., Spettel B., Clayton R. N., and Mayeda T. K. (1994) Origin of dark clasts in the Acfer 059/EI Djouf 001 CR2 chondrite. *Meteoritics* 29, 26-40.
- Endreß M., Zinner E., and Bischoff A. (1996) Early aqueous activity on primitive meteorite parent bodies. *Nature* 379, 701–703.
- Faure G., Hoefs J., Jones L. M., Curtis J. B., and Pride, D. E. (1988) Extreme  $^{18}\text{O}$  depletion in calcite and chert clasts from the Elephant Moraine on the East Antarctic ice sheet. *Nature* 332, 352-354.
- Fujiya W., Sugiura N., Hotta H., Ichihiro K., and Sano Y. (2012) Evidence for the late formation of hydrous asteroids from young meteoritic carbonates. *Nature Communications* 627, 1-6.
- Fujiya W., Sugiura N., Sano Y., and Hiyagon H. (2013) Mn-Cr ages of dolomites in CI chondrites and the Tagish Lake ungrouped carbonaceous chondrite. *Earth & Planetary Science Letters* 362, 130–142.
- Garvie L. A. J. (2013) Mineralogy of the Sutter's Mill carbonaceous chondrite. 44<sup>th</sup> Lunar and Planetary Science Conference # 2148 (Abstract).
- Glavin D. P., Kubny A., Jagoutz E., and Lugmair G. W. (2004) Mn-Cr isotope systematics of the D'Orbigny angrite. *Meteoritics & Planetary Science* 39, 693-700.
- Gomes C.B., and Keil K. (1980) *Brazilian stone meteorites*. Univ. of New Mexico Press. Albuquerque, pp. 1-161.
- Gooding J. L. (1986) Weathering of stony meteorites in Antarctica. *International Workshop on Antarctic Meteorites 1*, 48-54.

- Grady M. M., Fernandes C. D., Gilmour I., Harker A., Preston L., Verchobsky A. B. (2013) Light element geochemistry and spectroscopy of the Sutter's Mill carbonaceous chondrite. . 44<sup>th</sup> *Lunar and Planetary Science Conference* #3000 (Abstract).
- Grimm R. E. and McSween H. Y. (1989) Water and the thermal evolution of carbonaceous chondrite parent bodies. *Icarus* 82, 244-280.
- Grossman J.N. and Brearley A.J. (2005) The onset of metamorphism in ordinary and carbonaceous chondrites. *Meteoritics & Planetary Science* 40, 87-122.
- Guo W. and Eiler J. M. (2007) Temperatures of aqueous alteration and evidence for methane generation on the parent bodies of the CM chondrites. *Geochimica et Cosmochimica Acta* 71, 5565–5575.
- Haish K. E. Jr., Lada E. A., and Lada C. J. (2001) Disk frequencies and lifetimes in young clusters. *Astrophysical Journal* 553, L153-L156.
- Hanshaw B. B. and Hallet B. (1978) Oxygen isotope composition of subglacially precipitated calcite: possible paleoclimatic implications. *Science* 200, 1267-1270.
- Harju E. R., Rubin A. E., Ahn I., Choi B.-G., Ziegler K., and Wasson J. T. (2014) Progressive aqueous alteration of CR carbonaceous chondrites. *Geochimica et Cosmochimica Acta* 139, 267-292.
- Hays P. D., and Grossman E. L. (1991) Oxygen isotopes in meteoric calcite cements as indicators of continental paleoclimate. *Geology* 19, 441-444.
- Hoppe P., MacDougall D., and Lugmair G. W. (2007) High spatial resolution ion microprobe measurements refine chronology of carbonate formation in Orgueil. *Meteoritics & Planetary Science* 42, 1309–1320.
- Howard K. T., Alexander C. M. O'D., Schrader D. L., Dyl K. A. (2015) Classification of hydrous meteorites (CR, CM, and C2 ungrouped) by phyllosilicate fraction: PSD-XRD modal mineralogy and planetesimal environments. *Geochimica et Cosmochimica Acta* 149, 206-222.
- Hua X., Huss G. R., Tachibana S., and Sharp T. G. (2005) Oxygen, silicon, and Mn-Cr isotopes of fayalite in the Kaba oxidized CV3 chondrite: Constraints for its formation history. *Geochimica et Cosmochimica Acta* 69, 1333-1348.

- Huberty J.M., Kita N.T., Kozdon R., Heck P.R., Fournelle J.H., Spicuzza M.J., Xu H., and Valley J.W. (2010) Crystal orientation effects in  $\delta^{18}\text{O}$  for magnetite and hematite by SIMS. *Chemical Geology* 276, 269-283.
- Hughes D. W. (1978) A disaggregation and thin section analysis of the size and mass distribution of the chondrules in the Bjurböle and Chainpur meteorites. *Earth and Planetary Science Letters* 38, 391-400.
- Huss G. R. (2004) Implications of isotopic anomalies and presolar grains for the formation of the solar system. *Antarctic Meteorite Research* 17, 132-152.
- Huss G. R., Keil K., and Taylor G. J. (1981) The matrices of unequilibrated ordinary chondrites: implications for the origin and history of chondrites. *Geochimica Cosmochimica Acta* 45, 33-51.
- Huss G. R., MacPherson G. J., Wasserburg G. J., Russell S. S., and Srinivasan G. (2001) Aluminum-26 in calcium-aluminum-rich inclusions and chondrules from unequilibrated ordinary chondrites. *Meteoritics & Planetary Science* 36, 975-997.
- Huss G. R., Rubin A. E., Grossman J. N., (2006) Thermal Metamorphism in Chondrites. In *Meteorites and the Early Solar System II*, 567-586.
- Hutcheon I. D., Krot A. N., Keil K., Phinney D. L., and Scott E. R. D. (1998)  $^{53}\text{Mn}$ - $^{53}\text{Cr}$  dating of fayalite formation in the CV3 chondrites Mokoia: Evidence for asteroidal alteration. *Science* 282, 1865-1867.
- Hutcheon I. D., Marhas K. K., Krot A. N., Goswami J. N., and Jones R. H. (2009)  $^{26}\text{Al}$  in plagioclase-rich chondrules in carbonaceous chondrites: Evidence for an extended duration of chondrule formation. *Geochimica et Cosmochimica Acta* 73, 5080-5099.
- Ichikawa O. and Ikeda Y. (1995) Petrology of the Yamato-8449 CR chondrite. *Proceedings of the NIPR Symposium on Antarctic Meteorites* 8, 63-78.
- Ichimura K., and Sugiura N. (2015) Preparation of synthetic dolomite for determination of Mn/Cr relative sensitivity. *46<sup>th</sup> Lunar and Planetary Science Conference*. #1795 (Abstract).
- Ikeda Y. and Prinz M. (1993) Petrologic study of the Belgica 7904 carbonaceous chondrite: Hydrous alteration, oxygen isotopes, and relationship to CM and CI chondrites. *Geochimica et Cosmochimica Acta* 57, 439-452.

- Jenniskens P., Fries M. D., Yin Q.-Z., Zolensky M., Krot A. N., Sandford S. A., Sears D., Beauford R., Ebel D. S., Friedrich J. M., Nagashima K., Wimpenny J., Yamakawa A., Nishiizumi K., Hamajima Y., Caffee M. W., Welten K. C., Laubenstein M., Davis A. M., Simon S. B., Heck P. R., Young E. D., Kohl I. E., Thiemens M. H., Nunn M. H., Mikouchi T., Hagiya K., Ohsumi K., Cahill T. A., Lawton J. A., Barnes D., Steele A., Rochette P., Verosub K. L., Gattacceca J., Cooper G., Glavin D. P., Burton A. S., Dworkin J. P., Elsila J. E., Pizzarello S., Oglione R., Schmitt-Kopplin P., Harir M., Hertkorn N., Verchovsky A., Grady M., Nagao K., Okazaki R., Takechi H., Hiroi T., Smith K., Silber E. A., Brown P. B., Albers J., Klotz D., Hankey M., Matson R., Fries J. A., Puchtel I., Lee C.-T. A., Erdman M. E., Eppich G. R., Roeske S., Gabelica Z., Lerche M., Nuevo M., Girtten B., Worden S. P. (2012) Radar-enabled recover of the Sutter's Mill meteorite, a carbonaceous chondrite regolith breccia. *Science* 338, 1583–1587.
- Jewitt D., Chizmadia L., Grimm R., and Prrialnik D. (2007) Water in the small bodies of the Solar System. *Protostars and Planets V*, 863-878.
- Jilly C. E., and Huss G. R. (2012) Heterogeneous aqueous alteration in the CR2 chondrite Renazzo. 46<sup>th</sup> *Lunar and Planetary Science Conference*, #1348 (Abstract).
- Jilly C. E., Huss G. R., and Nagashima K. (2013) Mn-Cr dating of secondary carbonates in CR chondrites. *Lunar and Planetary Science Conference XLIV*, 2474 (Abstract).
- Jilly C. E., Huss G. R. Krot A. N., Nagashima K., Yin Q.-Z., and Sugiura N. (2014) <sup>53</sup>Mn-<sup>53</sup>Cr dating of aqueously formed carbonates in the CM2 lithology of the Sutter's Mill carbonaceous chondrite. *Meteoritics & Planetary Science* 49, 2104-2117.
- Jilly-Rehak C. E., Huss G. R., and Nagashima K. (2015) Oxygen isotopes in secondary minerals in CR chondrites: Comparing components of different petrologic type. 43<sup>rd</sup> *Lunar and Planetary Science Conference*, #1662 (Abstract).
- Jogo K., Nakamura T., Noguchi T., and Zolotov M. Y. (2009) Fayalite in the Vigarano CV3 carbonaceous chondrite: Occurences, formation age and conditions. *Earth and Planetary Science Letters* 287, 320-328.
- Jones R. H., Grossman J. N., and Rubin A. E. (2005) Chemical, mineralogical and isotopic properties of chondrules: clues to their origin. In *Chondrites and the Protoplanetary Disk. Vol. 341*, 251-285.

- Kallemeyn G. W., Rubin A. E. and Wasson J. T. (1994) The compositional classification of chondrites: VI. The CR carbonaceous chondrite group. *Geochimica et Cosmochimica Acta* 58, 2873–2888.
- Kallemeyn G. W., Rubin A. E., and Wasson J. T. (1996) The compositional classification of chondrites: VII. The R chondrite group. *Geochimica et Cosmochimica Acta* 60, 2243-2256.
- Keil K. (1962) On the phase composition of meteorites. *Journal of Geophysical Research* 67, 4055-4061.
- Keil K. (2012) Angrites, a small but diverse suite of ancient, silica-undersaturated volcanic-plutonic mafic meteorites, and the history of their parent asteroid. *Chemie der Erde* 72, 191-218.
- Kim S. T. and O'Neil J. R. (1997) Equilibrium and nonequilibrium oxygen isotope effects in synthetic carbonates. *Geochimica et Cosmochimica Acta* 61, 3461-3475.
- Kita N. T. and Ushikubo T. (2012) Evolution of protoplanetary disk inferred from  $^{26}\text{Al}$  chronology of individual chondrules. *Meteoritics & Planetary Science* 47, 1108–1119.
- Kita N. T., Nagahara H., Tachibana S., Tomomura S., Spicuzza M. J., Fournelle J. H., and Valley J. W. (2010) High precision SIMS oxygen three isotope study of chondrules in LL3 chondrites: Role of ambient gas during chondrule formation. *Geochimica et Cosmochimica Acta* 74, 6610–6635.
- Kita N.T., Huberty J.M., Kozdon R., Beard B.L., and Valley J.W. (2011) High precision SIMS oxygen, sulfur and iron stable isotope analyses of geological materials: accuracy, surface topography and crystal orientation. *Surface and Interface Analysis* 43, 427-431.
- Kleine T., Mezger K., Palme H., Scherer E., and Münker C. (2005) Early core formation in asteroids and late accretion of chondrite parent bodies: Evidence from  $^{182}\text{Hf}$ - $^{182}\text{W}$  in CAIs, metal-rich chondrites, and iron meteorites. *Geochimica et Cosmochimica Acta* 69, 5805-5818.
- Kleine T., Hans U., Irving A. J., and Bourdon B. (2012) Chronology of the angrite parent body and implications for core formation in protoplanets. *Geochimica et Cosmochimica Acta* 84, 186-203.
- Krot A. N., Zolensky M. E, Wasson J. T., Scott E. R. D, Keil K., and Ohsumi K. (1997) Carbide-magnetite assemblages in type-3 ordinary chondrites. *Geochimica et Cosmochimica Acta*, 61, 219–237.

- Krot A. N., Petaev M. I., Scott E. R. D., Choi B. G., Zolensky M. E., and Keil K. (1998) Progressive alteration in CV3 chondrites: More evidence for asteroidal alteration. *Meteoritics & Planetary Science* 33, 1065-1085.
- Krot A. N., Brearley A. J., Petaev M. I., Kallemeyn G. W., Sears D. W. G., Benoit P. H., Huchon I. D., Zolensky M. E., and Keil, K. (2000) Evidence for low-temperature growth of fayalite and hedenbergite in MacAlpine Hills 88107, an ungrouped carbonaceous chondrite related to the CM-CO clan. *Meteoritics & Planetary Science* 35, 1365-1386.
- Krot A. N., Meibom A., Weisberg M.K., and Keil K. (2002) The CR chondrite clan: Implications for early solar system processes. *Meteoritics & Planetary Science* 37, 1451-1490.
- Krot A. N. Huchon I. D., Brearley A. J., Pravdivtseva O. V., Petaev M. I., Hohenberg C. M. (2006) Timescales and settings for alteration of chondritic meteorites. In *Meteorites and the Early Solar System II*. 525–553.
- Krot A. N., Libourel G. and Chaussidon M. (2006) Oxygen isotope compositions of chondrules in CR chondrites. *Geochimica et Cosmochimica Acta* 70, 767–779.
- Krot A. N., Doyle P. M., Nagashima K., Jogo K., Wakita S., Ciesla F. J., Huchon I. D. (2013) Origin of asteroidal water: constraints from isotopic compositions of aqueously formed minerals. 76<sup>th</sup> Annual Meteoritical Society Meeting #5161 (Abstract).
- LaTourrette T., and Wasserburg G. J. (1998) Mg diffusion in anorthite: implications for the formation of early solar system planetesimals. *Earth and Planetary Science Letters* 158, 91-108.
- Lauretta D. S., Lodders K., Fegley B. Jr., and Kremser D. T. (1997) The origin of sulfide-rimmed metal grains in ordinary chondrites. *Earth & Planetary Science Letters* 151, 289-301.
- Lauretta D. S., Buseck P. R., and Zega T. J. (2001) Opaque minerals in the matrix of the Bishunpur (LL3.1) chondrite: constraints on the chondrule formation environment. *Geochimica et Cosmochimica Acta* 65, 1337-1353.
- Lee M. R., Lindgren P., Sofe M. R., Alexander C. M. O'D., and Wang J. (2012) Extended chronologies of aqueous alteration in the CM2 carbonaceous chondrites: Evidence from carbonates in Queen Alexandra Range 93005. *Geochimica et Cosmochimica Acta* 92, 148–169.

- Leshin L. A., Rubin A. E., and McKeegan K. D. (1997) The oxygen isotopic composition of olivine and pyroxene from CI chondrites. *Geochimica et Cosmochimica Acta* 61, 835–845.
- Lugmair G. W. and Shukolyukov A. (1998) Early solar system timescales according to  $^{53}\text{Mn}$ – $^{53}\text{Cr}$  systematics. *Geochimica et Cosmochimica Acta* 62, 2863–2886.
- Lyon I. C., Saxton J. M., and Cornah S. J. (1998) Isotopic fractionation during secondary ionisation mass spectrometry: crystallographic orientation effects in magnetite. *International Journal of Mass Spectrometry and Ion Processes* 172, 115-122.
- Maitland T., and Sitzman S. (2007) Electron backscatter diffraction (EBSD) technique and materials characterization examples. In *Scanning Microscopy for Nanotechnology: Techniques and Applications* (eds., Zhou W. and Wang Z. L.), 41-75.
- Makide K., Nagashima K., Krot A. N., Huss G. R., Hutcheon I. D., and Bischoff A. (2009) Oxygen- and magnesium-isotope compositions of calcium-aluminum-rich inclusions from CR2 carbonaceous chondrites. *Geochimica et Cosmochimica Acta* 73, 5018-5050.
- McCoy T. J., Keil K., Scott E. R. D., Benedix G. K., and Ehlmann A. J. (1994) Low-FeO ordinary chondrites: A nebular origin and new chondrite parent body. *Lunar and Planetary Science Conference XXV*, 865-866 (Abstract).
- McKibbin S. J., Ireland T. R., Amelin Y., O'Neill H. S. O., and Holden P. (2013) Mn-Cr relative sensitivity factors for secondary ion mass spectrometry analysis of Mg-Fe-Ca olivine and implications for the Mn-Cr chronology of meteorites. *Geochimica et Cosmochimica Acta* 110, 216-228.
- McKibbin S. J., Ireland T. R., Amelin Y., and Holden P. (2015) Mn-Cr dating of Fe- and Ca-rich olivine from 'quenched' and 'plutonic' angrite meteorites using Secondary Ion Mass Spectrometry. *Geochimica et Cosmochimica Acta* 157, 13-27.
- McSween H. Y. Jr. (1979) Alteration in CM carbonaceous chondrites inferred from modal and chemical variations in matrix. *Geochimica et Cosmochimica Acta* 43, 1761–1770.
- McSween H. Y. Jr and Huss G. R. (2010) *Cosmochemistry*. Cambridge University Press.
- Medlin W. L. (1959) The preparation of synthetic dolomite. *American Mineralogist* 44, 979-986
- Melosh, H. J. (2011) *Planetary surface processes* (Vol. 13). Cambridge University Press. p. 113.

- Mittlefehldt D. W., Killgore M., and Lee M. T. (2002) Petrology and geochemistry of D'Orbigny, geochemistry of Sahara 99555, and the origin of angrites. *Meteoritics & Planetary Science* 37, 345-369.
- Nagahara H. 1984. Matrices of type 3 ordinary chondrites—Primitive nebular records. *Geochimica Cosmochimica Acta* 48, 2581–2595.
- Nagashima K., Krot A. N., and Chaussidon M. (2007) Aluminum-magnesium isotope systematics of chondrules from CR chondrites. *Meteoritics & Planetary Science* 42, A115 (Abstract).
- Nagashima K., Krot A. N., and Huss G. R. (2008)  $^{26}\text{Al}$  in chondrules from CR carbonaceous chondrites. *39th Lunar and Planetary Science Conference*, #2224 (Abstract).
- Nakamura T., Noguchi T., Yoneda S. (2003) The conditions of aqueous alteration reaction recorded in the Sayama CM2 chondrite. *66<sup>th</sup> Annual Meteoritical Society Meeting*, #5080 (Abstract).
- Nishiizumi K., Elmore D., and Kubik P. W. (1989) Update on terrestrial ages of Antarctic meteorites. *Earth and Planetary Science Letters* 93, 299–313.
- Nyquist L. E., Kleine T., Shih C.-Y., and Reese Y. D. (2009) The distribution of short-lived radioisotopes in the early solar system and the chronology of asteroid accretion, differentiation, and secondary mineralization. *Geochimica et Cosmochimica Acta* 73, 5115-5136.
- Ogliore R. C., and Jilly C. E. (2013) Gigapixel Optical Microscopy for Meteorite Characterization. *Planetary Science* 2:3.
- Ogliore R. C., Huss G. R., and Nagashima K. (2011). Ratio estimation in SIMS analysis. *Nuclear Instruments and Methods in Physics Research Section B: Beam Interactions with Materials and Atoms* 269, 1910-1918.
- Papanastassiou D. A. (1986) Chromium isotopic anomalies in the Allende meteorite. *The Astrophysical Journal* 308, L27-L30.
- Pearson V. K., Sephton M. A., and Gilmour I. (2006) Molecular and isotopic indicators of alteration in CR chondrites. *Meteoritics & Planetary Science* 41, 1291-1303.
- Petit M., McKeegan K., Gounelle M., Mostefaoui S., Marrocchi Y., Meibom A., and Leshin L. A. (2009) Duration and sequence of carbonate crystallization on the Orgueil protolith:

- $^{53}\text{Mn}$ - $^{53}\text{Cr}$  systematics of their evolution in O and C isotopic evolution. *40<sup>th</sup> Lunar and Planetary Science Conference*, #1288 (Abstract).
- Petit M., Marrocchi Y., McKeegan K. D., Mostefaoui S., Meibom A., Zolensky M. E., and Gounelle M. (2011)  $^{53}\text{Mn}$ - $^{53}\text{Cr}$  ages of Kaidun carbonates. *Meteoritics & Planetary Science* 46, 275–283.
- Pingitore N. E., Eastman M. P., Sandidge M., Oden K., and Freiha B. (1988) The coprecipitation of manganese (II) with calcite: and experimental study. *Marine Chemistry* 25, 107-120.
- Qin L., Dauphas N., Wadhwa M., Masarik J., Janney P. E. (2008) Rapid accretion and differentiation of iron meteorite parent bodies inferred from  $^{182}\text{Hf}$ - $^{182}\text{W}$  chronometry and thermal modeling. *Earth and Planetary Science Letters* 273, 94–104.
- Quirico E., Raynal P.-I., and Bourot-Denis M. (2003) Metamorphic grade of organic matter in six unequilibrated ordinary chondrites. *Meteoritics & Planetary Science* 38, 795-811.
- Riciputi L. R., McSween H. Y., Johnson C. A., Prinz M. (1994) Minor and trace element concentrations in carbonates of carbonaceous chondrites, and implications for the compositions of coexisting fluids. *Geochimica et Cosmochimica Acta* 58, 1343–1351.
- Rodriguez-Blanco J. D., Shaw S., and Benning L. G. (2015) A route for the direct crystallization of dolomite. *American Mineralogist* 100, 1172-1181.
- Rowe M. W., Clayton R. N., and Mayeda T. K. (1994) Oxygen isotopes in separated components of CI and CM meteorites. *Geochimica et Cosmochimica Acta* 58, 5341-5347.
- Rubin A. E. (1997) Mineralogy of meteorite groups. *Meteoritics & Planetary Science* 32, 321-247.
- Rubin A. E., Sailer A. L., and Wasson J. T. (1999) Troilite in the chondrules of type-3 ordinary chondrites: Implications for chondrule formation. *Geochimica et Cosmochimica Acta* 63, 2281-2298.
- Rubin A. E., Trigo-Rodríguez J. M., Huber H., and Wasson J. T. (2007) Progressive aqueous alteration of CM carbonaceous chondrites. *Geochimica et Cosmochimica Acta* 71, 2361-2382.
- Ruzicka A., Killgore M., Mittlefehldt D W., and Fries M. D. (2005) Portales Valley: Petrology of a metallic-melt meteorite breccia. *Meteoritics & Planetary Science* 40, 261-295.

- Satterwhite C., and Righter K. (2012) *Antarctic Meteorite Newsletter* 35 (2).
- Sawlowicz, Z. (2000) Framboids: From their origin to application. *Prace Mineralogiczne (Mineral Transactions)* 88, 80 pp.
- Schrader D. L., Franchi I. A., Connolly H.C., Greenwood R. C., Lauretta D.S., and Gibson J.M. (2011) The formation and alteration of the Renazzo-like carbonaceous chondrites I: Implications of bulk-oxygen isotopic composition. *Geochimica et Cosmochimica Acta* 75, 308-325.
- Schrader D. L. Connolly H.C., Lauretta D.S., Nagashima K, Huss G.R., Davidson J., and Domanik K.J. (2013) The formation of the Renazzo-like carbonaceous chondrites II: Linking O-isotope composition and oxidation state of chondrule olivine. *Geochimica et Cosmochimica Acta* 101, 302-327.
- Schrader D. L., Nagashima K., Krot A. N, Ogliore R C., Yin Q.-Z., and Amelin Y. (2013) Testing the distribution of  $^{26}\text{Al}$  in the protoplanetary disk using CR chondrules. *76<sup>th</sup> Annual Meteoritical Society Meeting*, #5141 (Abstract).
- Schrader D. L., Davidson J., Greenwood R. C., Franchi I. A., Gibson J. M. (2014) A water-ice rich minor body from the early Solar System: The CR chondrite parent asteroid. *Earth and Planetary Science Letters* 407, 48-60.
- Schrader D. L., Connolly H. C., Lauretta D. S., Zega T. J., Davidson J., and Domanik K. J. (2015) The formation and alteration of the Renazzo-like carbonaceous chondrites III: Toward understanding the genesis of ferromagnesian chondrules. *Meteoritics & Planetary Science* 50, 15-50.
- Scott E. R. D. and Sanders I. S. (2009) Implications of the carbonaceous chondrite Mn-Cr isochron for the formation of early refractory planetesimals and chondrules. *Geochimica et Cosmochimica Acta* 73, 5137-5149.
- Sears D. W. G., Grossman J. N., Melcher C. L. Ross L. M., and Mills A. A. (1980) Measuring metamorphic history of unequilibrated ordinary chondrites. *Nature* 287, 791-795.
- Sears D. W. G., Hasan E. A., Batchelor J. D. and Lu. J. (1991) Chemical and physical studies of type 3 chondrites – XI: Metamorphism, pairing, and brecciation of ordinary chondrites. *Proceedings of the Lunar & Planetary Science Conference* 21, 493-512 (Abstract).
- Shukolyukov A. and Lugmair G. (2006) Manganese–chromium isotope systematics of carbonaceous chondrites. *Earth and Planetary Science Letters* 250, 200–213.

- Spivak-Birndorf L., Wadhwa M., and Janney P. E. (2009)  $^{26}\text{Al}$ – $^{26}\text{Mg}$  systematics in D’Orbigny and Sahara 99555 angrites: implications for high-resolution chronology using extinct chronometers. *Geochimica et Cosmochimica Acta* 73, 5202–5211.
- Steele R. C. J. and McKeegan K. D. (2014) Aqueous alteration on the CI parent body: Mn-Cr ages of secondary carbonate formation. *The 77<sup>th</sup> Annual Meteoritical Society Meeting*. 5438 (Abstract).
- Stöffler D., Keil K., and Scott E. R. D. (1991) Shock metamorphism in ordinary chondrites. *Geochimica Cosmochimica Acta* 55, 3845-3867.
- Sugiura N., Ichimura K., Fujiya W., and Takahata N. (2010) Mn/Cr relative sensitivity factors for synthetic calcium carbonate measured with a NanoSIMS ion microprobe. *Geochemical Journal* 44, e11-e16.
- Taylor H. P. (1977) Water/rock interactions and the origin of H<sub>2</sub>O in granitic batholiths. *Journal of the Geological Society* 133, 509-558.
- Tenner T. J., Nakashima D., Ushikubo T., Kita N. T., and Weisberg M. K. (2015) Oxygen isotope ratios of FeO-poor chondrules in CR3 chondrites: Influence of dust enrichment and H<sub>2</sub>O during chondrule formation. *Geochimica et Cosmochimica Acta* 148, 228-250.
- Tonui, E. K., Ngo, H. H., and Papanastassiou, D. A. (2003) Rb–Sr and Sm–Nd study of the D’Orbigny angrite. *Lunar and Planetary Science XXXIV*, #1812 (Abstract).
- Trinquier A., Birk J.-L., Allègre C. J., Göpel C., and Ulfbeck D. (2008)  $^{53}\text{Mn}$ – $^{53}\text{Cr}$  systematics of the early Solar System revisited. *Geochimica et Cosmochimica Acta* 72, 5146-5163.
- Tyra M. A., Farquhar J., Wing B. A., Benedix G. K., Jull A. J. T., Jackson T., and Thiemens M. H. (2007) Terrestrial alteration of carbonate in a suite of Antarctic CM chondrites: Evidence from oxygen and carbon isotopes. *Geochimica et Cosmochimica Acta* 71, 782-795.
- Tyra M. A., Brearley A. J., Hutcheon I. D., Ramon E., Matzel J., Weber P. (2009) Carbonate formation timescales vary between CM1 chondrites ALH84051 and ALH 84034. *40<sup>th</sup> Lunar and Planetary Science Conference*. #2474 (Abstract).
- Tyra M. A., Brearley A. J., Matzel J., and Hutcheon I. D. (2010) Types and timescales of secondary carbonates in CR1 chondrite GRO 95577. *41<sup>st</sup> Lunar and Planetary Science Conference*, #2614 (Abstract).

- Tyra M. A., Brearley A. J., and Guan Y. (2011) Oxygen isotopic composition of secondary carbonates in CR1 chondrite GRO 95577. *Lunar and Planetary Science Conference XLII*, #1639 (Abstract).
- Van Orman J. A., Cherniak D. J., and Kita N. (2014) Magnesium diffusion in plagioclase: Dependence on composition, and implications for thermal resetting of the  $^{26}\text{Al}$ - $^{26}\text{Mg}$  early solar system chronometer. *Earth and Planetary Science Letters* 385, 79-88.
- Van Schmus, W.R. and Wood, J.A., 1967. A chemical-petrologic classification for the chondritic meteorites. *Geochimica Cosmochimica Acta* 31, 747-765.
- Velbel M. A., Long D. T., and Gooding J. L. (1991) Terrestrial weathering of Antarctic stone meteorites: Formation of Mg-carbonates on ordinary chondrites. *Geochimica et Cosmochimica Acta* 55, 67-77.
- Walker R. J., Horan M. F., Morgan J. W., Becker H., Grossman J. N., Rubin A. E. (2002) Comparative  $^{187}\text{Re}$ - $^{187}\text{Os}$  systematics of chondrites: Implications regarding early solar system processes. *Geochimica et Cosmochimica Acta* 66, 4187-4201.
- Walker R. J., Puchtel I. S., Yin Q.-Z. (2013)  $^{187}\text{Re}$ - $^{187}\text{Os}$  isotopic and highly siderophile element abundance systematics of the Sutter's Mill meteorite: clues to late-stage secondary processes acting on chondrites. *44<sup>th</sup> Lunar and Planetary Science Conference* #1964 (Abstract).
- Weisberg M. K. and Huber H. (2007) The GRO 95577 CR1 chondrite and hydration of the CR parent body. *Meteoritics & Planetary Science* 42, 1495-1503.
- Weisberg M. K., Prinz M., Clayton R. N., and Mayeda T. K. (1993) The CR (Renazzo-type) carbonaceous chondrite group and its implications. *Geochimica et Cosmochimica Acta* 57, 1567-1586.
- Weisberg M. K., Prinz M., Clayton R. N., Mayeda T. K., Grady M. M. and Pillinger C. T. (1995) The CR chondrite clan. *Proceedings from the NIPR Symposium of Antarctic Meteorites* 8, 11-32.
- Weisberg M. K., McCoy T. J. and Krot A. N. (2006) Systematic and evaluation of meteorite classification. In *Meteorites and the Early Solar System II* (eds. Lauretta D. S. and McSween H. Y.), pp. 19-52.

- Wilson L., Keil K., Browning L. B., Krot A. N., and Bourcier W. (1999) Earth aqueous alteration, explosive disruption, and reprocessing of asteroids. *Meteoritics & Planetary Science* 34, 541-557.
- Wlotzka F. (1993) A weathering scale for the ordinary chondrites. *Meteoritics* 28, 460 (Abstract).
- Yamakawa A. and Yin Q.-Z. (2013) The chromium isotopic studies of Sutter's Mill CM-type carbonaceous chondrite: implications for isotopic heterogeneities of the Solar System. *44<sup>th</sup> Lunar and Planetary Science Conference* #2418 (Abstract).
- Young E. D. (2001) The hydrology of carbonaceous chondrite parent bodies and the evolution of planet progenitors. *Philosophical Transactions: Mathematical, Physical and Engineering Sciences* 539, 2095-2110.
- Young E. D. and Russell S. S. (1998) Oxygen reservoirs in the early solar nebula inferred from an Allende CAI. *Science* 282, 452– 455.
- Young E. D., Ash R. D., England P., and Rumble D. (1999) Fluid flow in chondritic parent bodies: Deciphering the compositions of planetesimals. *Science* 286, 1331-1335.
- Zanda B., Bourot-Denise M., Perron C., and Hewins R. H. (1994) Origin and metamorphic redistribution of silicon, chromium, and phosphorous in the metal of chondrites. *Science* 265, 1846-1849.
- Zhang F., Xu H., Konishi H., Kemp J. M., Roden E. E., and Shen Z. (2012) Dissolved sulfide-catalyzed precipitation of disordered dolomite: Implications for the formation mechanism of secondary dolomite. *Geochimica et Cosmochimica Acta* 97, 148-165.
- Zheng Y.-F. (1991) Calculation of oxygen isotope fractionation in metal oxides. *Geochimica et Cosmochimica Acta* 55, 2299-2307.
- Zheng Y.-F. (1993) Calculation of oxygen isotope fractionation in hydroxyl-bearing silicates. *Earth and Planetary Science Letters* 120, 247-263.
- Zheng Y.-F. (1995) Oxygen isotope fractionation in magnetites: structural effect and oxygen inheritance. *Chemical Geology* 121, 309-316.
- Zheng Y.-F. (1998) Oxygen isotope fractionation between hydroxide minerals and water. *Physics and Chemistry of Minerals* 25, 213-221.
- Zheng Y.-F. (1999) Oxygen isotope fractionation in carbonate and sulfate minerals. *Geochemical Journal* 33, 109-126.

- Zheng Y.-F. (2011) On the theoretical calculations of oxygen isotope fractionation factors for carbonate-water systems. *Geochemical Journal* 45, 341-354.
- Ziegler K. and Agee C. B. (2014) The oxygen isotope systematics of the unequilibrated ordinary chondrites. *Meteoritics & Planetary Science Supplement* 76, #5130 (Abstract).
- Ziegler K., and Garvie A. J. (2013) Bulk oxygen-isotope compositions of different lithologies in Sutter's Mill. *76<sup>th</sup> Annual Meteoritical Society Meeting*, #5225 (Abstract).
- Ziegler K., Agee C. B., and Connolly H. C. (2014) The oxygen isotope systematics of the L3.00 ordinary chondrite NWA 7731, and a comparison to LL3.00 Semarkona. *Lunar and Planetary Science Conference XLV*, #2468 (Abstract).
- Zolensky M. E., Barrett R., and Browning L. (1993) Mineralogy and composition of matrix and chondrule rims in carbonaceous chondrites. *Geochimica et Cosmochimica Acta* 57, 3123–3148.
- Zolotov M. Y., Morlok A., and Libourel G. (2015) Microchemical environments of aqueous alteration in CR chondrites: chemical equilibrium models. *46<sup>th</sup> Lunar and Planetary Science Conference*. #1470 (Abstract).